UCLouvain

Geodesic explorations in the gravimagnetic dipole spacetime: effective potentials for gravity's attraction

Doctoral dissertation presented by

Clémentine Dassy

in fulfilment of the requirements for the degree of Doctor in Sciences.

Thesis Jury

Prof. Jan Govaerts	Supervisor	Université catholique de Louvain
Prof. Philippe Ruelle	President	Université catholique de Louvain
Prof. Giacomo Bruno	Secretary	Université catholique de Louvain
Prof. Geoffrey Compère Research Director F.R.S. – F.N.R.S.		Université libre de Bruxelles
Prof. Andrea Campoleoni Research Associate F.R.S. – F.N.R.S.		Université de Mons

August 27, 2026

Remerciements/Acknowledgements

Il m'est impossible de nommer ici toutes les personnes qui m'ont permis de mener cette thèse à bien, à moins que vous n'ayez beaucoup de temps devant vous, des vivres, et de l'eau. Cependant, certaines d'entre elles méritent tout de même une mention spéciale.

Tout d'abord, je souhaiterais remercier le Prof. Jan Govaerts, mon promoteur, sans qui tout ceci n'aurait jamais été possible. Je me rappelle du premier cours de physique que j'ai pu suivre à l'UCLouvain, le vôtre (Physique Générale 1: Mécanique), où votre gentillesse, votre générosité dans le partage de la connaissance, et votre érudition (qui ne se limite pas à la physique) étaient déjà évidentes. Ces six années de thèse sous votre supervision m'ont énormément apporté, autant sur le plan scientifique qu'humain. Vous m'avez transmis bien plus que des connaissances en physique : une manière d'aborder les problèmes avec curiosité, rigueur et enthousiasme, mais aussi le plaisir de prendre le temps de réfléchir aux idées, d'en discuter, et de les partager. Je garderai un excellent souvenir de nos discussions. Merci de m'avoir aidée à prendre confiance en moi et d'avoir été un mentor aussi inspirant que bienveillant pendant toutes ces années.

Je souhaite également remercier les membres de mon jury pour le temps qu'ils m'ont consacré et leur lecture attentive. Vos commentaires sur le texte et vos questions lors de la défense privée m'ont donné l'occasion de compléter et clarifier plusieurs aspects de cette thèse.

Du CP3, je voudrais tout d'abord remercier Carinne, Stéphanie et Agnessa. Votre gentillesse et votre écoute attentive, mais également votre disponibilité et efficacité pour régler toutes sortes de questions administratives et pratiques, sans oublier vos biscuits, vos chocolats, ainsi que votre légendaire don lorsqu'il s'agit de résoudre tout problème lié à la machine à café ont indubitablement contribué à l'achèvement de cette thèse en temps et en heure.

Merci également à Antoine, Yannis et Valentin pour nos discussions interminables sur tous les sujets, nos commérages, et le soutien mutuel que nous nous sommes apporté.

I would also like to thank the DnD team—Karlijn, Mathieu, Zak, Chris, Paul, Rogan, Antoine—frantically stealing anything that was not nailed down, casually discussing the murder of NPCs in front of them, and

lecturing monsters about not eating people have been a great source of joy.

Many thanks as well to the lunch team at CP3. I'm not sure why we always ended up talking about cannibalism or useless inventions, but it sure was pleasant.

I am also grateful to the Physics Project Days team—Anna, Jérôme, Pierre, Baptiste—participating to the organisation of this project has been one of the most enriching experiences of my time at UCLouvain.

I would like to thank Rafael Aoude for talking about the sphere area curvature formula not holding on Earth during the Physics Project Days 2023 and other ant-ics.

Je remercie également les assistant.e.s de l'Ecole de Physique, nos vins chauds et nos diverses anecdotes concernant les séances d'exercices, laboratoires et monitorats vont me manquer.

En dehors du CP3, je me dois de remercier mes ami.e.s : Victoria, Corentin (cette primitive ne m'a finalement servi a rien mais merci de me l'avoir calculée quand même), Maxime, Marine, Sarah, Guillemette, Thibault, ainsi que le groupe des Math 8… Merci pour votre humour, votre soutien, les barbecues, les soirées de folie (cocktail ou thé), et les séances de sport, qui m'ont permis de rester (globalement) saine d'esprit.

Merci Corail et Rhubarbe. Miaou miaou, miaou miaou miaou.

Je souhaite également remercier l'entièreté de ma famille mais plus particulièrement ma cousine Marie, nos visionnages de films d'horreur m'ont permis de relativiser. Enfin, mes parents, sans qui je ne serais jamais arrivée jusque là, merci pour votre soutien inconditionnel, votre patience et votre confiance en moi. À mon frère Louis, tu sais toujours me dire ce que j'ai besoin d'entendre (et au bon moment en plus !). Merci pour votre soutien tout au long de ces années.

Une thèse est parfois décrite comme une longue quête solitaire (en effet), mais la mienne aurait certainement été beaucoup plus difficile (et beaucoup moins amusante) sans toutes les personnes qui m'ont accompagnée sur le chemin. Merci donc à toutes celles et ceux qui ont contribué, de près ou de loin, à cette aventure.

Ma gratitude va également à l'UCLouvain pour le poste d'assistante à l'École de Physique qui m'a été confié. Ce financement a rendu possible la réalisation de cette thèse et m'a aussi offert une expérience formatrice, tant sur le plan de l'enseignement que du développement académique.

Associated Publications:

[1] Clémentine Dassy and Jan Govaerts,"Deformed Hopfion-Rañada Knots in ModMax Electrodynamics", *J. Phys. A*, vol. 54, no. 26, pp. 265201, 2021.

[2] Clémentine Dassy and Jan Govaerts,"Velocity rotation curves in the equal mass and net null NUT charge gravimagnetic dipole spacetime", *Class. Quant. Grav.* vol. 43, pp. 035005, 2026.

Associated Proceedings:

[3] Clémentine Dassy and Jan Govaerts,"Light deflection in the gravimagnetic dipole spacetime", *J. Phys.: Conf. Ser.*, vol 317, no. 1, pp 012013, feb 2026.

Associated Unpublished Manuscripts:

[4] Clémentine Dassy and Jan Govaerts,"Integrating Numerically a Conservative Hamiltonian Dynamics: A Two-Step Iterative Process", 2023, unpublished.

TABLE OF CONTENTS

Introduction **1**

1 The gravimagnetic dipole **7**
1.1 A brief history of the gravimagnetic dipole solution 8
1.2 The metric and the metric functions 13
1.3 The metric functions in the equatorial plane 17
1.4 Structure 19
1.4.1 Condition on the absence of a ring singularity . . . 19
1.4.2 Misner string 21
1.4.3 Horizons and ergoregions 23
1.4.4 A detour in the closed timelike curves and causality 26
1.5 The global picture 33
1.6 Back to the Kerr spacetime 34
1.7 Summary 35

2 Circular orbits, proper distances and effective potentials in stationary spherically or axially symmetric spacetimes **37**
2.1 A definition of velocity 39
2.2 The geometric radial distance 44
2.3 Geodesics of free particles 46
2.4 Some considerations on effective potentials 47
2.4.1 Effective potential I: radial effective potential . . . 48
2.4.2 Effective potential II: Hamiltonian-constraint effective potential 49

2.4.3 Effective potential III: effective impact parameter potential . . . 52
2.5 Two examples of spacetime metrics . . . 56
2.6 The Schwarzschild spacetime . . . 57
2.6.1 The velocity . . . 58
2.6.2 The geometric radius . . . 62
2.6.3 The effective potential . . . 65
2.7 The Kerr spacetime . . . 70
2.7.1 The velocity . . . 73
2.7.2 The geometric radius . . . 79
2.8 Summary . . . 87

3 Velocity rotation curves in the equatorial plane of the gravimagnetic dipole spacetime 95
3.1 Proper distance and proper radius . . . 97
3.2 Geodesics of free particles . . . 100
3.3 The effective potential for circular orbits . . . 101
3.3.1 The massless case . . . 103
3.3.2 The massive case . . . 107
3.4 What happens on the chronology boundary? . . . 107
3.5 Velocities for circular orbits in the gravimagnetic dipole spacetime . . . 108
3.5.1 The massless case . . . 109
3.5.2 The massive case . . . 109
3.6 Constructing the velocity rotation curve: an example with $\nu = 0.6$ . . . 110
3.6.1 Retrograde orbits . . . 113
3.6.2 Prograde orbits . . . 119
3.7 General position and stability of circular orbits . . . 124
3.8 General velocity graphs . . . 129
3.8.1 Massless particle . . . 131
3.8.2 Massive particle . . . 135
3.8.3 Comparison with the gravito-electromagnetic approximation . . . 135
3.9 Summary . . . 136

4 Off the equatorial plane circular orbits **139**
4.1 The impact parameter effective potential specialised for the gravimagnetic dipole spacetime 140
4.1.1 Inside the ergoregion 141
4.1.2 Outside the ergoregion 143
4.2 Conditions to have circular orbits 143
4.3 Qualitative analysis of the impact parameter effective potential levels 147
4.3.1 Circular orbits 147
4.3.2 Bound orbits 150
4.4 Summary 152

5 A first foray into light bending **155**
5.1 Photon deflection in the equatorial plane 156
5.2 An exploration of light deflection along the vertical axis . . 164
5.3 Summary 169

Conclusion **175**

A Mathematical details **183**
A.1 A particle that starts out in the equatorial plane stays in the equatorial plane 183
A.2 Sphere area on Earth doesn't hold 187
A.3 Stability of circular orbits from an effective potential . . . 189
A.4 Integrals for the proper radius 191

B A detour in causality **193**
B.1 Some classical physics and causality 194
B.2 Can particles reach the chronology boundary in the equatorial plane of the gravimagnetic dipole spacetime? 197

C Electromagnetic Knots and ModMax **203**
C.1 Electromagnetic knots: non trivial vacuum solutions and the topological nature of electromagnetism 204
C.2 ModMax 205

Bibliography **207**

INTRODUCTION

> "Rien dans la vie n'est à craindre, tout est à comprendre. C'est maintenant le moment de comprendre plus, afin de craindre moins."
>
> — Maria Skłodowska-Curie (1867 – 1934)

At the very beginning of this year, a paper reported the discovery of baked sediments, heat-fractured tools, and iron pyrite fragments in the region that is now known as Suffolk, England [5, 6]. The authors argue that these artefacts provide evidence of fire-making by early Neanderthals approximately 400,000 years ago—350,000 years earlier than what was previously thought.

This discovery underscores, in my opinion, that it is much harder to prove the absence of something than its presence, and that one small piece of information can completely overturn the theories we have about a particular subject. We can extend this to the origins of human curiosity: when did we first look up and wonder? When did we first try to understand how we came to be, the motion of celestial bodies, the nature of light, the fabric of spacetime itself?

History has shown us, time and again, that science does not march steadily forward. Long periods of incremental progress through established framework are punctuated by sudden, dramatic shifts that rewrite the rules entirely [7]. Theories once considered true are abandoned: in physics, the ether, the steady-state universe, the existence of Vul-

can [8–10]; in other domains, the four cardinal humours, spontaneous generation, phrenology [11–13] to cite but a few. What we think we know today may well be overturned tomorrow.

This is particularly interesting to consider when we examine how we do science, and more specifically, who gets to participate in the scientific endeavour. Across all economic, ethnic, or social divides, I cannot help but notice how often women's contributions—direct or indirect—have been overlooked or minimised [14, 15]. What answers, and furthermore what questions are we missing today? Which of the answers that we accept today will we have to revisit tomorrow? The opportunity to contribute, even modestly, to this profoundly human quest for understanding certainly gives meaning to one's own scientific journey.

Among the many open questions in gravitation, one has persisted for several decades: the apparent mismatch between the observed rotation curves of galaxies and the predictions obtained from the visible matter alone [16]. Spiral galaxies rotate at velocities that remain approximately constant far beyond their luminous regions, whereas Newtonian gravity and general relativity would predict a significant decrease if only the observed baryonic matter were taken into account.

This discrepancy is illustrated in Fig. 1, where the observed rotation curve of NGC 3198—"one of the best poster children for flat rotation curves" [17]—is compared with the contribution expected from its measured baryonic content [18]. While the visible matter accounts for the inner part of the rotation curve, it fails to reproduce the nearly flat behaviour observed at large radii.

The standard interpretation of this discrepancy invokes the existence of dark matter [19], introducing an additional gravitating component whose nature remains unknown. Alternative approaches, based on modifications of gravity [20] or on the exploration of less familiar solutions of Einstein's equations, have also been investigated. In this context, understanding the behaviour of geodesics in non-trivial spacetimes provides a valuable connection between exact solutions of general relativity and observable gravitational phenomena.

Determining how the velocities of circular orbits emerge from increasingly complex exact solutions of Einstein's equations is therefore worthwhile in its own right, both as a mathematical problem and as a way of exploring the phenomenological implications of relativistic spacetimes.

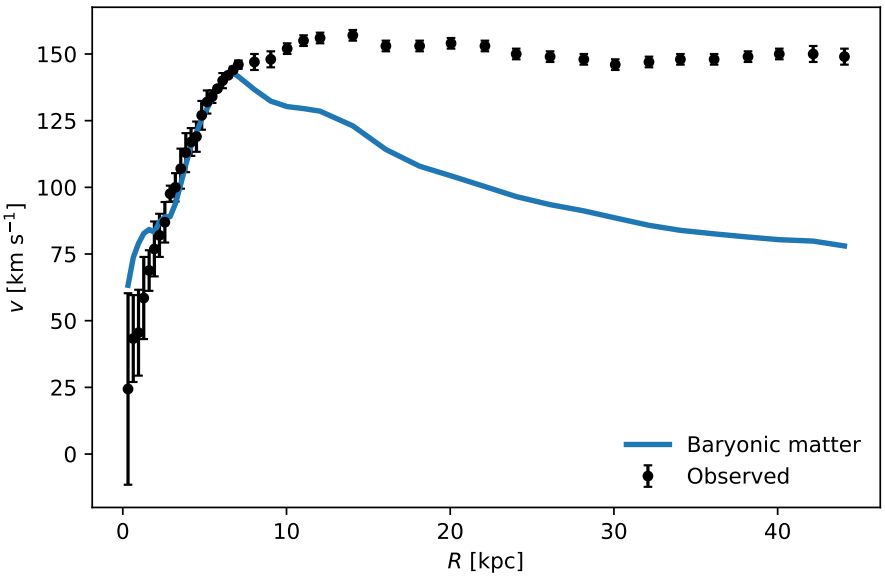


Figure 1: Rotation curve of the spiral galaxy NGC 3198. Black points show the observed circular velocities V_{obs} as a function of galactocentric radius R, with vertical error bars indicating observational uncertainties. The blue curve represents the contribution expected from the observed baryonic matter distribution, obtained from the SPARC Newtonian mass models. The data are taken from the SPARC database of Lelli, McGaugh and Schombert [18].

Motivated by these broader questions, I seek to contribute, through this thesis, a small piece to our understanding of the rich structure of general relativity. More precisely, I study the gravimagnetic dipole spacetime, which is constructed as the non-linear superposition of two NUT solutions to Einstein's vacuum equations. The resulting metric is stationary and asymptotically flat. This spacetime is particularly interesting because, for a certain range of its parameters, it represents the simplest double black hole system in equilibrium, a configuration long sought after in general relativity. Furthermore, when the distance between the two sources is appropriately chosen, the solution reduces to a single Kerr black hole—providing a familiar reference point within this otherwise exotic spacetime.

My work focuses on understanding the structure of the gravimagnetic dipole through the study of circular geodesics: their existence, stability and corresponding velocities, in and out of the equatorial plane. I also explore the deflection of light in this spacetime, offering preliminary insights into its gravitational lensing properties. The following is a brief summary, chapter by chapter, of the main text of this thesis.

In Chapter 1, I introduce the gravimagnetic dipole spacetime by considering the history of its discovery and the motivations for addressing this particular solution to Einstein's vacuum equations. I then proceed with the mathematical expressions of the metric functions, as well as the general structure of the spacetime. I specify the parameters domain such that the solution physically represents two black holes at a fixed distance, at equilibrium with each other.

I follow up in Chapter 2 with the theoretical summary of the tools that will be used in the next chapters, particularly focusing on different definitions of effective potentials.

In Chapter 3, I combine the two previous chapters to investigate circular orbits in the equatorial plane of the gravimagnetic dipole spacetime for massive and massless particles. I determine a condition on the existence and number of circular orbits, record observations regarding their stability, and finally determine their velocities.

Chapter 4 ventures out of the equatorial plane. Mathematically, the situation becomes slightly more complicated than in Chapter 3; thus graphical methods are used to determine the qualitative characteristics of the orbits. This leads to more insights about the evolution of the number of orbits. Furthermore, the stability status of the orbits is clarified.

Finally, some preliminary investigations of photon deflection are examined in Chapter 5.

The main text of the thesis then closes with a summary of what was discovered, further research directions, and some reflections on the nature of scientific inquiry.

There are also three appendices, containing either the mathematical details that I felt did not fit with the main text (Appendix A), or were somewhat tangential to the main topic (Appendix B discusses basic elements of causality). Finally, like in science, my path to this thesis was not straightforward; as such, you will find in Appendix C a short heuristic summary about electromagnetic knots and their generalisation to non-linear extension of Maxwell's theory of electrodynamics.

CHAPTER 1

THE GRAVIMAGNETIC DIPOLE

> "Right, you've got a crooked sort of cross..." He consulted *Unfogging the Future*. "That means you're going to have 'trials and suffering'—sorry about that—but there's a thing that could be the sun... hang on... that means 'great happiness'... so you're going to suffer but be very happy..."
> "You need your Inner Eye tested, if you ask me."
>
> — J. K. Rowling, *Harry Potter and the Prisoner of Azkaban* (1999)

This chapter presents the gravimagnetic dipole metric, which serves as the foundation for the analyses developed in this work. Our aim is thus not only to present its explicit form, but also to guide the reader through the conceptual and physical motivations that shaped it. We therefore begin in Section 1.1 with a brief historical overview that led to the construction of this metric.

The complete expression of the metric, with the metric functions and various definitions therein, are given in Section 1.2. This is followed by Section 1.3, where we specialise the metric to the equatorial plane. This

reduced form plays a central role in Chapter 3, and its (relative) simplicity makes it a valuable tool through which to explore our model.

Section 1.4 examines the global properties of the spacetime, though not exhaustively, since the main focus of this thesis lies on velocity rotation curves and lensing effects. Although the gravimagnetic dipole solution is in general characterised by three independent parameters (m, k, ν), not all combinations correspond to physically acceptable configurations. In particular, the parameter k controls the global structure of the symmetry axis, including the presence of a Misner string singularity, and away from the equilibrium (or tensionless) configuration, the solution no longer describes a physically admissible isolated system, as the balance between its constituents is not ensured. In this work, we restrict ourselves to the tensionless case, and the resulting parameter reduction—made explicit in this Section—allows us, after a rescaling, to describe the spacetime using only one parameter, here chosen to be ν. Nevertheless, we identify the horizons and ergoregions, discuss causality features, and explicitly present the parameter reduction adopted throughout the text. The overall shape and organisation of the spacetime, together with schematic figures, will be summarised in the synthesising Section 1.5.

To connect this geometry with more familiar territory (and show that indeed the choice of parameters undertaken is not completely baseless), Section 1.6 demonstrates that, when choosing specific limiting values of the parameters, the gravimagnetic dipole metric reduces to the well-known Kerr solution.

Finally, Section 1.7 concludes the chapter by summarising the main results and insights presented.

1.1 A brief history of the gravimagnetic dipole solution

In 1915, Albert Einstein published what would probably be one of the most influential papers [21] in the next hundred years, his foundational paper about General Relativity. In it, he described how matter and spacetime are closely linked; in laywoman's terms, space tells matter where it can go, and matter tells space how to curve.

In mathematical terms, this can be written as the *Einstein field equations*:

$$G_{\mu\nu} + \Lambda g_{\mu\nu} = \kappa T_{\mu\nu}, \qquad \text{where } \kappa = \frac{8\pi G}{c^4}. \tag{1.1}$$

This expression is constructed from two main parts:

- ✿ The expression on the left represents spacetime: $G_{\mu\nu}$ is the Einstein tensor,

  $$G_{\mu\nu} = R_{\mu\nu} - \frac{1}{2} g_{\mu\nu} R, \tag{1.2}$$

  where $g_{\mu\nu}$ is the metric tensor, and the Ricci curvature tensor $R_{\mu\nu}$ and the scalar curvature (or Ricci scalar) R are constructed from the Riemann curvature tensor $R_{\alpha\mu\beta\nu}$:

  $$R_{\mu\nu} = g^{\gamma\delta} R_{\gamma\mu\delta\nu} \qquad \text{and} \qquad R = g^{\mu\nu} R_{\mu\nu}. \tag{1.3}$$

  The Riemann tensor, finally, is a way of measuring the intrinsic curvature of space. Λ is the cosmological constant.

- ✿ On the right-hand side, κ is the Einstein gravitational constant (constructed with Newton's constant of gravitation G and the speed of light c) and $T_{\mu\nu}$ is the stress-energy tensor, describing matter, radiation and non-gravitational force fields.

Equations in hand, the main issue becomes to find their mathematical solutions and to decide if these solutions are physically sound.

In this work, the solution we are going to consider is a solution to the *vacuum field equations*, *i.e.* the aforementioned Einstein field equations (1.1), but with no cosmological constant ($\Lambda = 0$) and no stress-energy tensor ($T_{\mu\nu} = 0$).

The first (non-trivial) exact solution to Einstein's equations is the famous Schwarzschild metric [22], discovered in 1915—approximately one month after Einstein's paper was published!—whilst Schwarzschild was serving in the German army during the first world war, and published in January of 1916. It is interesting to note that Schwarzschild himself believed it to be a purely mathematical solution with no physical reality, like Einstein would attempt to prove in his 1939 paper [23].

This solution describes a static, spherically symmetric spacetime with a point-like singularity at the center, later called a black hole*, of mass m. The next order of ideas was then to find generalisations of this solution.

On the one hand, generalising the Schwarzschild metric was done by adding different parameters to the black hole, introducing combinations of a rotation and/or an electric charge parameter: in 1916-1921 the Reissner-Nordström solution [27,28]—non-rotating and charged; in 1963 the Kerr black hole [29]—rotating and uncharged; and lastly in 1965 the Kerr-Newman [30] solution—rotating and charged. Note that when the rotation parameter is non zero, it breaks the spherical symmetry but preserves the axial symmetry, making the Kerr and Kerr-Newman solutions part of the family of stationary axisymmetric spacetimes.

On the other hand, in 1963, at the same time that the Kerr solution was being discovered, Newman, Unti and Tamburino (NUT) were publishing their paper [31] *Empty-Space Generalization of the Schwarzschild Metric*, in which in addition to the usual mass parameter m, they introduced the NUT parameter, generalising the Schwarzschild solution in a new way†. Like the rotating parameter, this breaks the spherical symmetry and makes the NUT solution an axially symmetric spacetime. This new parameter, having no obvious interpretation, raised the question of what object could produce such a gravitational field. In the same vein, there is a semi-infinite singularity on the symmetry axis—called Misner string—

*The name *black hole* has complicated origins. Whilst often attributed to John A. Wheeler, who used it in a lecture in December of 1967, Wheeler actually said it was suggested during an earlier lecture, when a member of the audience grew tired of hearing "gravitationally completely collapsed object". However, according to a reminiscence talk of the 50th anniversary of the Texas Symposium on Relativistic Astrophysics of 2013, the term had already been used in Dallas in 1963 [24]—it would go on to be written down in the January 18, 1964 issue of Science News Letter [25]—by NASA astrophysicist Hong-Yee Chiu, who organized the session. Chiu had himself heard it from a seminar in Princeton, in 1960 or 1961, from Robert Dicke, who, according to his children, was prompt to shout, when something would be lost, "Ah, it must have been sucked into the black hole of Calcutta" [26]—the name of a prison in Fort William, Calcutta, where people would go in but never come out.

†In a retrospective paper [32], Roy P. Kerr explains that his derivation of the Kerr metric was initially more general, parametrised by a constant C_2 in his notation. If $C_2 \neq 0$, the resulting metric was singular at the origin in a way that spoiled asymptotic flatness. Therefore when he published his solution in 1963 he chose to set that constant to zero. The same paper states that the non-zero constant C_2 corresponds, up to a constant factor, to what is now known as the NUT parameter, sometimes referred to as *imaginary mass* in Kerr's original formalism.

where does it come from? Is it a true singularity or just a coordinate singularity?

In the following years, multiple interpretations of the NUT spacetime would be debated. Misner [33] attempted to eliminate the singular region by introducing a periodic time, which removed the divergence mathematically but imposed a physically unsatisfying structure on time.

Bonnor [34] interpreted the singularity (in spherical coordinates at $\theta = \pi$) as a massless source of angular momentum, effectively treating the Misner string as a physical spinning rod, with a separate mass source at the center of the spacetime. However, Israel [35] later developed a mathematically rigorous framework for line sources, showing that genuine line matter distribution must satisfy well-defined distributional curvature conditions. Within this framework the Misner string fails to meet these conditions, and therefore cannot be regarded as a physical line source.

Then in 2005 Manko and Ruiz [36] demonstrated that the object most accurately sourcing the spacetime would be two semi-infinite counter-rotating singular regions with negative masses and infinitely large angular momenta, adjacent to the poles of a non rotating mass.

So, a NUT object contains some unphysical properties, such as those negative mass regions, as well as closed timelike curves; but in 2015, Clément et al. [37] showed that spacetimes with NUTs are not necessarily pathological. They showed that giving up on the Misner time periodicity condition (thus keeping the Misner string as an irremovable, quasi-regular singularity) is not as pathological as it seems; it is actually transparent to geodesic motion. Then the analytical continuation at the horizon is not problematic (Miller et al. [38])—earlier treatment had found the horizon analytically problematic because enforcing Misner's periodic time identification obstructed smooth extension across it. Once this condition is abandoned, though, Miller et al.'s analysis shows that the metric admits a regular analytic continuation: the spacetime can be extended geodesically and there is no central singularity; the whole NUT spacetime turns out to be geodesically complete in this interpretation.

However, another approach was taken earlier in 2009, at first by Manko [39] then later further developed by Clément [40–43]: they considered the non linear superposition of two corotating* NUT objects of equal masses and opposite NUT charges, separated by a fixed distance and

*The published version of Clément's paper [42] in CQG contains a typographical error ('counterrotating'), which is corrected in the revised 2026 arXiv version [43].

positioned symmetrically on the vertical axis. These conditions guaranteed an asymptotically flat metric (since the asymptotic non-flatness is directly proportional to the total NUT charge of the system), and a finite Misner string between the NUT objects. The proof of concept consisted in showing that, for an appropriate choice of parameters, the system reduces to the Kerr metric [39].

This system would come to be called the gravimagnetic dipole spacetime, due to the effective interpretation of its source, discussed in the next paragraph.

An effective description From a more phenomenological point of view, the NUT spacetime can be interpreted as the gravitational equivalent to the magnetic monopole, the Misner string then being the gravitational analogue to the Dirac string. Superposing two instances of the NUT spacetime (with opposite NUT charges) then amounts to constructing a magnetic dipole out of two magnetic monopoles, the Misner strings then connecting between the two opposite NUT charges instead of extending to infinity. The dipole is then at equilibrium when the two monopoles are at a specific distance from each other, determined by the values of m and ν. This is shown on Fig. 1.1.

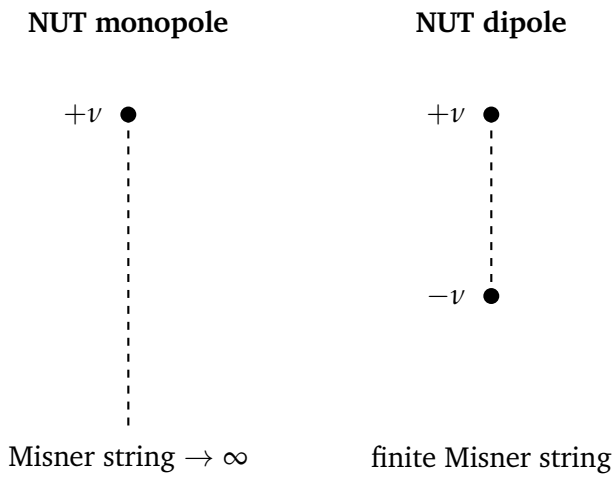


Figure 1.1: Comparison of the NUT monopole and NUT dipole in the gravitational Dirac–Misner analogy.

1.2 The metric and the metric functions

Let us now discuss the expression of the metric of the gravimagnetic dipole spacetime.

Generally, stationary and axisymmetric vacuum spacetimes admit two commuting Killing vector fields associated with their symmetries. It is therefore convenient to introduce adapted cylindrical coordinates $(x^0, x^i) = (ct, \rho, \varphi, z)$*, where the time coordinate t and the azimuthal coordinate φ are chosen such that the corresponding Killing vectors are given by ∂_t and ∂_φ, respectively. The remaining metric functions then depend only on the two coordinates (ρ, z).

In these coordinates, the Einstein vacuum equations reduce to a set of coupled partial differential equations for the metric functions. This coordinate representation, usually referred to as the Weyl–Lewis–Papapetrou form, and written in Weyl canonical coordinates [44–47], provides a particularly convenient framework for constructing and analysing exact stationary axisymmetric solutions.

One of its key features, besides its cylindrical nature, is that the geometry of stationary axisymmetric spacetimes can be conveniently represented in the half-plane (ρ, z). In particular, intervals on the boundary $\rho = 0$ correspond to rods, which encode symmetry axes, event horizons, and other distinguished loci of the spacetime.

Let us emphasize that this "rod structure" is not a physical property of the horizons themselves but rather a consequence of the Weyl coordinate representation. It provides a compact and intuitive way to visualise the global properties of stationary axisymmetric spacetimes.

Let us now consider the mathematical expression of the gravimagnetic dipole spacetime metric in these coordinates. It consists in the non linear superposition of two NUT objects with equal masses m, equal angular momenta, and opposite NUT charges $\pm\nu$, (without loss of generality we choose $\nu \geq 0$ for simplicity's sake) separated by a total distance $2k \geq 2m > 0$† and positioned symmetrically on the z-axis relative to

*Latin indices $i = 1, 2, 3$ run over space coordinates and Greek indices $\mu = 0, 1, 2, 3$ over spacetime coordinates.

†The parameter k controls the coordinate separation of the two constituents, and $k = m$ represents the limiting coalescence case (see Section 1.6). We do not consider the branch $k < m$, for which the interpretation of k as the real separation parameter is lost. More details on the constraints on the parameters (m, k, ν) will be given in Section 1.4.

$z = 0$. We work in the geometrized units system $G = 1 = c$, such that $m \equiv Gm/c^2$.

In Weyl's canonical coordinates (ct, ρ, φ, z), the metric takes the form

$$ds^2 = -f(cdt - \omega d\varphi)^2 + f^{-1}[e^{2\gamma}(d\rho^2 + dz^2) + \rho^2 d\varphi^2]. \tag{1.4}$$

The functions f, ω and $e^{2\gamma}$ depend only on (ρ, z) and are written as follows:

$$\begin{aligned} f &= \frac{|A|^2 - |B|^2}{|A+B|^2}, \\ e^{2\gamma} &= \frac{|A|^2 - |B|^2}{64 d^4 \alpha_+^2 \alpha_-^2 R_+ R_- r_+ r_-}, \\ \omega &= -4\frac{\Im[G(\bar{A} + \bar{B})]}{|A|^2 - |B|^2}, \end{aligned} \tag{1.5}$$

given the following definitions:

$$\begin{aligned} R_\pm(\rho, z) &= \sqrt{\rho^2 + (z \pm \alpha_+)^2}, \\ r_\pm(\rho, z) &= \sqrt{\rho^2 + (z \pm \alpha_-)^2}, \\ \alpha_\pm &= \sqrt{m^2 + k^2 - \nu^2 \pm 2d}, \\ d &= \sqrt{m^2 k^2 + \nu^2(k^2 - m^2)}. \end{aligned} \tag{1.6}$$

Note that these depend on our three parameters (m, k, ν), which will be further detailed later.

Finally, the functions A, B and G (which of course also depend only on (ρ, z)) are given by the following expressions:

$$\begin{aligned} A = \frac{1}{2}\Big[(d - m^2)^2 \alpha_+^2 + (d + m^2)^2 \alpha_-^2\Big](R_+ - R_-)(r_+ - r_-) \\ - \alpha_+ \alpha_- \Big[2(d^2 - m^4)(R_+ R_- + r_+ r_-) \\ + (d^2 + m^4)(R_+ + R_-)(r_+ + r_-)\Big] \\ - 2imk\nu d\Big[(\alpha_+ - \alpha_-)(R_+ r_+ - R_- r_-) \\ - (\alpha_+ + \alpha_-)(R_+ r_- - R_- r_+)\Big], \end{aligned} \tag{1.7}$$

$$
\begin{aligned}
B = & -4d\Big\{(d-m^2)\alpha_-\big[m\alpha_+(R_+ + R_-) + ik\nu(R_+ - R_-)\big] \\
& + (d+m^2)\alpha_+\big[m\alpha_-(r_+ + r_-) + ik\nu(r_+ - r_-)\big]\Big\},
\end{aligned} \tag{1.8}
$$

$$
\begin{aligned}
G = & -m(d^2+m^4)\alpha_+\alpha_-(R_+ + R_-)(r_+ + r_-) \\
& + \frac{m}{2}(R_+ - R_-)(r_+ - r_-)\big[(d-m^2)^2\alpha_+^2 \\
& \qquad + (d+m^2)^2\alpha_-^2 + 8ik\nu d^2\big] \\
& - 2m(d^2-m^4)\alpha_+\alpha_-(R_+R_- + r_+r_-) \\
& + d(R_+r_+ - R_-r_-)\Big[-(d-m^2)^2\alpha_+ + (d+m^2)^2\alpha_- \\
& \qquad - 2ik\nu m^2(\alpha_+ - \alpha_-)\Big] \\
& + d(R_+r_- - R_-r_+)\Big[(d-m^2)^2\alpha_+ + (d+m^2)^2\alpha_- \\
& \qquad + 2ik\nu m^2(\alpha_+ + \alpha_-)\Big] \\
& - 2d(d-m^2)\alpha_-\Big[(\alpha_+ + 2m - z)(m\alpha_+ + ik\nu)R_+ \\
& \qquad - (\alpha_+ - 2m + z)(m\alpha_+ - ik\nu)R_-\Big] \\
& - 2d(d+m^2)\alpha_+\Big[(\alpha_- + 2m - z)(m\alpha_- + ik\nu)r_+ \\
& \qquad - (\alpha_- - 2m + z)(m\alpha_- - ik\nu)r_-\Big].
\end{aligned} \tag{1.9}
$$

The functions f and $e^{2\gamma}$ are dimensionless whilst ω has a dimension of length, ensuring that every term in eq. (1.4) has proper dimensions.

For ease of use, here are the non-vanishing entries of the metric and its inverse:

$$
\begin{cases}
g_{tt} = -f, \\
g_{t\varphi} = f\omega, \\
g_{\varphi\varphi} = \dfrac{\rho^2}{f} - f\omega^2, \\
g_{\rho\rho} = g_{zz} = \dfrac{e^{2\gamma}}{f},
\end{cases}
\qquad
\begin{cases}
g^{tt} = -\dfrac{1}{f} + \dfrac{f\omega^2}{\rho^2}, \\
g^{t\varphi} = \dfrac{f\omega}{\rho^2}, \\
g^{\varphi\varphi} = \dfrac{f}{\rho^2}, \\
g^{\rho\rho} = g^{zz} = \dfrac{f}{e^{2\gamma}}.
\end{cases}
\tag{1.10}
$$

This metric is asymptotically flat, with total mass $M = 2m$ and total angular momentum $J = 2k\nu$ [39].

Introducing the parameters

$$\sigma \equiv \frac{\alpha_+ + \alpha_-}{2m}, \qquad \text{and} \qquad \delta \equiv \frac{\alpha_+ - \alpha_-}{2m}, \tag{1.11}$$

allows for a handful of useful identities involving $\alpha_\pm$, d, k, ν, σ, δ, and m:

$$\begin{aligned}
&4d = \alpha_+^2 - \alpha_-^2 = 4m^2\sigma\delta,\\
&k^2\nu^2 = m^4(\sigma^2-1)(\delta^2-1),\\
&k^2\nu^2 = (d \pm m^2)^2 - m^2\alpha_\pm^2,\\
&d^2 - m^4 = (m^2+\nu^2)(k^2-m^2),\\
&d \pm m^2 \pm m\alpha_\pm = m^2(\sigma+1)(\delta\pm 1),\\
&(d-m^2)\alpha_+ + (d+m^2)\alpha_- = 2m^3\delta(\sigma-1),\\
&(d+m^2)\alpha_+ + (d-m^2)\alpha_- + 4md = 2m^3\delta(\sigma+1)^2,\\
&k^2 - \nu^2 = \alpha_\pm \mp 2d - m^2.
\end{aligned} \tag{1.12}$$

Thus the metric only depends on three parameters, which can be chosen as three different sets: (m,k,ν), (m,α_+,α_-) or (m,σ,δ); in the literature, these sets of parameters are used interchangeably to minimise the length of mathematical expressions. In this work, we will use the (m,k,ν) set. Section 1.4 will provide the conditions on k required for the solution to remain in a physically acceptable regime, ensuring the absence of undesirable geometrical features and pathological structures.

A note on the construction of the metric We will not go into the full details of the solution's construction, since *(i)* it is not the focus of this thesis and *(ii)* it would be prohibitively long. Instead, we introduce here only those elements that will be relevant in the following, in particular in Section 1.4.1.

The gravimagnetic dipole solution is obtained by non linearly superposing two single corotating NUT solutions with the same mass but opposite values of the NUT parameter. For our purposes, it is sufficient to know that the construction makes use of the Ernst formulation of the Einstein equations for stationary axisymmetric spacetimes. In this formulation, finding such a solution to Einstein equations reduces to finding the complex function $\mathcal{E}$ satisfying the Ernst equation [48]:

$$[\mathrm{Re}\,(\mathcal{E})]\,\nabla^2\mathcal{E} = \nabla\mathcal{E}\cdot\nabla\mathcal{E}, \tag{1.13}$$

which can be expressed in Weyl-Papapetrou coordinates as

$$(\mathcal{E}+\bar{\mathcal{E}})\left(\mathcal{E}_{,\rho,\rho}+\rho^{-1}\mathcal{E}_{,\rho}+\mathcal{E}_{,z,z}\right)=2\left(\mathcal{E}_{,\rho}^{2}+\mathcal{E}_{,z}^{2}\right), \tag{1.14}$$

where the comma denotes partial differentiation with respect to the coordinate that follows, and the bar means complex conjugation. This reformulation provides a convenient framework for constructing and manipulating exact stationary axisymmetric solutions without working directly with the full Einstein equations.

The construction [39] proceeds by considering two identical NUT solutions (with opposite values of ν as their sole difference) in terms of their complex Ernst potentials [36,48–50], then symmetrically translating them along the symmetry axis with respect to the origin. Their Ernst potentials can then be combined to generate the gravimagnetic dipole solution*, which are themselves written in terms of the Kinnersley potentials A and B—which are defined in the next section:

$$\mathcal{E}=\frac{A-B}{A+B}. \tag{1.15}$$

In stationary axisymmetric spacetimes, curvature singularities arise where curvature invariants diverge. In terms of the Ernst potential, this occurs precisely where the denominator $A+B$ vanishes when $\rho\neq 0$. Therefore, the purpose of introducing $\mathcal{E}$ here is simply to identify the potential locations of such singularities, which will be done in Section 1.4.1.

1.3 The metric functions in the equatorial plane

The metric functions defined in eqs. (1.5) and (1.6) are highly non-trivial and often quite unwieldy, but are found to be a bit more simple on the equatorial plane. Since the equatorial plane will be the subject of a whole chapter, we find useful to provide these expressions of the metric functions on the equatorial plane $z=0$ hereafter:

$$\begin{aligned} R\equiv R_{\pm}(\rho,z=0)&=\sqrt{\rho^{2}+\alpha_{+}^{2}},\\ r\equiv r_{\pm}(\rho,z=0)&=\sqrt{\rho^{2}+\alpha_{-}^{2}}. \end{aligned} \tag{1.16}$$

*We use the same conventions for defining the Ernst potentials as in [39].

This allows for the redefinition of the functions A, B and G in the following way:

$$\begin{aligned}
A_0 &\equiv \frac{A(\rho, z=0)}{2\alpha_+\alpha_-} = -\Big[(d^2-m^4)(R^2+r^2)+2(d^2+m^4)Rr\Big],\\
B_0 &\equiv \frac{B(\rho, z=0)}{2\alpha_+\alpha_-} = -4dm\Big[m^2(r-R)+d(r+R)\Big],\\
G_0 &\equiv \frac{G(\rho, z=0)}{2\alpha_+\alpha_-} = G_r + iG_i,\\
G_i &\equiv \Im\left[\frac{G(\rho, z=0)}{2\alpha_+\alpha_-}\right] = -k\nu d\left[(d-m^2)R+(d+m^2)r\right],\\
G_r &\equiv \Re\left[\frac{G(\rho, z=0)}{2\alpha_+\alpha_-}\right] = -m\left[(d+m^2)r+(d-m^2)R\right]\times\\
&\qquad\qquad \times\left[m^2(R-r)+d(4m+r+R)\right].
\end{aligned} \tag{1.17}$$

In this way, A_0, B_0, G_r and G_i are real for any $\rho > 0$. Note that at this stage, no additional assumptions have been imposed on the domains of the parameters (m, k, ν), other than those already stated in the definition of the metric above eq. (1.4), *i.e.* $2k \geq 2m > 0$ and $\nu \geq 0$. Consequently, $\alpha_\pm$ may be either real or imaginary. The definition of A_0, B_0 and G_r, G_i were chosen so that these quantities remain independent of $\alpha_\pm$. In any case, $\alpha_\pm$ drop out when the metric functions f, ω and $e^{2\gamma}$ are written explicitly on the equatorial plane.

$$\begin{aligned}
f &\equiv f(\rho, z=0) = \frac{A_0-B_0}{A_0+B_0} = \frac{d(-4m+r+R)+m^2(R-r)}{d(4m+r+R)+m^2(R-r)}\\
&= 1-\frac{8dm}{d(4m+r+R)+m^2(R-r)},\\
\omega &\equiv \omega(\rho, z=0) = \frac{-4G_i}{A_0-B_0} = \frac{8dk\nu}{(m^2-d)r-(d+m^2)R+4dm},\\
e^{2\gamma} &\equiv e^{2\gamma}(\rho, z=0) = \frac{A_0^2-B_0^2}{4d^4R^2r^2}\\
&= \frac{[(d+1)r+(d-1)R]^2\left\{[R(d+1)+r(d-1)]^2-16d^2\right\}}{16d^4r^2R^2}.
\end{aligned} \tag{1.18}$$

It follows that, on the equatorial plane, all the metric functions are real for any value of $\rho > 0$, $2k \geq 2m > 0$ and $\nu \geq 0$.

1.4 Structure

For $\nu = 0$, $\alpha_\pm = k \pm m$ and $d = km$ are real, and the metric, which is then static, describes a system of two non-rotating black holes of equal masses m, joined by a cosmic string of length $2\alpha_- = 2(k-m)$. When $k = m$, the two black holes coalesce back into a single Schwarzschild one.

When $\nu \neq 0$, under the condition that $\alpha_\pm$ and d are real, the metric in eq. (1.4) is stationary and consists of two black holes separated by a distance $2k$ and connected by a spinning cosmic string—called Misner string—of length $2\alpha_-$. These correspond to three sections of the z axis; the two black holes horizons for $\alpha_- < z < \alpha_+$ and $-\alpha_+ < z < -\alpha_-$, and the Misner string for $-\alpha_- < z < \alpha_-$. This is shown in Figs. 1.3 and 1.5, which are further detailed in Section 1.5.

The equal masses of the black holes $M_{H_\pm}$ and their equal angular momenta* $J_{H_\pm} = -k\nu\frac{\sigma\delta+1}{\sigma^2-1}$ are functions of the three parameters m, ν and k. Since they will not be needed in this thesis, the interested reader is invited to consult [42, 43] for more details on how these values are determined.

Asking for $\alpha_\pm$ and d to be real and non zero can be reduced, by using the identities of eq. (1.12), to the condition

$$k > k_+ \text{ or } k < k_-, \quad \text{where} \qquad k_\pm(m,\nu) = \sqrt{m^2 + 2\nu^2} \pm |\nu| \,. \tag{1.19}$$

1.4.1 Condition on the absence of a ring singularity

We now wish to constrain the parameter k by requiring that no naked ring singularity be present. In the Kerr spacetime, a ring singularity is a well-known feature of the geometry, but it is hidden behind the outer horizon for sub-extremal Kerr black holes. Given the close relationship between the gravimagnetic dipole and the Kerr geometry (see Section 1.6), it is therefore important to determine whether an analogous singular structure arises in the present solution and, if so, whether it is covered by an horizon.

The condition given in eq. (1.19) is satisfied in two disjointed parameter domains. We are going to show, however, that only the upper domain,

*Note that the spin of the black holes is opposite to that of the resulting Kerr black hole when $k = m$ (see Section 1.6). This is because the total angular momentum of the gravimagnetic dipole, $J = J_{H_+} + J_{H_-} + J_S = 2k\nu$, comprises the angular momenta of the black holes $J_{H_\pm}$ and the angular momentum of the string, $J_S = 2k\nu\frac{\sigma(\sigma+\delta)}{\sigma^2-1}$ [42, 43].

$k > k_+$, is devoid of a ring singularity, whereas the lower domain, $k < k_-$, always contains a ring singularity.

Building on the singularity condition of the Ernst potential derived at the end of Section 1.2, we can check whether there is a ring singularity in the equatorial plane by checking if the expression $A + B$ cancels for some value of ρ.

In the equatorial plane, $z = 0$, $R_+ = R = R_-$ and $r_+ = r = r_-$ (more details in section 1.3), which leads to

$$\begin{aligned} A &= -2\alpha_+\alpha_- \left[(d^2 - m^4)(R + r)^2 + 4m^4 Rr\right], \\ B &= -8dm\alpha_+\alpha_- \left[(d - m^2)R + (d + m^2)r\right]. \end{aligned} \tag{1.20}$$

For $\rho \to \infty$, $R \approx r \approx \rho$ and

$$A + B \approx -8\alpha_+\alpha_- d^2\rho^2, \tag{1.21}$$

and for $\rho = 0$, $R = \alpha_+$ and $r = \alpha_-$*, which leads to:

$$A + B = -\frac{\alpha_-\alpha_+}{8}(\alpha_+ - \alpha_-)^2 \left[(\alpha_+ + \alpha_-)^4 - 16m^4\right]. \tag{1.22}$$

A necessary condition for $A + B$ to not change sign when ρ goes from 0 to infinity is then

$$(\alpha_+ + \alpha_-)^4 > 16m^4, \tag{1.23}$$

which reduces to $\alpha_+ + \alpha_- > 2m$ since $\alpha_\pm > 0$ (condition (1.19)). From eq. (1.12),

$$(\alpha_+ + \alpha_-)^2 - 4m^2 = \frac{16k^2\nu^2}{(\alpha_+ - \alpha_-)^2 - 4m^2}, \tag{1.24}$$

we also have that $(\alpha_+ - \alpha_-) > 2m$, and thus

$$d = \frac{(\alpha_+^2 - \alpha_-)^2}{4} = \frac{1}{4}(\alpha_+ - \alpha_-)(\alpha_+ + \alpha_-) > m^2, \tag{1.25}$$

which is equivalent to $k > m$.

On the other hand, also from eq. (1.12),

$$d^2 - m^4 = (m^2 + k^2)(k^2 - m^2), \tag{1.26}$$

*We already place ourselves in the parameter domain where eq. (1.19) is verified.

we find that $k > m$ implies $d > m^2$, so that $A < 0$ and $B \leq 0$. Therefore $A + B < 0$ cannot vanish, and there is no equatorial ring.

So the necessary and sufficient condition for the absence of an equatorial ring is

$$k > m, \tag{1.27}$$

which is clearly satisfied when $k > k_+$, but violated when $0 < k < k_-$. In the following we assume $k > k_+$.

1.4.2 Misner string

The string is the coordinate singularity of finite length at coordinates $\rho = 0$, $\alpha_- < z < \alpha_+$ connecting the two black holes. Its characteristics [42,43,51] can be computed from the values the metric takes in its center (at $(\rho = 0, z = 0)$, quantities are denoted by a subscript S), in particular the string spin

$$\begin{aligned} -\frac{\omega_S}{4} &\equiv \frac{-\omega(\rho = 0, z = 0)}{4} \\ &= 2kvd\frac{d(\alpha_+ + \alpha_- + 4m) + m^2(\alpha_+ - \alpha_-)}{[d(\alpha_+ + \alpha_-) - m^2(\alpha_+ - \alpha_-]^2} \end{aligned} \tag{1.28}$$

and tension per unit length

$$\begin{aligned} \frac{1 - e^{-\gamma_S}}{4} &\equiv \frac{1 - e^{-\gamma}(\rho = 0, z = 0)}{4} \\ &= \frac{1}{4} - \frac{\alpha_+\alpha_- d^2}{[d(\alpha_+ + \alpha_-) - m^2(\alpha_+ - \alpha_-)]^2}. \end{aligned} \tag{1.29}$$

We shall not discuss here the detailed derivation of the physical interpretation of the Misner string quantities; the interested reader is referred to Refs. [52–54]. We only summarise the aspects relevant for the present discussion. The string spin measures the gravimagnetic flow associated with the Misner string [51], while the string tension is associated with the conical defect present on the string and can be interpreted as the force required to balance the interaction between the two black holes [53].

The equal masses give rise to an attractive gravitational interaction, whereas the opposite NUT charges contribute a repulsive gravimagnetic interaction. In the present convention, $e^{\gamma_S} > 1$ corresponds to a positive string tension and therefore to a net repulsive interaction, while $e^{\gamma_S} < 1$

corresponds to a negative string tension and thus to a net attractive interaction.

In the absence of an external force*, the system is thus balanced if the string is tensionless, *i.e.* if

$$e^{\gamma_S} = 1. \tag{1.30}$$

This last condition may be expressed as

$$\left(\frac{\alpha_+ - \alpha_-}{2m}\right)^2 = 2 - \left(\frac{2m}{\alpha_+ + \alpha_-}\right)^2. \tag{1.31}$$

This equation gives four solutions as allowed values for k,

$$k(m,\nu) = \pm\sqrt{\frac{m^6 + 3m^4\nu^2 \pm m^2\nu\sqrt{4m^6 + 9m^4\nu^2 + 2m^2\nu^4 + \nu^6}}{m^4 - \nu^4}}. \tag{1.32}$$

Representing in our case a distance, the positive solutions are chosen:

$$k^T_\pm(m,\nu) = \sqrt{\frac{m^6 + 3m^4\nu^2 \pm m^2\nu\sqrt{4m^6 + 9m^4\nu^2 + 2m^2\nu^4 + \nu^6}}{m^4 - \nu^4}}. \tag{1.33}$$

Putting together the reality condition on $\alpha_\pm$ and d given eq. (1.19), the absence of ring singularity in eq. (1.27) and this last tensionless condition in eq. (1.33) gives rise to a unique solution for k:

$$k^T_+(m,\nu) = \sqrt{\frac{m^6 + 3m^4\nu^2 + m^2\nu\sqrt{4m^6 + 9m^4\nu^2 + 2m^2\nu^4 + \nu^6}}{m^4 - \nu^4}}. \tag{1.34}$$

The conditions detailed in the last paragraphs are presented in Fig. 1.2, where $m = 1$. The horizontal axis represents ν and the vertical axis the possible values of k. The orange dashed line (k_+) and red dotted line (k_-) represent the limiting values of k such that $\alpha_\pm$ and d are real and posi-

*When, for fixed m and ν, the parameter k is decreased (*i.e.* pushing the black holes together) to its lowest possible value k_+—see eq. (1.19)—e^{γ_S} diverges whilst the string length $2\alpha_-$ goes to 0, which means there is a singularity at $\rho = 0 = z$, unless, simultaneously, $\alpha_+ + \alpha_- \to 0$, *i.e.* $k \to m$, which is possible only if $\nu = 0$. In summary, when approaching $k \to k_+$ from above, whatever the values of m and $\nu \neq 0$, the repulsive force between the black holes diverges and they cannot coalesce together whatever the amount of external force applied. Interestingly enough, it is also possible for the black holes to coalesce back together when condition (1.19) is simply not verified, as will be seen in Section 1.6.

tive numbers; the corresponding lightly coloured (pale orange and pale green) zones depict the authorized values of k such that the inequality in eq. (1.19) is verified. The green dashdotdotted line (visually overlapping k_-) represents the negative value in eq. (1.33) that guarantees a tensionless Misner string but is smaller than $m \equiv 1$. The plain blue line represents k_+^T, and finally the purple dashdotted line represents the value of $k = m = 1$ such that the system reduces to a Kerr black hole (this will be explored in Section 1.6).

The system that was chosen to be studied hereafter is such that the two corotating black holes are at equilibrium with each other, at a fixed distance, so the value $k \equiv k_+^T$ will be used. The system can thus be entirely described with only two parameters, the NUT charge ν and the mass m.

A last simplification can occur: when the parameters ν, k and m, as well as the coordinates ρ, φ, z and ct are divided by m, the metric is fully dimensionless. The symbols will be kept the same for readability's sake, but keep in mind now that every quantity is dimensionless, and that $m = 1$.

1.4.3 Horizons and ergoregions

Since the metric elements defined in eq. (1.10) are independent of the coordinates (t, φ), any observer who moves along a world line of constant (ρ, z) with uniform angular velocity should see no change in the spacetime geometry around her. Such an observer is called *stationary* relative to the local geometry.

However, this observer cannot have just any value for her angular velocity Ω. The only values of Ω that are allowed are such that the 4-velocity of the observer is timelike, *i.e.* the 4-velocity lies in the future light cone. Mathematically, this can be expressed as asking:

$$g_{tt} + 2g_{t\varphi}\Omega + g_{\varphi\varphi}\Omega^2 < 0. \tag{1.35}$$

The angular velocities of stationary observers are thus constrained by

$$\Omega_- < \Omega < \Omega_+, \tag{1.36}$$

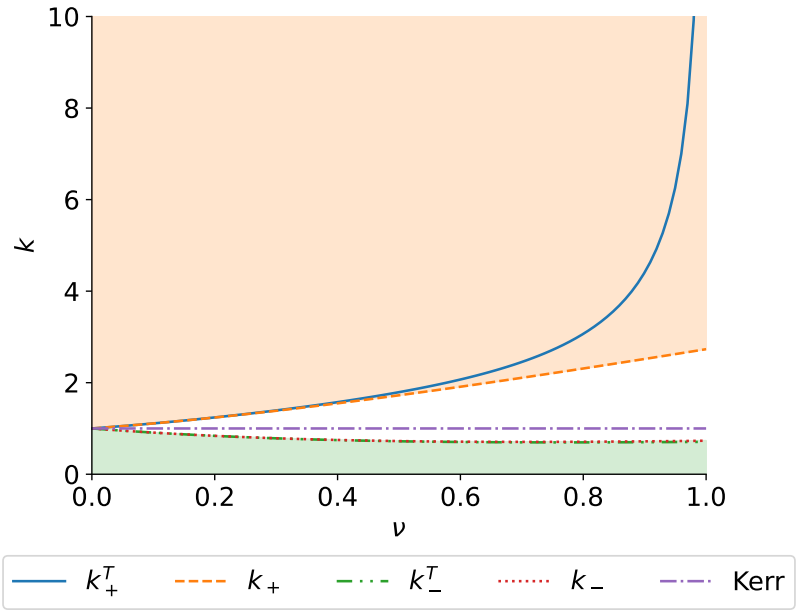


Figure 1.2: For this figure, $m = 1$. The horizontal axis represents ν and the vertical axis possible values of k. The orange dashed line (k_+) and red dotted line (k_-) represent the limiting values of k such that $\alpha_\pm$ and d are real and positive numbers; the corresponding lightly coloured (pale orange and pale green) zones depict the authorised values of k such that the inequality in eq. (1.19) is verified. The green dashdotdotted line (visually overlapping k_-) represents the negative value in eq. (1.33) that guarantees a tensionless Misner string but is smaller than $m = 1$. The plain blue line represents k_+^T, and finally the purple dashdotted line represents the value of k such that the system reduces to a Kerr black hole (this will be explored in Section 1.6).

where

$$\Omega_\pm = \frac{g_{t\varphi}}{g_{\varphi\varphi}} \pm \sqrt{\left(\frac{g_{t\varphi}}{g_{\varphi\varphi}}\right)^2 - \frac{g_{tt}}{g_{\varphi\varphi}}}. \tag{1.37}$$

In the gravimagnetic dipole metric—excluding the values (ρ, z) where $g_{\varphi\varphi} \leq 0$ where causality breaks (see Section 1.4.4)—this reduces to:

$$\Omega_\pm = \frac{\pm f}{\rho \pm f\omega} \tag{1.38}$$

What does this expression mean? As a black hole rotates, it twists spacetime in the direction of the rotation, at a speed that decreases as the distance from the black hole increases—this is called frame-dragging. This leads to the definition of static limit (also called ergosurface*) which is the hypersurface inside which no static observer can exist, *i.e.* the hypersurface inside which an observer would need a faster-than-light (relative to the local spacetime) speed to appear static to an outside observer. Mathematically, this corresponds to the hypersurface where the minimum velocity Ω_- is 0, since an observer has to have a velocity that is strictly superior to Ω_-. Going back to eq. (1.37), this corresponds to an hypersurface where $g_{tt} = 0$. The volume enclosed by this surface is called the ergoregion, and this is shown in two dimensions as a plain blue line in Fig. 1.3 and in three dimensions as a yellow-to-blue surface in Fig. 1.4.

Looking at the definitions of the metric functions, asking for $g_{tt} = 0$ is a non trivial computation:

$$g_{tt} = -f = 0. \tag{1.39}$$

Numerical solutions allows us to draw the general shape of the region defined by (1.39), but we can also gain a bit of insight by looking at the extremal values: when $z = 0$, there is no solution; so the static limit does not cross the equatorial plane. However, choosing $\rho = 0$ simplifies significantly eq. (1.39) and four analytical solutions $z = \alpha_\pm$ and $z = -\alpha_\pm$ can be found easily, giving the coordinates of the poles of the ergoregions. This is, again, shown on Figs. 1.3—1.5.

Going even more inwards inside the ergoregions (so for $-\alpha_+ < z < -\alpha_-$ or $\alpha_- < z < \alpha_+$), the frame-dragging increases, *i.e.* the minimal

*Or ergosphere, usually seen in the literature when talking about the Kerr black hole, even though the surface is not exactly a sphere, but more of a squashed sphere.

value of the velocity of the observer, Ω_- increases; at the same time, Ω_+ decreases, until $\Omega_- = \Omega_+$ (here at $\rho = 0$); this is the event horizon where no stationary observers can exist. This is shown as the dotted lines in Figs. 1.3 and 1.5; it touches the static limit at its poles $(0, \pm\alpha_+)$, $(0, \pm\alpha_-)$.

These horizons take here a characteristic (for Weyl's coordinates) rod shape. This is also the case for less exotic solutions, for example the Kerr spacetime*.

When $\nu \to 1$, the length of the horizon reaches a finite value $\alpha_+ - \alpha_- = 2\sqrt{2}m$. When $\nu \to 0$, the limit for the horizons length is again finite and goes to $\alpha_+ - \alpha_- = 2m$.

1.4.4 A detour in the closed timelike curves and causality

An interesting paradox coming out of the solutions to Einstein's equations is the existence of closed timelike curves (CTC), curves that seem to allow the violation of causality.

Consider a timelike curve γ representing the worldline of a particle. A closed timelike curve is a timelike path whose endpoint coincides with its starting event, meaning that an observer following it would eventually return to the same point in space*time*. Such structures theoretically allow an observer to move back along their own wordline. This raises the possibility of influencing events that would ordinarily lie in the observer's past, thereby challenging the usual causality of spacetime and potentially giving rise to paradoxes.

The earliest example of a solution to Einstein's equations with closed timelike curves is Van Stockum's 1937 solution [55, 56], which represents an infinite cylinder of rigidly rotating dust. This solution has usually been dismissed as unphysical due to the presence of an infinitely long source.

The second interesting example allowing for the presence of closed timelike curves would be Gödel's solution [57]†, describing a stationary, homogeneous cosmological model with nonzero cosmological constant, filled with rotating dust. Again, it was dismissed as unphysical because it does not resemble our universe whose rotation is small or zero.

*The shape of the event horizons when expressed in Weyl's coordinates is briefly discussed in Section 1.6.

†He was actually the first to notice the existence of closed timelike curves.

Some other examples include the well-known Kerr black hole [29, 51], Tipler's cylinder [58], Gött's cosmic strings [59], the Kerr-Newman generalization of Kerr's black hole [30, 60], the Taub-NUT solution [31], etc.

These spacetimes include chronological regions*, devoid of closed timelike curves and achronal region(s) that contain closed timelike curves. The common boundaries between these regions are called chronological horizons [61].

For example the Kerr solution has two event horizons, $r_- < r_+$. The region $r > r_-$ is chronological, whilst the region $r < r_-$ is achronal. The inner event horizon r_- is thus called the chronological boundary. However, this chronological boundary being "hidden" behind the event horizon r_+, it is causally unrelated to the rest of the universe and usually mostly ignored in the literature.

For the gravimagnetic dipole, this is not the case. The chronology boundary (depicted in orange dotted lines in Fig. 1.3 and Fig. 1.5, and as the yellow-purple surface in Fig. 1.4) is not hidden and some precautions will have to be taken to see under which conditions particles can reach it. We will not comment on the physical reality of time travel, as this is outside of the scope of this thesis.

Over the last few decades, comments, theories and protection mechanisms against causality violation have been suggested. Here is a non-exhaustive list of the most well-known ones for the worried reader.

Some proposals have been made that would allow time travel but prevent paradoxes, for example Novikov's principle†, also called the self-consistency principle [62–64], demanding that local worldlines would be admissible only when they did not violate causality. However, this principle relies on imposing a global topological constraint: only trajectories that fit into a spacetime geometry free of paradoxes are considered admissible. Such a restriction effectively forbids time-non-orientable manifolds, despite the fact that time orientability is not itself a physical law but an open, testable question which may ultimately require quantum-level considerations.

In quantum field theory without gravity, causality is closely tied to locality, although the status of this principle can depend on the interpretation of quantum mechanics [65, 66]. Since a complete theory of

*Different terminology exists. Chronological regions are also called chronal regions.

†Some comments about classical physics and time travel can be found in Appendix B.

quantum gravity is still lacking, semi-classical gravity provides an effective framework in which quantum fields are studied on curved spacetimes.

Within this context, several toy models have been proposed to explore the behaviour of quantum systems in the presence of closed timelike curves [67–69], although their physical interpretation remains debated and no universally accepted formulation exists.

However, within the standard framework of quantum field theory in curved spacetime, the presence of closed timelike curves leads to severe conceptual and technical difficulties [70], in particular regarding the definition of quantum states and the renormalised stress-energy tensor. In addition, it has been shown that the renormalised stress-energy tensor may become divergent or ill-defined on the chronology horizon, indicating a breakdown of the semiclassical approximation.

Of course, the ideal solution to the emergence of closed timelike curves and the paradoxes they could cause would be a universal mechanism that prevents any causality issues (whatever they may be), and not *ad hoc* solutions for each case. This is what Hawking tried to do with his *chronological protection conjecture* [71]: the proposal that there may exist laws of physics—perhaps through effects beyond classical General Relativity—preventing the formation of closed timelike curves and the causal paradoxes they entail.

Another argument, this time related to time travel in the context of wormholes, is that a beam of radiation entering a wormhole mouth would spontaneously refocus before reaching the other mouth, which would have a "pileup effect" that would become strong enough as to destroy the wormhole [72].

All these results suggest that a definite answer on the existence, or not, of closed timelike curves, and on the status of the chronology protection conjecture, would require a full theory of quantum gravity.

The physical consequences of closed timelike curves, and their appearance in a real, physical spacetime being under such undecided constraints, in the following we will just show that they exist, and see what the conditions are for test particles to reach such regions of space, in the context of the gravimagnetic dipole spacetime.

In this spacetime, closed timelike curves arise whenever $g_{\varphi\varphi} \leq 0$. More generally, if $g_{\varphi\varphi} > 0$ and the coordinate t is well-defined and non-periodic, then t defines a time function since its gradient is timelike. Consequently, no closed timelike curves can exist in that region [73]. In the present

spacetime, this condition is verified since

$$g^{\mu\nu}\partial_\mu t\,\partial_\nu t = g^{tt} = -\frac{g_{\varphi\varphi}}{g_{t\varphi}^2 - g_{tt}g_{\varphi\varphi}}, \tag{1.40}$$

with $g_{t\varphi}^2 - g_{tt}g_{\varphi\varphi} > 0$ throughout the domain under consideration. Hence,

$$\mathrm{sgn}(g^{tt}) = -\mathrm{sgn}(g_{\varphi\varphi}), \tag{1.41}$$

so that $g_{\varphi\varphi} > 0$ implies that the gradient of t is timelike, making t a valid time function. Consequently, no closed timelike curves can exist in this region. Conversely, when $g_{\varphi\varphi} \leq 0$, the closed orbits of the axial Killing vector field ∂_φ become timelike, giving rise to closed timelike curves.

In the gravimagnetic dipole spacetime, this can be rewritten as

$$g_{\varphi\varphi} = \frac{\rho^2}{f} - f\omega^2 \leq 0. \tag{1.42}$$

The chronology boundary is thus defined as

$$g_{\varphi\varphi} = \frac{\rho^2}{f} - f\omega^2 = 0. \tag{1.43}$$

For $\rho = 0$, this equation has two solutions, $z = \pm\alpha_-$ (with $f = 0$), which corresponds to the extremities of the Misner string and the interior poles of the ergoregions and event horizons. This is shown in Figs. 1.3 - 1.4.

For $z = 0$, $f \neq 0$ and eq. (1.43) reduces to

$$\begin{aligned} \rho^2 - f^2\omega^2 &= 0 \\ \rho^2 - \frac{16G_i^2}{(A_0 + B_0)^2} &= 0 \end{aligned} \tag{1.44}$$

with the conventions of eq.(1.17).

As the NUT parameter ν grows, the chronology boundary grows. See Fig. 1.3, 1.4 and 1.5.

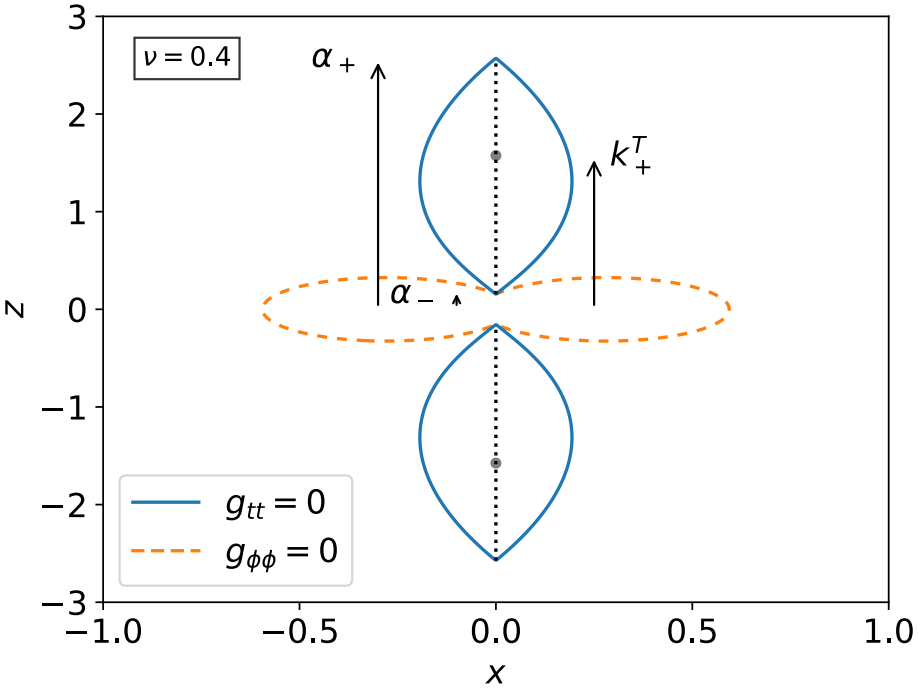


Figure 1.3: This graph shows a cut in the XZ plane of the spacetime for $\nu = 0.4, k = k^T_+$ such that the Misner string is tensionless and the system is at equilibrium. The plain blue lines represent the static limit on which $g_{tt} = 0$. The gray dots show the black holes. The dashed grey lines represent the black hole horizons. The zone between the static limit and the black hole horizons is known as the ergoregion (there are two here). The orange dashed line shows the chronology boundary $g_{\varphi\varphi} = 0$ separating the chronological region ($g_{\varphi\varphi} > 0$) from the achronal one ($g_{\varphi\varphi} < 0$). The quantities delimiting the horizons are also shown, with $\alpha_+ \approx 2.573$ and $\alpha_- \approx 0.154$, as well as the separation of the black holes $2k^T_+ \approx 3.150$.

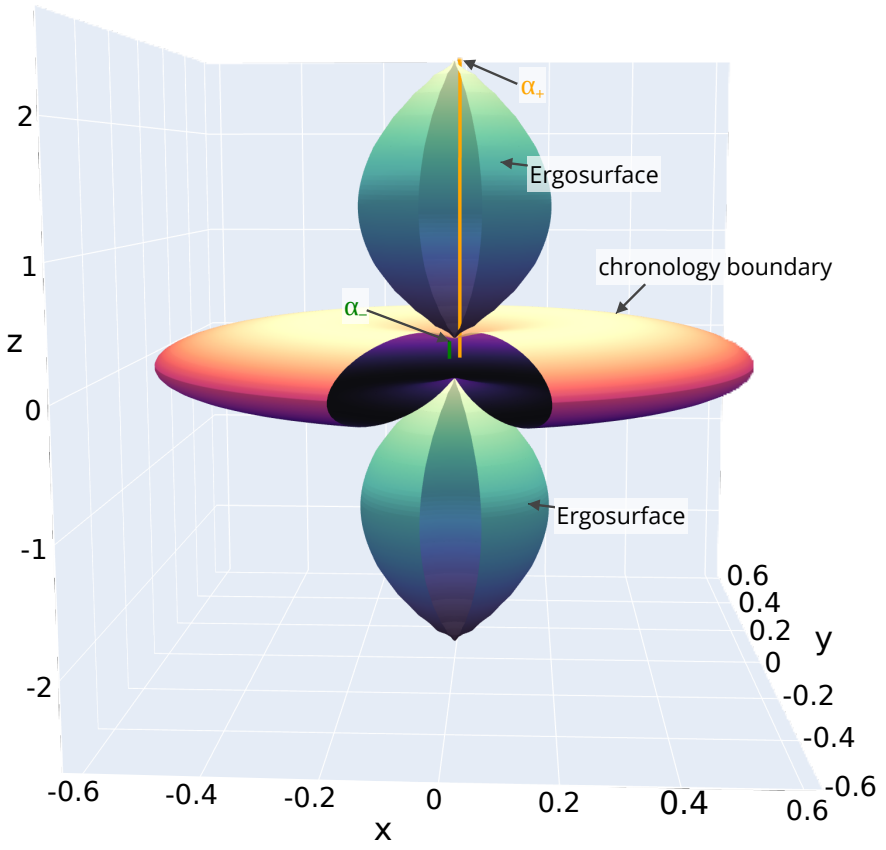


Figure 1.4: This is the 3D version of Fig. 1.3, where $\nu = 0.4$. The static limits, or ergoregions are shown in green-blue gradient. The chronology boundary is shown as a yellow-purple gradient. On the vertical axis, α_+ (orange) indicates the upper intersection of the ergosurface with the z-axis (and not pictured, the corresponding $-\alpha_+$ for the ergosurface in the negative z). The lower intersection of the ergosurface with the z axis, denoted α_- (green), is also the point where it meets the chronology boundary (again not pictured, $-\alpha_-$ corresponds to the equivalent in the negative z part of the space).

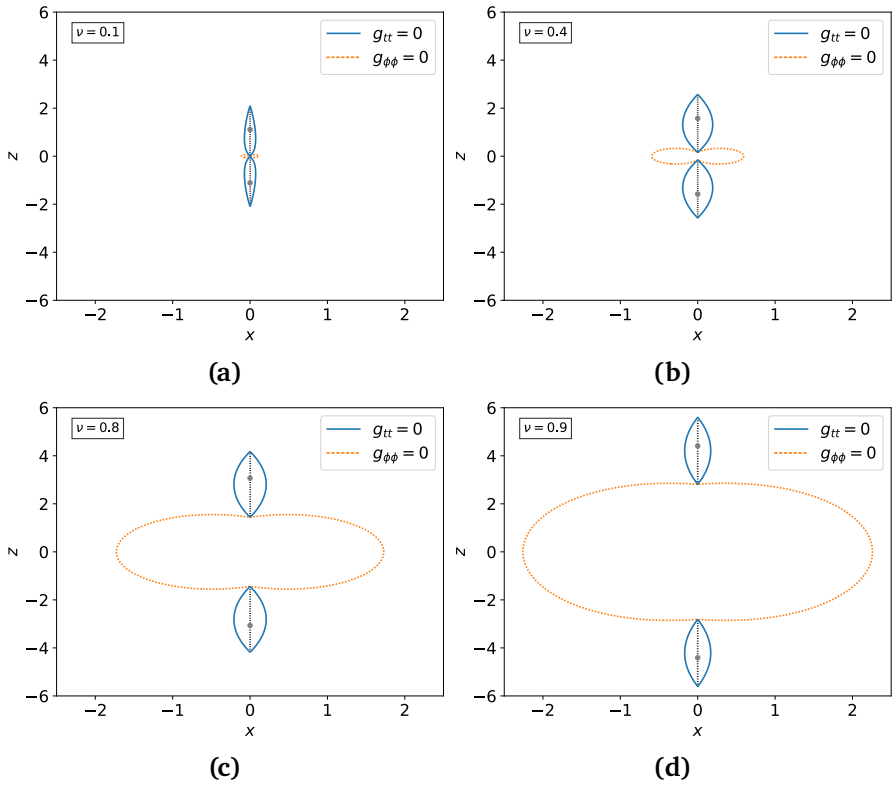


Figure 1.5: The four graphs show the cut of the spacetime along the XZ plane for four different values of the NUT parameter ν (1.5a $\nu = 0.1$, 1.5b $\nu = 0.4$, 1.5c $\nu = 0.8$, 1.5a $\nu = 0.9$. The grey dots represent the black holes. The plain blue lines represent the static limit ($g_{tt} = 0$) underwhich static observer cannot exist. The orange dotted line depicts the chronology boundary ($g_{\varphi\varphi} = 0$) inside which causality is broken. As can be seen, as the parameter ν grows, the black holes get further away from each other and their achronal region grows as well.

1.5 The global picture

In this section, we provide the global picture of the different surfaces at play in the gravimagnetic dipole spacetime.

Fig. 1.3 graph shows a cut in the XZ plane* of the spacetime for $\nu = 0.4$, $k = k_+^T$ such that the Misner string is tensionless and the system is at equilibrium. The plain blue lines represent the static limit on which $g_{tt} = 0$. The grey dots show the black holes. The dashed grey lines represent the black hole horizons, which reduce to rods on the symmetry axis in Weyl coordinates. The zone between the static limit and the black hole horizons is the ergoregion (there are two here). The orange dashed line shows the chronology boundary on which $g_{\varphi\varphi} = 0$, separating the chronological region (usual causality, $g_{\varphi\varphi} > 0$) from the achronal region ($g_{\varphi\varphi} < 0$). The numerical values of the delimitations of the horizons are also shown, with $\alpha_+ \approx 2.573$ and $\alpha_- \approx 0.154$, as well as the separation of the black holes $2k_+^T \approx 3.150$.

Fig. 1.4 is the three-dimensional version of Fig. 1.3. The static limits, or ergoregions are shown in a green-blue gradient. The chronology boundary is shown as a yellow-purple gradient. On the vertical axis, α_+ (orange) indicates the upper intersection of the ergosurface with the z-axis (and not pictured, the corresponding $-\alpha_+$ for the ergosurface in the negative z). The lower intersection of the ergosurface with the z axis, denoted α_-(green), is also the point where it meets the chronology boundary (again not pictured, $-\alpha_-$ corresponds to the equivalent in the negative z part of the space).

In Fig. 1.5, the four graphs show the cut of the spacetime along the XZ plane for four different values of the NUT parameter ν (1.5a $\nu = 0.1$, 1.5b $\nu = 0.4$, 1.5c $\nu = 0.8$, 1.5a $\nu = 0.9$). The grey dots represent the black holes. The plain blue lines represent the static limit ($g_{tt} = 0$) under which a static observer cannot exist. The orange dotted line depicts the chronology boundary ($g_{\varphi\varphi} = 0$) delimiting the achronal region in which causality is broken. As can be seen, as the parameter ν grows, the black holes get further away from each other and their achronal region grows. For $\nu \to 1$, $k_+^T \to +\infty$ and the achronal region takes up the whole space.

*In the cylindrical coordinates used throughout, this means that $\rho = |x|$ and that the right (respectively, left) half of the figure corresponds to $\varphi = 0$ (resp. $\varphi = \pi$).

1.6 Back to the Kerr spacetime

As was mentioned throughout Section 1.4, the gravimagnetic dipole spacetime is closely linked to the Kerr spacetime. In this section, we show that given a certain choice of parameters, it reduces to the Kerr spacetime [39, 46, 74].

Fixing $k = m$ in eq. (1.6), we get

$$\alpha_+ = \sqrt{4m^2 - \nu^2}, \qquad \alpha_- = \sqrt{-\nu^2} \qquad \text{and} \qquad d = m^2. \tag{1.45}$$

Provided that $\nu < 2m$, α_+ is real as well as d. The parameter α_- is pure imaginary, but it gets simplified out in the metric functions f, ω and $e^{2\gamma}$. The metric can then for example, be transformed to Boyer-Lindquist coordinates (r, θ), which are related to Weyl's canonical coordinates (ρ, z) by

$$\rho = \sqrt{r^2 - 2Mr + a^2}\sin\theta, \quad z = (r - M)\cos\theta, \tag{1.46}$$

where $M = 2m$ is the total mass of the Kerr metric and the total angular momentum is given by $J = 2k\nu$ [39], *i.e.* $J = 2m\nu = M\nu$, leading to the Kerr parameter $a = \nu$.

On another note, this also allows us to check that in Weyl's cylindrical coordinates, the event horizon of the Kerr black hole has the shape of a rod. In Boyer-Lindquist coordinates, the event horizons* for the Kerr black hole correspond to:

$$r_H^{\pm} = \frac{r_s}{2}\left(1 \pm \sqrt{1 - 4\frac{a^2}{r_s^2}}\right). \tag{1.47}$$

Converting in Weyl's canonical coordinates—-being careful that in this case, with our adimensionalisation scheme,

$$r_s = \frac{2GM}{c^2} = \frac{4Gm}{c^2} = 4, \tag{1.48}$$

we find that

$$\rho_H = 0 \tag{1.49}$$

*See Section 2.7 around eq. (2.7) for more details.

and

$$z_H = \pm\sqrt{4-a^2}\cos\theta = \pm\sqrt{4-\nu^2}\cos\theta = \pm\alpha_+\cos\theta \qquad (1.50)$$

The range of the cosine function being $[-1,1]$, we deduce that the shape of the event horizon for a Kerr black hole in Weyl's cylindrical coordinates is that of a rod at $\rho = 0$, with $z \in [-\alpha_+, \alpha_+]$.

1.7 Summary

We have described the general characteristics of the gravimagnetic dipole spacetime, a spacetime that is axially symmetric and stationary, as well as asymptotically flat. It consists of the non linear superposition of two NUT solutions to Einstein's vacuum equations, and in the range of parameters that have been chosen ($0 < \nu < 1$, $k = k_+^T(\nu)$), it represents a system of two black holes separated by a distance $2k$, at equilibrium with each other. The symmetry axis can be represented as a series of three rods, symmetric about the equatorial plane: the central rod, a tensionless spinning cosmic string called Misner string, has a length of $2\alpha_-$ and joins the two other rods, the event horizons of length $(\alpha_+ - \alpha_-)$. The event horizons are wrapped in two ergoregions that are shaped like rugby balls, meeting the symmetry axis at the extremities of the event horizons. Finally, the Misner string itself is wrapped in an achronal region, of which the chronology boundary also meets the symmetry axis at the inner extremities of the event horizons and ergoregions.

CHAPTER 2

CIRCULAR ORBITS, PROPER DISTANCES AND EFFECTIVE POTENTIALS IN STATIONARY SPHERICALLY OR AXIALLY SYMMETRIC SPACETIMES

> "I'm going to need a SWAT team ready to mobilise, street-level maps covering all of Florida, a pot of coffee, twelve Jammie Dodgers and a fez."
>
> — The Doctor, *Doctor Who* (1963 – ...)

In this chapter, we establish the main results that will be used throughout the remainder of this thesis. Namely, we will develop the Hamiltonian formulation of geodesic motion in curved spacetimes, which provides a convenient framework whenever the spacetime symmetries are insufficient to completely integrate the geodesic equations. We will be particularly interested in the circular orbits that test particles—massive or massless—can follow, as well as their velocity along these trajectories; this will naturally

lead to the velocity rotation curves corresponding to the spacetimes under study.

In stationary axisymmetric spacetimes, the existence of the two Killing vector fields ∂_t and ∂_φ immediately provides two conserved quantities along geodesics, namely the energy and the angular momentum. However, contrary to highly symmetric spacetimes such as Kerr, no additional Killing tensor is expected in the general case, so that the geodesic equations are not completely integrable from symmetry arguments alone. It is therefore convenient to adopt a Hamiltonian formulation, in which the conserved quantities arise naturally as first integrals while the remaining degrees of freedom are described through the mass-shell constraint and effective potentials.

Whilst remaining within the class of stationary spacetimes, we first consider the spherically symmetric case for its simplicity, before turning to the stationary axisymmetric case, which is more directly relevant to the gravimagnetic dipole spacetime.

We illustrate these two cases using the Schwarzschild and Kerr solutions, respectively. Their analytical tractability provides useful insight into the underlying physics before tackling the gravimagnetic dipole spacetime.

Since the gravimagnetic dipole case will not be as easy to treat—as Chapter 1 will have shown—we will also introduce the concept of effective potential and different possible definitions, each with its own advantages and disadvantages, which will be used in the following chapters.

However there is first some subtlety we will have to address in the way we define the velocity. In Newtonian mechanics, time is usually considered as absolute, meaning that it flows in the same way for any observer, whatever her status. This allows for a unique definition of velocity relative to some inertial frame. Considering the motion of a test particle from the points of view of two distinct inertial observers in relative motion, the velocity they will measure for the test particle will only differ by the addition of constants characteristic of the corresponding Galilean transformation.

In General Relativity, this is not necessarily the case. Coordinate spatial distance intervals and absolute time are no longer meaningful and invariant geometrical and physical concepts [75–79]. Space and time are intimately intertwined, with each being relative to any given spacetime observer [75]. Notably, the flow of time is dependent on the position.

Being able to define more than one distance and one time interval [80] between two events means that there is also more than one definition available for the velocity.

To clarify all of this, we will start by defining in Section 2.1 the infinitesimal distance between two simultaneous events for a generic spacetime, leading to a definition for velocity. The definition of distance is then particularised in Section 2.2 for a stationary (spherically or axially symmetric) spacetime.

We will then take a look at the geodesics of a free particle in a stationary metric in Section 2.3. At first, this metric will be general, but we will particularise it to be first spherically symmetric, then axially symmetric. To keep the discussion relevant to both a massive ($\mu_0 > 0$) or a massless ($\mu_0 = 0$) particle whilst minimizing the amount of repeated similar developments, a worldline einbein field [81, 82] will be used and either gauge fixed to proper time or left as a gauge degree of freedom for the massless case.

We will then take a brief detour, in Section 2.4, to explore the different definitions of effective potentials, and which advantages and drawbacks each of them have. These equivalent but different tools will be used in further chapters for the gravimagnetic dipole, (as you have seen in Chapter 1, the minimisation of computation is of utmost importance).

Finally, having explored the theoretical machinery, we will apply the steps detailed above, and thus compute the velocity rotation curves as function of the coordinate radii, compared to the geometric radii, for the Schwarzschild and Kerr spacetimes, respectively in Sections 2.6 and 2.7.

2.1 A definition of velocity

In ordinary Galilean space, as everybody knows, the surface area A of a sphere is related to its radius R—*i.e.* the distance from the surface to the center—by the formula

$$A = 4\pi R^2. \tag{2.1}$$

In general relativity, this is not necessarily the case: take the Schwarzschild case for example: the black hole in the center curves spacetime, such that

this relationship does not necessarily hold* [77]. However it is convenient to label the spheres in a curved spacetime by the parameter defined by their surface and the above formula: we keep calling R the radius of the sphere, even though it is not necessarily equal to the distance between the surface of the sphere and the origin.

To construct our velocity rotation curves, however, we would like to plot them as functions of the distance radius, *i.e.* the physical radius, in order to compare different spacetimes in a meaningful way. Since the coordinate radius R does not, in general, correspond to a proper distance, we must first introduce a geometrically well-defined notion of radial distance. In the following, we mostly follow § 84 in [83] to define the physical (also called proper or geometric) distance.

In this section as well as in the next two, the following conventions are used: $x^\mu = (x^0, x^i)$ is a local coordinate system of the 3+1 dimensional curved spacetime, $x^0 = ct$ with t the local time coordinate and c the speed of light in vacuum, and $g_{\mu\nu}(x^\mu) \equiv g_{\mu\nu}$ the dimensionless metric tensor of mostly positive signature. The 4-dimensional length element is then given by:

$$ds^2 = -c^2 d\tau^2 = g_{\mu\nu} dx^\mu dx^\nu. \tag{2.2}$$

First, let us find the relation identifying the proper time, τ, given the coordinate time, t. From eq. (2.2), for two events occurring at the same point in space but different times differing by the time element dx^0, the proper time element is identified from

$$d\tau = \frac{1}{c}\sqrt{-g_{00}}dx^0, \tag{2.3}$$

which can be integrated to obtain the finite proper time interval between two events occurring at a same point in space:

$$\tau = \frac{1}{c}\int \sqrt{-g_{00}}dx^0. \tag{2.4}$$

Note that in view of the previously defined conventions one has $g_{00} < 0$, thus guaranteeing a real integrand.

Let us now address the issue of the element $d\ell$ as a geometric invariant spatial distance element. In Minkowski spacetime and Cartesian

*Eq. (2.1) is actually already false on Earth due to space deformation, see Section A.2 in Appendix A.

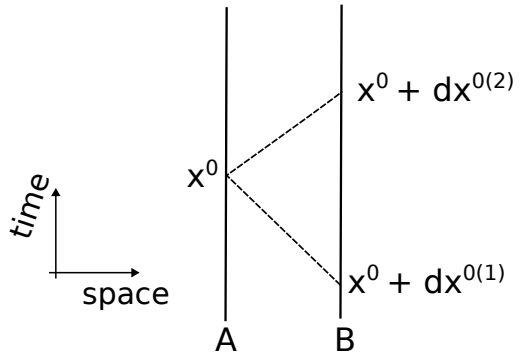


Figure 2.1: Inspired from Figure 18, §84 in [83]. The time dimension is vertical, and space is reduced to one horizontal dimension. The solid lines represent the worldlines of the points A and B. A light signal (dashed line) is sent from point B in space to point A, infinitesimally closeby, and then is sent back over to B on the same spatial path. The travel time is twice this distance, divided by c.

coordinates, $d\ell$ is defined by considering the invariant line element

$$ds_M^2 = -(dx^0)^2 + dx^i dx^i, \tag{2.5}$$

and by setting $dx^0 = 0$, thus meaning that the spatial distance is defined between two events that are infinitesimally spatially separated but occurring at the same time. However, *a priori* such a procedure may not be considered for finite elements in the case of a generic curved spacetime since the proper time at different points in space has different dependencies on the time coordinate x^0.

Suppose a light signal is sent from a point B in space (with spatial coordinates $x^i + dx^i$) to a point A infinitesimally closeby (x^i) and then back to B over the same path. The time needed for this, observed from B, is twice de distance between the two points, divided by c. In Fig. 2.1, time flows along the vertical axis and space is reduced to only one dimension along the horizontal axis. The solid lines represent the worldlines of the points A and B and the dashed lines the worldlines of the light signal.

Let us write the spacetime line element ds^2 by separating the contributions of the space and time coordinate elements:

$$ds^2 = g_{ij}dx^i dx^j + 2g_{0i}dx^0 dx^i + g_{00}(dx^0)^2. \tag{2.6}$$

Solving now for the condition $ds^2 = 0$, provides the following two roots:

$$\begin{aligned} dx^{0(1)} &= \frac{1}{-g_{00}}\Big\{g_{0i}dx^i - \sqrt{(g_{0i}g_{0j} - g_{ij}g_{00})dx^i dx^j}\Big\}, \\ dx^{0(2)} &= \frac{1}{-g_{00}}\Big\{g_{0i}dx^i + \sqrt{(g_{0i}g_{0j} - g_{ij}g_{00}))dx^i dx^j}\Big\}, \end{aligned} \tag{2.7}$$

namely the coordinate time elements associated to the propagation of the light signal between A and B. If x^0 corresponds to the arrival (and departure) time of the signal in A, then the times when it left B and arrived back to it are, respectively, $x^0 + dx^{0(1)}$ and $x^0 + dx^{0(2)}$. It is then easy to see that the total time elapsed while the signal goes from B to A then back to B is given by:

$$dx^{0(2)} - dx^{0(1)} = \frac{2}{-g_{00}}\sqrt{(g_{0i}g_{0j} - g_{ij}g_{00})dx^i dx^j}. \tag{2.8}$$

The corresponding interval of proper time is obtained by multiplying this expression by $\sqrt{-g_{00}}/c$, and the spatial distance $d\ell$ by multiplying once more by $c/2$, hence,

$$d\ell^2 = \left(g_{ij} - \frac{g_{0i}g_{0j}}{g_{00}}\right)dx^i dx^j. \tag{2.9}$$

This expression provides the definition of what will be called, in the following, the geometric distance*. It differs from the purely spatial distance by this additional term,

$$\frac{-g_{0i}g_{0j}}{g_{00}}dx^i dx^j, \tag{2.10}$$

which takes into account the spatial deformation due to the advancement of time (note that it is also, of course, of the right dimension). It can be rewritten in the form [83]:

$$d\ell^2 = \gamma_{ij}dx^i dx^j, \qquad \text{with} \qquad \gamma_{ij} = g_{ij} - \frac{g_{0i}g_{0j}}{g_{00}}. \tag{2.11}$$

Let us note that the tensor γ_{ij} is the reciprocal of the contravariant spatial tensor g^{ij}. Indeed, from the relation $g^{\alpha\gamma}g_{\gamma\beta} = \delta^\alpha_\beta$, it follows that

$$g^{ij}g_{jk} + g^{i0}g_{0k} = \delta^i_k, \qquad g^{i0} = -\frac{g^{ij}g_{j0}}{g_{00}}, \tag{2.12}$$

*Also called proper distance or radar distance.

and by inserting g^{i0} in the first of these two relations, one finds,

$$g^{ij}\gamma_{jk} = \delta^i_k. \tag{2.13}$$

Since in the general case $g_{\mu\nu}$ depends on x^0, it is meaningless to integrate $d\ell$ given a generic curved spacetime. The integral would be ill-defined since it would depend on the worldline, *i.e.*, the chosen path between the two points. Thus, generally speaking, in the context of generic curved spacetimes the concept of geometric distance remains valid at best only for infinitesimally small distances.

However, in the case of a stationary metric, $g_{\mu\nu}$ does not depend on x^0 and as such, the integral $\int d\ell$ is well-defined and can be used to determine the finite geometric distance between two simultaneous events. Hence in the following, only stationary metrics will be considered and in Section 2.2 we will particularise eq. (2.11) for stationary spherically symmetric or axially symmetric spacetimes.

But before that, let us turn to the definition of proper velocity (also known as celerity), which can be defined as follows relative to the proper time along the worldline:

$$v_\tau^2 \equiv \gamma_{ij}\frac{dx^i}{d\tau}\frac{dx^j}{d\tau}, \tag{2.14}$$

as well as the velocity relative to the coordinate time, or coordinate velocity:

$$v_t^2 \equiv \gamma_{ij}\frac{dx^i}{dt}\frac{dx^j}{dt} = \left(\frac{d\tau}{dt}\right)^2 v_\tau^2, \qquad v_\tau^2 = \left(\frac{dt}{d\tau}\right)^2 v_t^2. \tag{2.15}$$

The coordinate velocity, denoted as $v_t > 0$ in the following, represents the particle's velocity as recorded by an asymptotic observer*. The proper velocity, $v_\tau > 0$, represents the velocity that the particle registers in its own rest frame. In the following, focus is being put on the coordinate velocity as must be measured by an asymptotic observer, hence its physical relevance.

*In view of the physical context, it is implicitly assumed herein that the stationary metric is asymptotically flat.

2.2 The geometric radial distance

The radar, proper, spatial or geometric distance [80], that was defined in the previous section can be further particularised for the spacetimes that occupy us here: stationary and either spherically or axially symmetric. Our expression this far is such that

$$d\ell^2 = \left(g_{ij} - \frac{g_{0i}g_{0j}}{g_{00}} \right) dx^i dx^j. \tag{2.16}$$

We will look at what happens in both symmetries. First, let us consider a spherically symmetric stationary metric. Using spherical coordinates (ct, r, θ, φ), if we freeze time such that $dx^0 = cdt = 0$ and by looking only at radial displacements, thus choosing $d\theta = d\varphi = 0$, the spacetime geometric invariant element ds^2 necessarily reduces to, since there is no cross term ($g_{0r} = 0$),

$$d\ell^2 = \gamma_{rr} dr^2 = g_{rr} dr^2 = ds^2, \tag{2.17}$$

with dr the radial coordinate distance element and $d\ell$ the radial geometric distance element.

In the same way, but now for an axially symmetric stationary metric with the usual cylindrical or Weyl coordinates (ct, ρ, φ, z), let us freeze time and only consider radial distances transverse to the axial symmetry axis, thus choosing $d\varphi = dz = 0$. The spacetime geometric invariant element ds^2 then becomes, since once again $g_{0\rho} = 0$,

$$d\ell^2 = \gamma_{\rho\rho} d\rho^2 = g_{\rho\rho} d\rho^2 = ds^2, \tag{2.18}$$

with $d\rho$ the radial coordinate distance element and $d\ell$ the radial geometric distance element.

In the case of a stationary metric, $g_{\mu\nu}$ does not depend on x^0 and as such, the integral $\int d\ell$ is well-defined and can be used to determine the finite physical spatial distance between two simultaneous events.

Furthermore, let us also note that in the axisymmetric spacetime under consideration here, the only cross term is $g_{t\varphi}$ and there is no $g_{t\rho}$ cross term. As such, the spatial radial distance corresponds to the proper distance $\bar{\rho}$ between ρ and ρ_0 defined as

$$\bar{\rho} = \int_{\rho_0}^{\rho} \sqrt{g_{\rho\rho}}\, d\rho. \tag{2.19}$$

The **geometric radial distance** d_r (resp., d_ρ) between two points of radial coordinates r_0 and r (resp., ρ_0 and ρ) can then be obtained by integrating the spacetime geometric invariant element $d\ell = ds$ along dr (resp., $d\rho$):

$$d_r = \int d\ell = \int_{r_0}^{r} \sqrt{g_{rr}}\, dr \qquad \text{or} \qquad d_\rho = \int d\ell = \int_{\rho_0}^{\rho} \sqrt{g_{\rho\rho}}\, d\rho. \quad (2.20)$$

The value of the lower bound at r_0 (resp., ρ_0) must be carefully chosen. It will depend on the specific spacetime and set of coordinates being used. In this chapter, we have chosen to place r_0 (resp., ρ_0) at the photon sphere* for each spacetime, ensuring that the energy of a massive particle remains real when considering its velocity rotation curve. However, in the case of the gravimagnetic dipole spacetime in Chapter 3, due to (i) the number of photon spheres and (ii) the difficulty in localising them, we will choose $\rho_0 = 0$.

The total geometric radial distance d_r (resp., d_ρ) is then the geometric radial distance between the coordinate radius of the photon sphere r_0 (resp., ρ_0) and the coordinate radius of the particle r (resp., ρ). The (total) **geometric radius** is defined (in a somewhat arbitrary way†) as the geometric radial distance shifted by the coordinate radius of the photon sphere—in the gravimagnetic dipole spacetime, the geometric radius will thus be equal to the geometric distance defined above. Thus:

$$\bar{r}(r) = r_0 + \int_{r_0}^{r} \sqrt{g_{rr}}\, dr, \qquad \text{or} \qquad \bar{\rho}(\rho) = \rho_0 + \int_{\rho_0}^{\rho} \sqrt{g_{\rho\rho}}\, d\rho. \quad (2.21)$$

Hence in particular, $\bar{r}(r_0) = r_0$ and $\bar{\rho}(\rho_0) = \rho_0$.

Let us emphasize once again that the geometric radial distance d_r or d_ρ is well-defined only if the spacetime metric is stationary, since otherwise the factor $\sqrt{g_{rr}}$ (resp., $\sqrt{g_{\rho\rho}}$) would depend on time.

*The photon sphere is the region where massless particles can follow circular null geodesics. It is often called photon sphere even when it is *not* in the shape of a sphere. In this thesis, we will prefer the term photon orbit, or photon circular orbit, to avoid any confusion in that case.

†Writing this thesis and looking back on everything that was done, it now appears that it would be more logical to choose as values for r_0 or ρ_0 the coordinate of the (external) event horizon for each spacetime. Then, since there is no such horizon in the equatorial plane for the gravimagnetic dipole, each case would follow the exact same rule.

2.3 Geodesics of free particles

Consider the general case of a free point particle—be it massive or massless—propagating in a spacetime whose geometry in coordinates (x^0, x^i) is characterised by the following metric and line element:

$$ds^2 = g_{\mu\nu}dx^\mu dx^\nu. \tag{2.22}$$

From the outset, herein the metric $g_{\mu\nu}$ is taken to be stationary (and asymptotically flat). Let us note that $x^0 = ct$ is the time coordinate with a dimension of length, and the x^i are spacelike (in general, curvilinear) coordinates of that same physical dimension.

As is well-known [81, 82, 84], the particle's dynamics is derived from the Hamiltonian first-order action:

$$\begin{aligned} S[x^\mu, p_\mu; e] &= \int du(\dot{x}^\mu p_\mu - H), \\ H &= \frac{1}{2}e(u)(g^{\mu\nu}p_\mu p_\nu + (\mu_0 c)^2), \end{aligned} \tag{2.23}$$

with $u \in \mathbb{R}$ being an arbitrary worldline parametrisation (the dot standing for a derivative relative to u), μ_0 the mass of the particle ($\mu_0 > 0$ for a massive particle and $\mu_0 = 0$ for a massless one) and H the first-class Hamiltonian.

The conjugate momentum p_t is constant due to the stationarity of the metric, and satisfies $p_t = -E/c$, where E is the energy of the particle. Additionally, when the metric is axisymmetric or spherically symmetric, p_φ is conserved and such that $p_\varphi = L$ with L the (orbital) angular momentum. The positive definite einbein field $e(u)$ is playing the role of the Lagrange multiplier (and pure gauge degree of freedom) for the first-class constraint:

$$g^{\mu\nu}p_\mu p_\nu + (\mu_0 c)^2 = 0, \qquad c^2 g^{\mu\nu}p_\mu p_\nu + (\mu_0 c^2)^2 = 0. \tag{2.24}$$

The geodesic equations then read,

$$\frac{dx^\mu}{du} = e g^{\mu\nu}p_\nu, \qquad \frac{dp_\mu}{du} = -\frac{1}{2}e\frac{\partial g^{\rho\sigma}}{\partial x^\mu}p_\rho p_\sigma, \tag{2.25}$$

while being subjected as well to the first-class constraint in eq. (2.24) to ensure invariance under orientation preserving worldline diffeomor-

phisms. Additionally, when the constraint is satisfied in the massive case,

$$e = \pm \frac{1}{\mu_0 c} \sqrt{-g_{\mu\nu} \dot{x}^\mu \dot{x}^\nu}, \tag{2.26}$$

the upper sign corresponding to the standard square-root action for a relativistic massive particle, such that in a Minkowski spacetime solutions of positive energy propagate to the future.

2.4 Some considerations on effective potentials

An effective potential is, broadly speaking, a tool commonly used in physics that gets rid of the "irrelevant" information, simplifying the problem and allowing the physicist to focus on relevant aspects of the problem.

In General Relativity, an *effective potential* is typically a scalar function that describes the kind of motion a particle can undergo, and it is obtained by any or all of the following:

- ✿ exploiting the symmetries of the spacetime;
- ✿ using the constants of motion;
- ✿ eliminating irrelevant variables;
- ✿ *etc*.

This leads to multiple possible definitions of an effective potential [75, 85–88], with different characteristics, advantages and disadvantages. These effective potentials will, more or less effectively, allow for

- ✿ the identification turning points;
- ✿ the study of the existence and position of orbits;
- ✿ the study of the stability of the aforementioned orbits;
- ✿ the visualisation of the conditions required for a scattering versus a bound motion;
- ✿ the connection with (everyday) intuition;
- ✿ *etc*.

This kind of formalism is typically used when doing qualitative analyses of spacetimes (*e.g.* in the Kerr spacetime, the value of the Kerr parameter affects the shape of the potential, *i.e.* the position of the photon sphere).

Furthermore, Chapter 1 has shown that the gravimagnetic dipole spacetime metric functions are quite long; using effective potentials will allow us to obtain, in Chapter 3, a qualitative analysis of the structure of the circular orbits without having to solve the highly non-trivial equations that will arise.

In the following Section 2.4.1, we will briefly introduce the most well-known effective potential definition—the *radial effective potential from conserved quantities* [75], which will be used for our two case studies in Section 2.5.

In Subsection 2.4.2 the focus will be on the closely related *Hamiltonian-constraint effective potential* [87]. This form of the potential will prove useful in the context of circular orbits in the equatorial plane in Chapter 3, as well as in the study of light deflection in Chapter 5.

Finally in Section 2.4.3, we will explore the *effective impact parameter potential* [88], which will be more easily usable in the context of off-equatorial circular orbits, at least for a qualitative analysis, in Chapter 4.

For brevity's sake, we will develop the latter two effective potentials' formalisms only in axisymmetric spacetimes.

2.4.1 Effective potential I: radial effective potential

For the Schwarzschild and Kerr cases, the definition of the effective potential that will be used is that of the minimum possible value of the energy for each position in a given motion. It is probably the most intuitive way of defining an effective potential for circular orbits.

It consists in using the Hamiltonian constraint to extract the value of the energy as a function of the position in spacetime, the angular momentum, and the radial conjugated momentum. In the equatorial plane, the conjugated momentum corresponding to the off-equatorial coordinate (p_θ in spherical coordinates, or p_z in cylindrical coordinates) will be identically 0. Necessarily, the minimal possible value of the energy for a particle on a circular orbit will be reached when the radial conjugated momentum is zero, which allows to define the corresponding effective potential.

With this definition, the stable (respectively unstable) circular orbits correspond to the values of the radius such that the radial effective potential is at a minimum (resp. maximum), *i.e.* such that the derivative of the

radial effective potential is 0 and the second derivative is positive (resp. negative).

Plotting this effective potential as a function of the radius provides an intuitive graph of the behaviour of particles according to the value of their energy, especially in the Schwarzschild case since there is no cross term between the energy and the angular momentum. However when the cross term is non zero, it can become quite complicated. Thus another definition of the effective potential, easier to manipulate for the gravimagnetic dipole, was chosen for this work and is presented in the following section.

2.4.2 Effective potential II: Hamiltonian-constraint effective potential

In this section, we will describe and derive the Hamiltonian-constraint effective potential for massive or massless particles in general axisymmetric spacetimes [87].

Consider a generic stationary and axisymmetric spacetime in the canonical Weyl-Papapetrou form of the metric [46]:

$$\mathrm{d}s^2 = -e^{2\psi}(\mathrm{d}t + A\mathrm{d}\varphi)^2 + e^{-2\psi}\left[e^{2\gamma}(\mathrm{d}\rho^2 + \mathrm{d}z^2) + \rho^2\mathrm{d}\varphi^2\right], \quad (2.27)$$

where ψ, γ and A are functions of ρ and z.

From Section 2.3, the Hamiltonian constraint can be written very simply, for massive ($\mu_0 > 0$) or massless ($\mu_0 = 0$) particles, as

$$g^{\mu\nu}p_\mu p_\nu + (\mu_0 c)^2 = 0 \quad (2.28)$$

where the p_μ are the quadri-momenta of the particle and $g^{\mu\nu}$ the inverse of the metric. In our generic stationary axisymmetric spacetime, there are two conserved quantities: the energy $E = -p_t/c$ and the (orbital) angular momentum $L = p_\varphi$; the Hamiltonian constraint, in Weyl-Papapetrou coordinates (ct, ρ, φ, z) and with these conserved quantities E and L, can be written as :

$$g^{\rho\rho}(p_\rho^2 + p_z^2) + g^{tt}\frac{E^2}{c^2} - 2g^{t\varphi}\frac{EL}{c} + g^{\varphi\varphi}L^2 + (\mu_0 c)^2 = 0. \quad (2.29)$$

Note that in eq. (2.27), the metric functions $g_{\rho\rho} = g_{zz}$ and $g^{\rho\rho} = g^{zz}$ allow for the minor simplification.

Let us now restrict our attention to the equatorial plane $z = 0$; in this case, the associated momentum p_z is constantly zero—this is not necessarily trivial, but it is actually the case for Schwarzschild and Kerr spacetimes, and demonstrated in Section A.1 of Appendix A for the gravimagnetic dipole spacetime.

From eq. (2.25), the energy E and angular momentum L can be written in term of the dot quantities as:

$$\begin{aligned} \frac{E}{c} &= -p_t = -cg_{tt}\dot{t} - g_{t\varphi}\dot{\varphi}, \\ L &= p_\varphi = cg_{t\varphi}\dot{t} + g_{\varphi\varphi}\dot{\varphi}, \end{aligned} \tag{2.30}$$

leading to the following expression for $\dot{\varphi}$:

$$\begin{aligned} \dot{\varphi} &= \frac{\left(\frac{E}{c}\right) g_{t\varphi} + g_{tt}L}{g_{\varphi\varphi}g_{tt} - \left(g_{t\varphi}\right)^2} = \frac{E}{c}\frac{g_{t\varphi} + g_{tt}\frac{cL}{E}}{g_{\varphi\varphi}g_{tt} - \left(g_{t\varphi}\right)^2} \\ &= \frac{E}{c}e^{2\psi}\frac{A + \frac{cL}{E}}{\rho^2}. \end{aligned} \tag{2.31}$$

Dividing each side of eq. (2.29) by $\dot{\varphi}^2$ (assumed to be non zero), and using

$$\frac{\dot{\rho}}{\dot{\varphi}} = \frac{\mathrm{d}\rho}{\mathrm{d}\varphi}, \tag{2.32}$$

and defining the impact parameter $b = cL/E$, eq. (2.29) can be reduced to the form

$$\left(\frac{\mathrm{d}\rho}{\mathrm{d}\varphi}\right)^2 + \frac{\rho^2}{e^{2\gamma}}\left\{1 - \frac{\rho^2}{e^{4\psi}(b+A)^2}\left[1 - e^{2\psi}\left(\frac{\mu_0 c^2}{E}\right)^2\right]\right\} = 0, \tag{2.33}$$

where the second term takes the form of an effective potential:

$$V(\rho, b) = \frac{\rho^2}{e^{2\gamma}}\left\{1 - \frac{\rho^2}{e^{4\psi}(b+A)^2}\left[1 - e^{2\psi}\left(\frac{\mu_0 c^2}{E}\right)^2\right]\right\}. \tag{2.34}$$

Circular orbits are then located at radii $\rho = \rho_c^{\pm}$, which are determined by the conditions $V = 0 = \partial_\rho V$*. These conditions give rise to the critical

*A short demonstration of this fact, as well as the determination of the stability of these orbits, can be found in Section A.3 of Appendix A.

impact parameters

$$b_c^{\pm} = -A_c^{\pm} \pm \rho_c^{\pm} e^{-2\psi_c^{\pm}} \sqrt{1 - e^{2\psi_c^{\pm}} \left(\frac{\mu_0 c^2}{E}\right)^2}, \tag{2.35}$$

where the $^{\pm}_{c}$ quantities satisfy

$$\partial_\rho \psi = \frac{\sqrt{1 - e^{2\psi}\left(\frac{\mu_0 c^2}{E}\right)^2}\left(\sqrt{1 - e^{2\psi}\left(\frac{\mu_0 c^2}{E}\right)^2} \mp e^{2\psi}\partial_\rho A\right)}{\rho\left(2 - e^{2\psi}\left(\frac{\mu_0 c^2}{E}\right)^2\right)}, \tag{2.36}$$

with the corresponding values of the critical radii $\rho_{c,\pm}$.

The stability of the orbits is determined by the sign of the second derivative of the potential with respect to ρ, such that the condition

$$\partial_\rho^2 V_{c,\pm} > 0 \tag{2.37}$$

corresponds to a stable orbit, where

$$\begin{aligned}
\partial_\rho^2 V_{c,\pm} = {} & \frac{2e^{-2\gamma}}{(\mathcal{M}^2-2)^2(\mathcal{M}^2-1)} \\
& \Big\{ \pm\rho(\mathcal{M}^2-2)^2\left[\pm\rho(\mathcal{M}^2-2)\partial_\rho^2\psi - e^{2\psi}\partial_\rho^2 A\sqrt{1-\mathcal{M}^2}\right] \\
& + (\mathcal{M}^2-1)(\mathcal{M}^4-2\mathcal{M}^2+4) \\
& \pm 4\mathcal{M}^2 e^{2\psi}\partial_\rho A\sqrt{1-\mathcal{M}^2} \\
& + e^{4\psi}\left(\partial_\rho A\right)^2(\mathcal{M}^4-6\mathcal{M}^2+4)\Big\},
\end{aligned} \tag{2.38}$$

as well as

$$\mathcal{M}^2 = \left(\frac{\mu_0 c^2}{E}\right)^2 e^{2\psi}. \tag{2.39}$$

Eqs. (2.33) to (2.38) are valid for massive and massless particles continuously, but for clarity's sake, here are the massless expressions, which are easier to manipulate.

For $\mu_0 = 0$, the potential V of eq. (2.34) reduces to

$$V(\rho, b) = \frac{\rho^2}{e^{2\gamma}}\left[1 - \frac{\rho^2}{e^{4\psi}(b+A)^2}\right], \tag{2.40}$$

with the impact parameter in eq. (2.35) as

$$b_c^{\pm} = -A_c^{\pm} \pm \rho_c^{\pm} e^{-2\psi_c^{\pm}}, \tag{2.41}$$

and the condition corresponding to eq. (2.36):

$$\partial_\rho \psi = \frac{1 \mp e^{2\psi} \partial_\rho A}{2\rho}. \tag{2.42}$$

Finally, the second derivative of the potential of eq. (2.38) simplifies to:

$$\partial_\rho^2 V_{c,\pm} = 2e^{-2\gamma} \left[\pm \rho e^{2\psi} \partial_\rho^2 A + 2\rho^2 \partial_\rho^2 \psi + 1 - e^{4\psi} \left(\partial_\rho A \right)^2 \right]. \tag{2.43}$$

The definition of the potential that was presented in this section is particularly useful to compute deflection angles, as will be shown in Chapter 5, by going back to eq. (2.33) and expressing $d\varphi$ as a function of $d\rho$, then integrating along ρ.

It also allows to directly find circular orbits by solving eq. (2.36) (or eq. (2.42)); whilst it is not necessarily always analytically possible, the graphical solution that can be extracted is simpler that using the full Hamiltonian machinery, and still allows some insight into the behaviour of the circular orbits. This will be further used in Chapter 3.

2.4.3 Effective potential III: effective impact parameter potential

Another way of looking at the problem is to introduce the concept of impact parameter effective potential. This new framework can be seen from two points of view; either determining the allowed range of values for the impact parameter for a (massive or massless) particle at a given point in spacetime; or conversely, for a fixed impact parameter, identifying the regions of spacetime accessible to the particle. Because the impact parameter is a conserved quantity ($b = cL/E$), this second approach provides a straightforward interpretation of the dynamics, even off the equatorial plane since it allows us to avoid having to solve increasingly complex equations.

By plotting the allowed ranges of impact parameters on a spacetime slice (since the case that occupies us is stationary and axisymmetric, a slice of spacetime is actually just a 2D-plane), we obtain an intuitive graphical representation of the possible orbits.

Note that we are not restricting ourselves the the equatorial plane any more, and let us now go back to the Hamiltonian constraint from eq. (2.23). It can be further divided [88] in a kinetic energy $\mathcal{T}$ and a potential energy $\mathcal{V}$ such that

$$\mathcal{H} = \mathcal{T} + \mathcal{V} = 0, \tag{2.44}$$

where the kinetic energy

$$\mathcal{T} = \frac{e(u)}{2}\left\{g^{\rho\rho}p_\rho^2 + g^{zz}p_z^2\right\} \geq 0 \tag{2.45}$$

is positive definite and the potential energy is necessarily negative or zero:

$$\mathcal{V} = \frac{e(u)}{2}\left\{g^{tt}\left(\frac{E}{c}\right)^2 - 2g^{t\varphi}\frac{E}{c}L + g^{\varphi\varphi}L^2 + (\mu_0 c)^2\right\} \leq 0, \tag{2.46}$$

with the conjugated momenta p_φ and p_t already expressed in terms of the conserved quantities L and E.

A rescaled potential energy can be written in terms of the covariant metric and the impact parameter $b = cL/E$:

$$V = -\frac{2\Delta c^2}{E^2 e(u)}\mathcal{V} = g_{\varphi\varphi} + 2g_{t\varphi}b + g_{tt}b^2 - \Delta\left(\frac{\mu_0 c^2}{E}\right)^2 \geq 0. \tag{2.47}$$

where $\Delta = \left(g_{t\varphi}\right)^2 - g_{tt}g_{\varphi\varphi}$.

As has been hinted at earlier, this inequality can be considered under two points of view. Either one knows the position of a particle in space, *i.e.* knows the value of (ρ, z)—since our stationary axisymmetric spacetime is cyclic in t and φ—, and has thus a condition on the value of the impact parameter b, or one knows the value of the impact parameter b of a particle, and can thus determine the region of space (ρ, z) that particle is allowed to access. We are going to look independently at these two points of view in the following.

The rescaled potential energy V can be written in the form

$$V = g_{tt}(b - b_+)(b - b_-) \geq 0, \tag{2.48}$$

where*

$$b_\pm = \frac{-g_{t\varphi} \mp \sqrt{\Delta\left(1 + g_{tt}\left(\frac{\mu_0 c^2}{E}\right)^2\right)}}{g_{tt}}, \tag{2.49}$$

which will be called the impact parameter effective potentials in the following. The problem can now be examined as a simple quadratic inequality, in which the sign of g_{tt} plays a primordial role.

There are essentially three separate cases, for the three possible values of the sign of g_{tt}: $g_{tt} > 0$ inside the ergoregion, $g_{tt} < 0$ outside the ergoregion, and $g_{tt} = 0$ on the ergosurface.

2.4.3.1 Inside the ergoregion

Inside the ergoregion, $g_{tt} > 0$, leading to

$$\sqrt{\Delta} = \sqrt{\left(g_{t\varphi}\right)^2 - g_{tt}g_{\varphi\varphi}} < \left|g_{t\varphi}\right|. \tag{2.50}$$

This means, on the one hand, that the factor of the term quadratic in b in eq. (2.48) is positive and the shape of the potential V as a function of b is that of a concave-up parabola. On the other hand, $b_+ < b_-$. Assuming that $g_{t\varphi} < 0$†, $0 < b_+ < b_-$.

As a consequence, the acceptable values of b for a massive particle at some point of space (ρ, z) will be such that

$$b \in \left]-\infty, b_+\right] \cup \left[b_-, +\infty\right[. \tag{2.51}$$

This is shown in panel (a) of Fig. 2.2.

From the expression of $b_\pm$ in eq. (2.49), the factor $\left(\frac{\mu_0 c^2}{E}\right)$ extremises the roots $b_\pm$:

$$b_+|_{\mu_0=0} > b_+|_{\mu_0>0} \quad \text{and} \quad b_-|_{\mu_0=0} < b_-|_{\mu_0>0}. \tag{2.52}$$

So the range of acceptable values shrinks as the factor $\left(\frac{\mu_0 c^2}{E}\right)$ grows.

*The apparent misordering of $\pm$ and $\mp$ is chosen so that the notation makes more sense in the gravimagnetic dipole case later.

†This is the case for the gravimagnetic dipole.

2.4.3.2 Outside the ergoregion

Outside the ergoregion, $g_{tt} < 0$ leading to

$$\sqrt{\Delta} = \sqrt{\left(g_{t\varphi}\right)^2 - g_{tt}g_{\varphi\varphi}} > \left|g_{t\varphi}\right|. \tag{2.53}$$

In either case, the factor of the term quadratic in b in eq. (2.48) is negative, and the shape of the potential V as a function of b is that of a concave down parabola. We also have that $b_- < b_+$. All in all, this means that for a particle to be at some point (ρ, z) in space, its impact parameter b has to be in the interval

$$b \in [b_-, b_+]. \tag{2.54}$$

The signs of $b_\pm$ depend on the sign of $g_{\varphi\varphi}$. In the achronal region, $g_{\varphi\varphi} < 0$ and $b_- < b_+ < 0$. Outside of it, $g_{\varphi\varphi} > 0$ and $b_- < 0 < b_+$.

This is shown in panel (b) and (c) of Fig. 2.2.

In contradistinction with the inside of the ergoregion, as the factor $\left(\frac{\mu_0 c^2}{E}\right)$ grows, the roots $b_\pm$ shrink towards each other:

$$b_-|_{\mu_0=0} < b_-|_{\mu_0>0} \quad \text{and} \quad b_+|_{\mu_0=0} > b_+|_{\mu_0>0}. \tag{2.55}$$

Since the order of the roots is reversed, the final effect stays the same: the allowed range of values of b shrinks as the factor $\left(\frac{\mu_0 c^2}{E}\right)$ grows.

2.4.3.3 On the ergosurface

On the ergosurface, $g_{tt} = 0$, and eq. (2.47) reduces to a first degree inequality

$$V = g_{\varphi\varphi} + 2g_{t\varphi}b - \Delta\left(\frac{\mu_0 c^2}{E}\right)^2 \geq 0 \tag{2.56}$$

with as solution

$$b \geq \tilde{b} = \frac{\Delta\left(\frac{\mu_0 c^2}{E}\right)^2 - g_{\varphi\varphi}}{2g_{t\varphi}}. \tag{2.57}$$

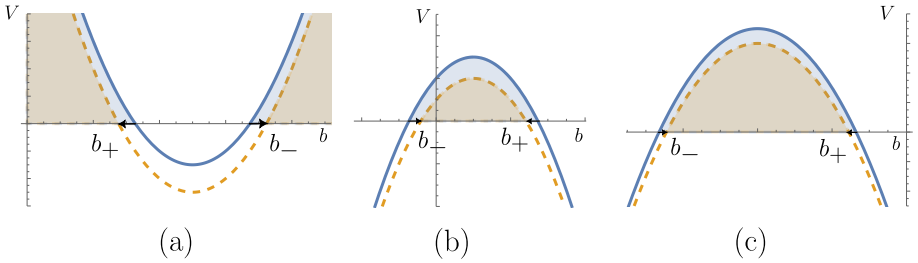


Figure 2.2: These three panels present a schematic version of the rescaled potential energy as a function of the impact parameter b. The leftmost panel illustrates the case inside the ergoregion ($g_{tt} > 0$, $g_{\varphi\varphi} > 0$), where the permissible ranges of impact parameters are disconnected. The two other panels correspond to the exterior of the ergoregion ($g_{tt} < 0$), with the middle panel representing the outside of the achronal region ($g_{\varphi\varphi} > 0$) and the rightmost panel showing the interior ($g_{\varphi\varphi} < 0$). In each graph, the plain blue (respectively, orange dashed) line corresponds to a massless particle (resp. a massive particle). The black arrows show the shift in value for $b_\pm$ as the factor $(\mu_0 c^2/E)$ grows. As the factor $(\mu_0 c^2/E)$ grows, the regions of acceptable values for the impact parameter shrink.

This is consistent with the two previous cases, since in the limit $g_{tt} \to 0$, assuming that $g_{t\varphi} < 0$, $b_+ \to \tilde{b}$ and b_- goes to infinity—if $g_{t\varphi} > 0$, the converse is true.

The definition of the impact parameter effective potentials given in eq. (2.49) allows for the identification of circular orbits off the equatorial plane in a graphical manner, which will be shown for the gravimagnetic dipole case in Chapter 4.

2.5 Two examples of spacetime metrics

Having in hand the tools that will help us to construct the rotation velocity curve as a function of the geometric radius, it is now time to look at two relatively easy examples, namely the Schwarzschild and the Kerr spacetimes. The Schwarzschild case was chosen for its simplicity, all of the necessary calculations being straightforward enough to be performed by hand. The Kerr spacetime was chosen for its stationary and axisymmetric structure, resembling in that sense the gravimagnetic dipole but being easier to apprehend.

The order of operations is as follows: First, we determine the corresponding energy, angular momentum and velocity of a particle on a circular orbit at some value of the coordinate radius.

In the Schwarzschild case, this is done by directly solving the geodesic equations, together with the Hamiltonian constraint. Even though not strictly necessary, the radial effective potential described in Section 2.4.1 will also be determined for comparison's sake with the Kerr case. In the Kerr case, this is done by using the radial effective potential.

The second step consists in determining the proper radius as a function of the coordinate radius, as described in Section 2.2.

Finally, for the last step, we plot the velocity rotation curve as a function of the proper radius.

2.6 The Schwarzschild spacetime

In Schwarzschild spherical coordinates $(x^0, x^i) = (ct, r, \theta, \varphi)$ the Schwarzschild spacetime metric is given as

$$\begin{aligned} ds^2 &= -f(r)c^2dt^2 + f(r)^{-1}dr^2 + r^2d\theta^2 + r^2\sin^2\theta d\varphi^2, \\ \text{where} \quad f(r) &= 1 - \frac{r_s}{r}, \qquad r_s = \frac{2Gm}{c^2}, \end{aligned} \tag{2.58}$$

with r_s being the Schwarzschild radius, m the mass of the black hole, G Newton's gravitational constant, and c the speed of light in vacuum.

Note that given the general relation between coordinate and proper time discussed above, $d\tau = \sqrt{-g_{tt}}\,dt/c$, for the Schwarzschild metric in the above coordinate system this relation specifically reads,

$$\frac{dt}{d\tau} = \frac{1}{\sqrt{-g_{tt}(r)}} = \frac{1}{\sqrt{1-\frac{r_s}{r}}}, \qquad \frac{d\tau}{dt} = \sqrt{1-\frac{r_s}{r}}, \tag{2.59}$$

which clearly requires $r > r_s$.

In view of the non vanishing components of the inverse metric $g^{\mu\nu}$,

$$\begin{aligned} g^{tt}(r) &= -f^{-1}(r), \\ g^{rr}(r) &= f(r), \\ g^{\theta\theta}(r) &= \frac{1}{r^2}, \\ g^{\varphi\varphi}(r,\theta) &= \frac{1}{r^2\sin^2\theta}, \end{aligned} \tag{2.60}$$

the geodesic equations in Hamiltonian form (2.24) and (2.25) are evaluated to be, for the spacetime coordinates,

$$\begin{aligned} c\frac{dt}{du} &= -e\, f^{-1}(r)\, p_t, \\ \frac{dr}{du} &= e\, f(r)\, p_r, \\ \frac{d\theta}{du} &= e\frac{1}{r^2}\, p_\theta, \\ \frac{d\varphi}{du} &= e\frac{1}{r^2\sin^2\theta}\, p_\varphi, \end{aligned} \tag{2.61}$$

and for the conjugate momenta,

$$\begin{aligned} \frac{dp_t}{du} &= 0, \\ \frac{dp_r}{du} &= -\frac{1}{2}e\left(\frac{df^{-1}(r)}{dr}p_0^2 + \frac{df(r)}{dr}p_r^2 - \frac{2}{r^3}p_\theta^2 - \frac{2}{r^3\sin^2\theta}p_\varphi^2\right), \\ \frac{dp_\theta}{du} &= -\frac{1}{2}e\,\frac{\partial g^{\varphi\varphi}(r,\theta)}{\partial\theta}p_\varphi^2 = e\frac{1}{r^2}\frac{\cos\theta}{\sin^3\theta}\, p_\varphi^2, \\ \frac{dp_\varphi}{du} &= 0, \end{aligned} \tag{2.62}$$

with the constraint,

$$-f^{-1}(r)p_t^2 + f(r)p_r^2 + \frac{1}{r^2}p_\theta^2 + \frac{1}{r^2\sin^2\theta}p_\varphi^2 + (\mu_0 c)^2 = 0. \tag{2.63}$$

2.6.1 The velocity

For a circular rotation curve in the equatorial plane, one requires both* r and $\theta = \pi/2$ to remain constant, independent of u, namely $\dot{r} = 0$ and $\dot{\theta} = 0$. In view of the above equations of motion for $r(u)$ and $\theta(u)$, such solutions obviously require vanishing values for the associated conjugate momenta,

$$p_r = 0, \qquad p_\theta = 0. \tag{2.64}$$

*To be exact, one should require that the geometric radius $\bar{r}$ be constant, not the coordinate radius r. But since requiring the first is equivalent to requiring the second for a spherically or axially symmetric spacetime, here one keeps to this simpler-to-use condition.

On the other hand, given the conserved values of the other two conjugate momenta, with $p_t = -E/c$ and $p_\varphi = L$, the values of all four conjugate momenta for such circular trajectories are thus identified, and thereby as well that of the Hamiltonian whose expression at $\theta = \pi/2$ thus reduces to,

$$\begin{aligned} H &= \frac{e}{2}\left(-f^{-1}(r)p_t^2 + \frac{1}{r^2}p_\varphi^2 + (\mu_0 c)^2\right) \\ &= \frac{e}{2}\left(-\frac{E^2}{c^2 f(r)} + \frac{L^2}{r^2} + (\mu_0 c)^2\right) \\ &= 0, \end{aligned} \tag{2.65}$$

but whose value however, must identically vanish since up to the einbein factor $e/2$ it coincides with the constraint equation.

Hence for the spacetime coordinates, only the two equations for $t(u)$ and $\varphi(u)$ remain to be considered, which for circular trajectories at $\theta = \pi/2$ and coordinate radius $r > r_s$ are in the form of,

$$\begin{aligned} c\frac{dt}{du} &= -\frac{ep_t}{f(r)} = \frac{eE}{cf(r)}, \\ \frac{d\varphi}{du} &= \frac{ep_\varphi}{r^2} = \frac{eL}{r^2}, \\ \frac{d\varphi}{dt} &= \frac{f(r)}{r^2}\frac{c^2 L}{E}. \end{aligned} \tag{2.66}$$

The first of these three relations may be used to define the change of coordinate between coordinate time t and the worldline parameter u:

$$\frac{dt}{du} = \frac{eE}{c^2 f(r)}, \qquad \frac{du}{dt} = \frac{c^2 f(r)}{eE}, \qquad \frac{d}{dt} = \frac{du}{dt}\frac{d}{du} = \frac{c^2 f(r)}{eE}\frac{d}{du}. \tag{2.67}$$

However, the values $p_r = 0 = p_\theta$ necessary to achieve circular trajectories at $\theta = \pi/2$ must also be consistent with the two equations of motion for these two conjugate momenta. From the above expression for dp_θ/du, it is clear that at $\theta = \pi/2$ one has indeed $dp_\theta/du = 0$ as is required for the constant value $p_\theta(u) = 0$. In contradistinction, the situation for $p_r(u) = 0$ is different, in which case the condition $dp_r(u)/du = 0$ translates into the following additional non-trivial constraint on the conserved

quantities E and L, given any value of $r > r_s$ as well,

$$\begin{aligned}\frac{dp_r}{du} &= \frac{e}{2}\left(\frac{df^{-1}(r)}{dr}\frac{E^2}{c^2} + \frac{2}{r^3}L^2\right)\\ &= \frac{e}{2}\left(-\frac{r_s}{r^2 f^2(r)}\frac{E^2}{c^2} + \frac{2}{r^3}L^2\right)\\ &= 0.\end{aligned} \tag{2.68}$$

Hence for any such a circular orbit of coordinate radius $r > r_s$ at $\theta = \pi/2$, two conditions have to be met by the conserved quantities E and L:

$$\begin{aligned}&\text{constraint equation:} \quad -\frac{E^2}{f(r)} + \frac{c^2L^2}{r^2} + (\mu_0 c^2)^2 = 0,\\ &\text{equation of motion:} \quad c^2L^2 - \frac{rr_s}{2f^2(r)}E^2 = 0.\end{aligned} \tag{2.69}$$

As a consequence one must have,

$$\frac{1-\frac{3}{2}\frac{r_s}{r}}{\left(1-\frac{r_s}{r}\right)^2}E^2 = (\mu_0 c^2)^2, \qquad \frac{1-\frac{3}{2}\frac{r_s}{r}}{\frac{1}{2}r\,r_s}(cL)^2 = (\mu_0 c^2)^2. \tag{2.70}$$

Clearly the cases of a massive particle with $\mu_0 > 0$ and a massless one with $\mu_0 = 0$ must now be addressed separately.

2.6.1.1 The massive case: $\mu_0 > 0$.

A physically meaningful solution must certainly correspond to real values of E and L, namely $E^2 > 0$ and $L^2 > 0$. Hence to be relevant, the above solution only applies for $r > r_0$ with $r_0 = \frac{3}{2}r_s$. This is then the value of the lower bound $r_0 = 3r_s/2$ to be used in the integral defining the geometric radial distance, $d_r(r)$. Furthermore by requiring solutions with asymptotically positive energy at $r \to \infty$, one then finally obtains the

values of E and L as function of the coordinate radius r,

$$\begin{aligned} E &= \mu_0 c^2 \frac{1-\frac{r_s}{r}}{\sqrt{1-\frac{3r_s}{2r}}}, \\ cL &= \pm\,\mu_0 c^2 r_s \sqrt{\frac{r}{2r_s}}\,\frac{1}{\sqrt{1-\frac{3r_s}{2r}}}, \\ \frac{cL}{E} &= \pm\, r_s\,\frac{\sqrt{\frac{r}{2r_s}}}{1-\frac{r_s}{r}}, \end{aligned} \tag{2.71}$$

where the choice of sign in L corresponds to the two possible rotation directions along the circular trajectory.

The coordinate velocity defined in (2.15) reduces to

$$v_t^2 = g_{\varphi\varphi}\left(\frac{d\varphi}{dt}\right)^2. \tag{2.72}$$

Using (2.66) and (2.71), for the Schwarzschild metric one then finds,

$$r > \frac{3}{2}r_s: \qquad \frac{v_t}{c} = \sqrt{\frac{r_s}{2r}} = \sqrt{\frac{Gm}{c^2 r}}, \qquad v_t = \sqrt{\frac{Gm}{r}}, \tag{2.73}$$

which obviously reminds one of the Keplerian velocity rotation curve of a point mass source in Newtonian gravity (yet, in the Schwarzschild spacetime the radial coordinate r ought not to be identified with the geometric radius, as discussed hereafter). Correspondingly the proper velocity $v_\tau = (dt/d\tau)\,v_t$ also reads,

$$r > \frac{3}{2}r_s: \qquad \frac{v_\tau}{c} = \frac{1}{\sqrt{1-\frac{r_s}{r}}}\cdot\sqrt{\frac{r_s}{2r}}. \tag{2.74}$$

Note that the following limits apply,

$$\lim_{r\to 3r_s/2} E = \infty, \quad \lim_{r\to 3r_s/2} L = \infty, \quad \lim_{r\to 3r_s/2}\frac{cL}{E} = \pm\frac{3}{2}\sqrt{3}\,r_s, \tag{2.75}$$

$$\lim_{r\to 3r_s/2} v_t = \frac{c}{\sqrt{3}}, \quad \lim_{r\to 3r_s/2} v_\tau = c. \tag{2.76}$$

The last of these results points to the fact that the value $r_0 = 3r_s/2$ ought to actually correspond to the coordinate radius for the photon sphere of the Schwarzschild black hole, as is well known.

2.6.1.2 The massless case: $\mu_0 = 0$.

In this case the conditions (2.69) have a physical relevant solution with finite real values of E and L provided r takes exactly the specific sole and single possible value,

$$r = \frac{3r_s}{2} = r_0, \tag{2.77}$$

while the conserved quantities E and L, with E assumed positive are then such that

$$\frac{cL}{E} = \pm\frac{3}{2}\sqrt{3}\, r_s. \tag{2.78}$$

Hence massless particles, as is the photon, may follow circular orbits only for that unique value of the coordinate radius,which is the radius of the so-called photon sphere (or photon ring). The coordinate and proper velocities at this orbit are then given by $v_t/c = 1/\sqrt{3}$ and $v_\tau/c = 1$, respectively.

2.6.2 The geometric radius

The geometric radial distance element is identified from the metric in the form of, since $g_{tr} = 0$,

$$ds^2 = g_{rr}dr^2 = \left(1 - \frac{r_s}{r}\right)^{-1} dr^2 = d\ell^2. \tag{2.79}$$

By taking the positive square root on each side and integrating over the coordinate r, the geometric radial distance d between r_0 an $r > r_0$ is given by

$$r > r_0 : \qquad d(r) = \int_{r_0}^{r} \frac{1}{\sqrt{1 - \dfrac{r_s}{r'}}} dr' \; > \; 0. \tag{2.80}$$

This integral has an analytic solution. As indicated previously, the lower bound r_0 is the minimal radius at which the energy E of a massive particle

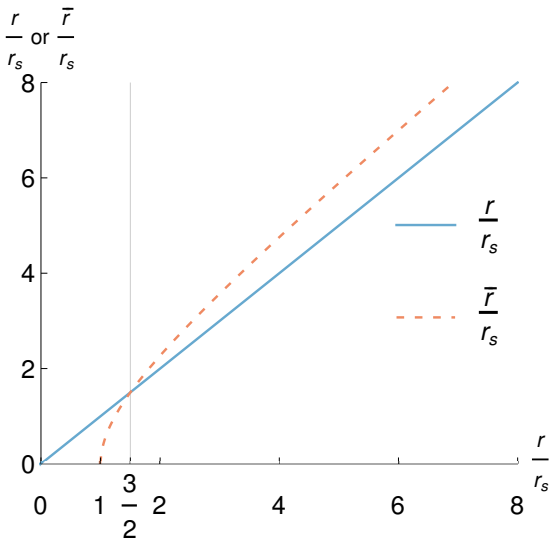


Figure 2.3: Both axes represent radial distance quantities in units of the Schwarzschild radius r_s. As function of the coordinate radius r/r_s on the horizontal axis, the plain blue line is the coordinate radius r/r_s itself (thus the identity), and the dashed orange line is the geometric radius $\bar{r}(r)/r_s$ (for $r > 3r_s/2$). As pointed out in the main text, $\bar{r}(r = 3r_s/2) = 3r_s/2$.

is still real, *i.e.*, the photon sphere at $r_0 = 3r_s/2$. Thus the geometric radial distance $d(r) > 0$ of the point with coordinate radius $r > 3r_s/2$ from the photon sphere at $r = 3r_s/2$ is given by: for $r > \frac{3}{2}r_s$:

$$d(r) = r\sqrt{1-\frac{r_s}{r}} + r_s \tanh^{-1}\left(\sqrt{1-\frac{r_s}{r}}\right) - r_s\left[\frac{\sqrt{3}}{2} + \tanh^{-1}\left(\frac{1}{\sqrt{3}}\right)\right]. \tag{2.81}$$

The geometric radius is the geometric radial distance $d(r)$ shifted by the photon sphere radius $r_0 = 3r_s/2$: for $r > \frac{3}{2}r_s$:

$$\bar{r}(r) = 3\frac{r_s}{2} + r\sqrt{1-\frac{r_s}{r}} + r_s \tanh^{-1}\left(\sqrt{1-\frac{r_s}{r}}\right) - r_s\left[\frac{\sqrt{3}}{2} + \tanh^{-1}\left(\frac{1}{\sqrt{3}}\right)\right]. \tag{2.82}$$

The comparison between the geometric radius $\bar{r}(r)$ and the coordinate radius r, both in units r_s, is shown in Fig. 2.3. Both its axes represent radial distances in units of the Schwarzschild radius r_s. The plain blue line is the coordinate radius r/r_s as function of r/r_s itself (thus the identity). The dashed orange line is the geometric radius $\bar{r}(r)/r_s$, namely $d(r)$ shifted by $r_0/r_s = 3/2$ and in units of r_s. The physical interpretation is as follows. An observer at infinity from the Schwarzschild black hole cannot see inside the event horizon at $r = r_s$ since no light can escape. She will then see r_s as being in the "center" of the system *. By construction however, at the photon sphere radius the geometric radius and the coordinate radius coincide, $\bar{r}(r_0) = r_0 = 3r_s/2$.

To obtain the rotation coordinate velocity $v_t(r)$ in relation to the geometric radius $\bar{r}$, the first idea would be to invert the geometric radius $\bar{r}(r)$ relation with the coordinate radius r to produce an expression for $r(\bar{r})$ and thus for the velocity as a function of the geometric radius, $\bar{v}_t(\bar{r}) \equiv v_t(r(\bar{r}))$. However, the relation (2.82) is not easily invertible in analytic form. Consequently, a more pragmatic and ready method is to use a parametric plot depicting, on the horizontal axis, the values of the geometric radius $\bar{r}$ evaluated as a function of the coordinate radius r, and on the vertical

*Note that even though no circular trajectory is physically possible for $r_s < r < 3r_s/2$, the geometric radius $\bar{r}(r)$ remains well defined within that interval, with $\bar{r}(r = r_s)/r_s = 3/2 - \sqrt{3}/2 - \tan^{-1}(1/\sqrt{3}) \simeq -0.0245$.

axis, the corresponding values of the coordinate velocity v_t obtained for a same value of the coordinate radius r, namely $\bar{v}_t(\bar{r}(r)) = v_t(r)$. This is done in Fig. 2.4, which also displays a comparison with the classical Newtonian result as a function of the geometric radius, namely*,

$$\bar{r} > \frac{3}{2} r_s : \qquad \frac{v_{\text{Newton}}(\bar{r})}{c} = \sqrt{\frac{r_s}{2\bar{r}}}. \tag{2.83}$$

As is observed from the figure, the value of the coordinate velocity $\bar{v}_t(\bar{r})$ at the photon sphere coincides with the value of the Newtonian velocity $v_{\text{Newton}}(\bar{r})$, since $\bar{r}(r_0) = r_0 = 3r_s/2$ while

$$\bar{r} > \frac{3}{2} r_s : \qquad \frac{\bar{v}_t(\bar{r})}{c} = \sqrt{\frac{r_s}{2r(\bar{r})}}. \tag{2.84}$$

Note the slight flattening out of the curve $\bar{v}_t(\bar{r})$ as compared to the Newtonian one, $v_{\text{Newton}}(\bar{r})$, in the region slightly above $\bar{r} = r_0$ and the photon sphere, hence necessarily due to relativistic gravitational effects.

2.6.3 The effective potential

Since the concept of effective potential will be used in the Kerr spacetime case, let us also discuss it here, as a first simple step. Whilst the term "effective potential" seems to be widely used in many Schwarzschild spacetime studies, the specific definition is not unique and varies depending on the sources [75, 85, 86].

Here the effective potential will be defined as the minimum possible value of the energy [75] for each position in a given motion. Thus for a circular orbit in the Schwarzschild case, from (2.63), by using $p_t = -E/c$, $p_\theta = 0$ and $p_\varphi = L$, the constraint can be rewritten as

$$-f^{-1}(r)\frac{E^2}{c^2} + f(r)p_r^2 + \frac{L^2}{r^2} + (\mu_0 c)^2 = 0. \tag{2.85}$$

Extracting the value of the energy for any position (r, θ, φ) gives

$$\frac{E^2}{c^2} = f(r)\left(f(r)p_r^2 + \frac{L^2}{r^2} + (\mu_0 c)^2\right), \tag{2.86}$$

*Note that the extrapolation of the Newtonian velocity inside the photon sphere at $\bar{r} = 3r_s/2$ diverges at a distance $\bar{r}$ slightly above the Schwarzschild horizon at $r = r_s$, since $\bar{r}(r_s)/r_s \simeq -0.0245 < 0$, and $\bar{r}(r)$ vanishes at $r/r_s \simeq 1.00015011$.

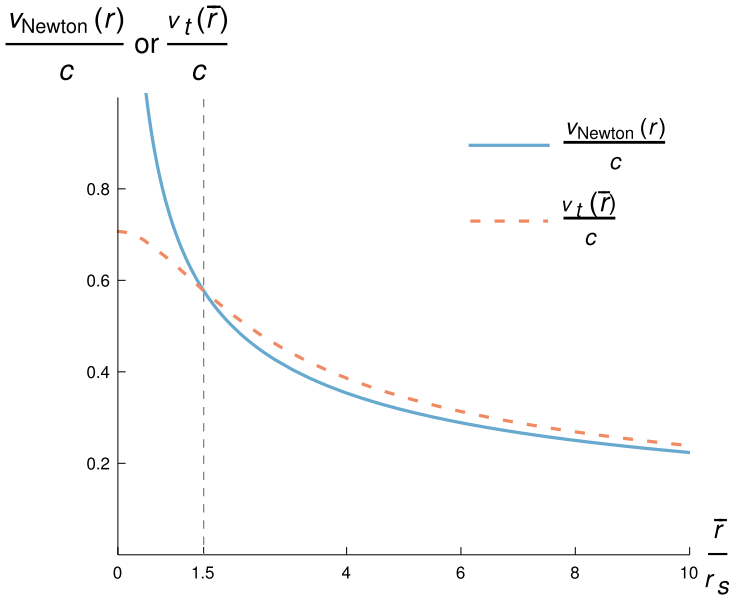


Figure 2.4: The horizontal axis represents the geometric radius $\bar{r}$ in units of the Schwarzschild radius r_s. The plain blue line represents the Newtonian velocity (2.83) (normalised to c). The dashed orange line shows the coordinate velocity (2.84) (normalised to c).

from which the minimum attainable value for the energy of a circular orbit can be found (*i.e.*, when $p_r = 0$). This is the definition for the effective potential that will be used in the present work. For the case being considered, it can be written as:

$$\begin{aligned} \frac{V_r(r)}{\mu_0 c^2} &= \sqrt{\left(1-\frac{r_s}{r}\right)\left(\left(\frac{L}{\mu_0 c r}\right)^2+1\right)}, \\ V_r(r) &= \sqrt{\left(1-\frac{r_s}{r}\right)\left(\left(\frac{cL}{r}\right)^2+(\mu_0 c^2)^2\right)}, \end{aligned} \tag{2.87}$$

so that ((2.86)) is equivalent to,

$$\left(1-\frac{r_s}{r}\right)^2 (cp_r)^2 + V_r^2(r) = E^2. \tag{2.88}$$

Without loss of generality, the potential has been chosen to be the positive square root of (2.86) (with $p_r = 0$), as it is most often done in the literature. With this definition, the stable (resp., unstable) circular orbits correspond to the local minima (resp., maxima) of the effective potential.

For a circular orbit to exist, the value r_M of r at which (2.87) is extremal has to be real (and positive, which is always true in this case). This gives a condition on the minimum value of the angular momentum L, namely,

$$r_{M,\pm} = \frac{L^2 \pm \sqrt{L^2(L^2-3(\mu_0 c)^2 r_s)}}{(\mu_0 c)^2 r_s}, \qquad \frac{|L|}{\mu_0 c} \geq \sqrt{3} r_s. \tag{2.89}$$

The absolute value of L takes care of the fact that the rotation motion can be either prograde or retrograde, but since the Schwarzschild black hole has no angular momentum, the sign of L does not have any effect other than specifying the direction of rotation of the particle on its circular geodesic.

Fig. 2.5 depicts the potential (2.87) normalised to $(\mu_0 c^2)$ for different values of the angular momentum L, itself normalised to $\mu_0 c r_s$. As was mentioned before, the sign of L does not have any particular effect other than specifying the particle's direction of rotation on its circular trajectory, and as such, only positive values of L have been depicted. The left (resp., right) graph shows the effective potential as function of the coordinate

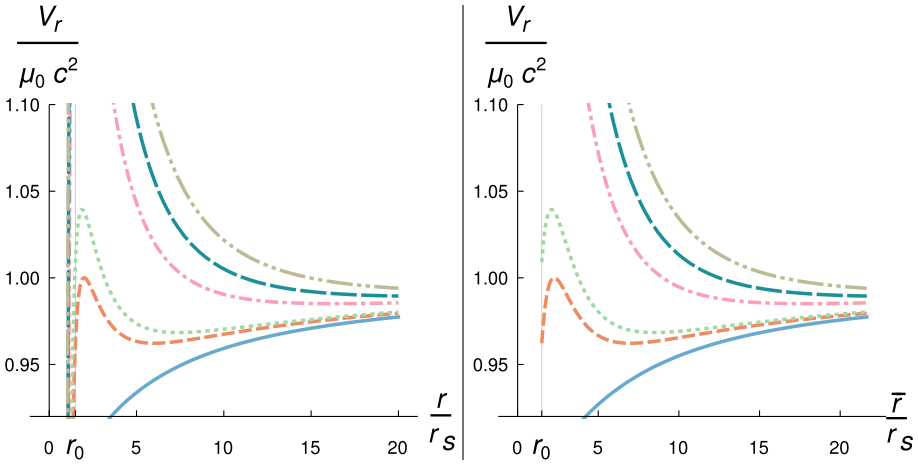


Figure 2.5

These two graphs show the effective potential (in units of $\mu_0 c^2$) for a massive particle of mass μ_0 in the equatorial plane of the Schwarzschild spacetime. Each line ordered from bottom to top for increasing values of $L/(\mu_0 r_s c)$ depicts a different value of the angular momentum. The left (resp., right) graph shows the effective potential as a function of the coordinate (resp., geometric) radius. The thin vertical lines show the photon orbit radius, r_0.

(resp., geometric) radius. The grey vertical lines show the photon orbit radius r_0.

As can be seen, the position of the stable (minima of the curves) and unstable (maxima of the curves) radii vary depending on the value of the angular momentum.

In the massless case, the effective potential is found in the same way as for the massive one, but with $\mu_0 \to 0$ in (2.63), namely,

$$\mu_0 = 0: \qquad \frac{V_r(r)}{c^2} = \sqrt{\left(1-\frac{r_s}{r}\right)\left(\frac{L}{cr}\right)^2} = \frac{|L|}{cr}\sqrt{1-\frac{r_s}{r}}, \tag{2.90}$$

so that in this case ((2.24)) is equivalent to,

$$\left(1-\frac{r_s}{r}\right)^2 (cp_r)^2 + V_r^2(r) = E^2. \tag{2.91}$$

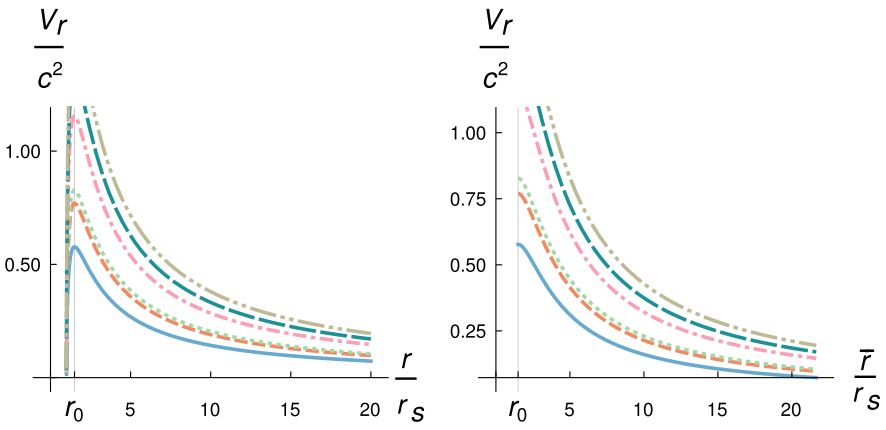


Figure 2.6

These two graphs show the effective potential (in units of c^2) for a photon in the equatorial plane of the Schwarzschild spacetime. Each coloured line ordered from bottom to top for increasing values of $L/(r_s c)$ depicts a different value of the angular momentum (namely, from 1.5 to 4). The left (resp., right) graph shows the effective potential as a function of the coordinate (resp., geometric) radius (in units of r_s). The thin vertical lines show the photon sphere orbit radius r_0. As expected, the photon sphere radius corresponds to the maximum of the effective potential. Note that the scale of the vertical axis is not the same as for the massive case.

Since the photon being retrograde or direct does not affect the expression of the effective potential, Fig. 2.6 shows only two graphs for the effective potential of a massless particle; the left (resp., right) graph depicts the effective potential (in units of c^2) as function of the coordinate (resp., geometric) radius (in units of r_s). Each coloured line represents a different value of the angular momentum (normalised to $r_s c$). The thin vertical lines show the photon orbit radius of the photon sphere. As expected, the photon sphere radius corresponds to the maximum of the effective potential.

2.7 The Kerr spacetime

In Boyer-Lindquist [74] (or oblate spheroidal) coordinates $(x^0, x^i) = (ct, r, \theta, \varphi)$, the Kerr spacetime metric is defined by the invariant line element,

$$ds^2 = -\alpha c^2 dt^2 + \frac{\Sigma}{\Delta} dr^2 + \Sigma d\theta^2 + \beta d\varphi^2 - 2\gamma c dt d\varphi, \tag{2.92}$$

with the metric functions

$$\Sigma = r^2 + a^2 \cos^2\theta, \qquad \Delta = r^2 - r_s r + a^2, \tag{2.93}$$

and

$$\begin{aligned} &\alpha = 1 - \frac{r_s r}{\Sigma}, \quad \beta = (r^2 + a^2 + \gamma a)\sin^2\theta \\ &\gamma = \frac{r_s r a \sin^2\theta}{\Sigma}, \quad r_s = \frac{2Gm}{c^2}. \end{aligned} \tag{2.94}$$

In these relations, m denotes the mass of the black hole, $a = \frac{J}{mc}$ ($0 \leq a \leq r_s/2$) the Kerr parameter with J the total angular momentum of the black hole, G Newton's gravitational constant, and c the speed of light in vacuum. It is useful to note the identity,

$$\alpha\beta + \gamma^2 = \Delta \sin^2\theta. \tag{2.95}$$

In the limit $a = 0$, the above line element reduces to that of the Schwarzschild black hole in spherical coordinates $(x^0 = ct, r, \theta, \varphi)$.

The nonvanishing components of the metric tensor $g_{\mu\nu}$ are thus,

$$g_{tt} = -\alpha, \quad g_{t\varphi} = -\gamma, \quad g_{\varphi\varphi} = \beta, \quad g_{rr} = \frac{\Sigma}{\Delta}, \quad g_{\theta\theta} = \Sigma, \tag{2.96}$$

while for the inverse metric tensor $g^{\mu\nu}$,

$$g^{tt} = -\frac{\beta}{\Delta}, \quad g^{t\varphi} = -\frac{\gamma}{\Delta}, \quad g^{\varphi\varphi} = \frac{\alpha}{\Delta}, \quad g^{rr} = \frac{\Delta}{\Sigma}, \quad g^{\theta\theta} = \frac{1}{\Sigma}. \tag{2.97}$$

Two surfaces are of noteworthy interest for the rotating Kerr black hole. The surface where $g_{rr} = \infty$ or $1/g_{rr} = 0$ delimits the event horizon, and is such that

$$\Delta = 0, \qquad r^2 - r_s r + a^2 = 0. \tag{2.98}$$

The two roots of this equation are real with the values,

$$r_H^{\pm} = \frac{1}{2} r_s \pm \sqrt{\left(\frac{1}{2} r_s\right)^2 - a^2} = \frac{1}{2} r_s \left(1 \pm \sqrt{1 - 4\frac{a^2}{r_s^2}}\right), \tag{2.99}$$

and $r_H \equiv r_H^+$ thus being the outer event horizon. As a increases from 0 to $r_s/2$, the outer event horizon r_H moves inward and decreases from r_s to $r_s/2$ (while the inner horizon r_H^- increases from 0 to $r_s/2$). Note that for $r_H^- < r < (r_H \equiv r_H^+)$, Δ is strictly negative, $\Delta < 0$.

The surface where g_{tt} vanishes and changes sign delimits the ergoregion, and is such that,

$$1 - \frac{r_s r}{\Sigma} = 0, \qquad r^2 - r_s r + a^2 \cos^2\theta = 0. \tag{2.100}$$

The two roots of this equation are real with the values,

$$\begin{aligned} r_E^{\pm}(\theta) &= \frac{1}{2} r_s \pm \sqrt{\left(\frac{1}{2} r_s\right)^2 - a^2 \cos^2\theta} \\ &= \frac{1}{2} r_s \left(1 \pm \sqrt{1 - 4\frac{a^2}{r_s^2}\cos^2\theta}\right), \end{aligned} \tag{2.101}$$

and $r_E(\theta) \equiv r_E^+(\theta)$ thus being the outer ergosurface. As a increases from 0 to $r_s/2$, the outer ergosurface $r_E(\theta)$ moves inward and decreases from r_s to $r_s(1+\sin\theta)/2$. In particular in the equatorial plane at $\theta = \pi/2$ one has $r_E(\theta = \pi/2) = r_s$ (and $r_E^-(\theta = \pi/2) = 0$) irrespective of the value for $0 \leq a \leq r_s/2$. Finally, note the following ordering in these different surfaces, valid whatever the values of $0 \leq \theta \leq \pi$ and $0 \leq a \leq r_s/2$,

$$0 \leq r_E^-(\theta) \leq r_H^- \leq \left(r_H \equiv r_H^+\right) \leq \left(r_E(\theta) \equiv r_E^+(\theta)\right) \leq r_s. \tag{2.102}$$

Given the metric components, the general relation between coordinate time and proper time is expressed as,

$$\frac{dt}{d\tau} = \frac{1}{\sqrt{-g_{tt}(r,\theta)}} = \frac{1}{\sqrt{1-\dfrac{r_s r}{\Sigma(r,\theta)}}}, \qquad \frac{d\tau}{dt} = \sqrt{1-\frac{r_s r}{r^2+a^2\cos^2\theta}}. \tag{2.103}$$

Furthermore, in Hamiltonian form, the geodesic equations of motion read as follows, for the spacetime coordinates,

$$\begin{aligned} c\frac{dt}{du} &= e\left(g^{tt}p_t + g^{t\varphi}p_\varphi\right), \\ \frac{d\varphi}{du} &= e\left(g^{t\varphi}p_t + g^{\varphi\varphi}p_\varphi\right), \\ \frac{dr}{du} &= e\,g^{rr}p_r, \\ \frac{d\theta}{du} &= e\,g^{\theta\theta}p_\theta, \end{aligned} \tag{2.104}$$

and for the conjugate momenta,

$$\begin{aligned} \frac{dp_t}{du} &= 0, \\ \frac{dp_\varphi}{du} &= 0, \\ \frac{dp_r}{du} &= -\frac{1}{2}e\frac{\partial g^{\mu\nu}}{\partial r}p_\mu p_\nu, \\ \frac{dp_\theta}{du} &= -\frac{1}{2}e\frac{\partial g^{\mu\nu}}{\partial \theta}p_\mu p_\nu, \end{aligned} \tag{2.105}$$

subjected to the following constraint,

$$g^{tt}p_t^2 + 2g^{t\varphi}p_t p_\varphi + g^{\varphi\varphi}p_\varphi^2 + g^{rr}p_r^2 + g^{\theta\theta}p_\theta^2 + (\mu_0 c)^2 = 0. \tag{2.106}$$

Due to the stationary and axisymmetric nature of the spacetime metric in this coordinate system, the conjugate momenta p_t and p_φ are conserved,

$$p_t = -\frac{E}{c}, \qquad p_\varphi = L, \tag{2.107}$$

where E is the particle's relativistic energy and L its angular-momentum (component along the axial symmetry axis), both taking constant and real values.

2.7.1 The velocity

In the same way as done above in the case of the Schwarzschild spacetime, for a circular rotation curve in the equatorial plane one requires both* r and $\theta = \pi/2$ to remain constant, independent of u, namely $\dot{r} = 0 = \dot{\theta}$. In view of the above equations of motion for $r(u)$ and $\theta(u)$, such solutions require vanishing values for the associated conjugate momenta,

$$p_r(u) = 0, \qquad p_\theta(u) = 0. \tag{2.108}$$

To proceed further let us point out that at $\theta = \pi/2$ the quantities in terms of which the metric components are defined now take the following values, distinguished by the subscript 0,

$$\begin{aligned}
\Sigma_0(r) &= \Sigma(r, \theta = \pi/2) = r^2, \\
\Delta(r) &= r(r - r_s) + a^2, \\
\alpha_0(r) &= \alpha(r, \theta = \pi/2) = 1 - \frac{r_s}{r}, \\
\beta_0(r) &= \beta(r, \theta = \pi/2) = r^2 + a^2 + a^2\frac{r_s}{r}, \\
\gamma_0(r) &= \gamma(r, \theta = \pi/2) = a\frac{r_s}{r},
\end{aligned} \tag{2.109}$$

such that

$$\alpha_0\beta_0 + \gamma_0^2 = \Delta. \tag{2.110}$$

Given the constant values $p_t(u) = -E/c$, $p_\varphi(u) = L$, $p_r(u) = 0$ and $p_\theta(u) = 0$,the Hamiltonian, which needs to vanish identically for being proportional (with the einbein $e/2$) to the constraint, is expressed as,

$$H = \frac{e}{2}\left(-\frac{\beta_0}{\Delta}\left(-\frac{E}{c}\right)^2 - 2\frac{\gamma_0}{\Delta}\left(-\frac{E}{c}\right)L + \frac{\alpha_0}{\Delta}L^2 + (\mu_0 c)^2\right) = 0. \tag{2.111}$$

*Again, one should ask that the geometric radius $\bar{r}$ be constant, not necessarily the coordinate radius r. But since requiring the first is equivalent to requiring the second for an axisymmetric spacetime, here one keeps the easier to use condition.

For the remaining two equations to be considered for spacetime coordinates one then has,

$$\begin{aligned} c\frac{dt}{du} &= e\left(-\frac{\beta_0}{\Delta}\left(-\frac{E}{c}\right)-\frac{\gamma_0}{\Delta}L\right)=\frac{e}{c\Delta}\left(\beta_0 E-\gamma_0(cL)\right), \\ \frac{d\varphi}{du} &= e\left(-\frac{\gamma_0}{\Delta}\left(-\frac{E}{C}\right)+\frac{\alpha_0}{\Delta}L\right)=\frac{e}{c\Delta}\left(\gamma_0 E+\alpha_0(cL)\right), \\ \frac{d\varphi}{dt} &= c\frac{\gamma_0 E+\alpha_0(cL)}{\beta_0 E-\gamma_0(cL)}. \end{aligned} \tag{2.112}$$

The first of these relations determines the change of variable between coordinate time t and the worldline parameter u,

$$\begin{aligned} \frac{dt}{du} &= \frac{e}{c^2\Delta}\left(\beta_0 E-\gamma_0(cL)\right), \\ \frac{du}{dt} &= \frac{c^2\Delta}{e}\frac{1}{\beta_0 E-\gamma_0(cL)}, \\ \frac{d}{dt} &= \frac{c^2\Delta}{e}\frac{1}{\beta_0 E-\gamma_0(cL)}\frac{d}{du}. \end{aligned} \tag{2.113}$$

However this still leaves to consider the equations of motion for p_r and p_θ to ascertain the conditions to guarantee their constantly vanishing values. However as may readily be established from their expressions above, the quantities $\partial_\theta g^{tt}$, $\partial_\theta g^{t\varphi}$ and $\partial_\theta g^{\varphi\varphi}$ evaluated at $\theta=\pi/2$ all vanish identically. Hence the equation of motion for dp_θ/du indeed trivially reduces to $dp_\theta/du=0$ as it should for the circular trajectory to remain confined within the equatorial plane at all times. Consequently only the equation of motion for p_r which does not cancel identically, namely

$$\frac{dp_r}{du}=-\frac{1}{2}e\left(\partial_r g^{tt}p_t^2+2\partial_r g^{t\varphi}p_t p_\varphi+\partial_r g^{\varphi\varphi}p_\varphi^2\right), \tag{2.114}$$

needs to vanish for consistency with the choice $p_r(u)=0$. It thereby leads to a second condition involving the conserved quantities E and L for a given choice of r.

Hence for any circular trajectory in the equatorial plane of coordinate radius $r>r_s$ at $\theta=\pi/2$, its conserved quantities E and L must take values, function of r, such that the following two conditions are met, a constraint equation:

$$\frac{\beta_0}{\Delta}E^2-2\frac{\gamma_0}{\Delta}E(cL)-\frac{\alpha_0}{\Delta}(cL)^2-(\mu_0c^2)^2=0, \tag{2.115}$$

and an equation of motion:

$$\partial_r\left(\frac{\beta_0}{\Delta}\right)E^2 - 2\partial_r\left(\frac{\gamma_0}{\Delta}\right)E(cL) - \partial_r\left(\frac{\alpha_0}{\Delta}\right)(cL)^2 = 0, \tag{2.116}$$

with

$$\begin{aligned}\Delta &= r(r-r_s)+a^2,\\ \alpha_0 &= 1-r_s/r,\\ \beta_0 &= r^2+a^2+a^2r_s/r,\\ \gamma_0 &= ar_s/r.\end{aligned} \tag{2.117}$$

In explicit form these equations read, for the constraint

$$\begin{aligned}\frac{1}{r(r-r_s)+a^2}\Bigg[\left(r^2+a^2+a^2\frac{r_s}{r}\right)E^2 - 2a\frac{r_s}{r}E(cL) - \\ \left(1-\frac{r_s}{r}\right)(cL)^2\Bigg] - (\mu_0c^2)^2 = 0,\end{aligned} \tag{2.118}$$

and for the equation of motion

$$\begin{aligned}\frac{1}{r^2(r(r-r_s)+a^2)^2}\Big[r_s\left((r^2+a^2)^2-2a^2r_sr\right)E^2 \\ -2ar_s\left(3r^2-2r_sr+a^2\right)E(cL) \\ +\left(a^2r_s-2r(r-r_s)^2\right)(cL)^2\Big] = 0.\end{aligned} \tag{2.119}$$

Note the necessary condition that $r^2\Delta^2 \neq 0$, namely that r does not coincide with the event horizon at $r = r_H^{\pm}$, with in particular the outer event horizon at

$$r_H = r_H^+ = \frac{1}{2}r_s\left(1+\sqrt{1-4\frac{a^2}{r_s^2}}\right), \tag{2.120}$$

which is such that $r_H = r_s$ for $a = 0$ and $r_H = r_s/2$ for $a = r_s/2$. This observation hence implies already a necessary restriction on the physical region, namely $r > r_H$, unless a still higher lower bound would be required from further physical considerations.

2.7.1.1 The massive case: $\mu_0 > 0$.

The identification of the effective potential follows the same considerations as those applied above to the Schwarzschild case; from the constraint (2.106), after replacing the conjugate momenta p_t and p_φ by their associated conserved quantities and putting $\theta = \pi/2$, $p_\theta = 0$, the energy can be expressed as:

$$E = \frac{1}{g^{tt}}\Bigg[g^{t\varphi}(cL) \pm \sqrt{[g^{t\varphi}(cL)]^2 - g^{tt}[g^{\varphi\varphi}(cL)^2 + g^{rr}(cp_r)^2 + (\mu_0 c^2)^2]}\Bigg]. \quad (2.121)$$

Of these two possible values, one must take the negative square-root so that the four-momentum points towards the future [75]. The minimum possible value of the energy will occur when $p_r = 0$, giving the expression of the radial effective potential V_r:

$$V_r(r) = \frac{1}{g^{tt}}\Bigg[g^{t\varphi}(cL) - \sqrt{[g^{t\varphi}(cL)]^2 - g^{tt}\,[g^{\varphi\varphi}(cL)^2 + (\mu_0 c^2)^2]}\Bigg], \quad (2.122)$$

$$V_r(r) = \frac{1}{r\beta_0}\left\{a\, r_S(cL) + r\,\Delta\sqrt{\frac{[\beta_0(\mu_0 c^2)^2 + (cL)^2]}{\Delta}}\right\}, \quad (2.123)$$

with $r\beta_0 = r\beta_0(r) = a^2(r + r_s) + r^3$ and $\Delta = a^2 + r(r - r_s)$.

Stable circular orbits correspond to the minima of V_r, *i.e.*, at r such that $dV_r/dr = 0$ and $d^2V_r/dr^2 > 0$. Finite solutions for E and cL to these equations, and such that $\lim_{r\to\infty} E > 0$, are then the same as the ones to (2.116) or (2.118). They are given by the expressions [85],

$$\begin{aligned} E^{\pm} &= \mu_0 c^2 \frac{r^{3/2} - r_s r^{1/2} \pm a(r_s/2)^{1/2}}{r^{3/4}(r^{3/2} - \frac{3}{2}r_s r^{1/2} \pm a(2r_s)^{1/2})^{1/2}}, \\ cL^{\pm} &= \pm\mu_0 c^2 \frac{(r_s/2)^{1/2}(r^2 \mp a(2r_s r)^{1/2} + a^2)}{r^{3/4}(r^{3/2} - \frac{3}{2}r_s r^{1/2} \pm a(2r_s)^{1/2})^{1/2}}. \end{aligned} \quad (2.124)$$

In these relations as well as those hereafter, the upper (resp., lower) sign corresponds to the direct (resp., indirect), or prograde (resp., retrograde) orbits, thus rotating in the same (resp., opposite or counterrotating) direction as the black hole, namely with $L > 0$ (resp., $L < 0$) (or $aL > 0$ (resp., $aL < 0$) since $0 \leq a \leq r_s/2$ is taken positive in the present analysis). By direct substitution of these expressions in (2.118), one may indeed check that these quantities are solutions to the required conditions.

For the energy $E^{\pm}$ and angular momentum $cL^{\pm}$ to be real, the argument of the square root factor in their common denominator in (2.124) needs to be positive:

$$r^{3/2} - \frac{3}{2} r_s r^{1/2} \pm a(2r_s)^{1/2} > 0, \tag{2.125}$$

while when it vanishes both $E^{\pm}$ and $cL^{\pm}$ acquire infinite values which then can only correspond to lightlike photon geodesics with as well the limit $\mu_0 c^2 \to 0$.

A dedicated separate analysis establishes that this inequality has as physical roots*, for pro- and retro-grade trajectories, respectively [85],

$$r_0^{\pm} = r_s \left[1 + \cos\left(\frac{2}{3} \arccos\left(\mp \frac{2a}{r_s} \right) \right) \right], \tag{2.126}$$

which are the pro- and retro-grade photon orbit spheres (or radii) in the equatorial plane (here, $\arccos z$ stands for the principal evaluation in the interval $[0, \pi]$ of the reciprocal cosine function). These radii are distinct at the equatorial plane, with $\theta = \pi/2$, but coalesce into a single common value when going to the poles, with $\theta = 0, \pi$, for out-of-plane photon spheres.

Thus for a direct (resp., retrograde) massive particle, the limiting minimal radius is the direct (resp., retrograde) photon orbit radius, $r > r_0^{\pm}$. Its energy $E^{\pm}$ and angular momentum $cL^{\pm}$ are given by (2.124) with the upper (resp., lower) sign.

The velocity defined in (2.15) reduces to

$$v_t^2 = \gamma_{\varphi\varphi} \left(\frac{d\varphi}{dt} \right)^2 = \gamma_{\varphi\varphi} \left(\frac{du}{dt} \right)^2 \left(\frac{d\varphi}{du} \right)^2, \tag{2.127}$$

*In case of more than a single root as happens for prograde trajectories, only the largest root qualifies as the value for the photon sphere.

with

$$\gamma_{\varphi\varphi} = g_{\varphi\varphi} - \frac{g_{t\varphi}^2}{g_{tt}} = \beta_0 - \frac{\gamma_0^2}{-\alpha_0} = \frac{\Delta}{\alpha_0} = \frac{r^2 - r_s r + a^2}{1 - r_s/r}. \tag{2.128}$$

Using the expressions for $d\varphi/du$ and du/dt established above, one then finds, for the pro- and retro-grade trajectories, respectively,with $r > r_0^{\pm}$,

$$\begin{aligned}\left(\frac{v_t^{\pm}}{c}\right)^2 &= \frac{\Delta}{\alpha_0}\left(\frac{\gamma_0 E^{\pm} + \alpha_0(cL^{\pm})}{\beta_0 E^{\pm} - \gamma_0(cL^{\pm})}\right)^2 \\ &= \frac{r^2 - r_s r + a^2}{1 - \frac{r_s}{r}}\left(\frac{a\frac{r_s}{r} + (1 - \frac{r_s}{r})\left(\frac{cL^{\pm}}{E^{\pm}}\right)}{(r^2 + a^2 + a^2\frac{r_s}{r}) - a\frac{r_s}{r}\left(\frac{cL^{\pm}}{E^{\pm}}\right)}\right)^2,\end{aligned} \tag{2.129}$$

where

$$r > r_0^{\pm}, \qquad \frac{cL^{\pm}}{E^{\pm}} = \pm\sqrt{\frac{r_s}{2}}\,\frac{r^2 \mp a(2r_s r)^{1/2} + a^2}{r^{3/2} - r_s r^{1/2} \pm a(r_s/2)^{1/2}}. \tag{2.130}$$

Upon direct substitution, one also has,

$$\left(\frac{v_t^{\pm}}{c}\right)^2 = \frac{r r_s\left(a^2 + r(r - r_s)\right)}{(r - r_s)\left(a\left(a r_s \pm 2\sqrt{2}\sqrt{r^3 r_s}\right) + 2r^3\right)}. \tag{2.131}$$

The proper velocities $v_\tau^{\pm}$ are then evaluated from,

$$r > r_0^{\pm}, \qquad \frac{v_\tau^{\pm}}{c} = \frac{1}{\sqrt{1 - \frac{r_s}{r}}}\,\frac{v_t^{\pm}}{c}. \tag{2.132}$$

Note that in the limit of a vanishing black hole angular momentum, $a \to 0$, for any given value of $r > r_0^{\pm}$ the pro- and retro-grade trajectories width and results coalesce, while all the above results and expressions then reduce to those that apply in the case of the Schwarzschild spacetime metric.

2.7.1.2 The massless case: $\mu_0 = 0$.

The radial effective potential is found by taking $\mu_0 \to 0$ in (2.121) and then following the same procedure as for the massive case, which leads

to,

$$V_r(r) = \frac{1}{g^{tt}}\left[g^{t\varphi}(cL) - \sqrt{\left[g^{t\varphi}(cL)\right]^2 - g^{tt}g^{\varphi\varphi}(cL)^2}\right] \tag{2.133}$$

$$V_r(r) = \frac{1}{a^2(r+r_s)+r^3}\left[ar_s(cL) + r\,\Delta\sqrt{\frac{(cL)^2}{\Delta}}\right], \tag{2.134}$$

with $\Delta = a^2 + r(r - r_s)$.

In this case the conditions (2.116) and (2.118) possess physically relevant solutions for circular equatorial lightlike geodesics with finite real values of E and cL provided r takes exactly one of the then only two possible values corresponding to the only two possible orbits, whether a pro- or a retro-grade one, respectively,

$$r = r_0^{\pm} = r_s\left[1 + \cos\left(\frac{2}{3}\arccos\left(\mp\frac{2a}{r_s}\right)\right)\right]. \tag{2.135}$$

In the limit $a = 0$, both these values coalesce to the single value $r_0 = 3r_s/2$ of the photon sphere for the Schwarzschild spacetime metric.

The coordinate velocities for the direct and retrograde photons then take the form, with $r = r_0^{\pm}$,

$$\left(\frac{v_t^{\pm}}{c}\right)^2 = \frac{a^2\left[\cos^2(2\zeta)+1\right] + r_s^2\left[\cos^2(2\zeta) + 2\cos(2\zeta) + 1\right]}{a^2 \pm 8ar_s\cos^3\zeta + 16r_s^2\cos^6\zeta}, \tag{2.136}$$

where,

$$\zeta = \frac{1}{3}\arccos\left(\mp\frac{2a}{r_s}\right), \qquad r_0^{\pm} = r_s\left[1 + \cos(2\zeta)\right]. \tag{2.137}$$

2.7.2 The geometric radius

The geometric radial distance in the equatorial plane at $\theta = \pi/2$ is defined from the Kerr metric line element $d\ell^2$ as,

$$\begin{aligned} d\ell^2 &= \gamma_{rr}(r,\theta=\pi/2)dr^2 = g_{rr}(r,\theta=\pi/2)dr^2 = \frac{\Sigma_0(r)}{\Delta(r)}dr^2, \\ \gamma_{rr} &= g_{rr} - \frac{g_{tr}^2}{g_{tt}} = g_{rr}. \end{aligned} \tag{2.138}$$

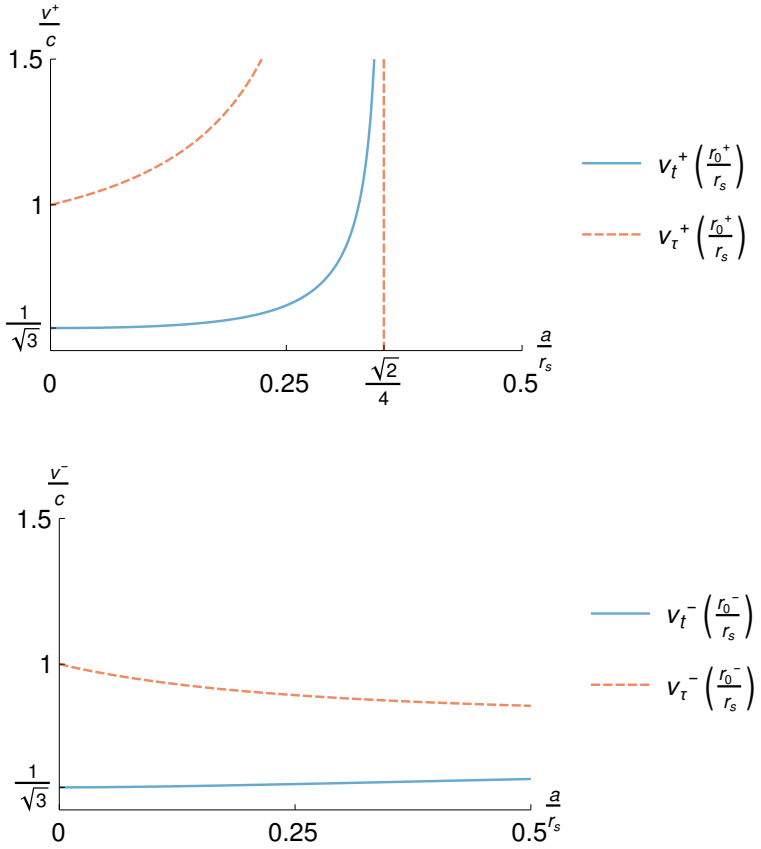


Figure 2.7: In these two graphs for the direct (upper panel) and retrograde(lower panel) photons, the horizontal axes represent the normalised black hole angular momentum a/r_s, and the vertical axes represent the velocity of the photons normalised to c. For each graph, the plain blue (resp., dashed orange) line depicts the coordinate (resp., proper) velocity. Coordinate velocities for $a/r_s = 0$ are equal to the Schwarzschild coordinate velocity $1/\sqrt{3}$ on the photon sphere. Proper velocities for $a/r_s = 0$ are equal to c.

By taking the positive square root on each side and integrating over the coordinate r, the geometric distance $d(r)$ between r_0 and r is given by

$$d(r) = \Delta\ell = \int_{r_0}^{r} \sqrt{\frac{r'^2}{r'(r'-r_s)+a^2}}\, dr'. \tag{2.139}$$

The associated indefinite integral may be evaluated analytically, thereby defining a function $\delta(r)$,

$$\begin{aligned}\delta(r) &\equiv \int \sqrt{\frac{r^2}{r(r-r_s)+a^2}}\, dr \\ &= \frac{1}{2}\left\{2\sqrt{a^2+r(r-r_s)} + r_s \tanh^{-1}\left(\frac{2r-r_s}{2\sqrt{a^2+r(r-r_s)}}\right)\right\}.\end{aligned} \tag{2.140}$$

In the above definite integral for $d(r)$, according to our previous considerations the lower bound r_0 is chosen to correspond to the photon sphere coordinate radius. In the case of the Kerr metric, this lower bound is thus not the same for a prograde or a retrograde rotating massive particle. Given this choice, whether for a pro- or a retro-grade trajectory, one has, respectively,

$$r > r_0^{\pm}: \qquad d_{\pm}(r) = \delta(r) - \delta(r_0^{\pm}). \tag{2.141}$$

Finally, again whether for the pro- or retro-grade case, the geometric radius of the particle is given by adding to $d_{\pm}(r)$ the corresponding value for the photon sphere coordinate radius. Namely,

$$r > r_0^{\pm}: \qquad \bar{r}_{\pm}(r) = r_0^{\pm} + d_{\pm}(r). \tag{2.142}$$

Note that by construction, one simply has,

$$\bar{r}_{\pm}(r_0^{\pm}) = r_0^{\pm}. \tag{2.143}$$

In four different graphs for four different values of $0 \leq a/r_s \leq 1/2$, Fig. 2.8 displays the behaviour of the geometric radii $\bar{r}_{\pm}(r)$ as function of r/r_s. For comparison, the gray line represents the coordinate radius r/r_s itself (thus the identity). The plain blue line is the geometric radius for a prograde rotating massive particle, $\bar{r}_{+}(r)$, and the dashed orange line is the geometric radius for a retrograde rotating massive particle,

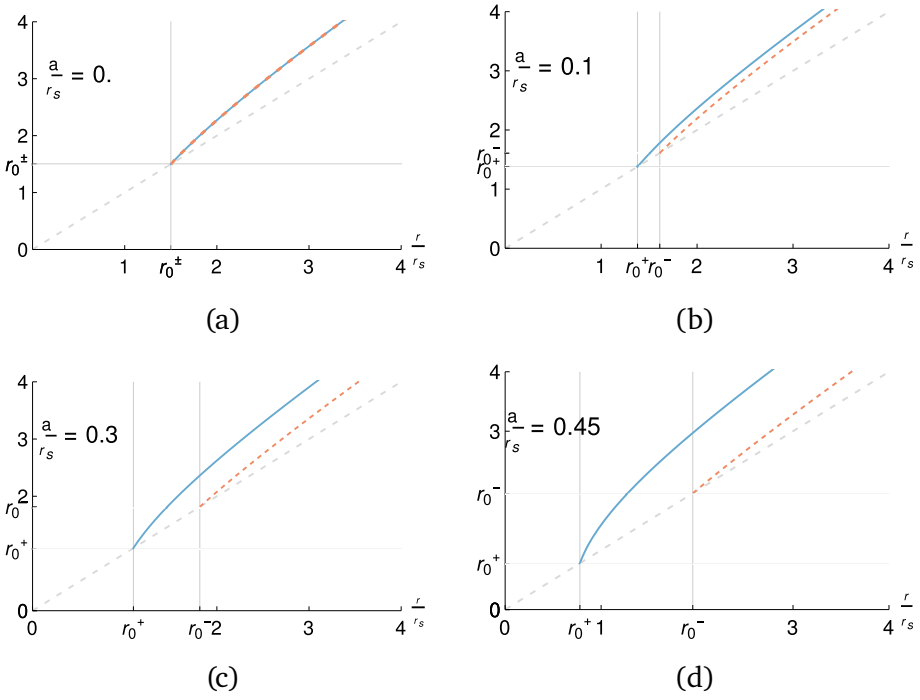


Figure 2.8: In these four graphs for four different values of the normalised black hole angular momentum a/r_s (from left to right, top to bottom, $a/r_s = 0, 0.1, 0.3, 0.45$), both axes represent radial distance quantities in units of the length scale $r_s = 2Gm/c^2$. In each case and as a function of the coordinate radius r/r_s on the horizontal axis, the dashed gray line is the coordinate radius r/r_s itself (thus the identity) displayed for comparison. The plain blue (resp., dashed orange) line depicts the geometric radius for a prograde (resp., retrograde) rotating particle, namely $\bar{r}_\pm(r)$. By construction (see the main text), one has $\bar{r}_\pm(r_0^\pm) = r_0^\pm$.

$\bar{r}_-(r)$. As may be noted from these figures, as a increases from $a = 0$ for which $r_0^{\pm} = 3r_s/2$, the two photon spheres are moving away from each other. The prograde value r_0^+ decreases to get closer to the event horizon at $r_H = r_s(1 + \sqrt{1 - 4a^2/r_s^2})/2$, in such a manner that at the extremal value $a = r_s/2$, $r_0^+ = r_s/2 = r_H$. In contradistinction, the retrograde value r_0^- increases with a to reach the value $r_0^- = 2r_s$ at the extremal value $a = r_s/2$* Not depicted here is the fact that at the poles, the two photon spheres coalesce back into one.

To obtain the rotation coordinate velocities $\bar{v}_t^{\pm}(\bar{r}_{\pm}) = v_t^{\pm}(r(\bar{r}_{\pm}))$ in relation to the geometric radii $\bar{r}_{\pm}$, the same approach as the one used in the case of the Schwarzschild spacetime is applied here as well. Namely, to consider in a graph the curve representing the pairs of values $(\bar{r}_{\pm}(r), \bar{v}_t^{\pm}(\bar{r}_{\pm}(r)))$ as being parametrised by r. This is done in Fig. 2.9.

Each plain blue (resp., dashed orange) line depicts the rotation velocity $v_t^+(\bar{r}_+)$ (resp., $-\bar{v}_t^-(\bar{r}_-)$) of the prograde (resp., retrograde) rotating particle, which has as minimum radius the prograde (resp., retrograde) photon sphere, $r_0^{\pm}$. For convenience, the retrograde velocities $\bar{v}_t^-(\bar{r}_-)$ are always depicted as a negative. As may be seen for the case when $a = 0$, *i.e.*, the Schwarzschild case, the photon spheres coalesce back into the Schwarzschild photon sphere at $r = 3r_s/2$, with a velocity at that radius of $v_t/c = 1/\sqrt{3}$. The prograde and retrograde velocities then have the same absolute value, and the opposite sign stands for the possibility that a particle may rotate clockwise or counter clockwise. For useful comparison, shown in these graphs is also the Newton velocity curve in the form of,

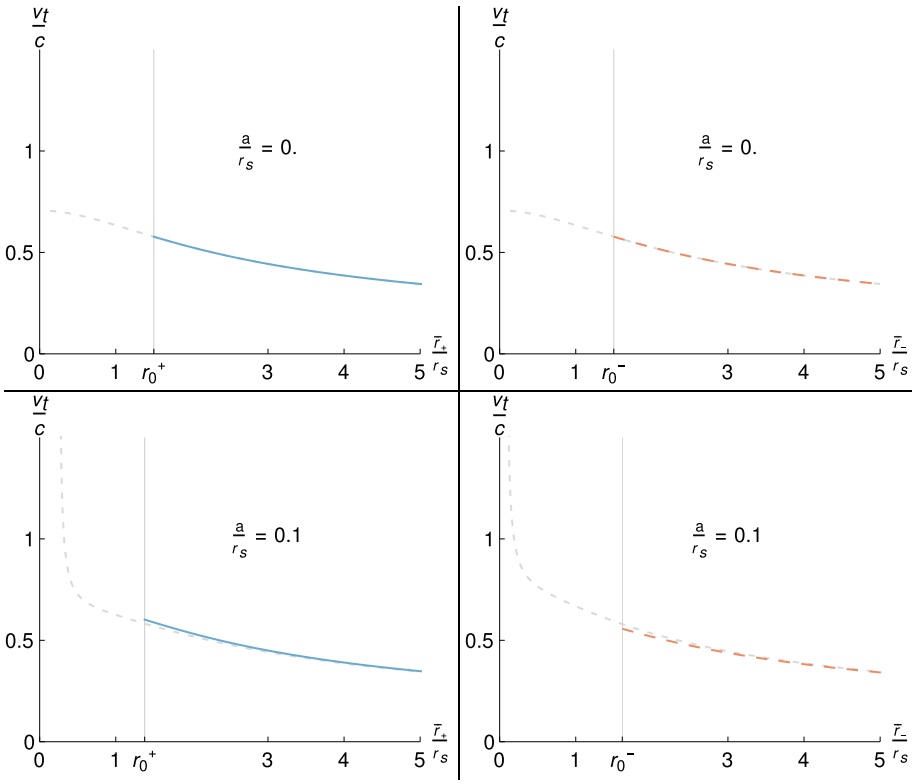
$$\frac{v^{\pm}_{\text{Newton}}(\bar{r}_{\pm})}{c} = \sqrt{\frac{r_s}{2\bar{r}_{\pm}}}. \tag{2.144}$$

Clearly, a flattening effect due to relativistic gravitational corrections is effective in the velocity curves $\bar{v}_t^{\pm}(\bar{r}_{\pm})$ as compared to the Newtonian curve, and the more strongly so for prograde equatorial circular trajectories relative to retrograde ones.

Figs. 2.10 and 2.11 depict the effective potential in eq. (2.123) of a massive particle in the Kerr spacetime, normalised to $(\mu_0 c^2)$, for different values of the angular momentum L (normalised to $\mu_0 c r_s$). Fig. 2.10 (resp.,

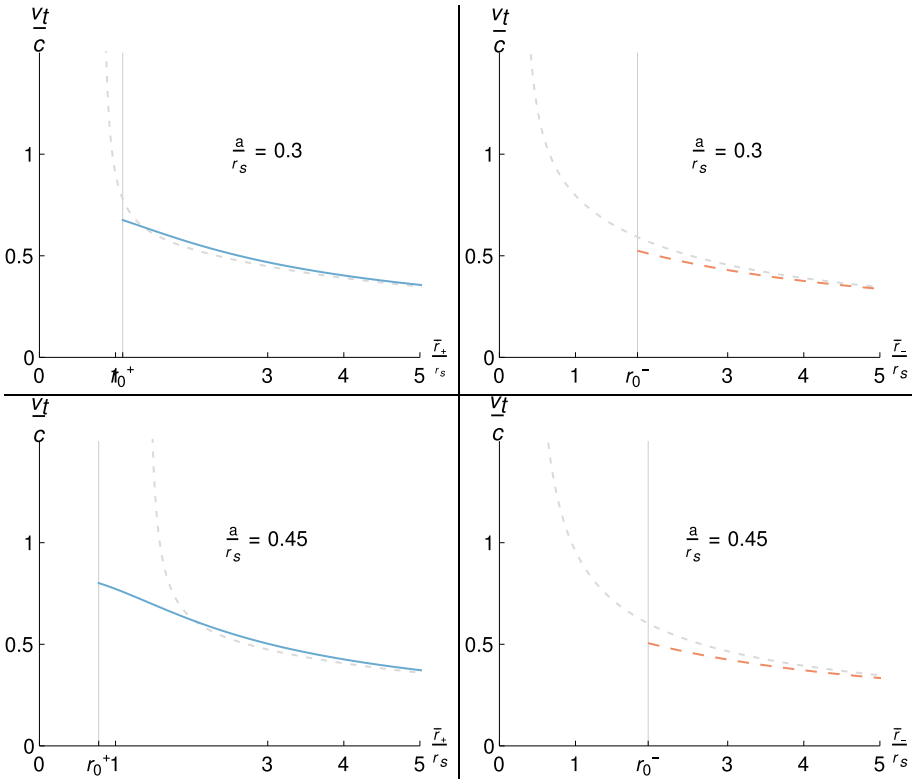
*Note that the prograde photon sphere value r_0^+ crosses the ergosurface radial value $r_E(\theta = \pi/2) = r_s$ for $a/r_s = 1/(2\sqrt{2}) \simeq 0.35355$.

Fig. 2.11) shows the potentials for a direct (resp., retrograde) rotating particle. On each figure, the left (resp., right) column shows the potential as a function of coordinate (resp., geometric) radius. Each row depicts a different value of the Kerr parameter, *i.e.*, the angular momentum of the black hole itself. The thin vertical lines show the photon sphere radii.



(a)

Figure 2.9: The horizontal axis of the graphs in the left (respectively, right) column represents the direct (resp. retrograde) geometric radius $\bar{r}_+$ (resp. $\bar{r}_-$) in units of r_s, while the vertical axis is the velocity $\bar{v}_t^+(\bar{r}_+)$ (resp. $-\bar{v}_t^-(\bar{r}_-)$) in units of c. Plain blue lines represent velocities for prograde trajectories. Dashed orange lines represent the negative—for convenience—of velocities for retrograde trajectories. Four different values for the Kerr parameter a in units of r_s are depicted (namely, in Fig. 2.9a, $a/r_s = 0$ on the first line and 0.1 on the second line, and in Fig. 2.9b, $a/r_s = 0.3$ on the first line and 0.45 on the second line.). The Newtonian curve (2.144) is also represented in dashed gray.

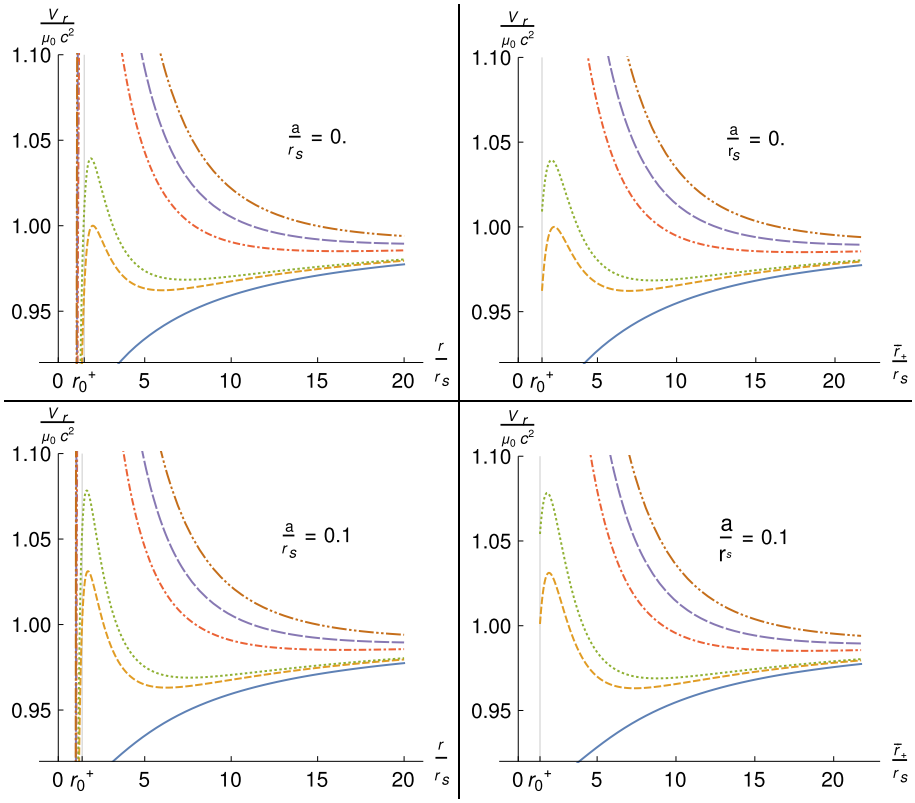


(b)

Figure 2.9

As can be seen, in the direct rotating direction, the faster the black hole is rotating, the more energy/angular momentum one needs to stay in a circular orbit, be it stable or unstable. While in the retrograde rotating direction, it is exactly the opposite phenomenon that happens.

Fig. 2.12 (resp., Fig. 2.13) shows the potentials for direct (resp., retrograde) rotating massless particles (in units of c^2) in the equatorial plane of the Kerr spacetime. Each coloured line depicts a different value of the angular momentum (in units of $r_s c$, from 1.5 to 4). The left (resp., right) column shows the effective potentials as functions of coordinate (resp., geometric) radius. Four different values for the Kerr parameter a in units of r_s are depicted (namely, in Fig. 2.12a and Fig. 2.13a, $a/r_s = 0$ on the first line and 0.1 on the second line, and in Fig. 2.12b and Fig. 2.13a,



(a)

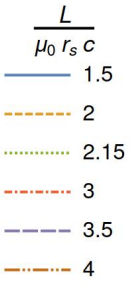
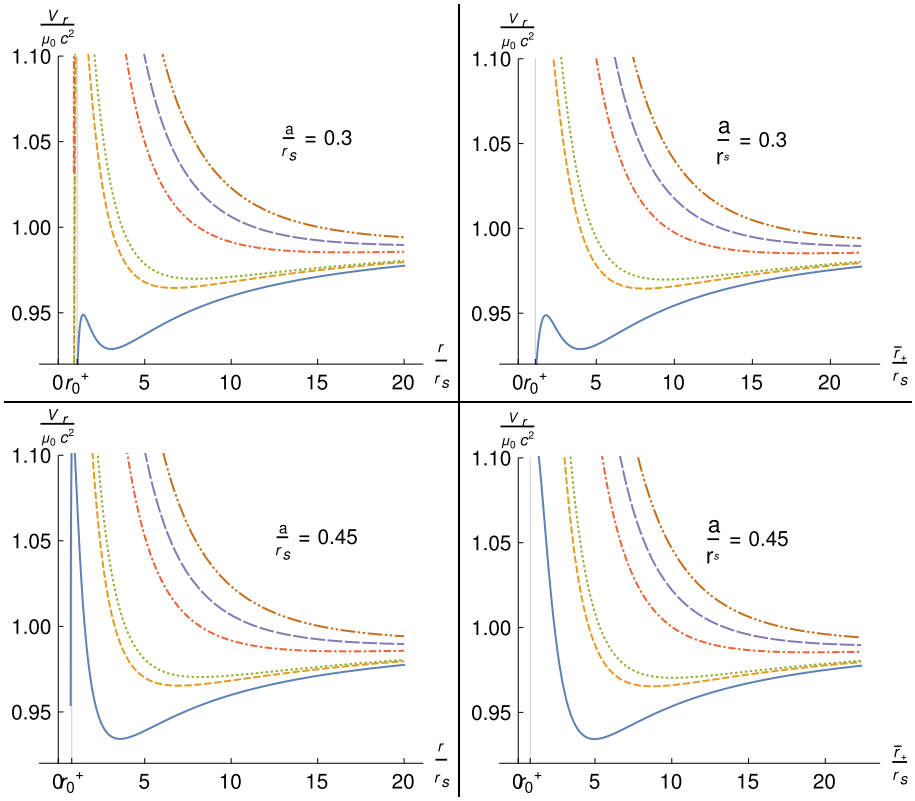


Figure 2.10: These graphs show the effective potential (in units of $\mu_0 c^2$) for a massive particle of mass μ_0, rotating in the direct direction in the equatorial plane of the Kerr spacetime. Each coloured line ordered from bottom to top for increasing values of L depicts a different value of the angular momentum (in units of $\mu_0 r_s c$, from 1.5 to 4). The left (resp., right) column shows the effective potentials as functions of coordinate (resp., geometric) radius. Four different values for the Kerr parameter a in units of r_s are depicted (namely, in Fig. 2.10a, $a/r_s = 0$ on the first line and 0.1 on the second line, and in Fig. 2.10b, $a/r_s = 0.3$ on the first line and 0.45 on the second line.). The thin vertical lines show the photon sphere radii.



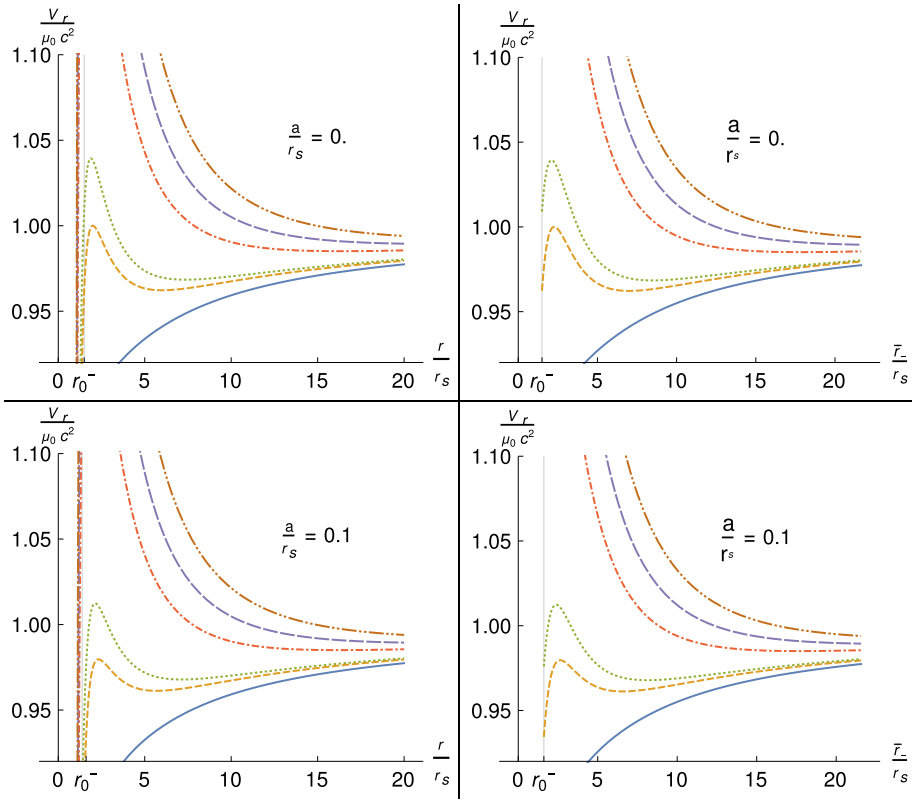
(b)

Figure 2.10

$a/r_s = 0.3$ on the first line and 0.45 on the second line.). The thin vertical lines show the photon sphere radii. The thin vertical lines show the photon sphere radii.

2.8 Summary

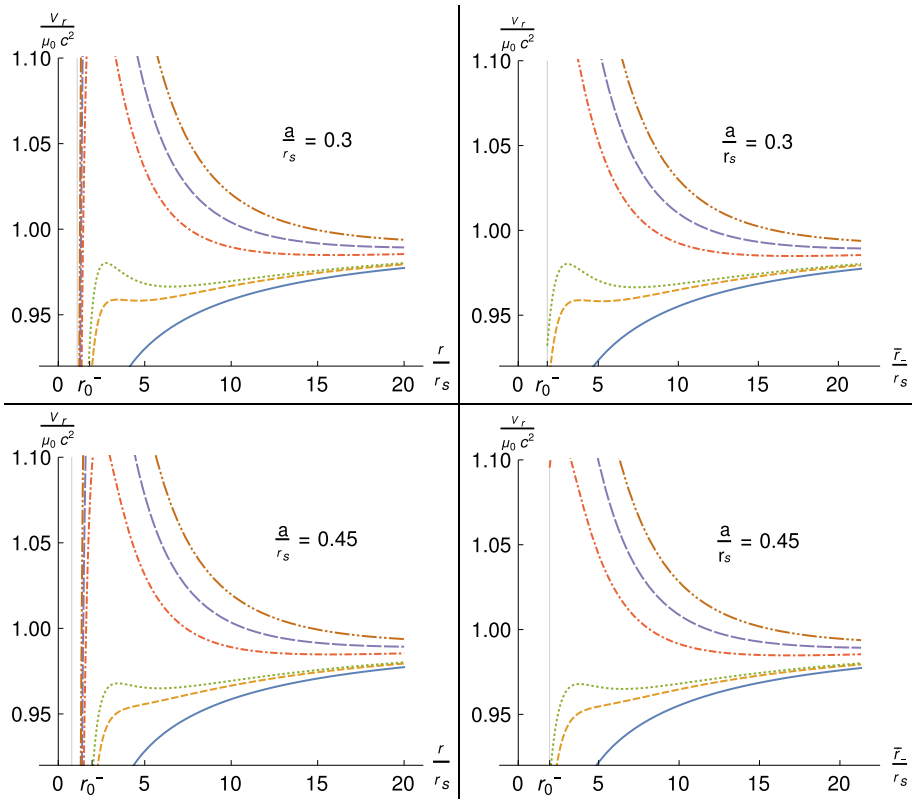
In this chapter, we have presented a general approach to defining—in a geometrically invariant manner—the velocity of a massive (or massless) particle on a circular orbit in the equatorial plane of a stationary asymptotically flat spacetime metric, whether spherical or axial symmetry. This velocity is defined with respect to the coordinate time of the particle



(a)



Figure 2.11: These graphs show the effective potential (in units of $\mu_0 c^2$) for a massive particle of mass μ_0, rotating in the retrograde direction in the equatorial plane of the Kerr spacetime. Each coloured line ordered from bottom to top for increasing values of L depicts a different value of the angular momentum (in units of $\mu_0 r_s c$, from 1.5 to 4). The left (resp., right) column shows the effective potentials as functions of coordinate (resp., geometric) radius. Four different values for the Kerr parameter a in units of r_s are depicted (namely, in Fig. 2.11a, $a/r_s = 0$ on the first line and 0.1 on the second line, and in Fig. 2.11b, $a/r_s = 0.3$ on the first line and 0.45 on the second line.).The thin vertical lines show the photon sphere radii.



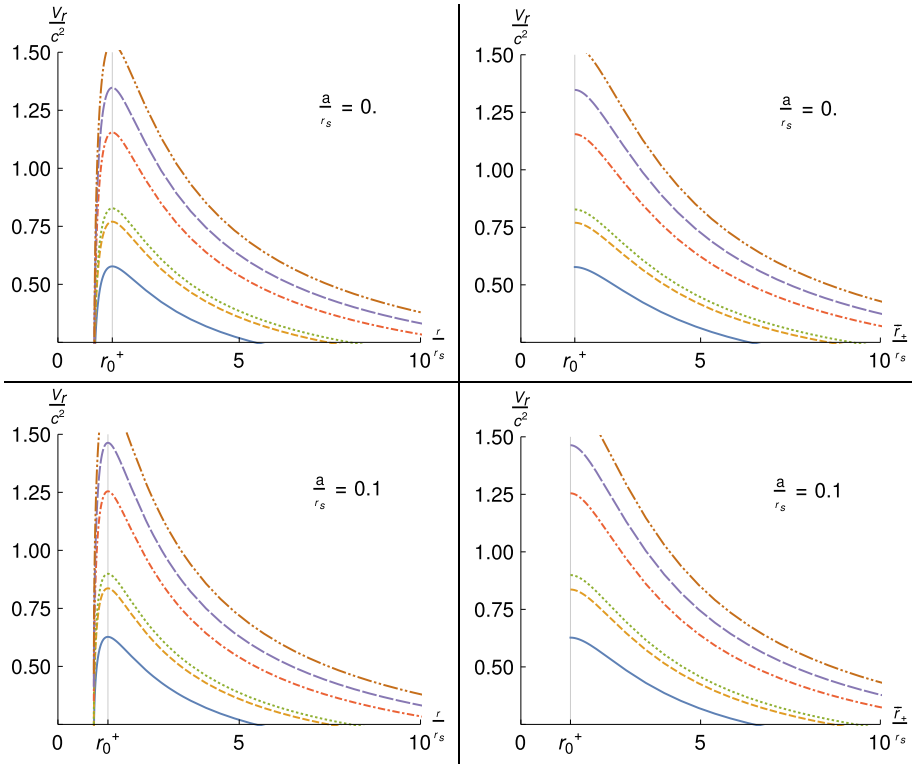
(b)

Figure 2.11

and its invariant geometric radial position as measured by an asymptotic stationary observer.

We have also explored three different definitions of an effective potential, each with its advantages and disadvantages. Whilst the first one was used in the same chapter, the latter two will find their uses in later chapters.

Two different metrics were then used as working examples. First, the Schwarzschild spacetime, whose simplicity allows us to compute everything by hand. Second, the Kerr metric, which has an additional parameter—the black hole's non-vanishing angular momentum— permitting the consideration of prograde and retrograde orbits, depending on the particle orientation direction relative to the black hole rotation direction.



(a)

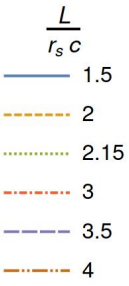
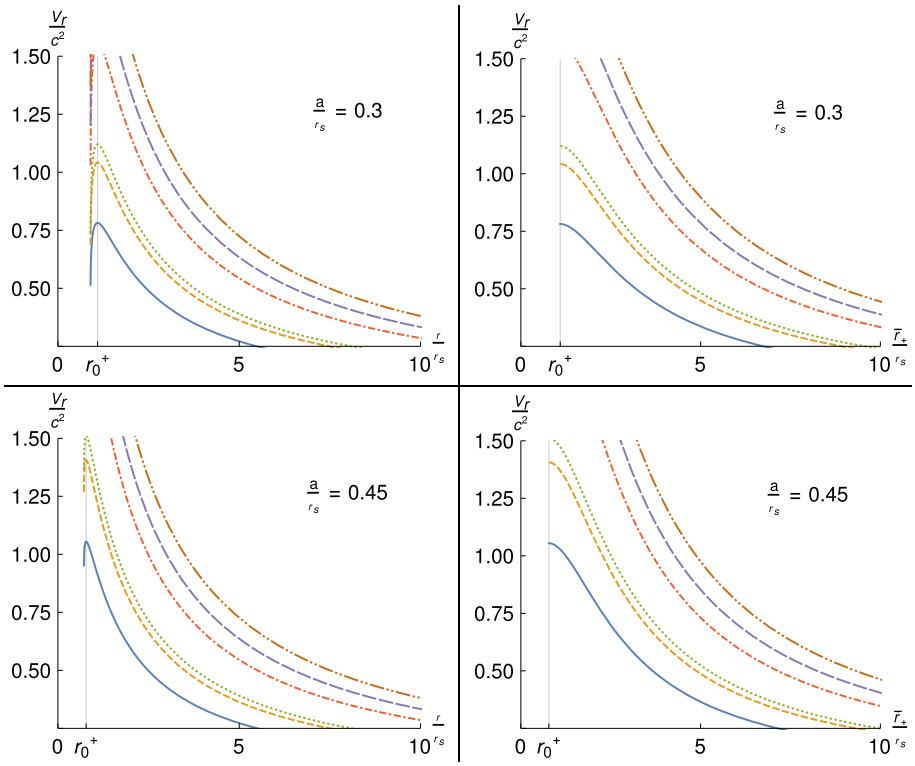


Figure 2.12: These graphs show the effective potential (in units of c^2) for a massless particle with $\mu_0 = 0$, rotating in the direct direction in the equatorial plane of the Kerr spacetime. Each coloured line ordered from bottom to top for increasing values of L depicts a different value of the angular momentum (in units of $r_s c$, from 1.5 to 4). The left (resp., right) column shows the effective potentials as functions of coordinate (resp., geometric) radius. Four different values for the Kerr parameter a in units of r_s are depicted (namely, in Fig. 2.12a, $a/r_s = 0$ on the first line and 0.1 on the second line, and in Fig. 2.12b, $a/r_s = 0.3$ on the first line and 0.45 on the second line.). The thin vertical lines show the photon sphere radii.

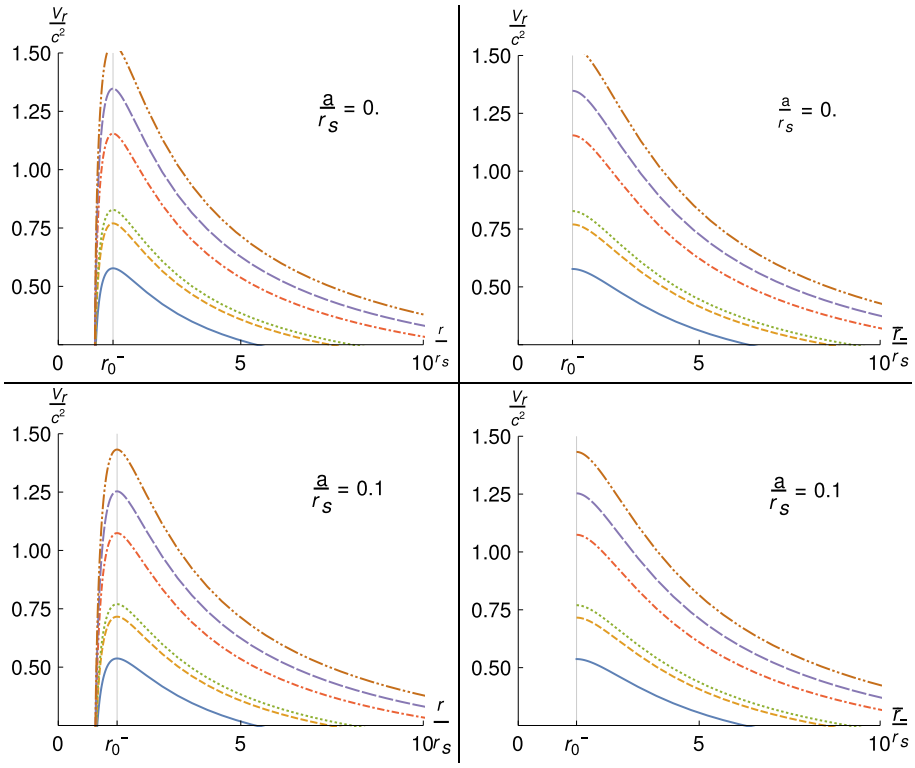


(b)

Figure 2.12

This approach provides a consistent framework for comparing velocities and their rotation curves across different metrics.

The next chapter will apply the ideas developed here to the gravimagnetic dipole spacetime metric that was presented in Chapter 1.



(a)

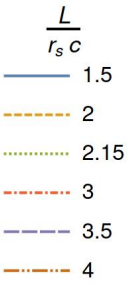
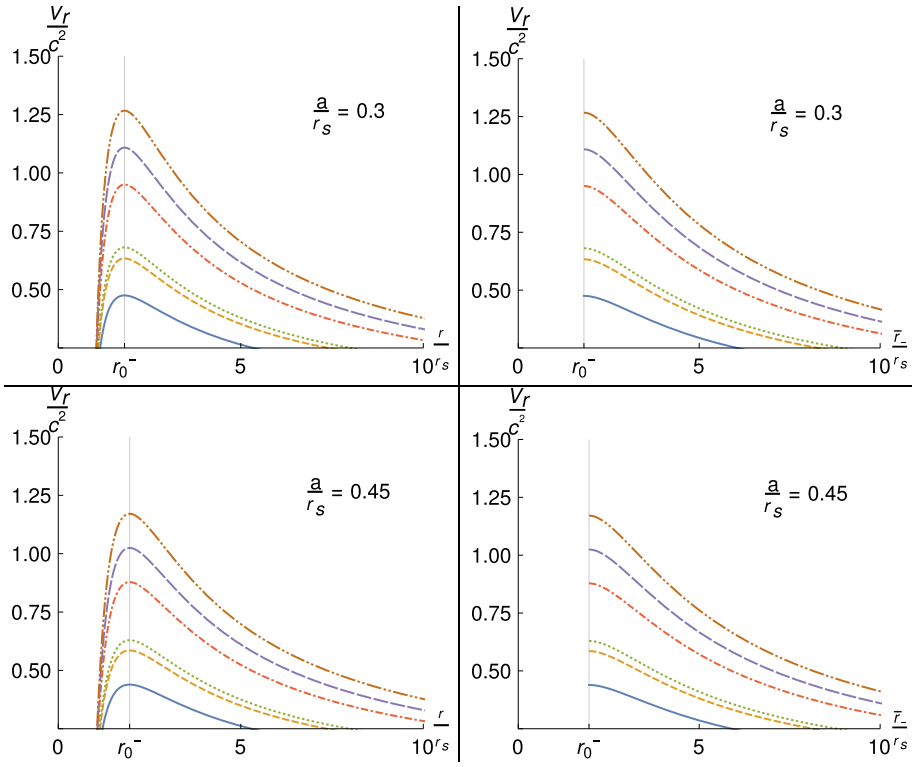


Figure 2.13: These graphs show the effective potential (in units of c^2) for a massless particle with $\mu_0 = 0$, rotating in the retrograde direction in the equatorial plane of the Kerr spacetime. Each coloured line ordered from bottom to top for increasing values of L depicts a different value of the angular momentum (in units of $r_s c$, from 1.5 to 4). The left (resp., right) column shows the effective potentials as functions of coordinate (resp., geometric) radius. Four different values for the Kerr parameter a in units of r_s are depicted (namely, in Fig. 2.13a, $a/r_s = 0$ on the first line and 0.1 on the second line, and in Fig. 2.13b, $a/r_s = 0.3$ on the first line and 0.45 on the second line.). The thin vertical lines show the photon sphere radii.


$\frac{V_r}{c^2}$
1.50
1.25
1.00
0.75
0.50
$\frac{a}{r_s}$ = 0.3
0
r_0^-
5
10^{r_s}
$\frac{r}{r_s}$
$\frac{a}{r_s}$ = 0.45

(b)

Figure 2.13

CHAPTER 3

VELOCITY ROTATION CURVES IN THE EQUATORIAL PLANE OF THE GRAVIMAGNETIC DIPOLE SPACETIME

> "The idea hovered and shimmered delicately, like a soap bubble, and she dared not even look at it directly in case it burst. But she was familiar with the way of ideas, and she let it shimmer, looking away, thinking about something else."
>
> — Philip Pullman *His Dark Materials, Book 1: Northern Lights* (1995)

Having established in the previous chapter the main theoretical framework, we now apply these tools to our objective: constructing velocity rotation curves in the gravimagnetic dipole spacetime. The term "rotation curve" is used here in the theoretical sense, to denote the velocity profile of test particles on a circular orbit. These curves serve more as a qualitative study of the spacetime geometry and of the gravimagnetic

dipole influence of the NUT parameter, rather than a direct counterpart of observed galaxy rotation curves. Nevertheless, given that the weak-field limit of this spacetime can yield approximately flat velocity profiles [89] qualitative analogies with dark-matter-motivated rotation curves may be noted, though no detailed observational nor theoretical comparison is attempted in the present work. Such a comparison would at the very least require a modelled inclusion of the contributions of ordinary and visible mass distributions in generic galaxies and their effects, probably challenging the equilibrium condition for the Misner string that was established in Chapter 1, the presence (or at least, the position) of closed timelike curves and various other features.

Our analysis will proceed in several stages, loosely following the order of what was presented in Chapter 2. Section 3.1 presents the computation of the proper radius as a function of the coordinate radius and the NUT parameter.

In Section 3.2, we determine the explicit expressions of the Hamiltonian equations and constraint, which naturally leads us to the expression of the effective potential in Section 3.3—we use the second definition of effective potential, the Hamiltonian-constraint effective potential, that was presented in Section 2.4.2. We then particularise this definition for, in turn, massless and massive particles, leading to explicit equations that we will not solve immediately because of their complexity. Before proceeding any further, we briefly mention in Section 3.4 the achronal region issue, which will be dealt with more in depth in Appendix B.

In Section 3.5 we determine the expressions for the velocity on the circular orbits as a function of the radius, again separately for massless and massive particles.

As was said above, the determination of the position of the circular orbits, as well as their stability, is quite an involved process. To make it as painless as possible, an example is presented in Section 3.6: we choose a fixed value for the NUT parameter, then for a few different values of the energy of the massive particle, we examine the first and second derivatives of the effective potential, allowing us to determine the location of circular orbits in the prograde or retrograde direction, as well as their stability. This then leads to the construction of the corresponding velocity rotation curves.

A more general approach is then taken in Section 3.7, giving some pointers on the stability and location of the circular orbits, whatever the

value of ν. It is followed by the determination of the general shape of the velocity rotation curves in Section 3.8. The comparison with the gravito-electromagnetic approximation, which describes the weak-field and slow motion of general relativity through an analogy with electromagnetism, is made in its subsection 3.8.3, showing good agreement in the relevant domain of parameters.

Finally, Section 3.9 summarises this whole Chapter.

3.1 Proper distance and proper radius

As was discussed in Sections 2.1 and 2.2, we now need the proper radius defined specifically for the gravimagnetic dipole spacetime to be able to plot physically relevant velocity rotation curves. We follow the procedure that was outlined in the aforementioned sections, and thus need to compute the proper radius $\bar{\rho}$ as a function of the coordinate radius ρ, from the following definition:

$$\bar{\rho}(\rho) = \int_0^\rho \sqrt{g_{\rho\rho}(\rho', 0)}\, d\rho' \tag{3.1}$$

Note that the lower bound of the integral was chosen in a somewhat arbitrary way as the Misner string location. Indeed, there is no coordinate singularity like in the Schwarzschild spacetime, and choosing the location of the photon sphere like in the Kerr spacetime proves too difficult on account of their number in the gravimagnetic dipole case.

On the equatorial plane, $z = 0$, the factor $g_{\rho\rho}$ has quite a simple expression:

$$z = 0; \qquad g_{\rho\rho} = \frac{e^{2\gamma}}{f} = \frac{|A + B|^2}{64\alpha_+^2 \alpha_-^2 d^4 R^2 r^2}, \tag{3.2}$$

where $R \equiv R_+(\rho, 0) = R_-(\rho, 0)$ and $r \equiv r_+(\rho, 0) = r_-(\rho, 0)$.

When divided by $\alpha_+\alpha_-$, $A + B$ is real and strictly negative (even when not in the tensionless Misner string case). Furthermore, with our choice of parameters, α_+, α_-, d, R and r are all real and strictly positive. The

quantity under the square root can thus be expressed as

$$\begin{aligned}\sqrt{g_{\rho\rho}} &= -\frac{A+B}{\alpha_+\alpha_-}\frac{1}{8d^2Rr} \\ &= \frac{1}{2}+\left(\frac{1}{R}+\frac{1}{r}\right)+\frac{1}{d}\left(\frac{1}{R}-\frac{1}{r}\right) \\ &+\frac{1}{2d^2}+\frac{1}{4}\left(1-\frac{1}{d^2}\right)\left(\frac{r}{R}+\frac{R}{r}\right).\end{aligned} \tag{3.3}$$

All of the terms in this expression are trivial to integrate, except maybe for the last one, which requires the introduction of the incomplete elliptic integral of the second kind, defined as follows*:

$$E(x;\kappa)=\int_0^x \frac{\sqrt{1-\kappa^2t^2}}{1-t^2}\,dt. \tag{3.4}$$

This integral E can be evaluated with arbitrary numerical precision with the help of, for example, the computation software Mathematica [92]. The geometric radius is then expressed in the following manner †:

$$\begin{aligned}\int \sqrt{g_{\rho\rho}}\,d\rho =& \frac{-i(d^2-1)}{4d^2}\left\{\alpha_+E\left(\frac{i\rho}{\alpha_-};\frac{\alpha_-}{\alpha_+}\right)+\alpha_-E\left(\frac{i\rho}{\alpha_+};\frac{\alpha_+}{\alpha_-}\right)\right\} \\ &+\frac{1}{d^2}\Big\{d\left[(d-1)\log(\rho+r)+(d+1)\log(\rho+R)\right] \\ &+\frac{\rho}{2}\left(d^2+1\right)\Big\}.\end{aligned} \tag{3.5}$$

Let us emphasize that $\bar{\rho}(\rho)$ depends not only on ρ, but also on the value of the NUT parameter ν.

Fig. 3.1 shows the proper radius $\bar{\rho}$ as a function of the coordinate radius ρ for three different values of the NUT parameter $\nu = 0.05$, 0.6 and 0.9. As a reference the identity is also plotted with a thin grey line.

*There are multiple (somewhat confusing) conventions [90, 91] in the notation of incomplete elliptical integrals, involving different typographical rules to clarify which one is used. For example, the notation we use here $E(x=\sin\varphi;\kappa)=E(\varphi,\kappa)=E(\varphi|\kappa^2)$, with the amplitude φ and the elliptic modulus (or eccentricity) κ (the elliptic modulus is usually denoted k, which we will avoid here to prevent any confusion). Mathematica uses the notation $E(\varphi|m)$ with the parameter $m=\kappa^2$ instead of the elliptic modulus κ.

†More details can be found in Appendix A, Section A.4.

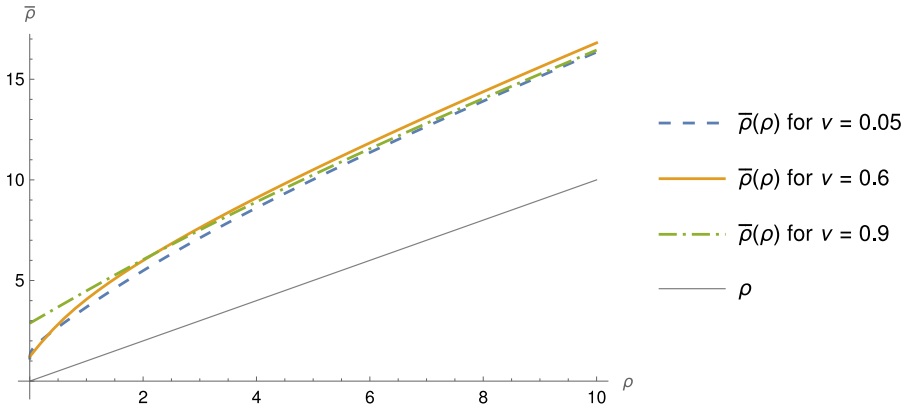


Figure 3.1: The proper radius for three values of the NUT parameter is plotted as a function of the coordinate radius. As a reference, the thin grey line is also the coordinate radius as a function of the coordinate radius, *i.e.* the identity.

The proper radius $\bar{\rho}(\rho)$ is a monotonically increasing function. The asymptotic behaviour of the terms in the above expression yield

$$\begin{cases} \lim\limits_{\rho\to\infty} \dfrac{i}{\rho} E\left(\dfrac{i\rho}{\alpha_-}, \dfrac{\alpha_-}{\alpha_+}\right) = \dfrac{-\alpha_-}{|\alpha_-|\,|\alpha_+|} = -\dfrac{1}{\alpha_+}, \\ \lim\limits_{\rho\to\infty} \dfrac{i}{\rho} E\left(\dfrac{i\rho}{\alpha_+}, \dfrac{\alpha_+}{\alpha_-}\right) = \dfrac{-\alpha_+}{|\alpha_-|\,|\alpha_+|} = -\dfrac{1}{\alpha_-}, \\ \lim\limits_{\rho\to\infty} \dfrac{\log(\rho + r)}{\rho} = 0, \\ \lim\limits_{\rho\to\infty} \dfrac{\log(\rho + R)}{\rho} = 0, \end{cases} \tag{3.6}$$

leading to

$$\lim_{\rho\to\infty} \frac{\bar{\rho}(\rho)}{\rho} = 1. \tag{3.7}$$

Although this behaviour is not immediately apparent from Fig. 3.1, it shows that the proper radius asymptotically agrees with the coordinate radius.

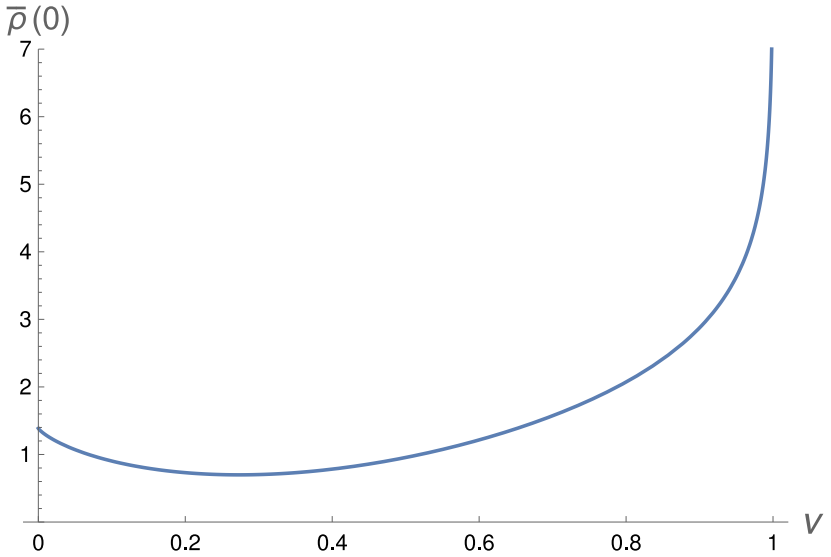


Figure 3.2: On the vertical axis, the value of $\bar{\rho}(\rho = 0)$ as a function of ν.

On the other hand, the proper radius at coordinate radius $\rho = 0$ is not a monotonic function of ν:

$$\bar{\rho}(\rho = 0) = \frac{(d-1)\log(\alpha_-^2) + (d+1)\log(\alpha_+^2)}{2d}. \tag{3.8}$$

The value of $\bar{\rho}(\rho = 0)$ is given as a function of ν in Fig. 3.2.

3.2 Geodesics of free particles

Let us now consider the Hamiltonian equations. Given the metric describing the gravimagnetic dipole spacetime in eqs. (1.4) and the considerations about the Hamiltonian in Section 2.3, the general relation between coordinate time t and proper time τ is expressed as,

$$\frac{dt}{d\tau} = \frac{1}{\sqrt{-g_{tt}}} = \frac{1}{\sqrt{f}}, \qquad \frac{d\tau}{dt} = \sqrt{f}. \tag{3.9}$$

Furthermore, in Hamiltonian form, the geodesic equations of motion read as follows, for the spacetime coordinates,

$$\begin{aligned} c\frac{dt}{du} &= e\left(g^{tt}p_t + g^{t\varphi}p_\varphi\right), \\ \frac{d\varphi}{du} &= e\left(g^{t\varphi}p_t + g^{\varphi\varphi}p_\varphi\right), \\ \frac{d\rho}{du} &= e\,g^{\rho\rho}p_\rho, \\ \frac{dz}{du} &= e\,g^{zz}p_z, \end{aligned} \tag{3.10}$$

and for the conjugate momenta,

$$\begin{aligned} \frac{dp_t}{du} &= 0, \\ \frac{dp_\varphi}{du} &= 0, \\ \frac{dp_\rho}{du} &= -\frac{1}{2}e\,\frac{\partial g^{\mu\nu}}{\partial\rho}p_\mu p_\nu, \\ \frac{dp_z}{du} &= -\frac{1}{2}e\frac{\partial g^{\mu\nu}}{\partial z}p_\mu p_\nu, \end{aligned} \tag{3.11}$$

subjected to the following constraint,

$$g^{tt}p_t^2 + 2g^{t\varphi}p_t p_\varphi + g^{\varphi\varphi}p_\varphi^2 + g^{\rho\rho}p_\rho^2 + g^{zz}p_z^2 + (\mu_0 c)^2 = 0, \tag{3.12}$$

with the conserved conjugate momenta p_t and p_φ,

$$p_t = -\frac{E}{c}, \qquad p_\varphi = L, \tag{3.13}$$

where E is the particle's relativistic energy and L its angular momentum (component along the axial symmetry axis), both taking constant and real values.

3.3 The effective potential for circular orbits

In the equatorial plane one has $p_z = 0 = z$ (see Section A.1 in Appendix A for the verification of $dp_z/du = 0$, which is a non-trivial property) while the Hamiltonian of a massive ($\mu_0 > 0$) or massless ($\mu_0 = 0$) particle can

be expressed as, using the conserved quantities E and L,

$$\mathcal{H} = \frac{e}{2}\frac{1}{c^2}\left[g^{tt}E^2 - 2g^{t\varphi}E(cL) + g^{\varphi\varphi}(cL)^2 + g^{\rho\rho}p_\rho^2 + (\mu_0 c^2)^2\right]. \quad (3.14)$$

This expression can be used to particularise the Hamiltonian-constraint effective potential described in Section 2.4.2.

First, we need to identify the generic expression of the Weyl-Papapetrou canonical form of the axisymmetric metric in eq. (2.27) with the gravimagnetic dipole; this is done by identifying the metric functions:

$$e^{2\psi} = f, \qquad A = -\omega, \quad e^{2\gamma} = e^{2\gamma}. \quad (3.15)$$

This allows us to rewrite the expression of the effective potential of eq. (2.34) in terms of our metric functions:

$$V(\rho, b) = \frac{\rho^2}{e^{2\gamma}}\left\{1 - \frac{\rho^2}{f^2}\frac{1}{(b-\omega)^2}\left[1 - f\left(\frac{\mu_0 c^2}{E}\right)^2\right]\right\}, \quad (3.16)$$

with $b = cL/E$ the impact parameter*, such that

$$\left(\frac{d\rho}{d\varphi}\right)^2 + V(\rho, b) = 0. \quad (3.17)$$

As was said earlier, circular orbits then correspond to the double condition that

$$V(\rho, b) = 0 \quad (3.18)$$

and

$$\partial_\rho V(\rho, b) = 0. \quad (3.19)$$

The easiest way to find the location of the corresponding radius is then to determine the critical impact parameter (here called $b_\pm$) from eq. (2.35), which reduces here to

$$b_\pm(\rho) \equiv b_c^\mp = \omega \pm \frac{\rho}{f}\sqrt{1 - f\left(\frac{\mu_0 c^2}{E}\right)^2} \quad (3.20)$$

*The name *impact parameter* was chosen as an analogy with the lensing case, with b_+ (respectively b_-) called the prograde (resp. retrograde) impact parameter. Looking at eq. (3.20), we can deduce that b_- is always negative and b_+ can be either positive or negative depending on the value of ρ. However for circular orbits, either massless or massive with $E > 0$, b_+ is always positive.

and is such that eq. (3.18) is verified for any value of ρ:

$$V\left[\rho, b = b_{\pm}(\rho)\right] = 0. \tag{3.21}$$

Eq. (3.19) then simplifies considerably: denoting a derivative relative to ρ with a prime, $'$, it reduces to:

$$V'(\rho,b)\Big|_{b=b_{\pm}} = \left(\frac{\rho^2}{e^{2\gamma}}\right)' \underbrace{\left\{...\right\}}_{=0 \text{ for } b=b_{\pm}} + \frac{\rho^2}{e^{2\gamma}} \underbrace{\left\{...\right\}'}_{=\Xi(\rho)}, \tag{3.22}$$

where the first term automatically cancels by choice of $b = b_{\pm}(\rho)$. The second term will need a bit more work. Since $e^{2\gamma} \neq 0$ for any value of (ν, ρ) such that $(\nu > 0,\, \rho > 0)$, the expression of interest will be only the rightmost term, which will be called $\Xi(\rho)$ in the following. The expression Ξ having only a dependence in ρ is to be understood as follows: the curly bracket expression depends on ρ and b. It is derived with respect to ρ, and afterwards b is replaced by its value $b_{\pm}(\rho)$:

$$\Xi(\rho) = \left(\frac{\partial}{\partial\rho} \left\{ 1 - \frac{\rho^2}{f^2} \frac{1}{(b-\omega)^2} \left[1 - f \left(\frac{\mu_0 c^2}{E} \right)^2 \right] \right\} \right)_{b=b_{\pm}(\rho)}. \tag{3.23}$$

A note on the sign of the impact parameter The convention chosen here is not the usual one. Typically, a prograde particle is defined as one that rotates in the same direction as the central black hole. In this work, however, the system consists of two corotating black holes, with the frame dragging (and thus the direction rotation) being negative (or clockwise) since $\omega < 0$. According to the standard convention, prograde particles co-rotate with the black hole. Here, we take prograde particles to be the ones that rotate in the opposite direction to the black hole, while those rotating in the same direction are called retrograde.

3.3.1 The massless case

In the case of massless particles, $\mu_0 = 0$, while the impact parameter reduces to

$$b_{\pm} = \omega \pm \frac{\rho}{f}. \tag{3.24}$$

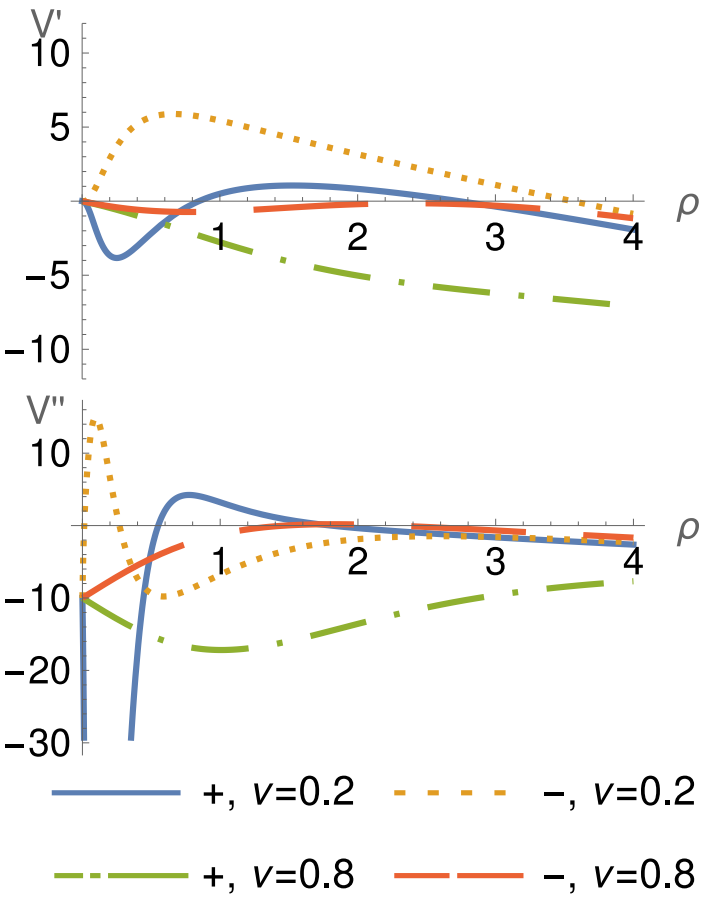


Figure 3.3: The top (resp. bottom) graph represents the first (resp. second) derivative of the potential as a function of ρ for massless particles, for two different rotation directions (prograde and retrograde) and two different values of ν. The number of possible circular orbits (from 0 to 4) depends on this parameter. The zeroes of the first derivative of the potential indicate the radii at which the photon orbits occur, and the values of the second derivative at these radii indicate if the corresponding orbit is stable or unstable. For example, for $\nu = 0.2$ and a retrograde photon (orange dotted line), there is a unstable orbit at $\rho \approx 3.6$.

The function $\Xi(\rho)$ in eq. (3.22) is then given by the following expression:

$$\Xi(\rho) = -\frac{2(\pm f^2\omega' + f - f'\rho)}{f\rho}. \tag{3.25}$$

The radii $\rho_\pm$ of the photon orbits are then given by the solutions of $\Xi(\rho) = 0$, the sign factor corresponding to the one of $b_\pm$ and thus either a prograde or retrograde orbit. Depending on the values of the NUT parameter ν and of the energy E, eq. (3.25) will have between four and zero possible solutions. Then, according to the value of the second derivative in ρ of the potential, V'', this orbit will be either stable ($V'' > 0$) or unstable ($V'' < 0$).

In Fig. 3.3, the top (resp. bottom) graph presents the first (resp. second) derivative of the potential for a massless particle as functions of ρ and evaluated at $b = b_\pm$. For each graph, two values of the NUT parameter ($\nu = 0.2$, $\nu = 0.8$) are represented for the prograde and retrograde directions. The zeroes of the first derivative of the potential indicate the radii at which the photon orbits occur, and the values of the second derivative at these radii indicate if the corresponding orbit is stable or unstable. For example, for $\nu = 0.2$ and a retrograde photon (orange dotted line), there is an unstable orbit at $\rho \approx 3.6$.

Eq. (3.25) can also be used to construct a bifurcation diagram*, providing a visualisation of how the number of solutions varies with the value of ν. This is done in Fig. 3.4. As the value of ν grows, the number of photon orbits decreases. The prograde (resp. retrograde) orbits coalesce into one prograde (resp. retrograde) degenerate orbit (shown by a black square), then disappear. The coordinates of the saddle-node bifurcation can be numerically computed: for the prograde orbit, $\nu = 0.27$, $\rho = 1.78$, and for the retrograde orbit $\nu = 0.79$, $\rho = 2.30$.

The stability of the photon orbits is quite simple and can be determined from the general shape of V''; whenever photon orbits exist, the one with the inner radius will be stable, whilst the outer radius corresponding one will be retrograde. When there is only one orbit, it is degenerate and the corresponding value of V'' is zero.

*The bifurcation diagram was inspired by [93], where the same phenomenon of duplication of the photon orbits is observed for some values of the distance separating two identical black holes modelled by an equal mass Majumdar-Papapetrou di-hole metric.

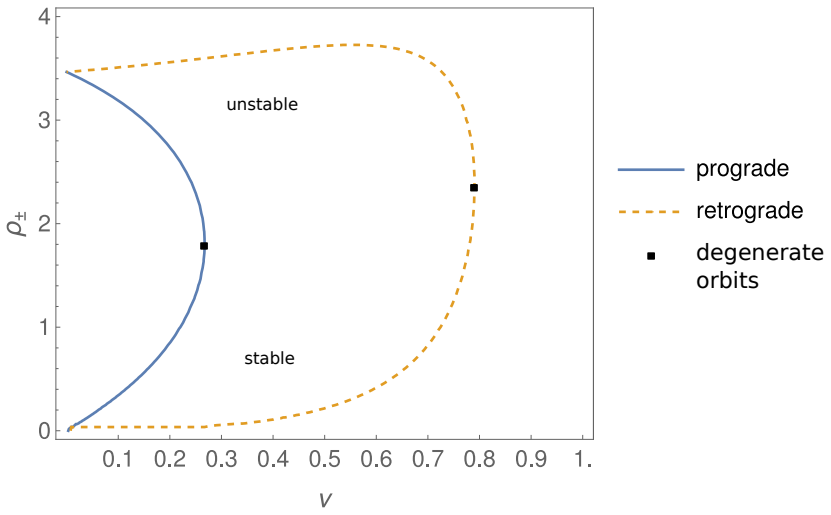


Figure 3.4: As functions of the parameter ν for massless particles, the radii of the possible circular orbits $\rho_\pm$ are represented. The plain line corresponds to prograde orbits, the dashed one to retrograde orbits. Depending on the value of ν, there will be between zero and four possible circular orbits. The black squares show the degenerate photon orbits, with the upper branches representing the unstable orbits, and the lower branches the stable orbits.

3.3.2 The massive case

Going back to eq. (3.22), we keep μ_0 non zero and the complete expression of $\Xi(\rho)$ is:

$$\begin{aligned}\Xi(\rho) &= \frac{\rho\left[\rho f'(2E^2 - c^4\mu_0^2 f) + 2f(c^4\mu_0^2 f - E^2)\right]}{E^2 f^3 (b_\pm - \omega)^2} + \frac{2\rho^2 f\omega'(c^4\mu_0^2 f - E^2)}{E^2 f^3 (b_\pm - \omega)^3} \\ &= \frac{2f^2(c^4\mu_0^2 \mp \beta E^2\omega') - f(c^4\mu_0^2\rho f' + 2E^2) + 2E^2\rho f'}{\beta^2 E^2 \rho f},\end{aligned} \tag{3.26}$$

where

$$\beta = \sqrt{1 - f\left(\frac{\mu_0 c^2}{E}\right)^2}, \quad b_\pm = \omega \pm \frac{\rho}{f}\beta. \tag{3.27}$$

The radii $\rho_\pm$ of the circular orbits are then given by the solutions of $\Xi(\rho) = 0$, the sign factor corresponding to the one of $b_\pm$ and thus either a prograde or retrograde orbit. Again, according to the value of the the second derivative in ρ of the potential, V'', this orbit will be either stable ($V'' > 0$) or unstable ($V'' < 0$). Depending on the values of the NUT parameter ν and of the energy E, eq. (3.26) will have between zero and four possible solutions.

The analysis of the corresponding graphs being quite involved, we will first conclude with the analytical computations before working with an example in Section 3.6. We will now take a look at what happens on the chronology boundary, before turning to the velocities on the circular orbits.

3.4 What happens on the chronology boundary?

As was mentioned in Chapter 1, the chronology boundary is the hypersurface where $g_{\varphi\varphi} = 0$. On the equatorial plane, this corresponds to a (unique) value of $\rho \geq 0$ satisfying the relation

$$g_{\varphi\varphi} = \frac{\rho^2}{f} - f\omega^2 = 0. \tag{3.28}$$

Since $f > 0$ and $\omega < 0$ for every value of ρ, and ν, this amounts to

$$\rho^2 = f^2\omega^2 \quad \Leftrightarrow \quad \rho = -f\omega \geq 0. \tag{3.29}$$

It is also worth noting that on the chronology boundary,

$$g^{tt} = -\frac{1}{f} + \frac{f\omega^2}{\rho^2} = 0, \tag{3.30}$$

but that $\dot{\varphi} \neq 0$;

$$\dot{\varphi} = -\frac{1}{g_{t\varphi}}\left(\frac{E}{c} + \frac{g_{tt}}{g_{t\varphi}}L\right). \tag{3.31}$$

The potential (2.33) can thus be worked out to be exactly the same as eq. (3.16).

The main question actually is if a particle can reach the achronal region. Notably, it has been shown that in the Kerr naked singularity spacetime [94] and in the Kerr-Newman (naked singularity or black hole) spacetime [60], there is some kind of chronology protection mechanism, such that the shape of the potential prevents certain particles arriving from infinity from penetrating the achronal region; they bounce back and go back to radial infinity. Whilst not being the focus of this work, some ideas regarding this issue are developed in Section B.2 of Appendix B.

3.5 Velocities for circular orbits in the gravimagnetic dipole spacetime

For a circular rotation curve in the equatorial plane, we have required $d\rho/du = 0$ and $z = 0$, $dz/du = 0$, meaning that the velocity can be written from eqs. (2.15) and (3.10) as:

$$\begin{aligned} v_t^2 &= \left(g_{\varphi\varphi} - \frac{(g_{t\varphi})^2}{g_{tt}}\right)\left(\frac{d\varphi}{dt}\right)^2 \\ &= \left(g_{\varphi\varphi} - \frac{(g_{t\varphi})^2}{g_{tt}}\right)\left(\frac{g^{\varphi\varphi}b - g^{t\varphi}}{g^{t\varphi}b - g^{tt}}\right)^2 \\ \Rightarrow \frac{v_t^2}{c^2} &= \frac{\rho^2 f^3 (b-\omega)^2}{[\rho^2 + f^2\omega(b-\omega)]^2}, \end{aligned} \tag{3.32}$$

where

$$b = b_{\pm} = \omega \pm \frac{\rho}{f}\sqrt{1 - f\left(\frac{\mu_0 c^2}{E}\right)^2}. \tag{3.33}$$

The expressions of the potentials that we have used until now give a nice representation of where the circular orbits might be, but are not very practical in order to compute the velocities since one has to solve eq. (3.26) (numerically) to find the energy needed for a circular orbit for each value of the radius. Consequently, another approach is being used hereafter to determine the energy corresponding to a particular value of ρ.

3.5.1 The massless case

In the massless case, the value of the radius of a photon orbit for some value of the NUT parameter is given by the solution of eq. (3.25). Replacing

$$b_{\pm} = \omega \pm \frac{\rho}{f} \tag{3.34}$$

in eq. (3.32), the velocity of the photons on their circular orbit is given by

$$\frac{v_{t,\pm}^2}{c^2} = \frac{\rho^2 f}{(\rho \pm f\omega)^2}, \tag{3.35}$$

where all functions are evaluated at $\rho = \rho_{\pm}$.

3.5.2 The massive case

Replacing the value of $b_{\pm}$ from eq. (3.33) in eq. (3.32), the velocity of a circular orbit as a function of the radius is given by

$$\frac{v_t^2}{c^2} = \frac{\beta^2\rho^2 f}{(\rho \pm \beta f\omega)^2}, \quad \text{where } \beta = \sqrt{1 - f\left(\frac{\mu_0 c^2}{E}\right)^2}. \tag{3.36}$$

As was mentioned earlier, the value of the energy E in this last equation can be found for each value of ρ by solving eq. (3.26), but can also be expressed in a simpler manner.

One of the conditions for a circular orbit is $dp_\rho/du = 0$ and eq. (3.11) can be used to rewrite it as

$$\partial_\rho g^{tt} - 2\partial_\rho g^{t\varphi}\frac{cL}{E} + \partial_\rho g^{\varphi\varphi}\left(\frac{cL}{E}\right)^2 = 0. \tag{3.37}$$

In conjunction with the constraint (3.12), this gives the expressions for the energy E and the angular momentum L for a circular orbit of radius ρ:

$$\begin{cases} E^2 = \dfrac{-(\mu_0 c^2)^2}{g^{tt} - 2g^{t\varphi}b + g^{\varphi\varphi}b^2}, \\ (cL)^2 = \dfrac{-(\mu_0 c)^2 b^2}{g^{tt} - 2g^{t\varphi}b + g^{\varphi\varphi}b^2}, \end{cases} \tag{3.38}$$

with

$$\frac{cL}{E} = b = \frac{\partial_\rho g^{t\varphi} \pm \sqrt{\left(\partial_\rho g^{t\varphi}\right)^2 - \partial_\rho g^{\varphi\varphi}\partial_\rho g^{tt}}}{\partial_\rho g^{\varphi\varphi}}. \tag{3.39}$$

With these equations in hand, it becomes easy, for a particular value of the radius ρ, to find, first, the impact parameter, then the squared value of the energy that a massive particle needs to possess to be allowed on a circular orbit. Of course, the sign of the squared value of the energy needs to be positive to ensure a physical value of the energy itself.

In the following sections, we are going to first determine the locations of the circular orbits, as well as their respective stability properties. We will then derive the corresponding velocity rotation curves. For these purposes, we will alternate between using the two equations previously introduced, and the effective potential formalism, selecting the approach that is most appropriate and easiest to implement for each step of the process.

3.6 Constructing the velocity rotation curve: an example with $\nu = 0.6$

From what we have seen, there are two approaches to circular orbits and their velocities. The first one we saw earlier in this chapter in Section 3.3: we use the effective potential, its derivatives and their roots, and for some specific value of the energy, we have one (highly non linear) equation to

solve to find the radius of the circular orbit. The drawback, of course, is that we do have to solve the highly non linear equation.

The second method, which we saw just above, lets us, for a specific value of the radius, compute first the impact parameter, then the value of the energy that is needed for such an orbit. This value, which needs to be real and positive, then also tells us if the circular orbit is actually permitted.

These two methods, whilst mathematically interchangeable, are used in the following in different ways; the first one, the effective potential, will be most useful when looking for a specific circular orbit (so, typically, for photon spheres), or when determining the actual existence, location and stability of the massive circular orbits; the second one, the squared energy, will be more useful when actually building the velocity curve, so when going through the values of the radius and plugging them in the velocity expression from eqs. (3.25) and (3.36).

Fig. 3.5 shows the the superposition of the bifurcation diagrams for, in thick black, a photon and in colours, a massive particle of mass $\mu_0 = 1$, with energies varying from $E = 0.5$ to $E = 1.5$. The plain lines represent prograde particles, and the dashed lines represent retrograde particles. The horizontal axis represents the values of the NUT parameter ν, and the vertical axis represents the radius $\rho_\pm$ at which the circular orbit happens (ρ_+ for a prograde orbit, ρ_- for a retrograde one, but they are on the same scale; this is still a coordinate radius).

The lines should be interpreted as representing existing solutions, *i.e.* each line is actually a collection of points, each point representing a solution (ρ, ν, E) to eq. (3.26). The purpose of this plot is to see that, for example, for the specific value of $\nu = 0.6$ (the red vertical line), there are no prograde photon orbits (the thick plain black line does not cross the $\nu = 0.6$ line). However there are two retrograde photon orbits, since there are two intersections between the red line, and the thick dashed black line. There are multiple massive prograde orbits for different values of the energy without apparent restriction on the radius; on the other hand, for a massive particle, retrograde orbits are possible only outside the region delimited by the two photon orbits (*i.e.* there are no dashed lines crossing the red vertical line between the photon dashed lines).

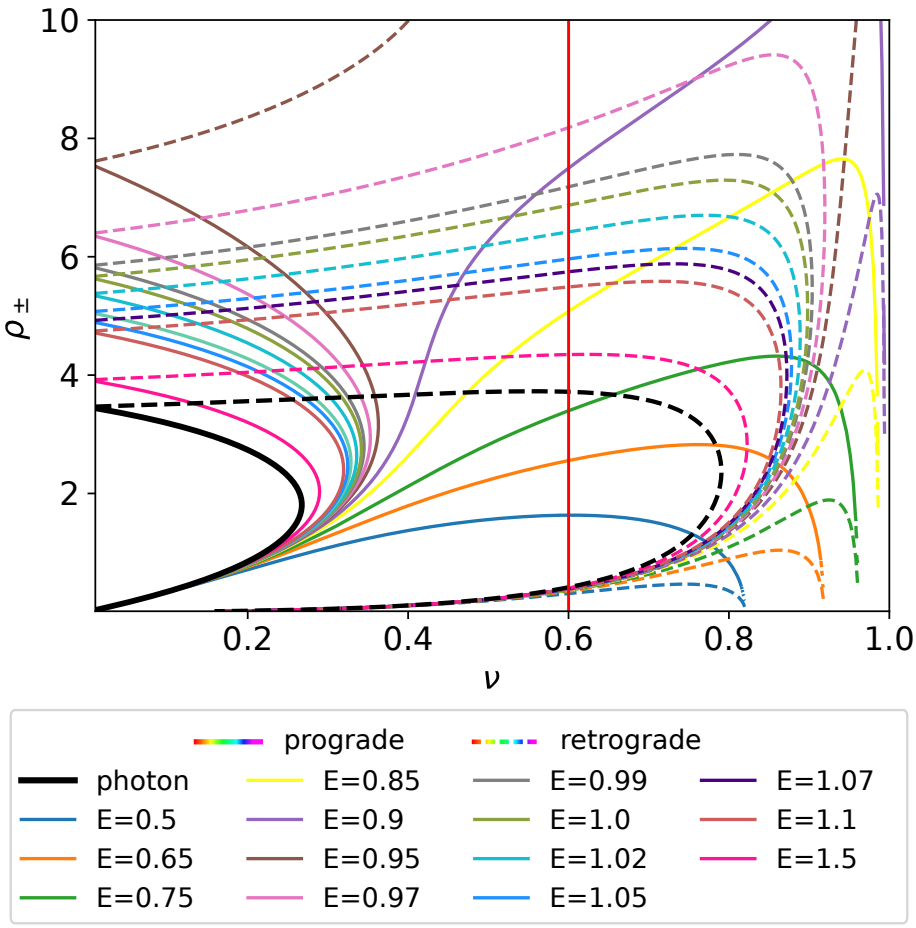


Figure 3.5: This is a bifurcation diagram showing how many solutions exist for any value of (ν, E). The thick black lines represent photons, and the coloured lines represent massive particles with $\mu_0 = 1$ with different values of the energies (see legend), and that are either prograde (plain lines) or retrograde (dashed lines). This graph can be read in the following way: for example, for $\nu = 0.6$, shown as the red vertical line, there are multiple intersections with different values of the energy. The two intersections with the hot pink dashed line mean that there are two retrograde circular orbits with energy $E = 1.5$ when $\nu = 0.6$. Not all energies could be represented, obviously, but the main point of interest is that there are no solutions between the corresponding photon orbits; so there are no retrograde massive orbits between the retrograde photon orbits, and no prograde massive orbits between the prograde photon orbits.

We are now going to look at the construction of the velocity rotation curves specifically for $\nu = 0.6$, first in the retrograde, then in the prograde direction.

3.6.1 Retrograde orbits

Fig. 3.5 being quite busy, let us now turn to Fig. 3.6, which has been particularised, when $\nu = 0.6$, to highlight retrograde particles, *i.e.* with $b = b_-$ as defined in eq. (3.27), with $0 \leq \rho \leq 10$. The thick black dashed line (retrograde photon) intersects the red vertical line ($\nu = 0.6$) in two points, marked by the blue and green stars, which will be called respectively the outer and inner retrograde photon orbits. In between these, the red vertical line intersects no dashed grey line, so there are no massive retrograde orbits.

Let us now consider the highlighted regions on the red vertical line. They indicate the values of ρ such that retrograde massive circular orbits can exist; the green portion corresponds to orbits with radii smaller than the inner retrograde photon orbit, and the blue portion to orbits with radii bigger than the outer retrograde photon orbit.

The next question is then, what about the stability of those orbits? The answer can be found in Fig. 3.7, where the potentials associated with the orbits described above are represented. The top plot shows the first derivative of the effective potential in eq. (3.16), and the bottom plot its second derivative. The green and blue stars mark the position of the photon orbits, and the highlighted zones the regions where massive retrograde orbits can happen. The green zone corresponds to positive values of the second derivative of the potential (this can be seen more clearly in Fig. 3.8, see next paragraph), thus to stable orbits, whilst the blue zone corresponds to decreasing values of the first derivative, or negative values of the second derivative, thus corresponding to unstable orbits.

Fig. 3.8 shows a zoom on the small values of ρ of Fig. 3.7. The black thick line corresponds to a retrograde photon, the coloured lines corresponds to the retrograde massive particles. Each value of ρ such that

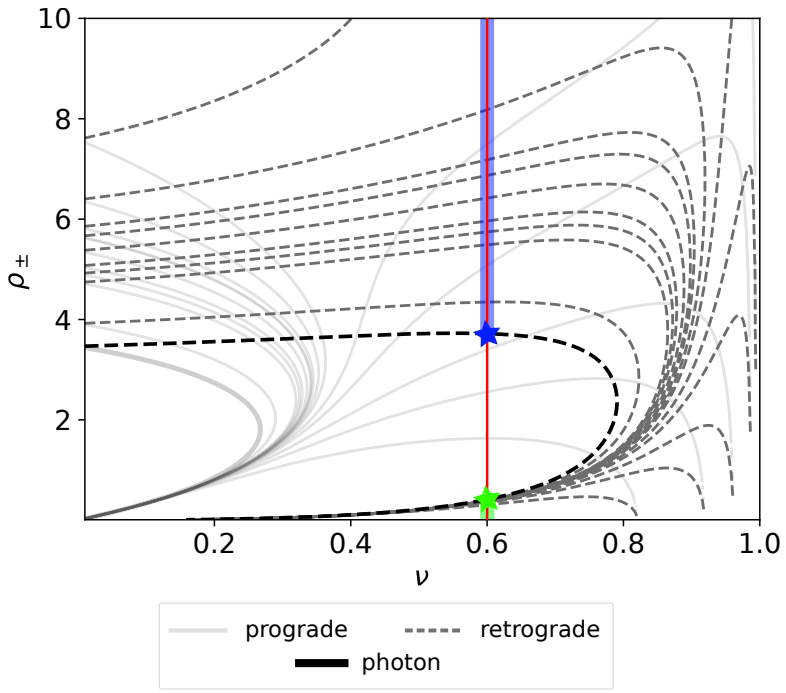


Figure 3.6: This is the simplified version of Fig. 3.5, which has been particularised to highlight retrograde orbits when $\nu = 0.6$. The thick black dashed line (retrograde photon) intersects the red vertical line ($\nu = 0.6$) in two places, marked by the blue and green stars, which will be called respectively the outer and inner retrograde photon orbits. In between these, the red vertical line intersects no dashed grey line, so there are no massive retrograde orbits. The blue highlighted region corresponds to circular orbits that are bigger than the outer retrograde photon orbit, and the green highlighted orbit corresponds to the massive circular orbits with a smaller radius than the inner retrograde photon orbit (depicted with the green star).

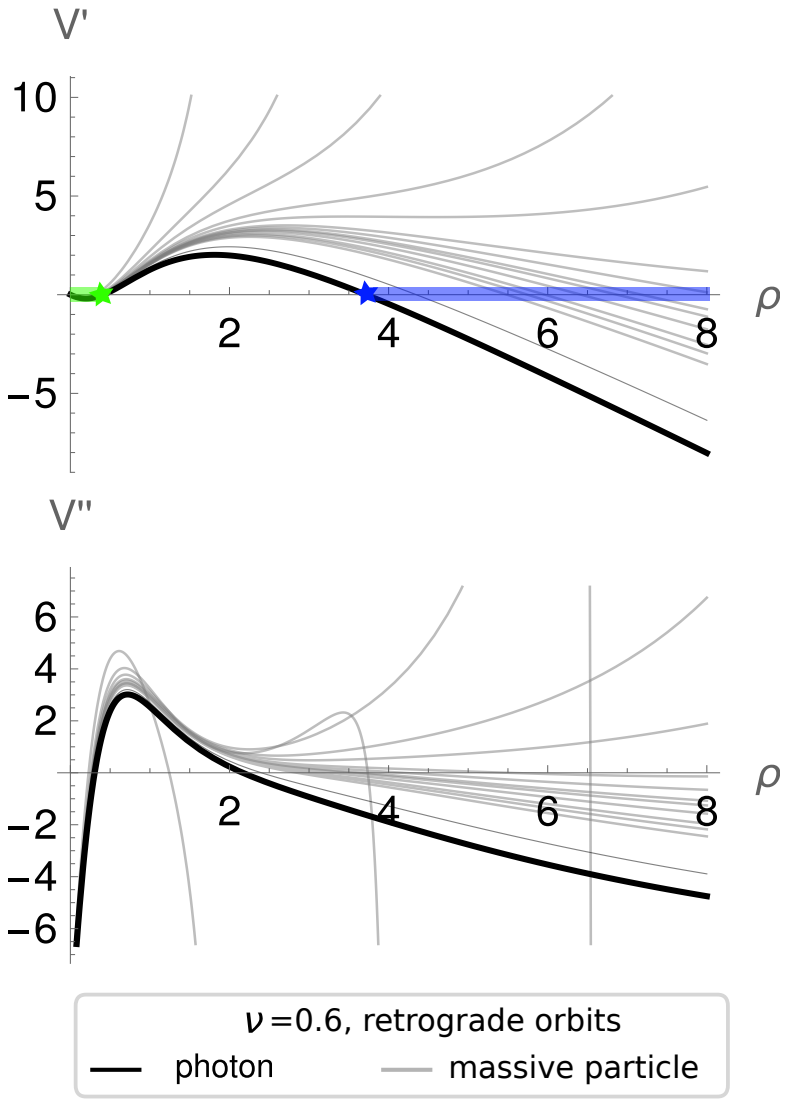


Figure 3.7: For $\nu = 0.6$, the top (respectively, bottom) graph depicts the first (resp., second) derivative of the potential for different values of the energy for a retrograde massive particle ($\mu_0 = 1$), evaluated as function of ρ with $b = b_-$. The blue highlight corresponds to unstable orbits (clearly, V' is decreasing), with a radius bigger than the outer photon orbit shown by the blue star. The green highlight corresponds to stable orbits, with a radius smaller than the inner photon orbit shown by the green star. Notice that whatever the value of the energy, the first derivative of the potential never goes to zero between the two photon orbits. Finally, notice that on this graph, $0 \leq \rho \leq 8$, and that the behaviour of V' and V'' is still non-trivial for $\rho \geq 8$.

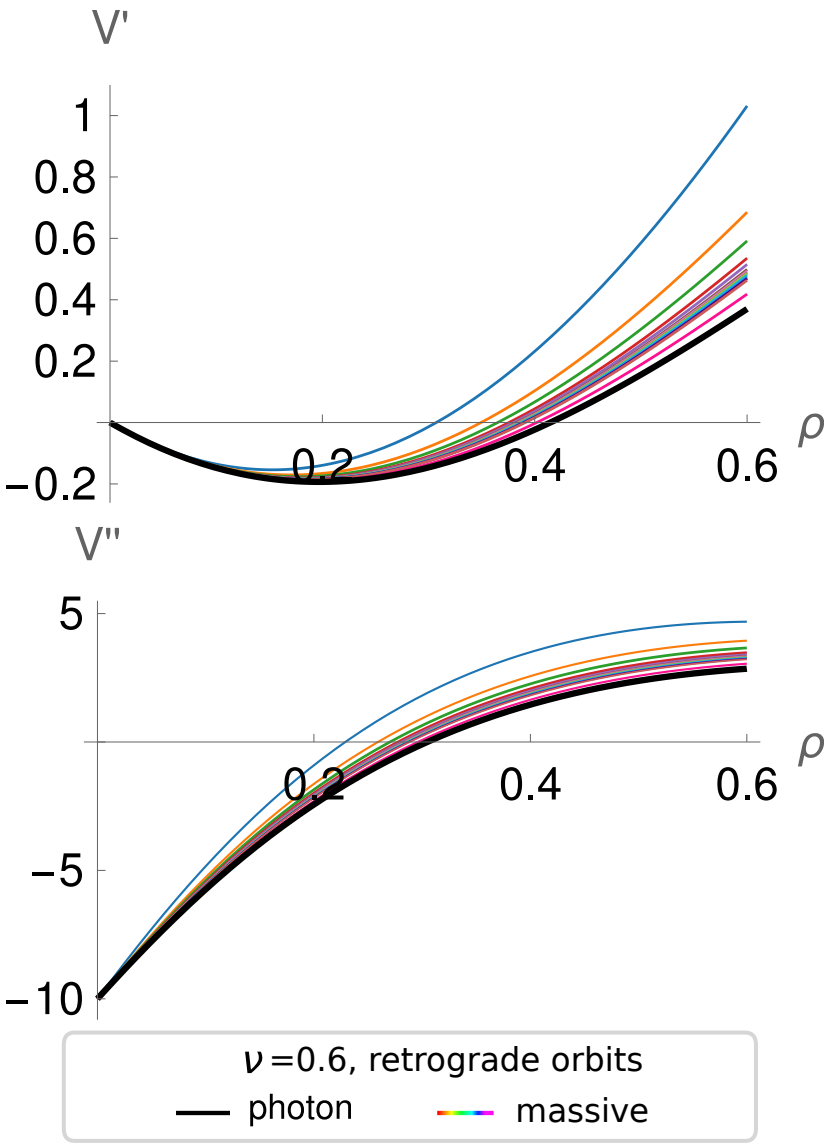


Figure 3.8: This is a zoom on the small values of ρ of Fig. 3.7. For $\nu = 0.6$, the top (respectively, bottom) graph depicts the first (resp., second) derivative of the potential for different values of the energy for a retrograde massive particle ($\mu_0 = 1$), evaluated as function of ρ with $b = b_+$. Each value of ρ such that $V' = 0$ can be traced down to retrieve the sign of V'', which are here all positive; thus the corresponding orbits are stable. (It is also clear that each V' is growing around $V' = 0$).

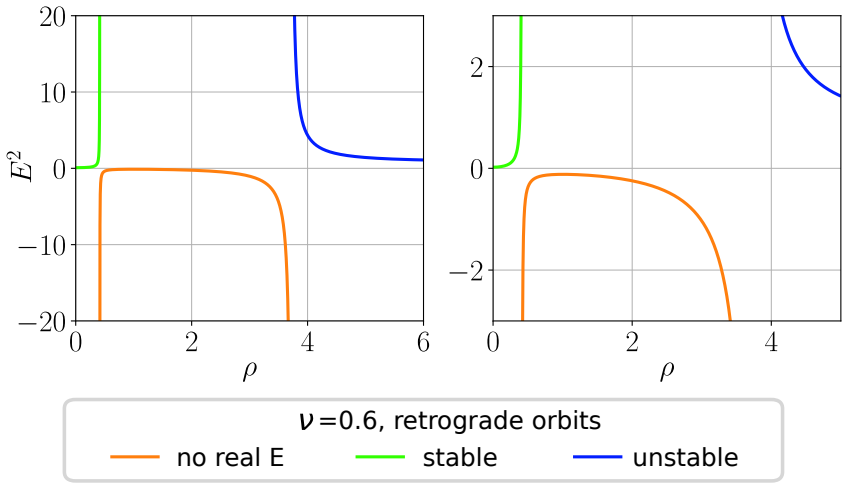


Figure 3.9: The squared value of the energy for a massive particle on a circular retrograde orbit (from eq. (3.38)) is shown on both panes for $\nu = 0.6$, with the right panel being just the zoomed version of the left panel. Since the energy E should be positive and real, the region where E^2 is negative has no physical solution. It actually corresponds to the values of ρ between the two photon orbits; the values of the energy going to (positive) infinity correspond to the photon orbits (since a massive particle should have infinite energy at that point).

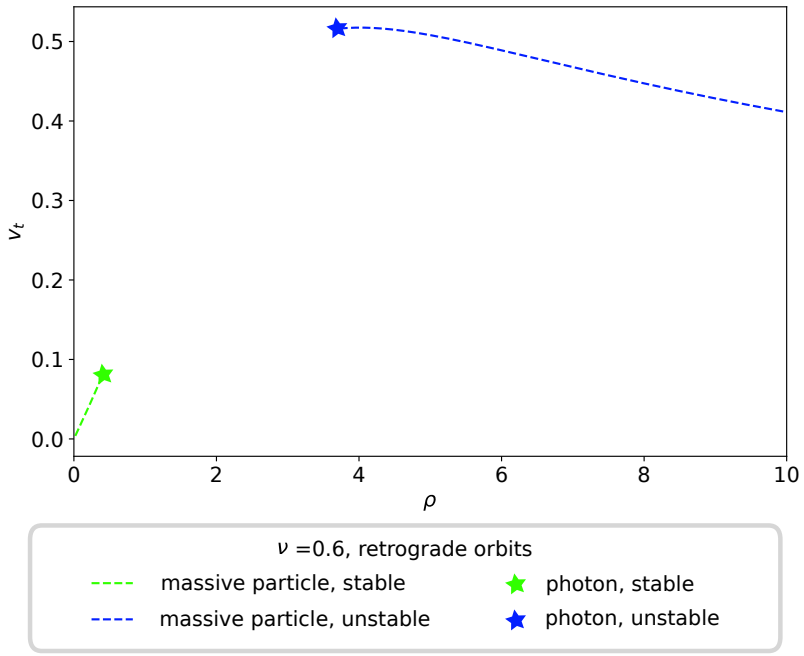


Figure 3.10: Velocity rotation curve for retrograde photons for $\nu = 0.6$. The blue part of the curve, depicting unstable orbits, corresponds to the blue highlighted zone of Fig. 3.6, and the star marker corresponds to the outer photon orbit. The green part of the curve, depicting stable orbits, corresponds to the green highlighted zone of Fig. 3.6, with the green star marker corresponding to the inner photon orbit.

$V' = 0$ can be traced down to retrieve the sign of V'', which are here all positive; thus the corresponding orbits are all stable.

Fig. 3.9 shows on both panes the value of the squared energy from eq. (3.38) (with a zoomed-in version on the right pane). Since the energy E should be a real quantity, the section where E^2 is negative has no solutions. It actually corresponds to the region between the two photon orbits; the asymptotes when the value of the squared energy goes to (positive) infinity correspond to the photon orbits themselves.

Finally, Fig. 3.10 shows the corresponding velocity rotation curve*: the stars correspond to velocities of photons given in eq. (3.35), and the blue and green parts correspond to the velocities of massive particles: for each value of ρ, the corresponding value of the energy to have a circular, retrograde orbit, is computed with eq. (3.38), then inserted in eq. (3.36).

3.6.2 Prograde orbits

Let us now repeat the same procedure for prograde orbits. Let us examine Fig. 3.11, which is a simplified version of Fig. 3.5: the red vertical line corresponds to a NUT parameter $\nu = 0.6$ still, but the curves correspond this time to prograde particles solutions (the b_+ value was chosen in eq. (3.27)), for a series of values of the energy E. The thick black line marks prograde photons solutions, whilst the grey plain lines correspond to massive particles with the different values of the energy. There are no intersections between the photon line and the $\nu = 0.6$ line; thus there are no prograde photon orbits possible. However, the pink highlighted zone corresponds to the values of ρ where massive prograde circular orbits are allowed, with each value of ρ having a corresponding value of the energy. Unlike the retrograde case, there is no "forbidden" zone for the massive particles circular orbits.

Let us now turn our attention onto Fig. 3.12, where the upper graph shows the first derivative of the potential, V', and the lower graph its second derivative V'', evaluated as functions of $\rho 8$ with $b = b_+$. The thick black line once more corresponds to the photon, and the grey lines to the massive particle with different values of the energy. For V', there are

*For retrograde orbits, in all of the following, the plotted velocity is of course the opposite of the actual velocity.

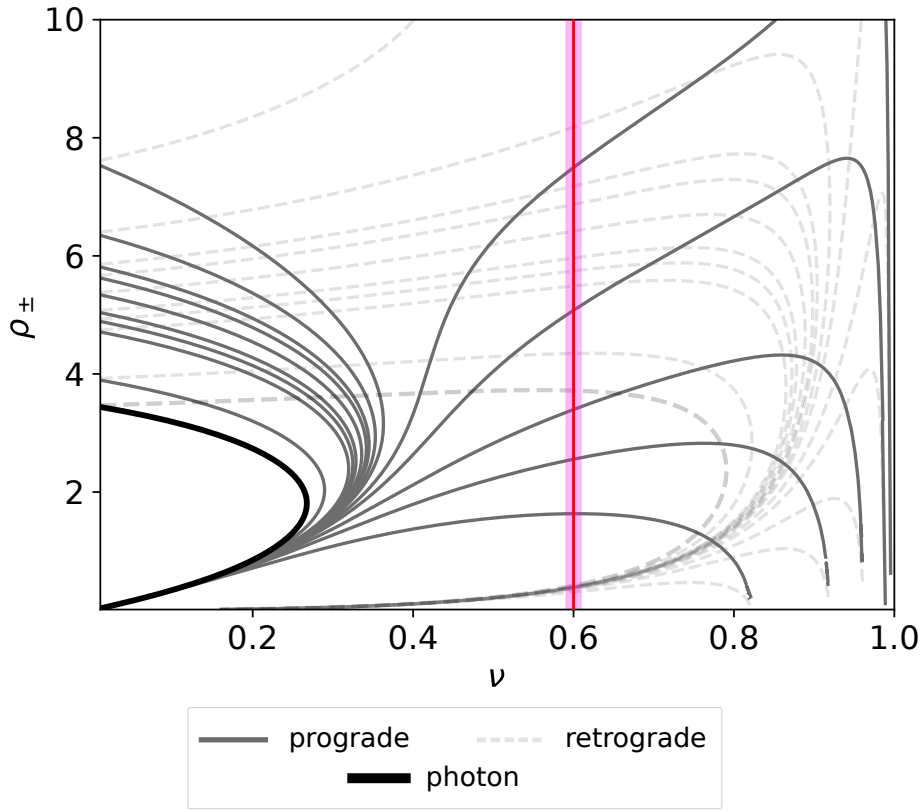


Figure 3.11: This is the simplified version of Fig. 3.5, which has been this time particularised to highlight prograde orbits when $\nu = 0.6$. The thick black plain line (prograde photon) does not intersect with the red vertical line ($\nu = 0.6$); thus there are no prograde photon orbits for this value of the NUT parameter. The pink highlighted part corresponds to the values of ρ where plain grey lines can intersect the red vertical line, which means that massive prograde circular orbits will be allowed, each value of ρ corresponding to a value of the energy.

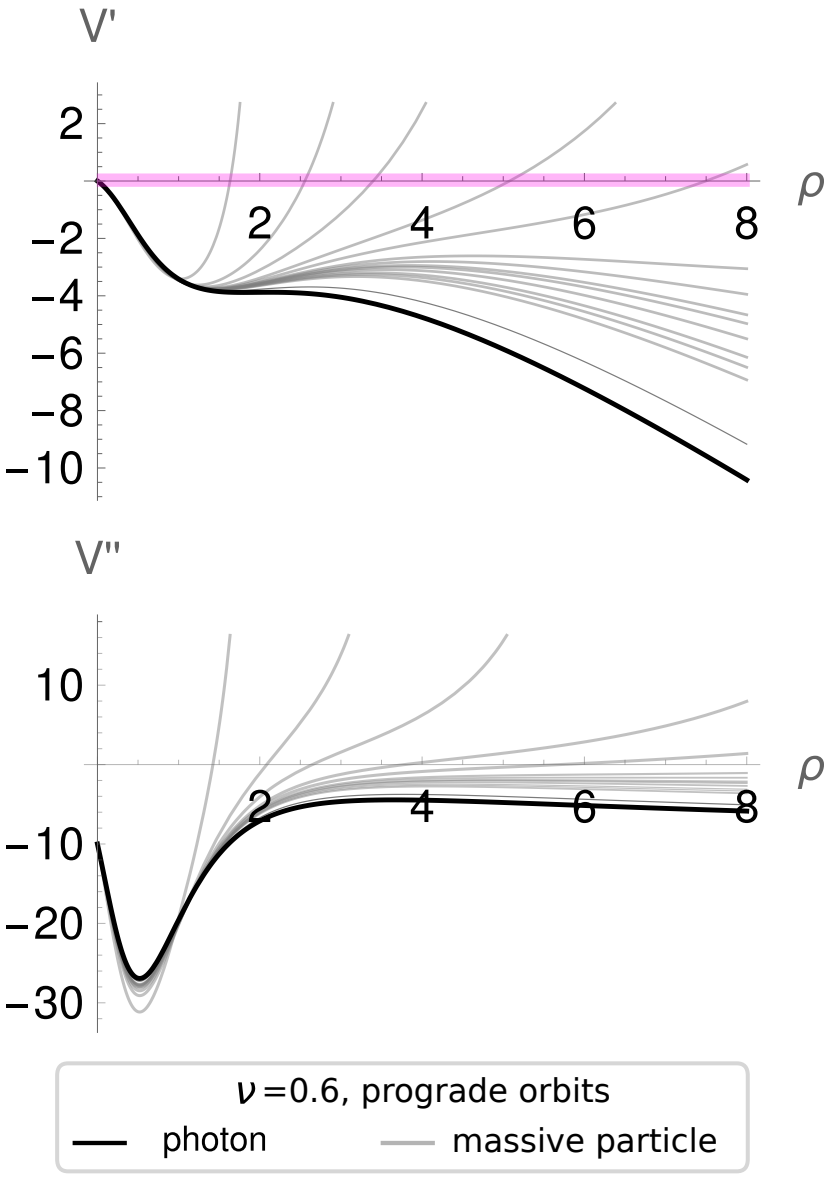


Figure 3.12: The upper graph shows the first derivative of the potential, V', and the lower graph its second derivative V'', evaluated as functions of ρ with $b = b_+$. The thick black line once more corresponds to the photon, and the grey lines to the massive particles with different values of the energy. For V', there are no roots for the photon; but each value of ρ has a corresponding value of the energy such that there is at least one circular orbit. This corresponds to the pink highlighted zone. Each corresponding V' is growing, (corresponding to a positive value of V''), thus all these orbits are stable.

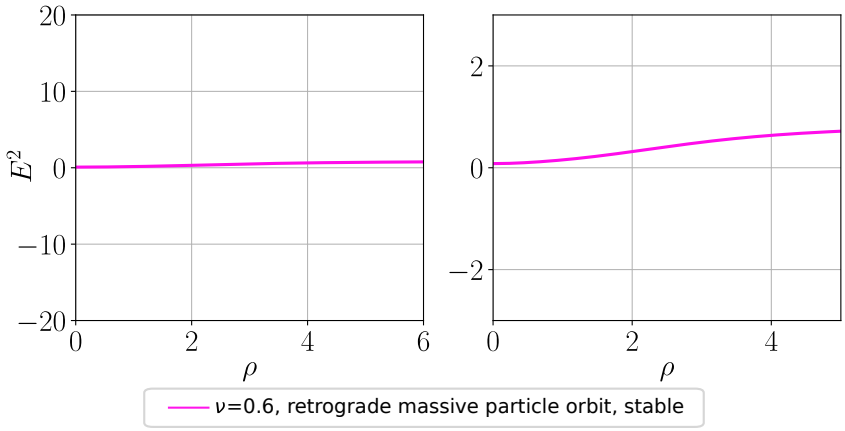


Figure 3.13: This figure shows the squared value of the energy that is necessary for the massive particle to be allowed on a circular orbit, given by eq. (3.38). The right panel is just the zoomed version of the left panel. As can be seen, the values are all positive, so there are also solutions E such that the energy is real.

no roots for the photon. For the massive particle, each value of ρ has a corresponding value of the energy such that there is at least one circular orbit. This corresponds to the pink highlighted zone. Each corresponding V' is growing, (corresponding to a positive value of V''), thus all these orbits are stable.

Fig. 3.13 shows the squared value of the energy, E^2, that is necessary for the massive particle to be permitted on a circular orbit, computed with eq. (3.38). The right panel is just the zoomed version of the left panel. As can be seen, the values are all positive, so there are also solutions E such that the energy is real, confirming the absence of the "forbidden" zone of the retrograde case.

Finally, Fig. 3.14 shows the corresponding velocity rotation curve: for each value of ρ, the corresponding value of E such that there is a prograde circular orbit (see Fig. 3.13) is computed with eq. (3.38) then inserted in eq. (3.36), giving rise to one continuous curve.

Now that we have a clearer image of how the equations and their solutions come together to determine the position, stability, and velocity of each circular orbit, we are going to construct synthetizing plots. We

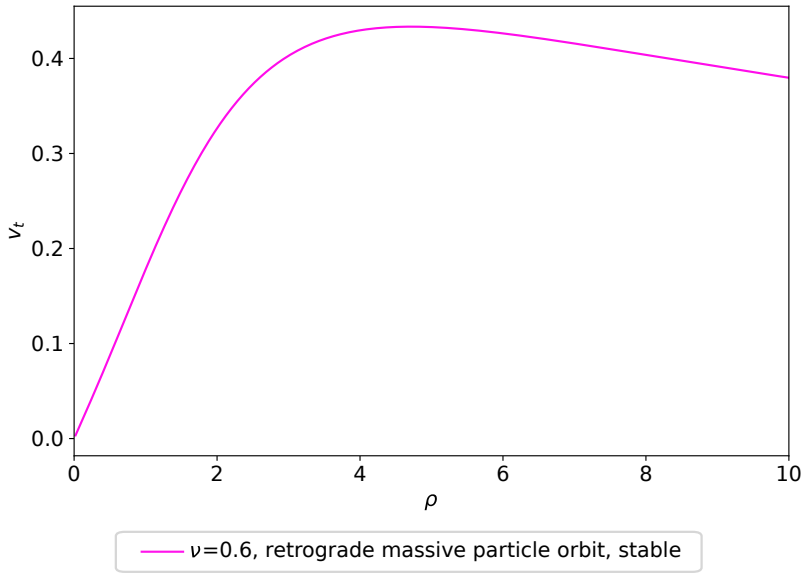


Figure 3.14: This plot presents the velocity rotation curve for the prograde massive particles: for each value of ρ, the corresponding value of E such that there is a prograde circular orbit is computed with eq. (3.38) then inserted in eq. (3.36). Since the corresponding values of the second derivative of the potential are all negative, these orbits are unstable.

are going to look at multiple values of the NUT parameter, and try to find some general rules on the behaviour of the circular orbits.

3.7 General position and stability of circular orbits

Now that we have seen how the graphs are constructed with one value of the NUT parameter, we can take a look at how the number of orbits evolves as the value of ν changes, and try to get some more insight on the stability of these orbits.

First, how does the number of orbits evolve as parameters change? In Fig. 3.15,for massive particles ($\mu_0 = 1$), the left column has a NUT parameter $\nu = 0.2$ and the right column $\nu = 0.8$. The first (resp. second) row presents the first (resp. second) derivative of the potential, as functions of ρ and evaluated at $b = b_{\pm}$. For each graph, two values of the energy are represented ($E = 2$ and $E = 500$) for the prograde and retrograde directions. The zeroes of the first derivative of the potential indicate the radii at which circular orbits are possible, and the value of the second derivative at these radii indicate if the corresponding orbit is stable or unstable. For example, for $\nu = 0.2$, with an energy of $E = 2$, (green dashdotted line in the left column) there are two prograde orbits: one stable one at $\rho \approx 0.8$ and one unstable one at $\rho \approx 3$.

It is quite clear, when comparing the two columns, that the main deciding factors in the number of circular orbits are the NUT parameter ν and the direction of rotation.

The existence of orbits can also be determined with the help of Fig. 3.16: when the squared value of the energy is positive, circular orbits may exist. When it is negative, the corresponding energy would be imaginary, so there are no circular orbits. This is the case for the prograde and retrograde orbits for $\nu = 0.05$, and the prograde orbits for $\nu = 0.6$. These intervals of values of ρ where no circular massive orbit can exist are framed by the points at which the energy necessary for a circular orbit for a massive particle goes to infinity; this corresponds to photon orbits.

We have also plotted, in Fig. 3.17, the squared value of the energy from eq. (3.38) for the two values of the NUT parameter where there are degenerate photon orbits: $\nu = 0.27$ for the degenerate prograde orbit

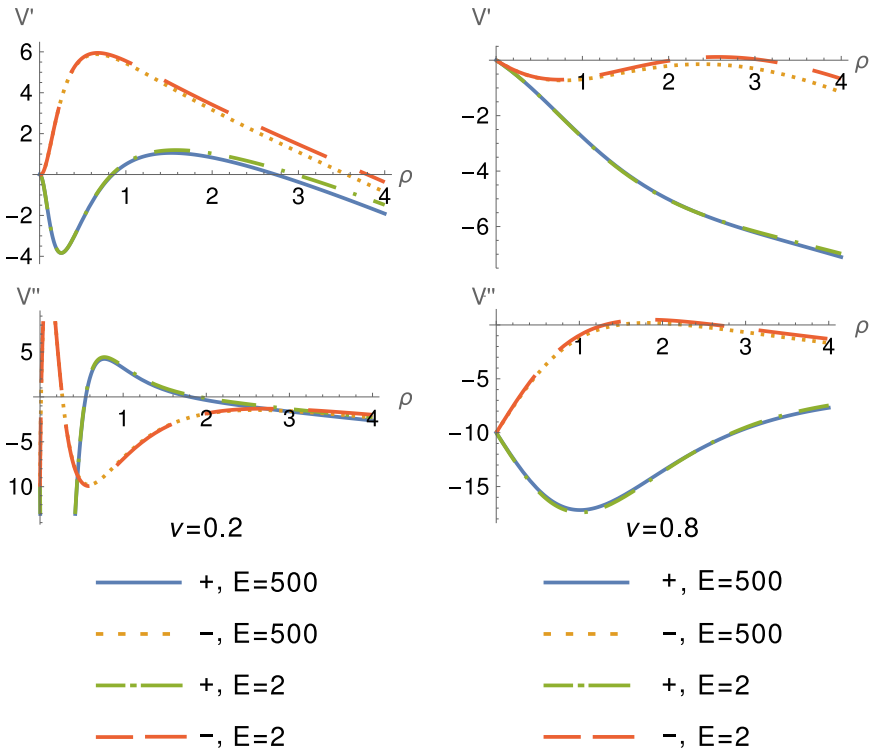


Figure 3.15: The left column has a NUT parameter $\nu = 0.2$ and the right column $\nu = 0.8$. The first (resp. second) row presents the first (resp. second) derivative V' (resp. V'') of the potential as functions of ρ and evaluated at $b = b_{\pm}$, with $\mu_0 = 1$. Two values of the energy are represented ($E = 2$ and $E = 500$) for the prograde and retrograde directions. The zeroes of the first derivative of the potential indicate the radii at which circular orbits are possible, and the value of the second derivative at these radii indicate if the corresponding orbit is stable or unstable. For example, for $\nu = 0.2$, with an energy of $E = 2$ (green dashdotted line on the left column), there are two prograde orbits: one stable one at $\rho \approx 0.8$ and one unstable one at $\rho \approx 3$.

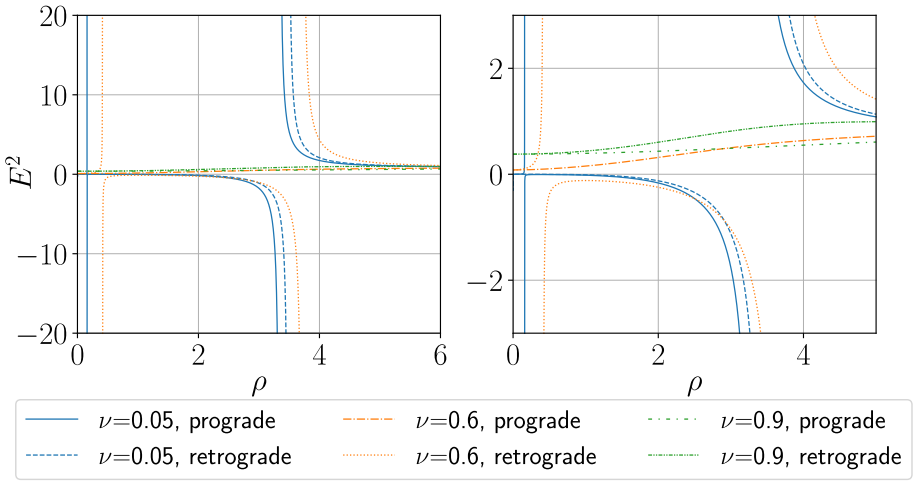


Figure 3.16: The squared value of the energy (eq. (3.38), with $\mu_0 = 1 = c$) is plotted as a function of the radius ρ for (prograde or retrograde) circular orbits and for different values of the NUT parameter. The right panel is the zoomed version of the left panel. The asymptotes towards positive infinity mark the radii at which photon orbits are permitted. In between, the energy is imaginary and there are no circular orbits. As $\rho \to \infty$, the energies go to 1, as is expected from our choice of $\mu_0 = 1 = c$.

and $\nu = 0.79$ for the retrograde one. Notice that the asymptotes where E^2 goes to positive infinity are not separated by negative values any more.

The stability of each orbit is more complicated to determine. To do this, let us again create a bifurcation diagram in Fig. 3.18, which provides a simpler visualisation of how the number of solutions of eq. (3.26) (*i.e.* the number of possible circular orbits) varies with the value of ν. This is what is shown, for the same values of the energy $E = 2$ and $E = 500$. The prograde (resp. retrograde) orbits coalesce into one prograde (resp. retrograde) orbit, then disappear. As for the stability, for $E = 2$ and $E = 500$, the upper branch of the prograde (and retrograde) orbits depict unstable orbits, whilst the lower branch depict stable orbits. The maximal value of ρ as a function of ν (*i.e.* the extremal points on the right of the curves, shown by a black square) depict the degenerate photon orbits.

When the energies are smaller, it becomes much more difficult to determine a general rule for the stability of the related orbits. Fig. 3.19 presents the corresponding second derivatives of the potential, V''.

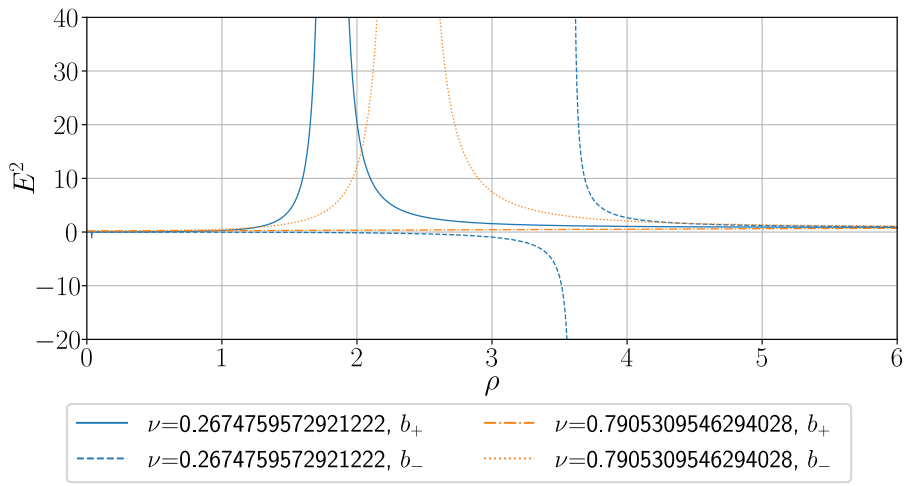


Figure 3.17: The squared value of the energy (eq. (3.38), with $\mu_0 = 1 = c$) is plotted as a function of the radius ρ for $\nu = 0.27$ and $\nu = 0.79$, *i.e.* the values of the NUT parameters at which the prograde (respectively retrograde) photon orbits are degenerate. The asymptotes towards positive infinity mark the radii at which photon orbits are permitted, with, for the degenerate ones, no negative values of the E^2 in between any more.

When $\nu = 0.05$, for retrograde particles, the (dashed dull blue) orbits between the outer retrograde photon orbit (dull blue star) and the degenerate orbit (grey square) at $\rho \approx 10$ are unstable since the second derivative of the potential is negative. The (dashed teal) orbits before the inner retrograde photon orbit (teal star) or after $\rho \approx 10$ are stable since the second derivative of the potential is positive. For prograde particles, the (plain maroon) orbits between the prograde orbit (maroon star) and the degenerate orbit at $\rho \approx 9.5$ are unstable, whilst the (plain purple) orbits after the degenerate orbit, are stable.

When $\nu = 0.6$, for retrograde particles, the (dashed bright green) orbits that are smaller than the retrograde inner photon orbit (bright green star) or bigger than the degenerate orbit at $\rho \approx 12$ will be stable; the (bright blue) orbits in between will be unstable. For prograde particles, all the (plain pink) orbits are stable.

When $\nu = 0.9$, for retrograde orbits, the (dashed brown) orbits "outside" the region delimited by the two degenerate orbits at $\rho \approx 5.5$ and $\rho \approx 13.5$ are stable, whilst in between the (dashed orange) orbits are

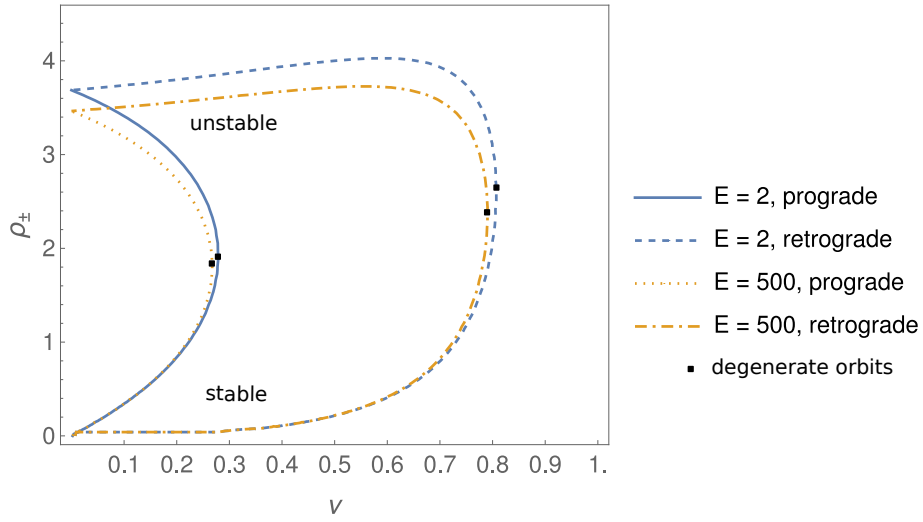


Figure 3.18: For different values of the energy E, as functions of the parameter ν, the radii of the possible circular orbits $\rho_\pm$ for massive particles. Depending on the value of the NUT parameter ν and the energy E, there is from 0 to 4 possible orbits. The value of the second derivative of the potential indicates the stability of the photon orbit. The degenerate orbits are shown as black squares.

unstable. Finally, for prograde orbits, the (plain dark green) orbits are all stable.

As the previous paragraphs show, determining the stability of an orbit is quite an involved process. Here are some general rules of thumb:

- ✿ Prograde orbits for "big ν" are always stable;
- ✿ When ν is small enough that two photon orbits are allowed (prograde or retrograde), the inner one will be stable, and the outer one will be unstable; the massive orbits in the vicinity (so, with "big E") will follow;
- ✿ For "big ρ", the orbits are stable.

To obtain a more complete (and rigorous) picture of the stability, we would need to compute, for each possible triad of values (ρ, ν, E) with E defined in eq. (3.38), corresponding to a circular orbit, the associated value of the second derivative of the potential. A possible way to do this would be to plot the bifurcation diagram corresponding to the following equation:

$$V''\left[\rho, \nu, E(\rho,\nu), b(\rho,\nu)\right] = 0, \tag{3.40}$$

directly on the bifurcation diagram of Fig. 3.18; the curve thus drawn would mark the transition between stable and unstable orbits. However, this is very heavy computation, and is left as a future endeavour.

3.8 General velocity graphs

In the following section, we will construct the general velocity graphs, *i.e.* superpose the velocity rotation curves for different values of ν, as functions of the proper radius that was defined in Section 3.1.

We will first start with the photon orbits, then move on to massive particles. In Section 3.8.3, we compare our results with the gravito-electromagnetic approximation [89].

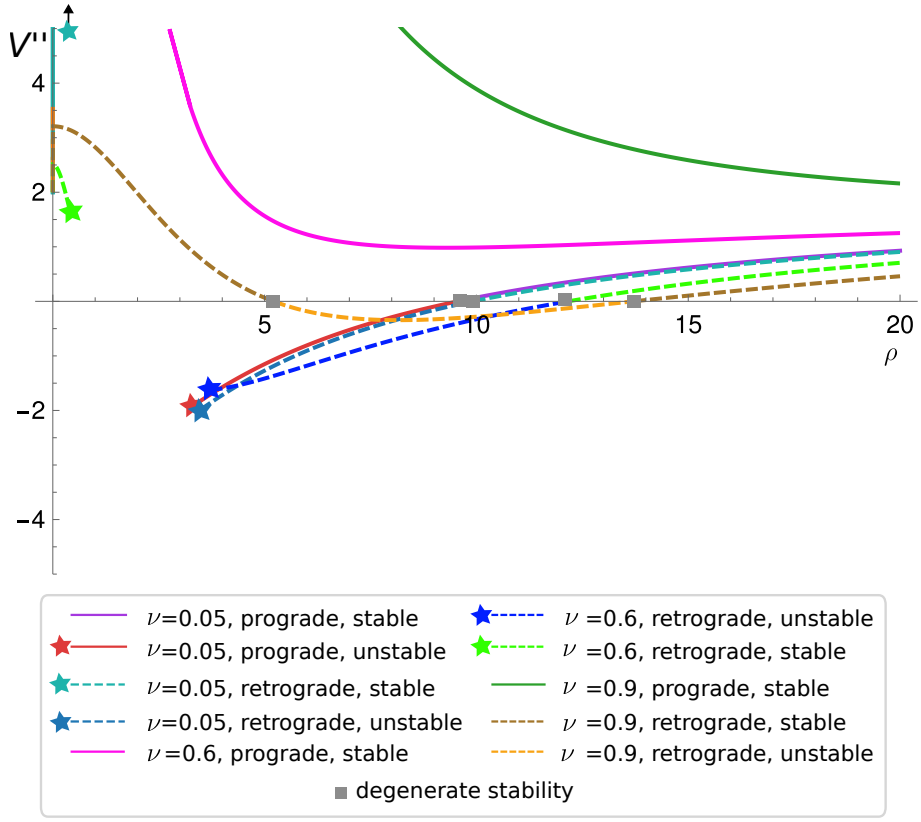


Figure 3.19: This graph shows the value of the second derivative for prograde and retrograde massive particles ($\mu_0 = 1$) for three different values of the NUT parameter. When $V'' > 0$ (respectively $V'' < 0$), the orbit is stable (resp. unstable). The orbits with $V'' = 0$ are degenerate. The stars depict the corresponding photon orbits, and the grey squares the degenerate orbits each time we pass from stable to unstable, and vice-versa. The teal star with the upward-pointing arrow, corresponding to the inner retrograde photon orbit for $\nu = 0.05$, should be at a value of $V'' \approx 80$. Notice that for $\nu = 0.6$, extending the graph shows that at $\rho \approx 12$, the orbits go from stable to unstable; this was out of frame in Figs. 3.8 to 3.10.

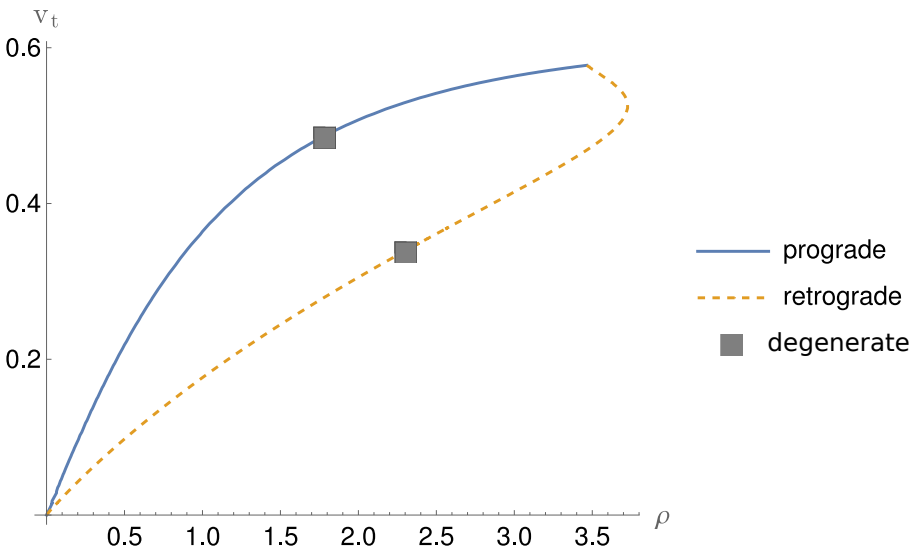


Figure 3.20: As functions of the circular orbit radii ρ, the velocities v_t for massless particles on circular orbits. The plain blue line corresponds to the prograde velocities, the dashed orange line to the opposite of the retrograde velocity. The leftmost (respectively. rightmost) branches represent stable (resp. unstable) orbits, coalescing back together on the degenerate orbits represented by the grey squares.

3.8.1 Massless particle

Since for massless particles there are at most, for one specific value of the NUT parameter ν, four circular orbits (two prograde and two retrograde), two kinds of velocity plots can be produced: either the velocity of the particles as a function of the circular orbit radii $\rho_\pm$, for which we need to keep in mind that they correspond to different values of ν and thus do not occur in the same spacetime; or conversely, the velocity as a function of ν, thus generating a kind of variant of the bifurcation diagram of Fig. 3.4, this time keeping in mind that the orbits occur at different values of ρ. Of course, these plots are complementary of each other.

For the sake of completeness, we are going to examine these two points of view. Each time, it is the opposite of the velocity that is plotted for retrograde orbits, for clarity's sake.

Fig. 3.20 shows the first option: the (coordinate) radius is shown on the horizontal axis and the velocity on the vertical axis, with the prograde (respectively retrograde) orbits in plain blue (resp. dashed

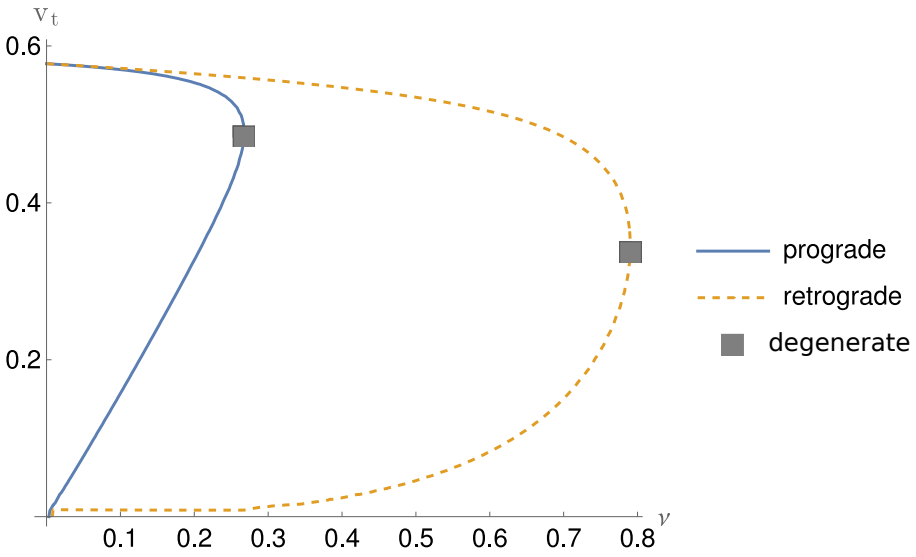


Figure 3.21: As functions of the NUT parameter ν, the velocities v_t for massless particles on circular orbits. The plain blue line corresponds to the prograde velocities, the dashed orange line to the opposite of the retrograde velocity. The upper (respectively lower) branches represent unstable (resp. stable) orbits. As ν grows and the stable/unstable circular orbits coalesce back together, so do the velocities.

orange). Comparing with Fig. 3.4, the stability of each branch (*i.e.* each portion of curve separated by the grey squares), can be deduced. The stable orbits correspond to smaller radii and thus smaller velocities, and the unstable orbits correspond to bigger radii and thus bigger velocities. Thus the leftmost branches correspond to stable orbits, the rightmost branch to unstable orbits, and joining them, the degenerate orbits are indicated by the grey squares.

Conversely, Fig. 3.21 represents the latter option, with the NUT parameter on the horizontal axis and the velocity again on the vertical axis. The plain blue (respectively dashed orange) line represents the prograde (resp. retrograde) orbits, and like in the bifurcation diagram, the upper branches represent unstable orbits, and lower branches stable ones.

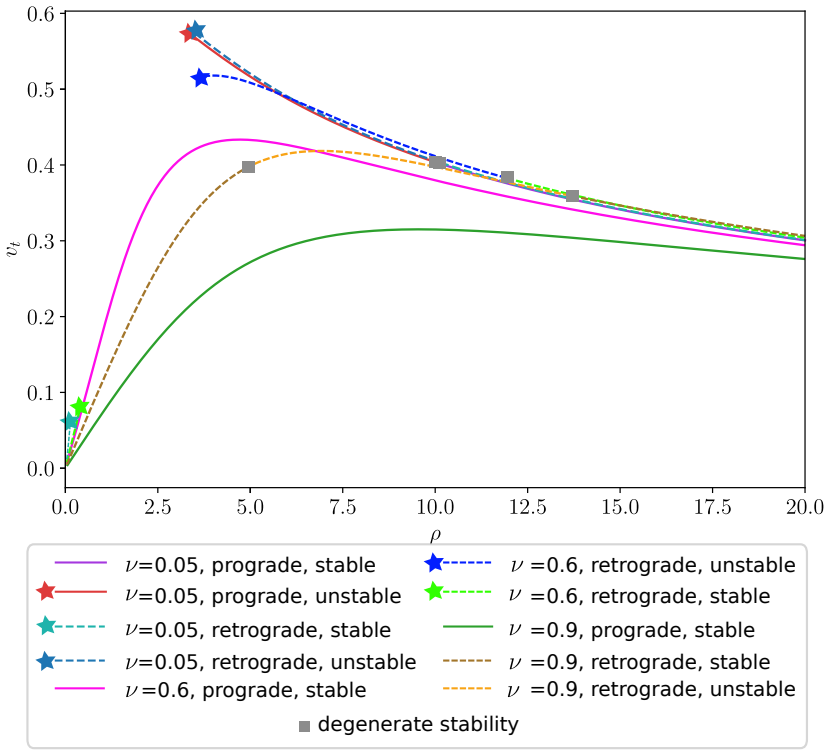


Figure 3.22: The velocity (vertical axis) is plotted as a function of the (coordinate) radius (on the horizontal axis) ρ for three different values of ν (0.05, 0.6 and 0.9). The stars denote photon orbits and the lines massive particles, with the colours and dashing patterns corresponding the the value of ν, the direction of rotation and the stability. For the retrograde orbits, the opposite of the velocity is plotted for clarity's sake. For $\nu = 0.05$ in the prograde direction, and $\nu = 0.6$ in both directions, there are no possible orbits between the photon orbits. This phenomenon does not occur for $\nu = 0.9$ since there are no photon orbits for this value of the NUT parameter. The grey squares depict degenerate orbits.

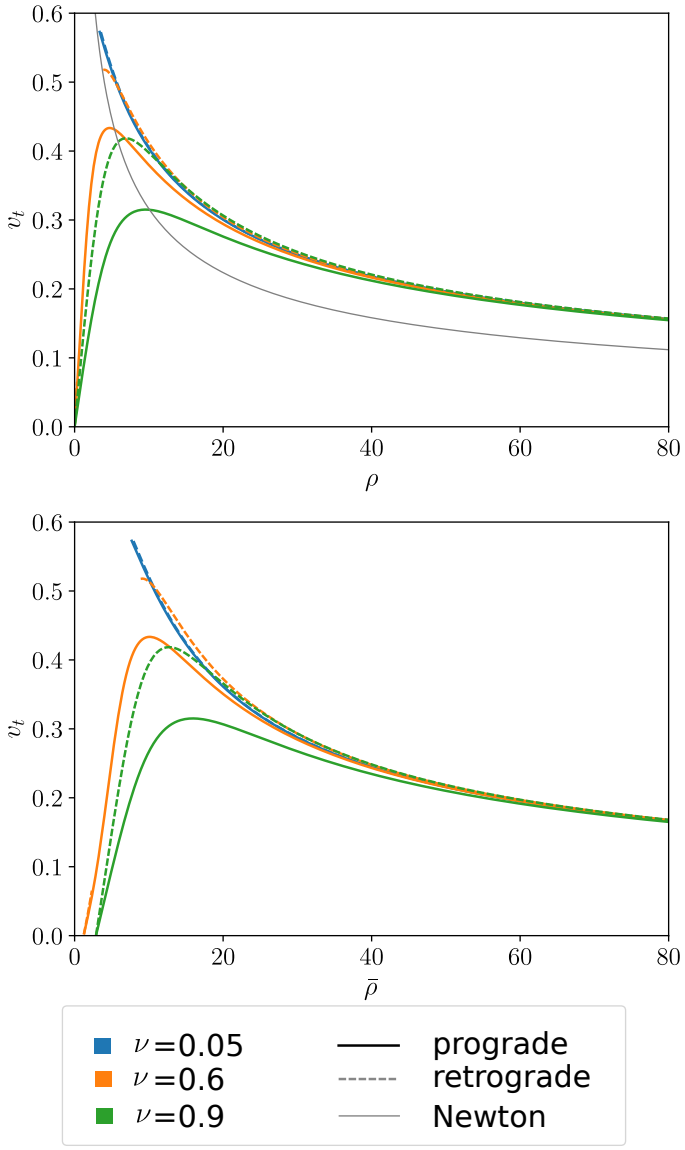


Figure 3.23: The velocity of a massive particle on a circular orbit is plotted as a function of, on the upper (resp. lower) plot, the radius ρ (resp. the proper radius $\bar{\rho}$), for different values of the NUT parameter ν. For clarity's sake, the opposite of the velocity is plotted for retrograde orbits, and the stability indications of Fig. 3.22 have been omitted. The Newtonian velocity curve, $\rho^{-1/2}$, is also displayed on the upper plot for comparison, but not on the lower one since the proper radius $\bar{\rho}(\rho)$ depends on the value of ν, and would give rise to three different curves.

3.8.2 Massive particle

For massive particles, we can build a more traditional-looking velocity rotation curve plot.

Let us first examine Fig. 3.22 (which is quite busy—a simplified version can be found just after). The horizontal axis represents the (coordinate) radius ρ, and the vertical axis represents the velocity. We have chosen only three values of the NUT parameter ($\nu = 0.05, 0.6$, and 0.9) as to not overload the plot. The stars correspond to photons, and the curves to massive particles*, with each colour and dashing pattern† corresponding to the value of ν, the direction of rotation, and the stability. The grey squares show the degenerate orbits. As has been explained in the previous section, when there are multiple photon orbits (*i.e.* stars), the energy necessary for a circular massive orbit in between the corresponding radii is imaginary; thus there are no orbits, and no velocities.

Fig. 3.23 is made out of two panels, the upper one being the simplified version of Fig. 3.22, with the addition of the Newtonian velocity curve, $\rho^{-1/2}$, for comparison. The lower panel depicts the velocity rotation curves but this time as functions of the proper radius $\bar{\rho}(\rho)$. The Newtonian velocity curve is *not* displayed; it would give rise to three different curves for the three values of ν.

3.8.3 Comparison with the gravito-electromagnetic approximation

In Fig. 3.24 the velocity rotation curve, computed at $\nu = 0.999$, is compared with the approximate expression given in eq. (79) of [89]. In this regime ($\nu \approx 1$, tensionless Misner string), where the gravito-electromagnetic approximation is expected to hold, we find close agreement between the two results. (For $\nu = 0.999$ the following values are found: $k = 44.716$, $\alpha_+ = 46.107, \alpha_- = 43.279$.)

*Again, for each retrograde orbit, it is the opposite of the velocity that is plotted.

†The colours were chosen to be as coherent as possible with Figs. 3.6, 3.7, 3.10, 3.11, 3.12, 3.14, for comparison's sake.

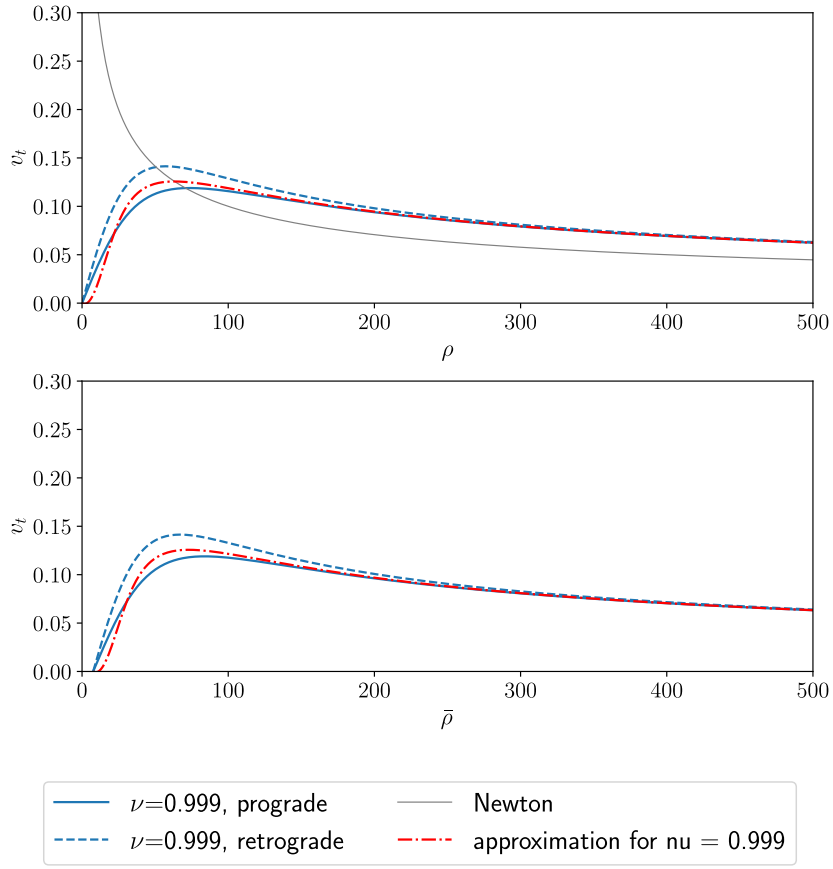


Figure 3.24: For a value of the NUT parameter of $\nu = 0.999$, the blue plain (resp. dashed) line depicts the exact velocity of a massive particle on a prograde (resp. retrograde) circular orbit. The red dashdotted line depicts the gravito-electromagnetic approximation in eq. (79) of Ref. [89].

3.9 Summary

In this chapter, we have constructed the velocity rotation curves for the gravimagnetic dipole for different values of the NUT parameter ν.

We first determined the proper radius as a function of the coordinate radius and the NUT parameter, then compared different such functions for three values of ν.

We then used the effective potential, as well as the Hamiltonian formulation, to determine two methods allowing us to relate a circular orbit radius, its energy and its velocity; this is not strictly needed but is quite useful since all the expressions are highly non trivial.

Using the potential formalism, we determined that for photons, there are between zero and four circular orbits for each value of ν, *i.e.* between zero and two prograde and retrograde orbits. As the NUT parameter grows, the prograde (respectively retrograde) orbits coalesce back together. For massive particles, the situation is a bit more complicated, but in general, there can also be between zero and two circular orbits in each direction for each value of ν. When ν is such that there are two prograde (resp. retrograde) orbits, the massive particle orbits always have radii that are outside the interval determined by the photon orbits. The stability of such orbits can be determined with the help of the second derivative of the potential and is *not* trivial.

Finally, we constructed the velocity rotation curves and were able to compare them, in the relevant domain of parameters, with the gravito-electromagnetic approximation, showing good agreement.

Of course, a lot of questions remain unanswered. In the next two chapters, we will explore the following two:

- ✿ In this chapter, we have stayed strictly in the equatorial plane, which has the advantage of trivially satisfying the potential equation $p_z = 0 = z$, whatever the value of ρ. Off the equatorial plane, this is not true any more. Are there any other circular orbits, stable or unstable, when $z \neq 0$? How do they behave under the evolution of the NUT parameter? This is explored in Chapter 4.

- ✿ What happens to photons that are not on circular orbits? What is the situation on light deflection? Do interesting patterns appear? This is explored in Chapter 5, for photons on or off the equatorial plane, through numerical evolution.

However, other questions have been raised in this chapter, that will not be explored in this work, but left as future prospects:

- ✿ What is the complete picture about stability ? This could be explored through a systematic stability study by adding, on the bifurcation diagram in Fig. 3.5, the zeroth level of the second derivative of the effective potential, *i.e.* the curve (ρ, ν) such that

$$V''\left[\rho, \nu, E(\rho,\nu), b(\rho,\nu)\right] = 0, \tag{3.41}$$

  The intersections of this curve with the circular orbit solutions would mark the degenerate orbits, and thus separate the stability "regions".

However, this is quite involved since for each point of the (ρ, ν) plane one would need to find the corresponding energy, then plug it back in the second derivative of the potential, then trace where it is zero.

- ✿ What happens when we add matter? It would have multiple consequences:
  - ❄ The equilibrium of the Misner string would be different, and would involve a recalculation of the value of the parameter k;
  - ❄ The circular orbits, the corresponding velocities and stabilities would be modified;
  - ❄ The chronology boundary pathological region would maybe become less of an issue (see section B.2 Appendix B).

CHAPTER 4

OFF THE EQUATORIAL PLANE CIRCULAR ORBITS

"Do what I do. Hold tight and pretend it's a plan."

— The Doctor, *Doctor Who* (1963 – ...)

Having thoroughly examined circular orbits confined to the equatorial plane, we now extend our investigation to consider more general circular trajectories—specifically, those occurring in planes parallel but outside the equatorial plane.

This chapter presents a first exploration of off-equatorial circular orbits, focusing primarily on massless particles while noting that the framework can readily be adapted to massive particles in future work. Our approach centres on three conditions that must be simultaneously satisfied. While the equatorial case benefited from the trivial satisfaction of $dp_z/du = 0$, the general case presents more substantial challenges. Although these conditions can be expressed relatively compactly in terms of the metric functions f, ω, and $e^{2\gamma}$, the resulting equations prove analytically intractable. We therefore adopt an alternative approach using the impact parameter effective potential framework introduced in Section 2.4.3. This

formulation yields three equations that, while simpler than the original system, still present significant analytical challenges.

Thus, rather than attempting to solve them directly, we will adopt a visual approach using level plotting techniques [88] to visualise the solution space. Through this methodology, we aim to identify the existence and qualitative behaviour of the circular orbits under variation of the NUT parameter.

The chapter is structured as follows: in Section 4.1, we revisit the impact parameter effective potential framework that was first introduced in Section 2.4.3, specialising it here to the gravimagnetic dipole spacetime. In Section 4.2 we derive the conditions for circular orbits directly from the impact parameter effective potential. The results of this analysis are presented and discussed in Section 4.3. Finally, Section 4.4 provides a comprehensive summary of the chapter's findings, as well as a non-exhaustive list of perspectives.

4.1 The impact parameter effective potential specialised for the gravimagnetic dipole spacetime

First, let us revisit the impact parameter potential that was introduced in Section 2.4.3 of Chapter 2. We have looked at it through the lens of "authorized regions" depending on the value of the impact parameter of a particle, but here we are going to use it as a simpler expression of the complete effective potential.

In this section, we are going to particularise the inequalities that were considered in Chapter 2, directly using the metric functions f, ω and $e^{2\gamma}$ to get a clearer idea of the inequalities at play.

Let us remember that the rescaled potential energy V can be written in the form of eq. (2.48)

$$V = g_{tt}(b - b_+)(b - b_-) \geq 0, \tag{4.1}$$

where the impact parameter effective potentials $b_\pm$ are then given by eq. (2.49):

$$b_\pm = \frac{-g_{t\varphi} \mp \sqrt{\Delta\left(1 + g_{tt}\left(\frac{\mu_0 c^2}{E}\right)^2\right)}}{g_{tt}}. \tag{4.2}$$

In Chapter 2, we followed with an analysis of the possible signs and orderings of the values of $b_\pm$ in the different regions of space; here, we can deduce these directly from the metric functions f, ω and $e^{2\gamma}$. Indeed, the explicit expression of the impact parameter effective potential will be

$$b_\pm = \omega \pm \frac{\rho}{f}\sqrt{1 - f\left(\frac{\mu_0 c^2}{E}\right)^2}, \tag{4.3}$$

which is consistent with the previous chapters. Let us now separate our analysis in function of the sign of g_{tt}.

4.1.1 Inside the ergoregion

Inside the ergoregion, $g_{tt} = -f > 0$, which means that f is negative and

$$b_+ < b_-. \tag{4.4}$$

The allowed range of values for b at some point (ρ, z) inside the ergoregion is thus

$$b \in \left]-\infty, b_+\right] \cup \left[b_-, +\infty\right[. \tag{4.5}$$

It follows that as the factor $\left(\frac{\mu_0 c^2}{E}\right)^2$ grows, the allowed region shrinks.

In Fig. 4.1, we show the rescaled potential V as a function of the impact parameter b at spatial coordinates $(\rho, z) = (0.01, 3)$ for a gravimagnetic dipole spacetime with NUT parameter $\nu = 0.7$. The three curves correspond to three different values of the mass factor—green plain curve for a massless particle, and blue dashed (respectively orange dotted) for a massive ($\mu_0 = 1$) particle with energy $E = 0.9$ (resp. $E = 0.6$). The lightly coloured zones underneath the curves represent the regions that are admissible for V to satisfy the inequality (4.5), leading to the identification of the possible values of the impact parameter b for the corresponding particle. The squares in the top corners exhibit a zoom on the values of

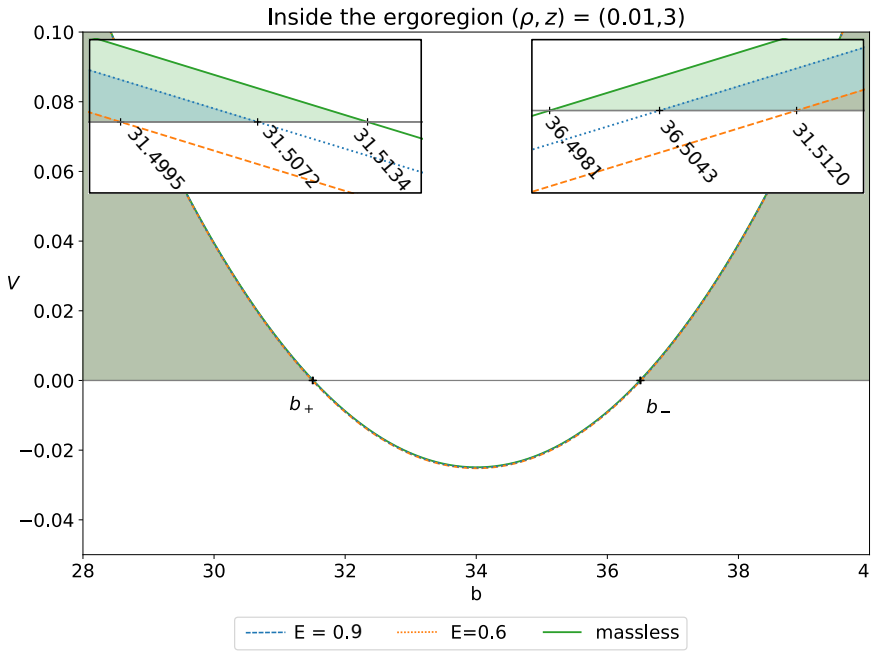


Figure 4.1: The rescaled potential V is plotted as a function of the impact parameter b at the point $(\rho, z) = (0.01, 3)$ for a gravimagnetic dipole spacetime with NUT parameter $\nu = 0.7$. The three curves correspond to three different values of the mass factor—green plain curve for a massless particle, blue dashed (respectively orange dotted) for a massive ($\mu_0 = 1$) particle with energy $E = 0.9$ (resp. $E = 0.6$). The lightly coloured zones underneath the curves represent the regions that are admissible for V to satisfy the inequality (4.5), leading to the identification of the possible values of the impact parameter b for the corresponding particle. The squares in the top corners exhibit a zoom on the values of b_+ (left) and b_- (right) to show that they are indeed different. This allows us to see that in the ergoregion, *i.e.* when $g_{tt} > 0$, a massive particle with more energy has more accessible values of b for the same coordinates (ρ, z).

b_+ (left) and b_- (right) to show that they are indeed different. In the ergoregion, *i.e.* when $g_{tt} > 0$, a massive particle with more energy has more accessible values of b for the same coordinates (ρ, z).

4.1.2 Outside the ergoregion

Outside the ergoregion, $g_{tt} = -f < 0$, leading to f being positive and

$$b_- < b_+, \tag{4.6}$$

whatever the value of $g_{\varphi\varphi}$. The allowed range of values for b at some point (ρ, z) outside the ergoregion is thus given by the inequality

$$b \in [b_-, b_+]\,. \tag{4.7}$$

As in the previous case, it follows that as the factor $\left(\frac{\mu_0 c^2}{E}\right)^2$ grows, the allowed region shrinks.

In Fig. 4.2, the rescaled potential V is shown, at a point $(\rho, z) = (2, 3)$, as a function of the impact parameter b, for a NUT parameter $\nu = 0.7$. Again, the three curves correspond to three different values of the mass factor—green plain curve for a massless particle, and blue dashed (respectively orange dotted) for a massive ($\mu_0 = 1$) particle with energy $E = 0.9$ (resp. $E = 0.6$). The lightly coloured regions underneath the curves represent the values that are admissible for V to satisfy the inequality (4.6), leading to the identification of the possible values of the impact parameter b for the corresponding particle.

4.2 Conditions to have circular orbits

The conditions for a particle to be on a circular orbit, as it has already been said, can be reduced to asking for $p_\rho = 0 = p_z$, as well as $dp_\rho/du = 0 = dp_z/du$.

By using the Hamiltonian equations in eqs. (2.25), these last two conditions can be expanded into

$$\begin{cases} \dfrac{dp_\rho}{du} = -\dfrac{e}{2}\left[\left(\partial_\rho g^{\rho\rho}\right) p_\rho^2 + \left(\partial_\rho g^{zz}\right) p_z^2 + \partial_\rho V\right], \\ \dfrac{dp_z}{du} = -\dfrac{e}{2}\left[\left(\partial_z g^{\rho\rho}\right) p_\rho^2 + \left(\partial_z g^{zz}\right) p_z^2 + \partial_z V\right]. \end{cases} \tag{4.8}$$

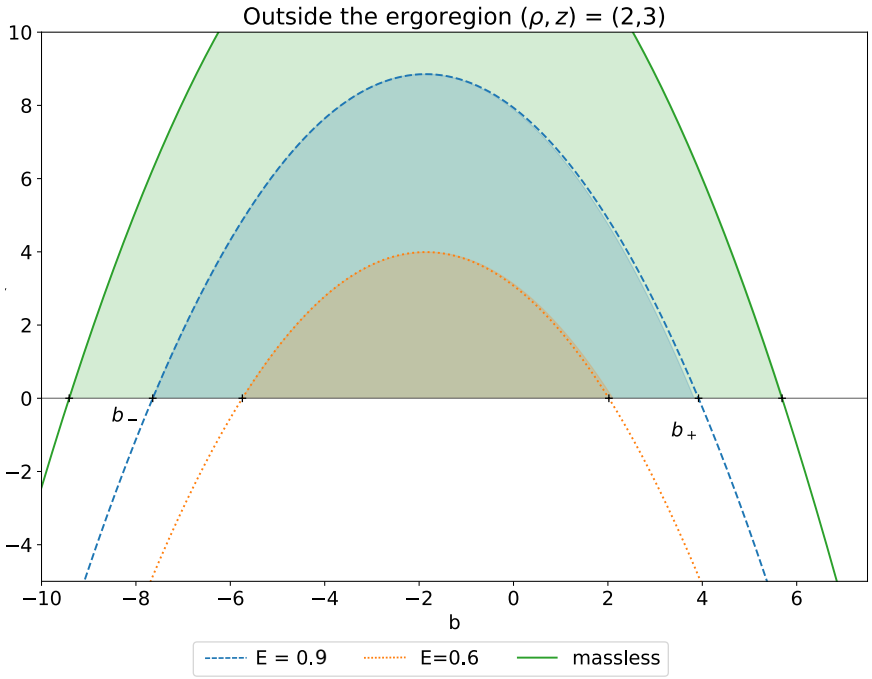


Figure 4.2: The rescaled potential energy V is plotted as a function of the impact parameter b, at a point with coordinates $(\rho, z) = (2, 3)$(outside the achronal region—but the behaviour would be the same either way), for $\nu = 0.7$. Again, the three curves correspond to three different values of the mass factor—green plain curve for a massless particle, blue dashed (respectively orange dotted) for a massive ($\mu_0 = 1$) particle with energy $E = 0.9$ (resp. $E = 0.6$). The lightly coloured zones underneath the curves represent the allowed intervals for V to satisfy the inequality (4.6), leading to the identification of the possible values of the impact parameter b for the corresponding particle.

Note that, thanks to the expression of the metric of the gravimagnetic dipole spacetime, we have that

$$g^{\rho\rho} = g^{zz} = \frac{f}{e^{2\gamma}} \quad \text{and} \quad g_{\rho\rho} = (g^{\rho\rho})^{-1}, \tag{4.9}$$

which simplifies eqs. (4.8) nicely:

$$\begin{aligned} \frac{dp_\rho}{du} &= -\frac{e}{2}\left[(\partial_\rho g^{\rho\rho})\left(p_\rho^2 + p_z^2\right) + \partial_\rho V\right], \\ \frac{dp_z}{du} &= -\frac{e}{2}\left[(\partial_z g^{\rho\rho})\left(p_\rho^2 + p_z^2\right) + \partial_z V\right]. \end{aligned} \tag{4.10}$$

Using again the definition of the Hamiltonian, as well as the potential energy $\mathcal{V}$ and the rescaled potential energy V that we defined in eqs. (2.46) and (2.47), these expressions can be rewritten as follows:

$$\begin{aligned} \mathcal{H} = \mathcal{T} + \mathcal{V} = 0, \\ \Leftrightarrow \mathcal{V} = -\mathcal{T} = -e\left(g^{\rho\rho}p_\rho^2 + g^{zz}p_z^2\right) = e\,g^{\rho\rho}(p_\rho^2 + p_z^2), \\ \Rightarrow p_\rho^2 + + p_z^2 = -\frac{\mathcal{V}}{e\,g^{\rho\rho}} = \frac{E^2}{2\Delta c^2}\frac{V}{g^{\rho\rho}}. \end{aligned} \tag{4.11}$$

Finally, inserting this last expression in eq. (4.10), we arrive to

$$\begin{aligned} \frac{dp_\rho}{du} &= -\frac{1}{2}\left(\frac{\partial_\rho g^{\rho\rho}}{g^{\rho\rho}}\frac{E^2}{2\Delta c^2}V + \partial_\rho V\right), \\ \frac{dp_z}{du} &= -\frac{1}{2}\left(\frac{\partial_z g^{\rho\rho}}{g^{\rho\rho}}\frac{E^2}{2\Delta c^2}V + \partial_z V\right). \end{aligned} \tag{4.12}$$

Since asking for $p_\rho = 0 = p_z$ is equivalent to asking for $V = 0$, it means that for $dp_\rho/du = 0 = dp_z/du$ to be verified, we only need $\partial_\rho V = 0 = \partial_z V$.

Finally, let us show that the analysis of $b_\pm$ is equivalent to the analysis of the rescaled potential energy V. Our conditions for a circular orbit, for now, are the following:

$$\begin{cases} V = 0, \\ \partial_\rho V = 0, \\ \partial_z V = 0. \end{cases} \tag{4.13}$$

Let us first examine the second equation, the ∂_ρ case. We have that

$$V = g_{tt}(b - b_+)(b - b_-) \tag{4.14}$$

so the derivative with respect to ρ is

$$\begin{aligned} \partial_\rho V = &\left(\partial_\rho g_{tt}\right)(b - b_+)(b - b_-) \\ &+ g_{tt}\left(-\partial_\rho b_+\right)(b - b_-) \\ &+ g_{tt}(b - b_+)\left(-\partial_\rho b_-\right) \end{aligned} \tag{4.15}$$

Since we are in the case where $V = 0$, the first line is already trivially zero. Then either $b = b_+$ or $b = b_-$. In the first case, the third line is automatically zero and the second condition in eq. (4.13) becomes $\partial_\rho b_+ = 0$. In the second case, the second line is automatically zero and the condition becomes $\partial_\rho b_- = 0$.

The reasoning is the same for the third line of eq. (4.13), and finally we have two sets of conditions for our circular orbits:

$$\begin{cases} b = b_+, \\ \partial_\rho b_+ = 0, \\ \partial_z b_+ = 0, \end{cases} \quad \text{or} \quad \begin{cases} b = b_-, \\ \partial_\rho b_- = 0, \\ \partial_z b_- = 0. \end{cases} \tag{4.16}$$

These equations can be derived in analytic form quite easily, but as previously in the equatorial plane, finding their solutions is not trivial (one could argue it is actually twice as difficult).

In the following, we are only going to examine the massless case; the massive case is easily adaptable provided a few factors $\sqrt{1 - f\left(\frac{\mu_0 c^2}{E}\right)^2}$ are added here and there.

The radial equation we have to solve is given by

$$\partial_\rho b_\pm = \partial_\rho \omega \pm \frac{f - \rho\,\partial_\rho f}{f^2} = 0. \tag{4.17}$$

This is equivalent to eqs. (3.22) and (3.23), which were defined for the equatorial plane circular orbits. The equation in z reads

$$\partial_z b_\pm = \partial_z \omega \pm \frac{\rho}{f^2}\,\partial_z f = 0. \tag{4.18}$$

Since these equations are quite long when expressed in their complete analytic forms, we are not going to look for exact solutions. In the follow-

ing, we are going to examine qualitative solutions, especially to see how the number of solutions evolves as the NUT parameter changes.

4.3 Qualitative analysis of the impact parameter effective potential levels

As was said earlier, we are going to examine the level curves of the functions defined in eqs. (4.17) and (4.18).

4.3.1 Circular orbits

To illustrate our method, let us examine the first panel of Fig. 4.3. The plot represents a slice of the XZ plane, or the $(\rho, \varphi = 0, z)$ plane, with ρ on the horizontal axis and z on the vertical one. For a NUT parameter $\nu = 0.2$, we have computed the value of b_+ at each point, and have plotted it as colours—the range of values associated to each colour can be found in the legend at the bottom of the figure. Note that the thin lines correspond to constant values of b_+. The red dotted lines correspond to the ergosurfaces. We have then used the `contour()` function from Python's Matplotlib library [95], which draws the levels of a function. The cyan dashed lines correspond to the "zeroth-level" of the function $\partial_\rho b_+$. In other words, the cyan dashed lines trace the set of values (ρ, z) where the radial equation given in eq. (4.17) is verified. The yellow plain lines correspond to the axial equation from eq. (4.18). Thus the circular orbits are located at the intersections of the yellow and cyan dashed lines—*not* yellow-yellow or cyan-cyan intersections. In summary, the panel we are considering shows that there are two prograde photon orbits for $\nu = 0.2$, both in the equatorial plane. This corresponds to what we learnt in Section 3.7 of Chapter 3.

The two next panels show the evolution in the structure of the solutions as ν grows. In Chapter 3, we saw that in the equatorial plane there is a value of the NUT parameter ($\nu = 0.267$) such that the prograde orbits merge into one, then disappear. Here, we can see that the degenerate orbit does not actually disappear; it separates into two symmetric copies with non zero values of z.

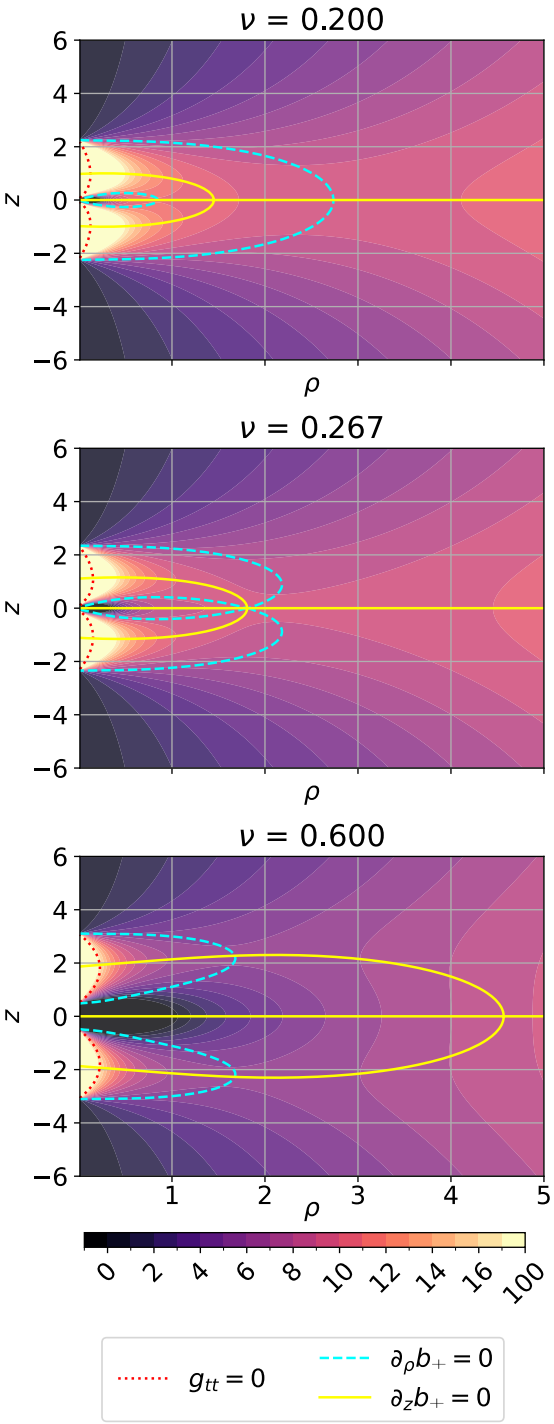


Figure 4.3: These three panels present a slice of space (ρ, z) for three different values of the NUT parameter. The horizontal axis represents the ρ dimension, the vertical one the z dimension. The colours represent the value of b_+ at each point. The red dotted lines represent the ergosurfaces, and the cyan dashed (respectively yellow plain) line the surface (ρ, z) where $\partial_\rho b_+ = 0$ (resp. $\partial_z b_+ = 0$) is verified. The circular orbits locations can be thus be found at the intersections of the yellow and cyan lines. In the first panel at $\nu = 0.2$, there are two circular orbits in the equatorial plane and as ν grows, the merge into one degenerate one at $\nu \approx 0.267$ (as found in Chapter 3). The last panel at $\nu = 0.6$ shows that the circular orbits did not simply disappear from the equatorial pane; they shifted out of it in a symmetrical manner.

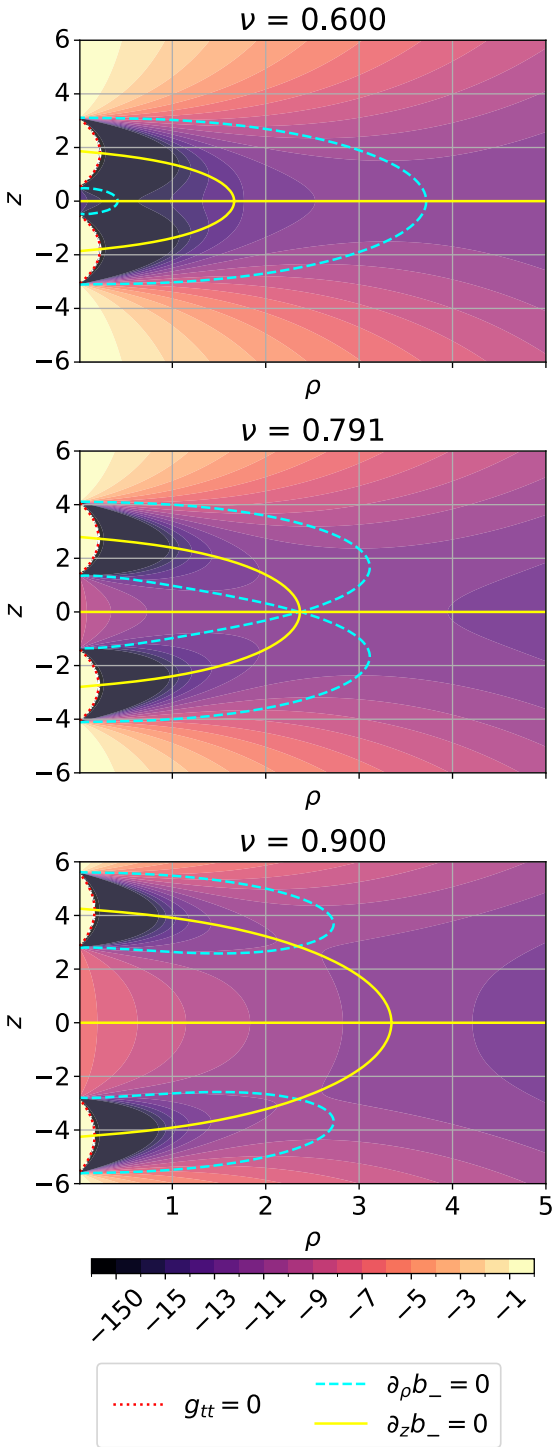


Figure 4.4: These three panels present a slice of space (ρ, z) for three different values of the NUT parameter ($\nu = 0.2, 0.267$ and 0.9). The horizontal axis represents the ρ dimension, the vertical one the z dimension. The colours represent the value of b_- at each point. The red dotted lines represent the ergosurfaces, and the cyan dashed (respectively yellow plain) line the surface (ρ, z) where $\partial_\rho b_+ = 0$ (resp. $\partial_z b_+ = 0$) is verified. The circular orbits locations can be thus be found at the intersections of the yellow and cyan lines. In the first panel for $\nu = 0.6$, there are two circular orbits in the equatorial plane and as ν grows, the merge into one degenerate one (as found in Chapter 3) at $\nu \approx 0.791$. The last panel, for at $\nu = 0.9$, shows that the circular orbits did not simply disappear from the equatorial pane; they shifted out of it in a symmetrical manner.

Let us now turn our attention to the retrograde case in Fig. 4.4. The method is the same: each plot presents a slice of space, with the values of b_- represented in a range colours—careful, the colour bar is different from Fig. 4.3—for different values of the NUT parameter ($\nu = 0.6, 0.791$ and 0.9). We draw the ergosurfaces in red dotted lines, and the zeroth-levels of the functions $\partial_\rho b_-$ in cyan dashed and $\partial_z b_-$ in plain yellow. The intersections of the yellow and cyan lines mark the positions of the retrograde circular orbits. The behaviour is the same as for the prograde case, except this time the value of ν at which there is a degenerate orbit is $\nu \approx 0.791$.

We have not explicitly computed the values of the second derivatives of impact parameters effective potentials, which could directly give the stability status of each orbit. However, they can be deduced by looking at the variations in the coloured plots. This is what is explored in the next section.

4.3.2 Bound orbits

Another interesting feature of these figures can be examined by considering the coloured regions of the plots whilst keeping in mind the "allowed regions" of eq. (4.1). As was said earlier, these zones represent ranges of values for $b_\pm$: the thin lines separating them mark constant values. As we know from Section 4.1, outside of the ergoregion, be it in or out of the achronal zone, a particle can access a region of space when its (fixed) impact parameter is within the permissible range $b \in [b_-, b_+]$.

Let us now examine Fig. 4.5, which shows side-by-side the first panel of Fig. 4.3 and its counterpart for a retrograde particle. Both of the panels show the same characteristics as previously, with this time the added blue dotted line that corresponds to the (ρ, z) set such that $b_+ = 10$ for the first panel, and $b_- = 10$ for the second one. The first panel has two of such curves, with a cyan one in between. Considering the range of colours between the two blue dotted curves, b_+ goes to a maximum (which correspond to the stable orbit at the intersection of the smaller cyan curve and the yellow line). This means that a photon with impact parameter 10 is allowed anywhere in the zone since we will always have $b = 10 < b_+$—note that the same zone always has $b_- < 0$. This "pocket" of colour is disconnected from spatial infinity, thus leading to bound orbits—which

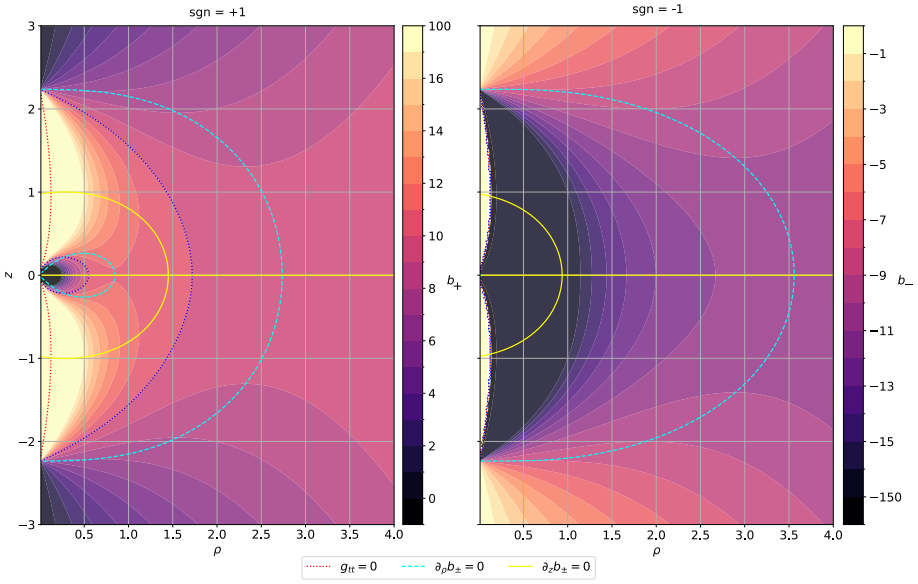


Figure 4.5: Both of these panel show slices of a spacetime with NUT parameter $\nu = 0.2$, with the value of the impact parameter (b_+ on the left panel, b_- on the right panel) as colours. As before, the yellow plain (respectively cyan dashed) lines show the sets of solutions to eqs. (4.17) and (4.18), and the red dotted line depicts the ergosurface. However this time the point of interest consists in the blue dotted lines, that depict a value of b_+ (respectively, b_-) of 10. The pocket that is thus formed on the left panel is disconnected from spatial infinity and thus contains bound orbits. The center of the pocket corresponds to the stable prograde orbit, and the saddle point corresponds to the unstable prograde orbit (that is thus connected to spatial infinity).

are not circular, except from the one at the intersection of the cyan and yellow lines. By contrast, the unstable orbit corresponds to a saddle point, from which the photon can escape through radial perturbations. The second panel does also present a pocket, leading to trapped orbits, and its minimum is at $\rho \approx 0$, as discovered in Chapter 3. Again, the unstable orbit corresponds to a saddle point. Note the sharp transition in the values of b_- at the ergosurface.

Going back to Figs. 4.3 and 4.4, we can deduce two things regarding stability. First, the degenerate orbits at $\nu = 0.267$ and 0.791 are unstable (since they are situated in saddle point structures). Second, this is also the case for mirror orbits on each side of the equatorial plane for larger values of ν.

4.4 Summary

This chapter has demonstrated the usefulness of the impact parameter effective potential framework for analysing circular orbits or bound orbits in the gravimagnetic dipole spacetime, out of the equatorial plane. By specialising this approach to our particular metric, we developed a method that significantly simplifies the search for circular orbits, at least in its qualitative characterisation.

When considering the rescaled potential energy the problem reduces to three simple equations, and only two equations to solve when considering the problem under the point of view of the impact parameter. Whilst these equations prove analytically very difficult to solve, we successfully employed level curves visualisation techniques to identify their solutions.

Our analysis reveals that the gravimagnetic spacetime consistently supports four circular orbits—two prograde and two retrograde—except in two degenerate cases where only one orbit exists in one of the directions, *i.e.* one prograde orbit for $\nu \approx 0.267$ and one retrograde orbit for $\nu \approx 0.791$. What seemed in Chapter 3 as orbits "disappearing" is actually a more subtle phenomenon: as the NUT parameter grows larger than the degenerate orbits inducing values, these orbits migrate away from the equatorial plane whilst maintaining their existence in mirrored pairs above and below it. We also learnt that the degenerate orbits, as well as the "mirror" orbits, are all unstable.

Now that we have a better idea of what happens out of the equatorial plane, we can also make a list of the new questions, or avenues of research, that have emerged:

- ✿ What happens for massive particles? We could determine whether the observed orbit migration phenomenon persists, and how the mass/energy ratio affects the structure of the orbits;
- ✿ Stability analysis: while we have identified qualitative features like "pocket" versus saddle-point behaviour, a rigorous stability analysis would quantify these observations and establish precise stability criteria for the identified orbits;
- ✿ The formation of bound orbits, be it in or out of the equatorial plane;
- ✿ Exploring the possibility of slanted circular orbits (neither purely equatorial nor purely vertical) could reveal new orbital regimes;
- ✿ Velocity profiles. Calculating orbital velocities for the identified circular orbits would provide additional physical insights and enable direct comparison with equatorial plane results.

These extensions would significantly enhance our understanding of orbital dynamics in the gravimagnetic dipole spacetime, potentially revealing novel gravitational phenomena characteristics of this metric.

CHAPTER 5

A FIRST FORAY INTO LIGHT BENDING

> Round I go, the moon a diet of light, sliver of pear
> wedge of lemon, slice of melon, half an orange, onion;
> your human music falling like petals through space,
> the childbirth song, the lover's song, the song of death.
>
> — Carol Ann Duffy, *The Woman in the Moon* (2011)

The first (published) mention of light bending by a massive object goes back to the German physicist, mathematician and astronomer Johann Georg von Soldner, in a paper written in 1801 and published in 1804 [96]: based on Newton's corpuscular theory of light, he understood that light would be diverted by massive bodies, and computed the numerical value by which a ray emitted by a star close to the Sun would be deviated. Since such observations were impossible at the time, he promptly concluded that the effect could be neglected.

A bit over one hundred years later, in 1911, Albert Einstein computed the same value [97] based only on the principle of equivalence that he was developing at the time—it is not clear whether he knew of Soldner's work, but one can surmise that if he did, he considered his own work to

be independent since he did not mention Soldner in any way. As Einstein completed the theory of General Relativity, he noted in 1915 that this value was wrong. With the help of Schwarzschild's solution to his own equations, he computed the right value—a deviation of 1.75 arcseconds for light that grazes the Sun—in time for it to be confirmed by Frank Watson Dyson and Arthur Stanley Eddington's 1919 experiment and subsequent 1920 paper [98].

What began as a theoretical prediction has since flourished into a robust field of study, encompassing concepts such as strong and weak lensing, caustics, magnification, critical curves, the lens equation, ... [99–104]. These tools were first developed for spherically symmetric spacetimes [105–107], then adapted for axisymmetric spacetimes [108, 109] in the equatorial plane, or outside of it [110]. Of course, solving exactly these equations proved difficult, which led to the analytic approximations in the weak or strong deflection limits [111–113]. More recently, comparison has been made between photon and ultra-relativistic massive particles in the Schwarzschild spacetime [114].

The investigation of the gravimagnetic dipole spacetime within the framework of all of these aspect of gravitational lensing would thus be the natural continuation of the previous chapters. The last chapter of this work thus occupies itself with revisiting a cornerstone result: the calculation of the deflection angle for photons travelling near the gravimagnetic dipole [115, 116].

Specifically, we will examine two key cases: in Section 5.1, we will examine the behaviour of photons in the equatorial plane by computing their deflection angle and see how it depends on the value of the NUT parameter. Second, in a more exploratory way, we will look at what happens to photons that come near the centre of the spacetime by following a trajectory along the symmetry axis, by letting the photons evolve by integrating numerically their Hamiltonian equations.

5.1 Photon deflection in the equatorial plane

In this first section, we will consider the deflection angle of photons in the equatorial plane.

For this we will use the Hamiltonian-constraint effective potential that was defined in Section 2.4.2 and later particularised for the gravidipole

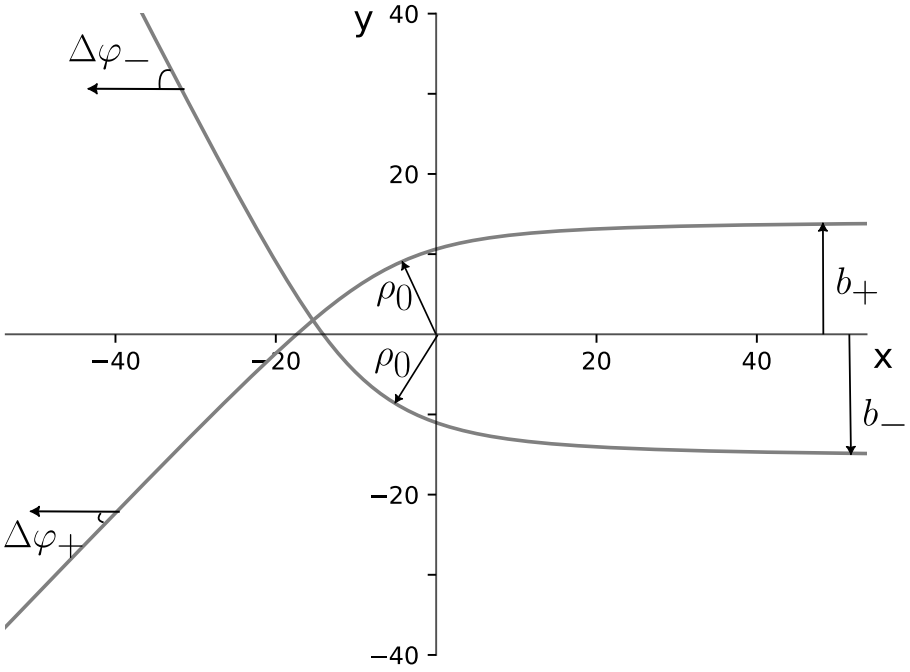


Figure 5.1: This graph depicts the equatorial plane. A deflected photon can be characterized by its closest approach radius (or turning point) ρ_0 or its impact parameter b. In our case since the metric is stationary (here $\nu = 0.6$), depending on the side of the origin that the photon arrives from, (*i.e.* if the photon is prograde or retrograde), there will be two values of the impact parameter associated to the same closest radius. Here for $\rho_0 = 10$, $b_+ \approx 14.20$ and $b_- = -15.39$. The two corresponding deflection angles, $\Delta\varphi_\pm$, are also shown. Note that for some values of (ρ_0, ν), both the impact parameters can be negative.

metric in eq. (3.16) of Section 3.3, directly for a massless particle:

$$\left(\frac{\mathrm{d}\rho}{\mathrm{d}\varphi}\right)^2 + V(\rho, b) = 0, \quad V(\rho, b) = \frac{\rho^2}{e^{2\gamma}}\left(1 - \frac{\rho^2}{f^2}\frac{1}{(b-\omega)^2}\right). \tag{5.1}$$

For a photon trajectory that reaches a turning point at $\rho = \rho_0$ (ρ_0 will be called the closest approach radius) and is scattered to infinity, the total deflection angle can be defined as [87, 115, 117]:

$$\Delta\varphi_{\pm}(\rho_0) = 2\int_{\rho_0}^{\infty} \frac{\mathrm{d}\rho}{\sqrt{-V(\rho, b_0^{\pm})}} - \pi, \tag{5.2}$$

with $b_0^{\pm}$ such that $V(\rho_0, b_0^{\pm}) = 0$, *i.e.* corresponding to the critical impact parameter that was defined earlier in Chapter 3, eq. (3.25):

$$b_0^{\pm} = b_{\pm}(\rho_0) = \omega_0 \pm \frac{\rho_0}{f_0}, \tag{5.3}$$

with the subscript 0 denoting the function being evaluated at the point $(\rho = \rho_0, z = 0)$. For one value of the closest approach radius there are thus two values of the impact parameter, and it follows that there are two values of the deflection angle. These quantities are shown on Fig. 5.1: from basic mechanics, if we use (x, y) coordinates on the equatorial plane, a particle coming from infinity along the x axis, with angular momentum L and energy E will have its value of $y = b = cL/E$.

The two different values of the total deflection angle for the same ρ_0 are due to the stationarity of the metric: space is being dragged around the origin, and the photon will not propagate through a same local spacetime geometric environment if it goes around the origin in one direction or the other, *i.e.* if it is prograde or retrograde. This effect will be more or less strong according to the value of the NUT parameter.

The results and interpretation of eq. (5.2) deserve quite a bit of careful consideration. We numerically perform the integration and plot the resulting $\Delta\varphi$'s as functions of the impact parameters $b_0^{\pm}$. Like for the velocity rotation curve of Fig. 3.23, what we actually do is generate a parametric plot with ρ_0 as the parameter. However, since a photon coming from radial infinity cannot reach every region of space (depending on the NUT parameter), the lower integration limit ρ_0 cannot be any value; this is what we are going to focus on first.

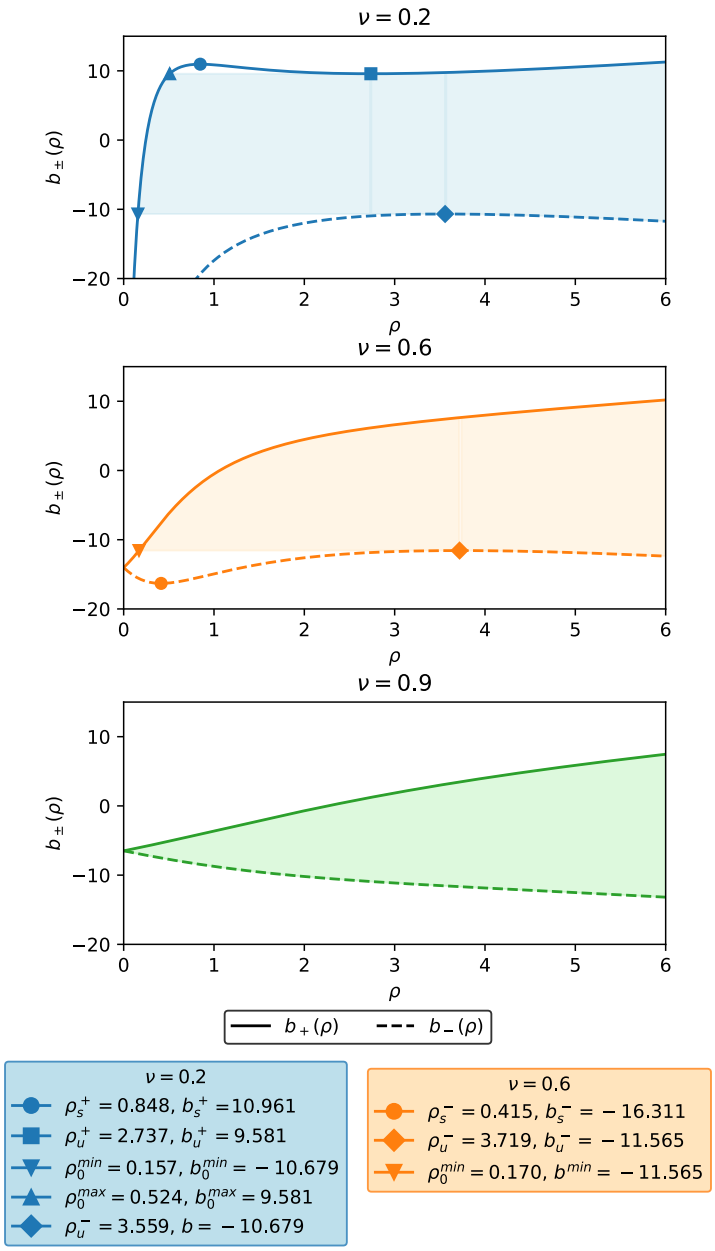


Figure 5.2: Each panel shows the prograde (respectively retrograde) impact parameter b_+ (resp. b_-) plain (resp. dashed) line, for three values ν. A photon, with a fixed value of its impact parameter, can come in on a "horizontal line", and thus reach the minimal corresponding radius at the boundary of the coloured region. The markers each depict the key values in determining the lower integration bounds of eq. (5.2).

For the following analysis, we have chosen three values of the NUT parameter, $\nu = 0.2, 0.6$ and 0.9. They are representative of the possible configurations: two pairs of photon orbits, one pair, and no photon orbits.

Fig. 5.2 is made out of three panels, each showing the prograde (respectively retrograde) impact parameter b_+ (resp. b_-) plain (resp. dashed) line, for the three ν. As was first discussed in Section 2.4.3*, the effective impact parameter potential formulation leads us to determine a range of the authorized impact parameter for some value of the radius, or conversely, a range of authorized radii for some value of the impact parameter. It is this second point of view that is useful here: a photon, with a fixed value of its impact parameter, can come in on a "horizontal line" in the panels of Fig. 5.2, and thus reach the minimal corresponding radius at the boundary of the coloured region. The markers each depict the key values in determining the lower integration bounds of eq. (5.2). The allowed ranges for the closest approach radius and the corresponding impact parameters can be found in Table 5.1.

Table 5.1: Allowed closest approach radii ρ and corresponding impact parameters b for photons in the equatorial plane, as a function of the NUT parameter ν.

ν	**Direction**	**Allowed ρ_0 range**	**Corresponding b_0 range**
0.2	Prograde	$\rho_0^{\min} < \rho < \rho_0^{\max}$	$b_0^{\min} < b < b_0^{\max}$
		$\rho_u^+ < \rho < +\infty$	$b_u^+ < b < +\infty$
	Retrograde	$\rho_u^- < \rho < +\infty$	$b_u^- < b < +\infty$
0.6	Prograde	$\rho_0^{\min} < \rho < +\infty$	$b_0^{\min} < b < +\infty$
	Retrograde	$\rho_u^- < \rho < +\infty$	$b_u^- < b < +\infty$
0.9	Every value of ρ_0 is permitted, regardless of photon direction. Discontinuity at $\rho_0 = 0$.		

Notation:

- Superscripts: $+$ (prograde), $-$ (retrograde).
- Subscripts: s (stable), u (unstable).
- $\rho_0^{\min/\max}$: Minimum/maximum reachable radii for scattered photons.

The markers are all defined with respect to the photon circular orbits. Indeed, the impact parameter $b_0^{\max}$ is equal to the impact parameter of

*There are more details in Appendix B, Section B.2.

the unstable prograde circular orbit b_u^+, and the corresponding radius can be found with eq. (5.3); the rest follows from the other correspondences; the numerical values can be found in the legend of Fig. 5.2.

Let us now turn to Fig. 5.3, where we finally have the total deflection angles as functions of the impact parameters (again, in three panels for each value of ν). The first thing to notice is the presence of vertical asymptotes; they correspond to the unstable photon orbits. When photons coming from radial infinity have their impact parameter close to the critical one, they do more and more turns around the origin before being scattered back to radial infinity. For $\nu = 0.2$ (respectively $\nu = 0.6$), the three (resp. two) pieces of the plot correspond to the three (resp. two) authorized intervals of values in Table 5.1; for $\nu = 0.9$, there is a discontinuity at $\rho = 0$, corresponding to $b_+ = b_- \approx -6.494$.

The stable orbits are of no consequence on this plot; indeed, photons cannot reach the corresponding radii with the critical value of the impact parameter necessary. Finally, notice that some values of the impact parameters allow for the photons to turn *away* from the origin ($\Delta\varphi < 0$), or to go on on a straight line $\Delta\varphi = 0$.

Finally, Figs. 5.4 and Fig. 5.5 exhibit a few example trajectories. In Fig. 5.4, photons do more and more turns around the origin as their impact parameter nears the critical impact parameter of the photon circular orbit. In Fig. 5.5, photons are deflected away or towards the origin, or not deflected at all, depending on their impact parameter.

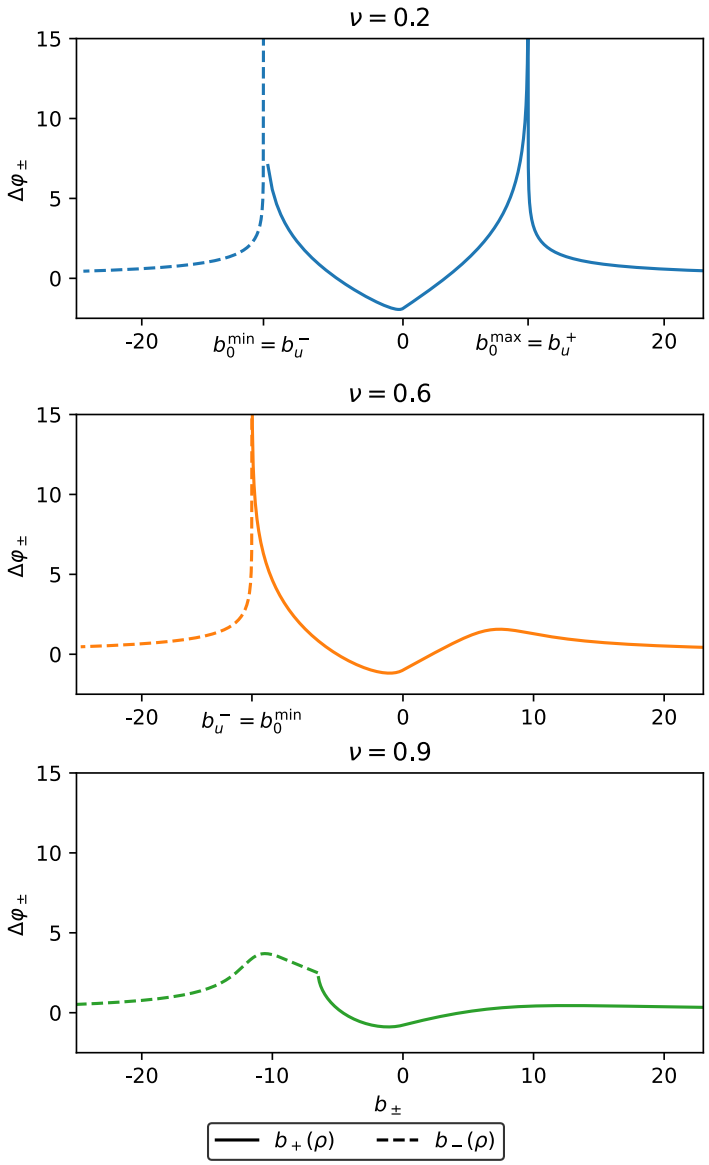


Figure 5.3: This figure presents the total deflection angle as a function the impact parameter, the prograde (resp. retrograde) part corresponding to the plain (resp. dashed) line, for three different values of the NUT parameter $\nu = 0.2, 0.6$ and 0.9. The asymptotes correspond to unstable photon orbits. Some values of the impact parameter that will lead the photon to be deflected *away* from the origin ($\Delta\varphi < 0$), or that will allow it to continue in a straight line ($\Delta\varphi = 0$). Finally, the discontinuity in the green curve ($\nu = 0.9$) corresponds to $\rho_0 = 0$, $b_0^+ = \omega_0 = b_0^-$.

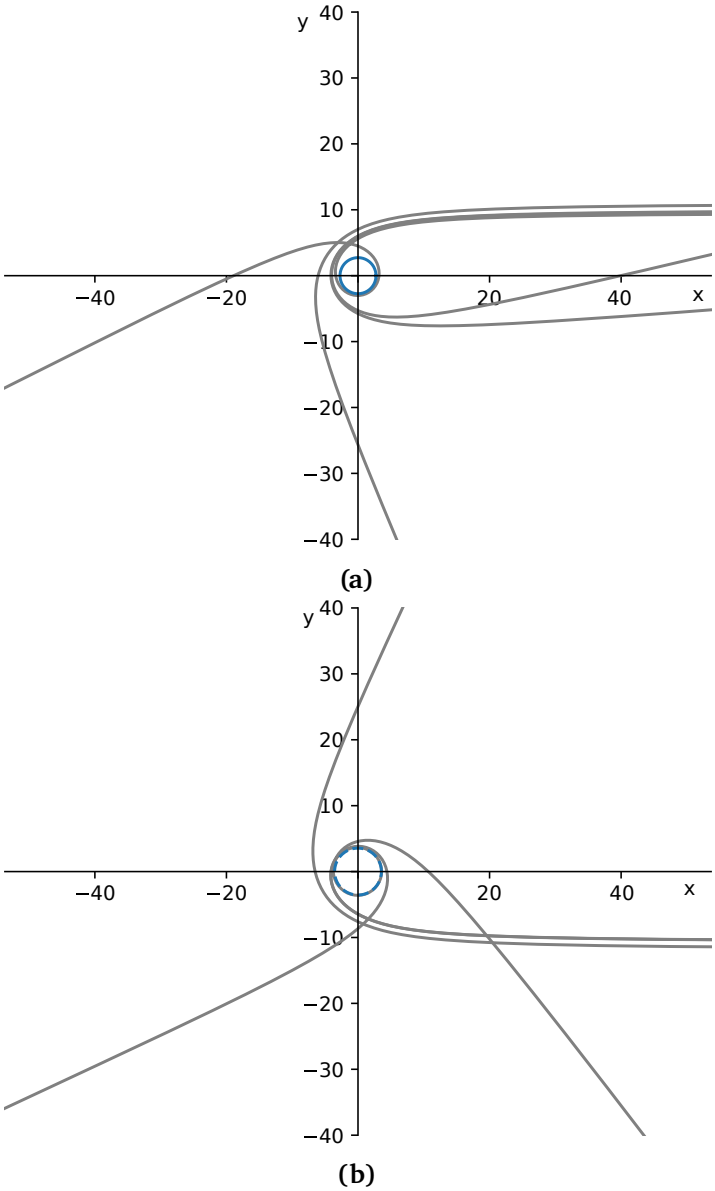


Figure 5.4: Trajectories of photons with a variety of impact parameters. The NUT parameter is $\nu = 0.2$. In the top panel, prograde photons with impact parameters 11, 10, 9.945, and 9.6 curve around the circular prograde photon orbit (shown in plain blue). In the bottom panel, retrograde photons with impact parameters -11.8, -10.7 and -10.67 curve more and more around the circular retrograde photon orbit (shown in dashed blue).

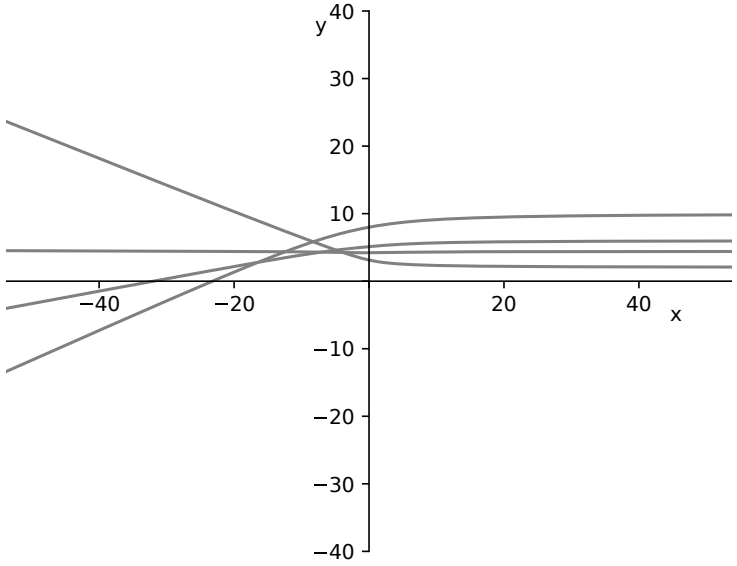


Figure 5.5: For a NUT parameter $\nu = 0.9$, a few photon trajectories. The impact parameters $b_+ = 10$ and $b_+ = 6$ lead to a deflection towards the origin, $b_+ = 4.4$ leaves the photon on a straight path, and $b_+ = 2$ deviates the photon away from the origin.

5.2 An exploration of light deflection along the vertical axis

Having explored the equatorial plane in some detail, let us now step beyond it. Suppose, for a moment, that gravimagnetic dipole spacetimes exist in our Universe—we can hardly expect them all to be so well oriented that Earth sits neatly in their equatorial plane. A general formula for photon deflection, valid for arbitrary incoming or outgoing directions, would be ideal, but that is beyond the scope of this work.

Instead, let us turn to another "simple" case. In this section, we will use numerical evolution of photons to get some insight about their behaviour along the symmetry axis. We have restricted ourselves to photons that *do not* enter the black holes horizons.

For photons coming "along the symmetry axis", *i.e.* with a finite value of ρ and from z-infinity, the integral in eq. (5.2) cannot be used any more. Indeed, it is not only the azimuthal coordinate of the photon that is going to change, but also its radial coordinate. We are thus going to define a

new deflection angle [114] $\Delta\alpha$ as

$$\cos\Delta\alpha = \frac{\dot{x}_i^k \dot{x}_{f,k}}{|\dot{x}_i|\,|\dot{x}_f|}, \text{ with } \dot{x}^k = \frac{\mathrm{d}x^k}{\mathrm{d}x^0}, |\dot{x}| = \sqrt{\dot{x}^k \dot{x}_k} \tag{5.4}$$

where $\dot{x}_{i,f}$ are respectively the initial and final velocities.

We will then generate a series of photons with varying initial conditions, numerically evolve them over time, and record their final positions and velocities to compute their deflection angle. This can be done in Mathematica, though some caution is warranted.

One of the main difficulties—beyond the actual time evolution—is that the function *arccosine* is multivalued and one has to use the principal value arccosine function:

$$\forall x \in [-1,1] \qquad \arccos x \in [0,\pi]. \tag{5.5}$$

This means that we have to carefully interpret the numerical results; this is done by checking in which quadrants the photons end up, and by counting how many "turns" they have done around the origin. Happily enough, if the distribution of photons is populated enough, their behaviour is essentially continuous, which allows to make an educated guess for the value of the factor λ:

$$\Delta\alpha = \arccos\left(\frac{\dot{x}_i^k \dot{x}_{f,k}}{|\dot{x}_i|\,|\dot{x}_f|}\right) + \lambda\pi, \tag{5.6}$$

that gives the 'true' deviation of the photon.

In Fig. 5.6, we have plotted the results of this procedure. We have generated approximately 300 photons, at initial positions of $z = 1 \times 10^4$, $\varphi = 0$, and a range of initial values for the radius that is shown on the horizontal axis. Their initial velocities are all the same, a unit vector ($c = 1$) aligned with z-axis towards the negatives. For four different values of the NUT parameter, the total deflection angles as defined in eq. (5.4) are shown. There a two main features to notice. First, looking at large values of ρ, the influence of the value of the NUT parameter decreases, and the system starts to behave like a single rotating black hole. Second, the total deflection angle function is piecewise: its discontinuities are accounted for by the photons falling in the black holes' event horizons.

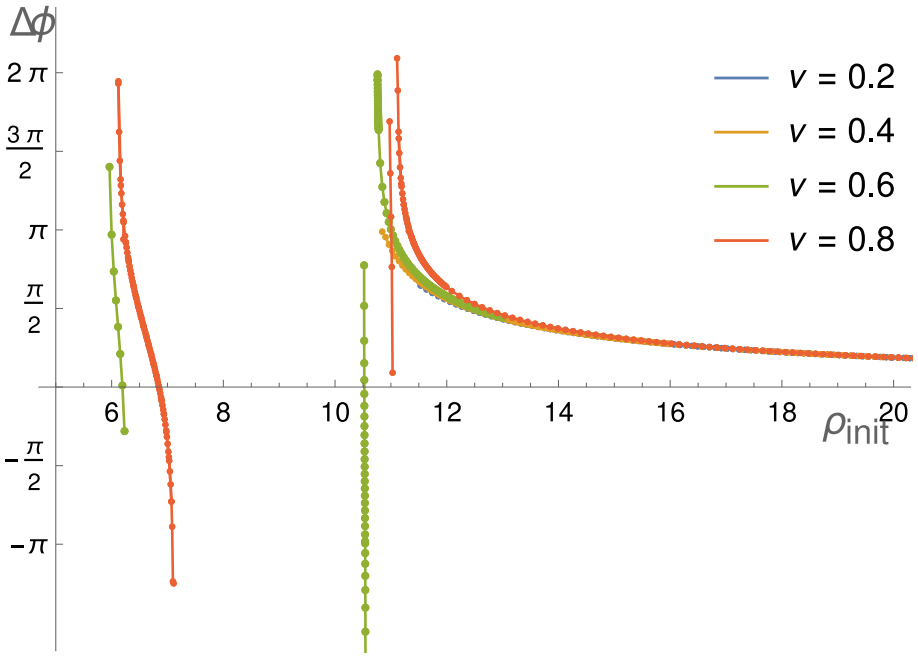


Figure 5.6: This plot is the result of the following procedure: we generate 300 photons with as initial positions $z = 10^4$, $\varphi = 0$, and ρ_{init} within a range of values as depicted on the horizontal axis. Their initial velocity is a unit vector ($c = 1$) along the negative z-axis. We then let them evolve in time with the Hamiltonian equations. The resulting deflection angle as defined in eq. (5.4) is then plotted as a function of ρ_{init}. The rightmost part resembles the deflection angle obtained from a single rotating black hole, with the influence of the value of the NUT parameter decreasing as ρ_{init} grows. The leftmost part shows that for ν large enough, the photons can pass between the black holes. The discontinuities account for the photons—that we have discarded—falling in the black holes horizons. Note that the results corresponding to $\nu = 0.2$ are mostly under those for $\nu = 0.4$.

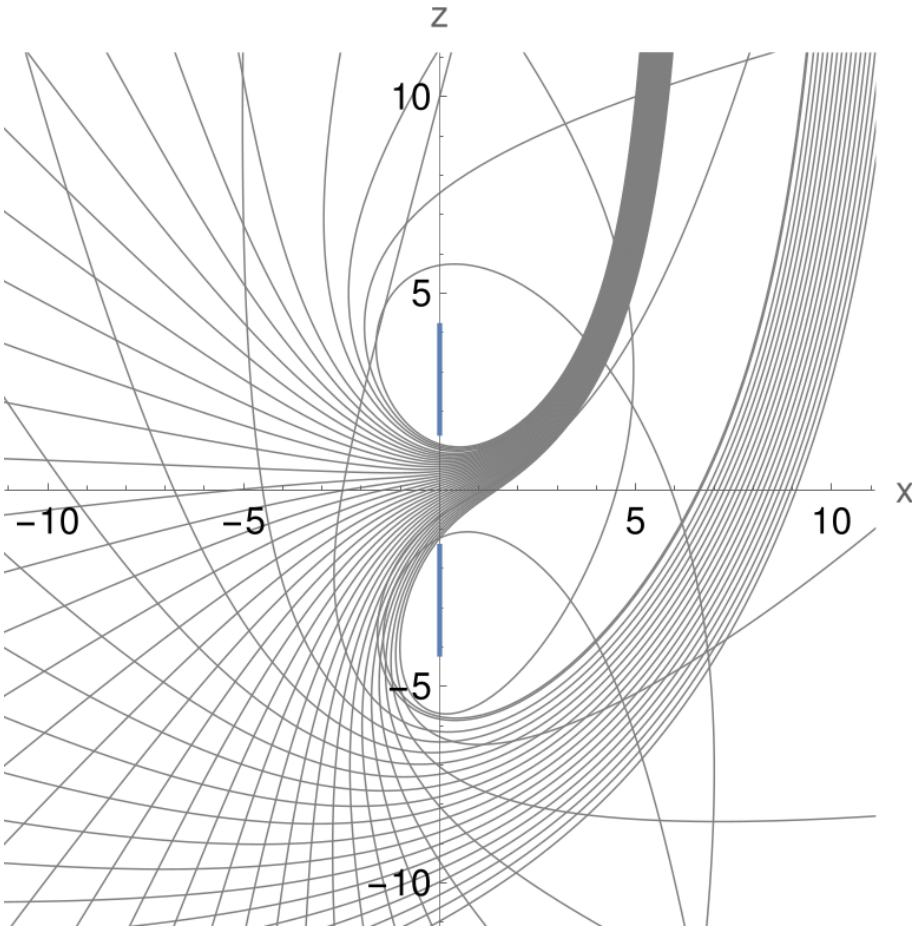


Figure 5.7: For $\nu = 0.8$, the black holes horizons have been drawn in blue. The trajectories of photons starting from $z = 10^4$, $\varphi = 0$ and a range of values ρ_{init} have been traced in grey. The photons that end up falling in the black holes have been removed as to not overload the picture. From $\rho_{\text{init}} > 10$ and onwards, the photons curve around the two black holes in a simple way. Under that, their behaviour is quite chaotic; they can pass between the black holes and go back from where they came, pass between them then fall in one of the horizons, *etc*. As ν decreases and the distance between the two horizons, $2\alpha_-$, shrinks, less and less photons can pass.

Before examining this last point in more detail, let us consider Fig. 5.7, which displays the trajectories of a selection of photons for $\nu = 0.8$. The blue vertical lines denote the black hole horizons; any photon falling in has been omitted to avoid visual clutter. Broadly speaking, the photons exhibit five generic types of behaviour:

- ✿ For $\rho_{\text{init}} \lesssim 6.1$, the photons directly fall in the upper horizon (not pictured);
- ✿ For $6.1 \lesssim \rho_{\text{init}} \lesssim 7.2$ the photons can pass between the black holes and escape to infinity;
- ✿ For $7.2 \lesssim \rho_{\text{init}} \lesssim 11$, the photons either fall in the lower black hole horizon, or curve around it and fall in the upper black hole horizon (not pictured);
- ✿ For $\rho \approx 11, 11.2$, the photons curve under the lower black hole and pass between the two black holes, then escape towards infinity;
- ✿ For $11.2 \lesssim \rho_{\text{init}}$, the photons avoid both black holes and leave towards infinity.

The five segments (and discontinuities) of the $\nu = 0.8$ curve in Fig. 5.6 correspond to these five distinct cases. To examine them in greater detail, we now turn to Fig. 5.8, which provides a magnified view of the leftmost segments for $\nu = 0.8$. Here, the curve has been simplified by interpolating between computed points to reduce visual complexity. Four key markers have been added, each representing an "interesting trajectory". These trajectories are further illustrated in Fig. 5.9 (as a projection onto the XZ-plane, with markers indicating the positions where photons first become visible in the frame) and in Figs. 5.10 (as a series of 3D depictions from various viewpoints).

This comparison highlights the limitations of the definition given in Eq. (5.4). For instance, consider the blue circular marker: whilst Fig. 5.8 suggests a zero deflection angle, Figs. 5.9 and 5.10 clearly show the photon is deviated.

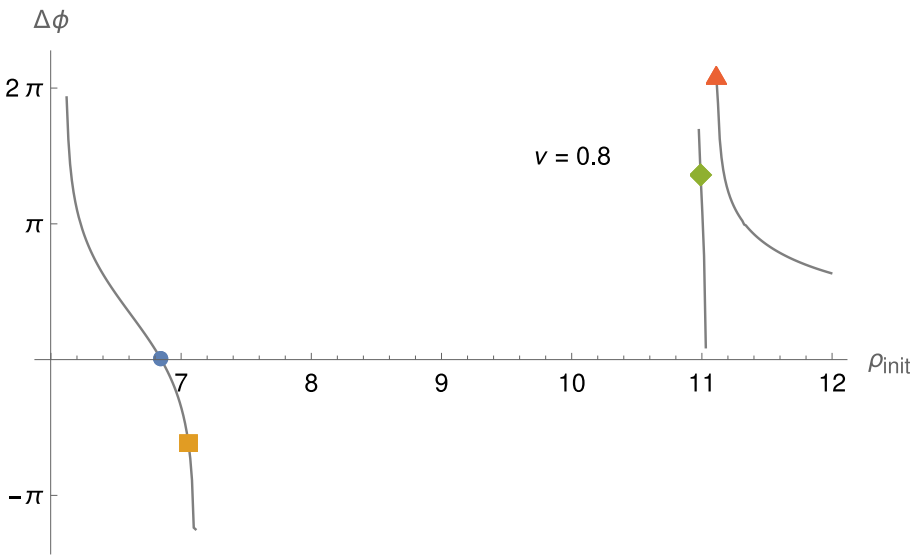


Figure 5.8: This is a zoom of the left part of Fig. 5.6, particularised for $\nu = 0.8$—the curve has been simplified by interpolating between computed points to reduce visual complexity. The markers refer to the trajectories depicted in Fig. 5.9.

5.3 Summary

This chapter has presented an investigation on the behaviour of photons scattered by the gravimagnetic dipole in two distinct ways. First, we have looked at a photon initially starting and then staying in the equatorial plane, and second, we have looked at photons starting far from the equatorial plane, starting and being directed along the symmetry axis, and going towards the center of the spacetime.

The equatorial plane analysis represents the more theoretically grounded portion of our work. We have been able to use the standard definition of deflection angle, calculating its values for different NUT parameters. For values of ν that admit photon circular orbits, we observe that the deflection angle of photons coming in from radial infinity with the adequate combination of impact parameter and closest approach radius goes in an asymptote, as would be expected. Furthermore due to the shape of the effective potentials, photons coming from radial infinity cannot enter stable orbits. Finally, a last interesting feature is that when ν is large enough so that there are no photon orbits, there is a discontinuity in the

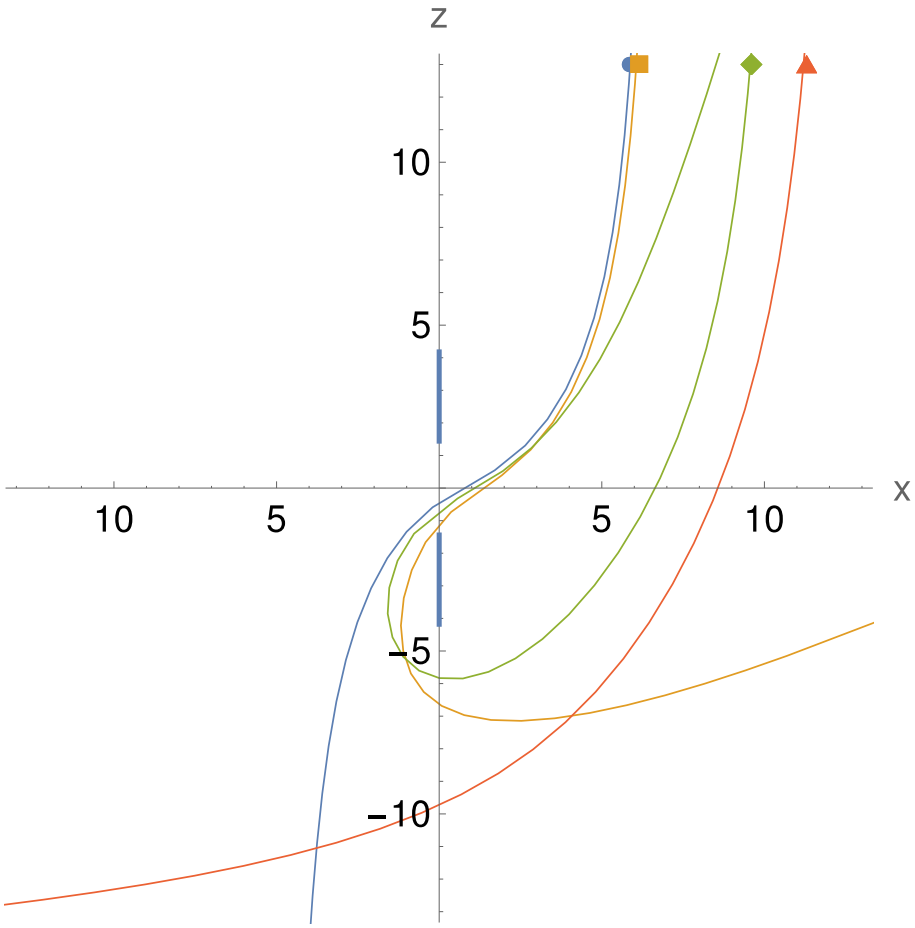


Figure 5.9: The four example trajectories corresponding to the markers of Fig. 5.8 have been traced as a projection on the XZ plane—the markers also show the entry point of the photons in the frame.

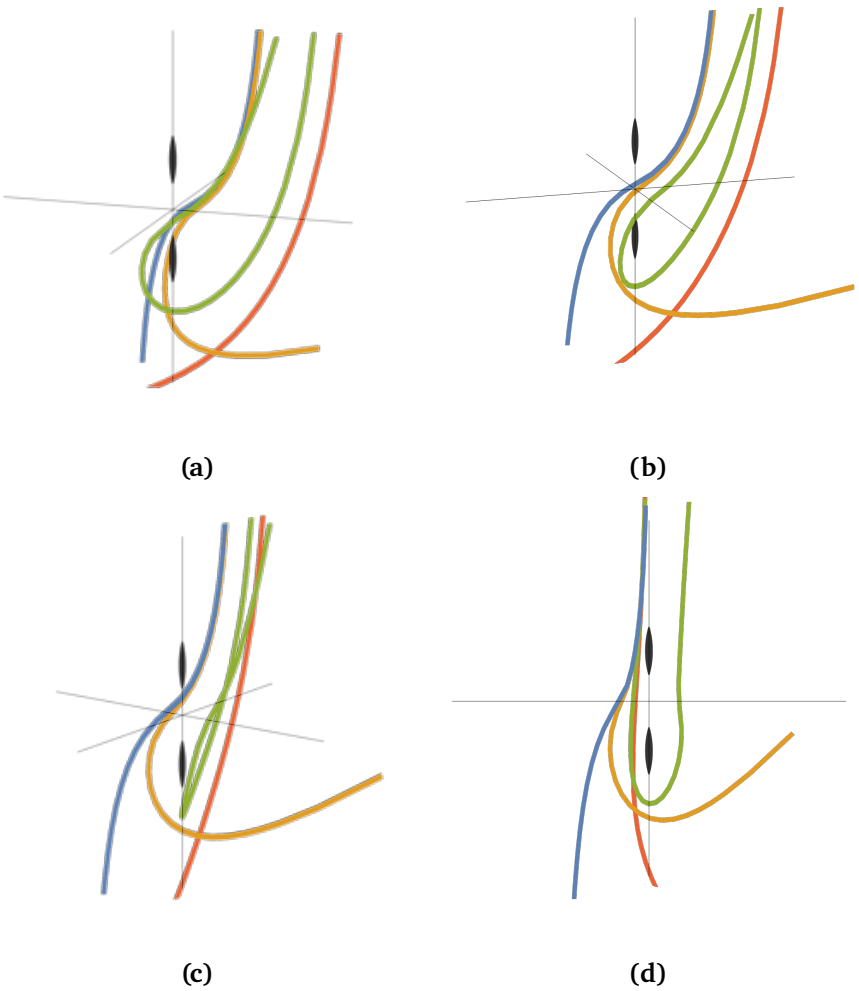


Figure 5.10: The trajectories of Fig. 5.9 are here plotted in 3D and projected, each panel corresponds to a different point of view.

deflection angle of photons when the closest approach radius goes to 0 from a retrograde or prograde direction.

The second portion of our investigation focused on photon propagation along the symmetry axis, representing a more exploratory endeavour, for which we have constructed a procedure that allows us to trace the paths that the photons will follow, and get an idea of the difference in direction between their initial and final velocities—which we also called a deflection angle, even though it is not the same as previously. This has taught us three main things; first, when the photons start out far-ish from the symmetry axis, they behave as if there was a single rotating black hole; second, their behaviour can be cut up in pieces, with five main generic behaviours; third, a more rigorous and complete analysis is imperative. Whilst our definition of deflection angle is serviceable, it clearly has limitations in capturing the full complexity of three-dimensional photon trajectories. Furthermore, the multivalued nature of the arccosine function introduces ambiguities and demands some post-processing based on continuity arguments and/or guesses, lacking the rigour that would be desirable in a complete theoretical framework. Finally, the computational expense reduces the completeness of the picture we can expect.

This leads us to the next steps that could be undertaken. First, in the equatorial plane:

- ✿ We mostly left untreated and uncommented the case where the closest approach radius goes to zero $\rho_0 \to 0$. As the photons approach the center of the spacetime, numerical computation becomes very costly. A more efficient algorithm could be developed to explore this region in more detail;

- ✿ The next logical step consists in examining the lens equation in the context of the equatorial plane of the gravimagnetic dipole; in a more or less closely related case*, the system modelled by an equal mass Majumdar-Papapetrou di-hole metric [93] gives rise to interesting phenomena. Depending on the distance between the black holes, new sets of infinitely many relativistic images and a radial caustic may appear. This could also be the case for the gravimagnetic dipole;

*We already mentioned this system in Section 3.3.1 regarding the number of photon orbits.

- ✿ All the other usual tools such as image distortion, brightness of images, *etc.*;
- ✿ This could be extended to a wider range of NUT parameters, particularly for its degenerate values where the number of prograde (respectively, retrograde) orbits go from two to one to zero.

Our exploration of off-equatorial photon scattering was exploratory, and as such, a lot of its aspects should be modified and/or improved.

- ✿ We need a better definition for the deflection angle;
- ✿ And a more dense sampling for the photons;
- ✿ Our analysis was mainly centred on one value of ν. How do the trajectories evolve as ν changes? How can the limiting values between the types of trajectories be analytically determined?

CONCLUSION

What you just read represents the culmination of three-and-a-half years of research, but as any PhD student knows, the final document captures only a fraction of the journey. Here, I aim to provide not just a summary of the results presented in the preceding chapters, but also a broader perspective on the research process itself—including the false starts, detours, and unanswered questions that all contributed in shaping this work. I will first give a chronological account of how this project evolved, then outline promising directions for future research, and finally reflect—shortly, do not be alarmed—on what this experience has taught me about the nature of scientific inquiry.

I completed my master's thesis under Prof. Jan Govaerts at the end of the academic year of 2019-2020 on the subject of electromagnetic null knots. In short*, topologically non-trivial solutions to Maxwell's electrodynamics can arise: the electric and magnetic field lines "knot" themselves in torus-like shapes. Electromagnetic knots reveal a wealth of interesting mathematical and physical phenomena: although after a contracting phase, these time-dependent configurations are expanding out—the energy density goes down as the knot expands—their winding number is a time independent topological invariant; large classes of solutions can be found by starting out from a perfectly trivial solution, then applying a variety of transformations under which Maxwell's equations are invariant. To me, this subject is particularly fascinating for two reasons: first, it is very surprising. We expect simplicity, triviality, and there is

*Appendix C provides more details.

none. Second, it really lies at the frontier of the different mathematical formulations of electrodynamics. Prof. Jan Govaerts suggested continuing on this subject in a PhD thesis, where we could explore the gravitational implications of these knots: since there are known analogies between electrodynamics and general relativity theories, why not imagine that these knot solutions might have a general relativistic companion, which might then lead to non trivial particle geodesics even in vacuum?

The first step we had to take was to translate the electromagnetic knots to General Relativity. This led to our first paper [1]: checking if the knots still existed (yes) and how they behaved (complicatedly) when letting go of the linearity of Maxwell electrodynamics. However, not long after that, we learnt that particle trajectories inside knots appeared unpromising [118] (they would typically shoot straight out of the knot and never come back...), which led to considering another avenue of research, the gravimagnetic dipole spacetime and its geodesics.

After a foray into the world of numerical resolution of conserved Hamiltonian dynamics (which lasted a year-and-a-half [4] but was not very conclusive), we started on the analytical exploration of particle behaviour in the equatorial plane. This is what finally led to the content of this thesis.

In the first chapter, I present a brief historical overview of the solution's discovery. In many ways, this story is both amusing and perhaps emblematic of theoretical physics as a discipline: when a mathematical solution proves too difficult to interpret physically—what, actually, is the NUT parameter?—or if some of its aspects seem unrealistic or undesirable—here, the absence of asymptotic flatness—the response is often to redefine it until it appears to make sense—in our case, doubling and symmetrising the solution with opposite values of the NUT parameters not only restores the asymptotic flatness, but also confines the singularity to a one-dimensional "small" region of space.

One of the most significant challenges I encountered early on was the sheer complexity of the gravimagnetic dipole metric. Having been trained, as bachelor's then master's student, on analytically solvable systems that typically yielded compact solutions—rarely more than two or three handwritten lines—I was unprepared for the length of these expressions. My first encounter with a multi-line solution (in a different context) made me rethink my life choices. The gravimagnetic dipole's metric functions, with their complicated dependencies on functions of function of functions

of functions and their parameters, represented an order-of-magnitude increase in complexity. Learning to manipulate these lengthy expressions became a significant hurdle, but also an unexpected opportunity to develop my skills in analytical and numerical computational techniques.

The second chapter delves into more theoretical considerations: I discuss how to identify circular orbits with the help of possible different definitions of some effective potential and how to compute the relevant velocity curves. As I worked to tame the gravimagnetic dipole spacetime and its geodesics, I used these different formulations of the effective potential in the chronological order they are presented in, which explains why I did not write the whole thesis with just one single such choice of effective potential. The illustrative examples, the Schwarzschild and Kerr spacetimes, provide first a clear example, and second an initial approach on solving the relevant equations (that get more and more complicated as the number of symmetries reduces; whilst the Kerr metric is stationary axisymmetric like the gravimagnetic dipole, its expression is considerably more compact, and the Carter constant allows for short analytic solutions for a lot of problems).

With these foundations in place, it was then time to plunge into the heart of the matter. The third chapter basically reunites the two previous chapters; applying the techniques developed in the second chapter to the metric described in the first one, *i.e.* computing the actual velocity rotation curves for the gravimagnetic dipole. Initially, I anticipated this to be the most difficult part; however, plotting the curves proved less complex than expected. The real challenge lay in identifying the circular orbits and their stability, particularly for massive particles. Their number varies with the NUT parameter, and they are doubled—a phenomenon I was relieved to find documented in [93], and later (for me) in [88], where similar doubling occurred depending on the distance between black holes. This reassurance came at a crucial moment, as I was simultaneously expanding this section in response to a referee comment about insufficient detail in the curve construction.

The final two chapters mark a pivotal moment in my doctoral work, when I began pursuing research directions with greater autonomy. My investigation of photon deflection originated from an unexpected source: an outreach activity in which I had the opportunity of playing with optical lenses to demonstrate gravitational lensing. I subsequently devoted significant effort to developing a photon-tracing program in Python. Although

rudimentary, this tool enabled the initial exploration of photon scattering outside the equatorial plane presented in Chapter 5.

We obtained some valuable results; namely, as would be expected, photons in the equatorial plane coming from radial infinity can reach and enter the unstable orbits, but not the stable ones. Furthermore when ν is sufficiently large that the photon orbits shift out of the equatorial plane, there is a discontinuity in the deflection angle of photons when the closest approach radius goes to zero from a retrograde or prograde direction.

While starting to investigate the lens equation, I came across the paper discussing the impact parameter effective potential [88], where the authors use a level-plotting method—which inspired mine—to determine the existence of bound orbits. I became very enthusiastic about that visual method, which led to Chapter 4, on the subject of off-equatorial circular orbits. It consists of a first exploration of geodesics out of the equatorial plane. The main result, in my opinion—at least the result I was the most excited about—is that it becomes very clear that the photon orbits of the equatorial plane do not *disappear* when a certain value of ν is exceeded, but they simply shift away from the equatorial plane in a symmetric manner, which is intellectually far more satisfying. Another significant result is the visualisation of bound orbits (in or out of the equatorial plane), as well as the stability of the different circular orbits, which could not be identified as easily in Chapter 3.

I have often heard that for young researchers, the hardest part is not the beginning the work, but finding time to write at the end. At this stage, one finally begins to grasp the ins and outs of the subject, and ideas flow freely—new questions arise, paths to explore beckon, and the temptation to follow the white rabbit down its ever-deepening hole grows. It is exactly what happened to me; as a very anxious person, I started my writing phase quite early in the last year of my thesis, just as a flurry of new areas to explore came to my mind. As I wrote this thesis, the summary of each chapter acted as a catalyst for a flood of new questions and ideas.

The questions that follow are not merely a (non-exhaustive) list of future projects, but rather a roadmap for how this research might evolve. By collecting them here, I hope to both organise my own thoughts and provide a starting point for others who may wish to explore these avenues. These questions are interconnected, and seeing them together might reveal patterns that would otherwise go unnoticed. Rather than organising

them in the order of the chapters in which they arose, I chose to organise them in three interconnected themes, that span from fundamental spacetime properties to observable gravitational effects.

First, the fundamental properties of the metric itself warrant deeper investigation. The physical interpretation of topological features like the Misner string remains an open question: does this structure represent a purely mathematical artifact, or does it have tangible physical consequences for particle trajectories? In the same vein, we identified the parameter k such that the system is at equilibrium and that the metric continues to describe it as time passes. How would the expression of the metric evolve if that was not the case? Another equally important question is that of matter in this system. The addition of matter would almost certainly modify the equilibrium distance k between black holes, raising questions about whether this value must remain constant or evolve as a dynamical equilibrium. Furthermore, the presence of matter might significantly alter the behaviour of both the Misner string and the achronal region, possibly modifying the potential barriers that govern particle access to these regions and thereby affecting the spacetime's causal structure. This could be good or bad news, depending on how physically realistic we want the spacetime to be.

The orbital dynamics in this spacetime reveal a particularly rich behaviour that remains to be fully characterized. If matter were added in the metric, how would this change the shape of the velocity curves, the balance between stable and unstable orbits? Beyond the equatorial plane, several other questions emerge about massive particle behaviour: does the orbit migration phenomenon persist, and how does the mass-energy ratio affect orbital structure? Whilst our qualitative analysis identified features like "pocket" versus saddle-point behaviour, a rigorous stability analysis would be needed to quantify these observations. Calculating velocity profiles for all of these orbits would not only provide physical insight but also a point of comparison with equatorial results. Finally, the formation of bound orbits—both within and outside the equatorial plane—represents another research direction.

Finally, the gravitational lensing properties of this spacetime offer several promising questions. Owing to time constraints, a thorough investigation of deflection along the symmetry axis was not possible; this remains an important direction. The next logical step should be to examine the lens equation in the equatorial plane, where related systems like

the equal-mass Majumdar-Papapetrou di-hole metric exhibit phenomena such as infinitely many relativistic images and radial caustics. These investigations could be extended across a wider range of NUT parameters, with particular attention to degenerate values where the number of prograde and retrograde orbits changes. For non-equatorial deflection, we would need to refine our definition of the deflection angle and increase sampling density to properly characterize the gravitational lensing signature.

Physics, to me, resembles the Hydra of Greek mythology, each question a head that, when answered—cut off—gives rises to two more questions—two more heads. These questions are the heads I am most curious to see cut off*; by my own hand, or by others'. But for now, let me step back from these possibilities and offer some final reflections.

What I love about physics is not the answers *per se*, but the act of asking the question—shaping it so precisely that the path to the answer becomes as visible as a yellow brick road. The real challenge does not lie in solving: it lies in asking. Once you have your question, finding the answer is a matter of ingenuity, talking to the right people, and a sufficient level of hard-headedness. Not hesitating to ask for help while staying true to yourself, and above all, staying humble and being ready to accept one has made a mistake.

One of the rules of magic is the following :"Never reveal the secret to a trick: it ruins the mystery." Physics is the only magic that does not get ruined by knowing the trick, because it opens even more questions. It fuels more curiosity, reveals new phenomena, creates more opportunities to get that *aha* moment. What we love is not knowing: it is understanding. That brief, fleeting moment where suddenly, everything makes sense, where we go from frustration to wonder.

The joy of learning certainly has a higher potential barrier than a lot of other activities, but I am convinced that it is still the most satisfying thing the human mind can experience. Some questions, I think, are not made to be answered. They are there to keep us on our toes. Why are we here? What are we here for? What's for dinner tonight? These are the questions that linger at the edges of our minds, reminding us that science, for all its power, is still a human endeavour. As ironic as it may sound in the context of this thesis, physics does not exist in a vacuum: it is shaped by the people who practice it, by their curiosities, their biases, and their limitations.

*I know. That sounded better in my head.

The questions will always outnumber the answers. Here's to the journey of discovery.

> *"For just one second, look at your life and see how perfect it is. Stop looking for the next secret door that is going to lead you in your real life. Stop waiting."*
>
> — Lev Grossman, *The Magicians* (2009)

> *"The past is no further away than the last breath you took."*
>
> — Robin Hobb, *The Fool's Errand* (2001)

APPENDIX A
MATHEMATICAL DETAILS

"J'aime pas les maths"

— Clémentine Dassy, aged 7, paper archive dated *circa* 2003)

A.1 A particle that starts out in the equatorial plane stays in the equatorial plane

The following equation should be trivially satisfied in $z = 0$ for any p_t and p_φ:

$$\begin{aligned} \frac{dp_z}{du} &= -\frac{1}{2} e \frac{\partial g^{\mu\nu}}{\partial z} p_\mu p_\nu \\ 0 &= \partial_z g^{tt} p_t^2 + 2\partial_z g^{t\varphi} p_t p_\varphi + \partial_z g^{\varphi\varphi}. \end{aligned} \tag{A.1}$$

The metric functions g^{tt}, $g^{t\varphi}$ and $g^{\varphi\varphi}$ can be written in terms of f and ω (see Section 1.2). Their derivatives with respect to z are then given by

the following expressions:

$$\begin{cases} \partial_z g^{tt} = f^{-2}\partial_z f + \dfrac{1}{\rho^2}\left(\omega^2\partial_z f + 2f\omega\partial_z\omega\right), \\ \partial_z g^{t\varphi} = \dfrac{1}{\rho^2}\left(\omega^2\partial_z f + 2f\omega\partial_z\omega\right), \\ \partial_z g^{\varphi\varphi} = \dfrac{1}{\rho^2}\partial_z f. \end{cases} \tag{A.2}$$

For eq. (A.1) to be verified $\forall\rho > 0$, $z = 0$, using eq. (A.2), we need only to verify that for $\rho > 0$, $z = 0$, $\partial_z f = 0$ and $\partial_z\omega = 0$.

Let us start by noticing the following relations when $z = 0$:

$$\begin{aligned} R_\pm(\rho,z) &= \sqrt{\rho^2 + (z \pm \alpha_+)^2} \quad \Rightarrow R_\pm|_{z=0} = \sqrt{\rho^2 + \alpha_+^2} \equiv R, \\ r_\pm(\rho,z) &= \sqrt{\rho^2 + (z \pm \alpha_-)^2} \quad \Rightarrow r_\pm|_{z=0} = \sqrt{\rho^2 + \alpha_-^2} \equiv r, \\ \partial_z R_\pm(\rho,z) &= \frac{z \pm \alpha_+}{R_\pm(\rho,z)} \quad \Rightarrow \partial_z R_\pm|_{z=0} = \frac{\pm\alpha_+}{R}, \\ \partial_z r_\pm(\rho,z) &= \frac{z \pm \alpha_-}{r_\pm(\rho,z)} \quad \Rightarrow \partial_z r_\pm|_{z=0} = \frac{\pm\alpha_-}{r}. \end{aligned} \tag{A.3}$$

As was suggested in Section 1.3,

$$\left.\frac{A(\rho,z)}{\alpha_+\alpha_-}\right|_{z=0} \equiv A_0 \in \mathbb{R} \quad \text{and} \quad \left.\frac{B(\rho,z)}{\alpha_+\alpha_-}\right|_{z=0} \equiv B_0 \in \mathbb{R}, \tag{A.4}$$

whilst the derivatives in z in the equatorial plane are purely imaginary:

$$\left.\partial_z\frac{A(\rho,z)}{\alpha_+\alpha_-}\right|_{z=0} \equiv \partial_z A_0 \in \mathbb{I} \quad \text{and} \quad \left.\partial_z\frac{B(\rho,z)}{\alpha_+\alpha_-}\right|_{z=0} \equiv \partial_z B_0 \in \mathbb{I}. \tag{A.5}$$

Thus we can write the following equalities (with the overbar denoting the conjugate of the quantity it is placed over):

$$\begin{aligned} \bar{A}_0 = A_0, \qquad \overline{(\partial_z A_0)} &= -\partial_z A_0, \\ \bar{A}_0 = B_0, \qquad \overline{(\partial_z B_0)} &= -\partial_z B_0. \end{aligned} \tag{A.6}$$

Let us now look at the expression for f and its derivative in z:

$$f = \frac{|A|^2 - |B|^2}{|A+B|^2} = \frac{A\overline{A} - B\overline{B}}{(A+B)\overline{(A+B)}}. \tag{A.7}$$

Its derivative in z, with $\partial_z A \equiv A'$ and $\partial_z B \equiv B'$ is thus given by:

$$\begin{aligned}\partial_z f =& \frac{1}{(A+B)^2(\overline{A}+\overline{B})^2}\times \\ &\times\Big\{(A'\overline{A}+A\overline{A}'-B'\overline{B}-B\overline{B}')(A+B)(\overline{A}+\overline{B}) \\ &-(A\overline{A}-B\overline{B})\left[(A'+B')(\overline{A}+\overline{B})+(A+B)(\overline{A}'+\overline{B}')\right]\Big\}.\end{aligned} \tag{A.8}$$

When $z=0$ and using eq. (A.6), this simplifies to

$$\begin{aligned}\partial_z f|_{z=0} =& \Bigg(\frac{1}{(A+B)^2(A+B)^2}\times \\ &\times\Big\{(A'A-AA'-B'B+BB')(A+B)(A+B) \\ &-(AA-BB)\left[(A'+B')(A+B)-(A+B)(A'+B')\right]\Big\}\Bigg)_{z=0} \\ &=0.\end{aligned} \tag{A.9}$$

For G, the situation is a bit more complex, because both the imaginary and the real parts survive when $z=0$. We will then denote G as $G \equiv G_r + iG_i$, with G_r, $G_i \in \mathbb{R}$.

We can then compute what happens to G and its derivative when $z=0$.

$$\left.\frac{G}{\alpha_+\alpha_-}\right|_{z=0} \equiv G_r + iG_i, \qquad \left.\partial_z\frac{G}{\alpha_+\alpha_-}\right|_{z=0} \equiv \partial_z G_r + i\partial G_i, \tag{A.10}$$

and in terms of these notations, it follows that:

$$\bar{G_0} = G_r - iG_i, \qquad \overline{(\partial_z G_0)} = \partial_z G_r - i\partial_z G_i. \tag{A.11}$$

We can now finally compute ω and its derivative in z. We know that the expression for ω is given by:

$$\omega(\rho,z) = -4\frac{\Im\left[G(\overline{A}+\overline{B})\right]}{|A|^2-|B|^2}, \tag{A.12}$$

thus its derivative in z should look like:

$$\begin{aligned}\partial_z\omega(\rho,z) =& \frac{-4}{(|A|^2-|B|^2)^2}\times \\ &\times\Big\{ -4\Im\left[G'\left(\overline{A}+\overline{B}\right)+G\left(\overline{A}'+\overline{B}'\right)\right]\left(|A|^2-|B|^2\right) \\ &\quad +4\Im\left[G\left(\overline{A}+\overline{B}\right)\right]\left(A'\overline{A}+A\overline{A}'-B'\overline{B}-B\overline{B}'\right)\Big\}.\end{aligned} \tag{A.13}$$

We now put $z=0$ and use eqs. (A.4) and (A.5) to reduce the expression to:

$$\begin{aligned}\partial_z\omega_0 =& \frac{-4}{(|A_0|^2-|B_0|^2)^2}\times \\ &\times\Big\{ -4\Im\left[G_0'\left(A_0+B_0\right)-G_0\left(A_0'+B_0'\right)\right]\left(|A_0|^2-|B_0|^2\right) \\ &\quad +4\Im\left[G_0(A_0+B_0)\right]\left(A_0'A_0-A_0A_0'-B_0'B_0+B_0B_0'\right)\Big\}.\end{aligned} \tag{A.14}$$

The second line vanishes, and we now just have to verify that

$$Q\equiv\Im\left[G_0'\left(A_0+B_0\right)-G_0\left(A_0'+B_0'\right)\right]=0. \tag{A.15}$$

To do that, let us use (A.10), we get

$$Q=\Im\left[\left(G_r'+iG_i'\right)\left(A_0+B_0\right)-\left(G_r+iG_i\right)\left(A_0'+B_0'\right)\right]. \tag{A.16}$$

Since we know that $A_0, B_0\in\mathbb{R}$ and $A_0', B_0'\in\mathbb{I}$,

$$Q=G_i'(A_0+B_0)-G_r(A_0'+B_0'), \tag{A.17}$$

which we will have to brute force our way through.

The easiest way is to notice that

$$\frac{G_i'}{A_0'+B_0'}=m, \tag{A.18}$$

then divide (A.17) by $(A_0'+B_0')$ and show that $m(A_0+B_0)-G_r=0$ by looking individually at the factors for R^2, r^2, Rr, R and r, which are all 0. Also, there is no independent term.

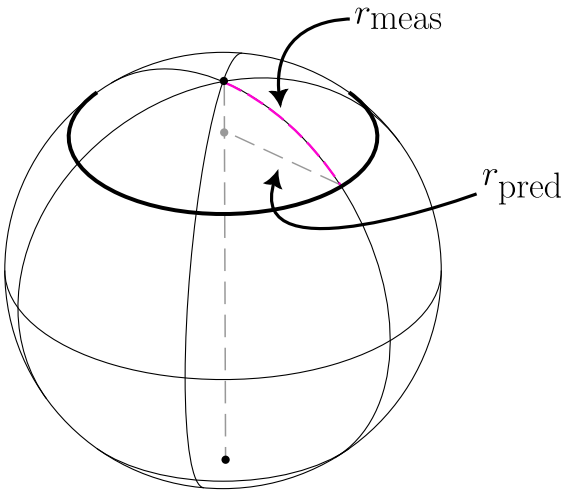


Figure A.1: Gertrude the ant measures the circumference C of the circle defined by the thick black lines, then measures the curved radius r_{meas}. She finds out that $C < 2\pi r_{\text{meas}}$.

Thus we find that $Q = 0$, which means that $\partial_z \omega_0 = 0$ and the derivatives in (A.2) are all identically 0, which trivially verifies the equation (A.1) for all $\rho > 0, z = 0$.

A.2 Sphere area on Earth doesn't hold

Let us first take an introducing example [119] in the following situation: Gertrude the ant loves geometry and wishes to make a circle and to measure its circumference. The circle Gertrude makes is shown in Fig. A.1. Measuring the radius (r_{meas}) and the circumference (C), Gertrude would soon discover that $C < 2\pi r_{\text{meas}}$. Of course, in our Figure it is obvious: $r_{\text{meas}} > r_{\text{pred}}$. Nevertheless, Gertrude would then be able to define an *excess radius* as follows:

$$r_{\text{excess}} \equiv r_{\text{meas}} - r_{\text{pred}} = r_{\text{meas}} - \frac{C}{2\pi}. \tag{A.19}$$

Until now, even if we have departed from Euclidean geometry, we have only curved a two dimensional surface and plunged it in three dimensions: this is quite easily picturable, even when projected on another 2D plane, namely this sheet of paper.

Let us now jump to the next level of geometrical thinking, and consider the curvature of three-dimensional space. Logically enough, a three-dimensional hypersurface would then be bent and live in a four dimensional space, which is arguably a bit more difficult to imagine.

We can define the curvature of our three-dimensional world by an analogous method as the one used above. We are going to measure the surface area of a sphere, for example, by laying out a finely gridded rectangular grid on its surface and adding up all the bits of area.

According to Euclidean geometry, the surface A we measure should correspond to a radius r_{pred} such that

$$A = 4\pi r_{\text{pred}}^2. \tag{A.20}$$

Furthermore, we can measure the actual radius, r_{meas}, by digging a hole to the center of the sphere and measuring its depth. We can then define the difference in these radii r_{excess} in the same way as above, namely

$$r_{\text{excess}} \equiv= r_{\text{meas}} - r_{\text{pred}} = r_{\text{meas}} - \sqrt{\frac{A}{4\pi}}. \tag{A.21}$$

This is a measure of the average curvature of the space in which the sphere is living.

Let us apply this to a concrete example and determine if *our* space is curved. To simplify the problem, we will approximate Earth by its sister planet, that we will call Gallifrey, identical to Earth in all aspects except in the fact that it is perfectly spherical and perfectly homogeneous.

The measured radius, r_{meas}, is none other than the radial distance we have defined in section 2.2, where the metric is the interior Schwarzschild one, which gives

$$\begin{aligned} r_{\text{meas}} &= \int_0^{r_{\text{pred}}} \sqrt{g_{rr}}\, dr \\ &= \int_0^{r_{\text{pred}}} \frac{r_{\text{pred}}^{3/2}}{\sqrt{r_{\text{pred}}^3 - r_s r^2}}\, dr \\ &= \sqrt{\frac{r_{\text{pred}}^3}{r_s}} \arcsin\left(\sqrt{\frac{r_s}{r_{\text{pred}}}}\right) \end{aligned} \tag{A.22}$$

where r_s is the Schwarzschild radius.

Expanding the arcsin for $\sqrt{r_s/r_{\text{pred}}} \to 0$, we get the approximation that

$$\arcsin\left(\sqrt{\frac{r_s}{r_{\text{pred}}}}\right) \approx \sqrt{\frac{r_s}{r_{\text{pred}}}} + \frac{1}{6}\left(\frac{r_s}{r_{\text{pred}}}\right)^{3/2} + O\left(\left(\frac{r_s}{r_{\text{pred}}}\right)^{5/2}\right), \tag{A.23}$$

which gives, for our definition of r_{excess} and with $r_s = 2GM/c^2$:

$$\begin{aligned} r_{\text{excess}} &= r_{\text{meas}} - r_{\text{pred}} \\ &= \frac{1}{3}\frac{GM}{c^2}. \end{aligned} \tag{A.24}$$

Taking the mass to be $M = 5.972 \times 10^{24}$ kg, the speed of light $c = 2.998 \times 10^8\,\text{m}\,\text{s}^{-1}$ and Newton's universal gravitational constant $G = 6.674 \times 10^{-11}\text{m}^3\,\text{kg}^{-1}\,\text{s}^{-2}$, one finds that $r_{\text{excess}} \approx 1.478 \times 10^{-3}$ m. Then the measured radius of Gallifrey would exceed the predicted radius r_{pred} by approximately 1.478 millimetres.

Doing the same thing for the Sun ($M \approx 1.989 \times 10^{30}$kg), one finds that

$$r_{\text{excess}} \approx 0.492 \times 10^3\ \text{m} = 492\ \text{m}. \tag{A.25}$$

A.3 Stability of circular orbits from an effective potential

Consider an equation of motion written in terms of an effective potential,

$$\left(\frac{d\rho}{d\varphi}\right)^2 + V(\rho) = 0. \tag{A.26}$$

A circular orbit at $\rho = \rho_0$ corresponds to a trajectory with constant radius, so that

$$\frac{d\rho}{d\varphi} = 0. \tag{A.27}$$

Substituting this condition into the equation of motion yields the first requirement for the existence of a circular orbit,

$$V(\rho_0) = 0. \tag{A.28}$$

However, this condition alone is not sufficient. Differentiating the equation of motion with respect to φ gives

$$2\left(\frac{d\rho}{d\varphi}\right)\left(\frac{d^2\rho}{d\varphi^2}\right) + V'(\rho)\left(\frac{d\rho}{d\varphi}\right) = 0, \tag{A.29}$$

with the prime denoting the differentiation with respect to ρ. In general, consistency requires

$$V'(\rho_0) = 0. \tag{A.30}$$

Therefore, a circular orbit at $\rho = \rho_0$ exists if and only if

$$V(\rho_0) = 0, \qquad V'(\rho_0) = 0. \tag{A.31}$$

To study the stability of such an orbit, we consider a small perturbation around the circular solution,

$$\rho(\varphi) = \rho_0 + \delta\rho(\varphi), \qquad |\delta\rho| \ll 1. \tag{A.32}$$

Expanding the effective potential in a Taylor series around ρ_0 gives

$$V(\rho) = V(\rho_0) + V'(\rho_0)\,\delta\rho + \frac{1}{2}V''(\rho_0)\,(\delta\rho)^2 + \mathcal{O}((\delta\rho)^3). \tag{A.33}$$

Using the circular orbit conditions $V(\rho_0) = 0$ and $V'(\rho_0) = 0$, the equation of motion reduces at leading order to

$$\left(\frac{d\,\delta\rho}{d\varphi}\right)^2 + \frac{1}{2}V''(\rho_0)\,(\delta\rho)^2 = 0. \tag{A.34}$$

Differentiating once more with respect to φ, we obtain the linearised equation

$$\frac{d^2\,\delta\rho}{d\varphi^2} + \frac{1}{2}V''(\rho_0)\,\delta\rho = 0. \tag{A.35}$$

The nature of the solutions depends on the sign of $V''(\rho_0)$:

- ✿ If $V''(\rho_0) > 0$, the solutions are oscillatory and the perturbation remains bounded. The circular orbit is therefore *stable*.
- ✿ If $V''(\rho_0) < 0$, the solutions grow exponentially and the perturbation increases without bound. The circular orbit is therefore *unstable*.

✿ If $V''(\rho_0) = 0$, the orbit is marginally stable and higher-order terms in the expansion of $V(\rho)$ around ρ_0 must be considered.

In summary, a circular orbit at $\rho = \rho_0$ is stable if and only if the effective potential has a local minimum at that point,

$$V(\rho_0) = 0, \qquad V'(\rho_0) = 0, \qquad V''(\rho_0) > 0. \tag{A.36}$$

A.4 Integrals for the proper radius

In this section, we show that the last term of eq. (3.3) can be integrated with the help of the incomplete elliptic integral of the second kind E in Jacobi's integral form:

$$E(x;\kappa) = \int_0^x \frac{\sqrt{1-\kappa^2 t^2}}{\sqrt{1-t^2}} dt. \tag{A.37}$$

Let us first consider the term R/r. On the equatorial plane,

$$R = \sqrt{\rho^2 + \alpha_+^2} \qquad \text{and} \qquad r = \sqrt{\rho^2 + \alpha_-^2}, \tag{A.38}$$

where the $\alpha_\pm$ are positive and non zero from our choice of parameters ν and k. We can then rewrite the integral as

$$I = \int_0^\rho \frac{R}{r} d\rho' = \int_0^\rho \frac{\sqrt{\rho'^2 + \alpha_+^2}}{\sqrt{\rho'^2 + \alpha_-^2}} d\rho' = \int_0^\rho \frac{\alpha_+}{\alpha_-} \frac{\sqrt{1 + \frac{\rho'^2}{\alpha_+^2}}}{\sqrt{1 + \frac{\rho'^2}{\alpha_-^2}}} d\rho'. \tag{A.39}$$

The change of variable $t \equiv i\rho'/\alpha_-$ leads to $d\rho' = -i\alpha_- dt$ and allows us to rewrite I as

$$I = \int_0^{\frac{i\rho}{\alpha_-}} -i\alpha_+ \frac{\sqrt{1 - \frac{\alpha_-^2 t^2}{\alpha_+^2}}}{\sqrt{1-t^2}} dt, \tag{A.40}$$

where we recognise Jacobi's algebraic form of the incomplete integral of the second kind $E(x;\kappa)$ with $x = i\rho/\alpha_-$ and $\kappa = \alpha_-/\alpha_+$, multiplied by an overall factor $(-i\alpha_+)$.

The same procedure can be followed for the term r/R in eq. (3.3), with this time as variable change $t \equiv i\rho'/\alpha_+$.

APPENDIX B
A DETOUR IN CAUSALITY

> "The only thing that makes life possible is permanent, intolerable uncertainty: not knowing what comes next."
>
> —— Ursula K. Le Guin *The Left Hand of Darkness* (1969)

This appendix explores two tangentially related but intriguing questions that emerged during our study of the gravimagnetic dipole:

- ✿ Can classical physics survive the "grandfather paradox" in spacetimes with Closed Timelie Curves (CTCs)? Whilst not strictly related to the subject of this thesis, I stumbled upon the question and found it interesting, at least to get some insight into what has been attempted to solve the possible paradoxes.
- ✿ Having pathological regions in spacetimes is not always a real issue (for example, the achronal region in the Kerr black hole spacetime is hidden behind the inner horizon). Is there any kind of mechanism saving us in the context of the gravimagnetic dipole spacetime?

While these topics stray from our main focus on rotation curves, they offer valuable insights for readers interested in the broader implications of CTCs in rotating spacetimes.

B.1 Some classical physics and causality

This section is heavily inspired from [64] and [120].

Consider now only classical physics in this context. Can the laws of classical physics hold in the presence of closed timelike curves? The primary concern is the preservation of causality. Specifically, if an observer can travel to the past, they might theoretically alter it: would this inevitably lead to causality violations?

Surprisingly, the answer is not always affirmative. Enter the principle of self-consistency [63, 64] (later colloquially known as *Novikov's principle*), which states [62]:

> *The only solutions to the laws of physics that can occur locally in the real Universe are those which are globally self-consistent*.

This principle does not forbid time travel to the past; rather, it forbids changing the past in a way that is not consistent with the future. To unpack this, consider the following:

On an open timelike curve γ, any event x divides the curve into two distinct regions: the future and the past of x. However, if the curve is closed, this global division vanishes. While the future remains a consequence of the past, the past also becomes a consequence of the future. Thus, all events on a CTC must be self-consistent: they must influence each other in a mutually adjusted manner.

For a concrete example, consider the billiard ball(s) problem [62] (for mathematical details, see [121, 122]). A perfectly elastic, solid ball moves at non-relativistic speeds near the mouths of a wormhole. The ball enters the wormhole through mouth B, emerges from mouth A in the past, and may collide with its past self.

The paradox is depicted in Fig. B.1a and unfolds as follows [62, 64]:

1. The ball is initially set on trajectory γ_1 toward mouth B.
2. It exits mouth A on trajectory γ_2 and collides with its past self at point C.

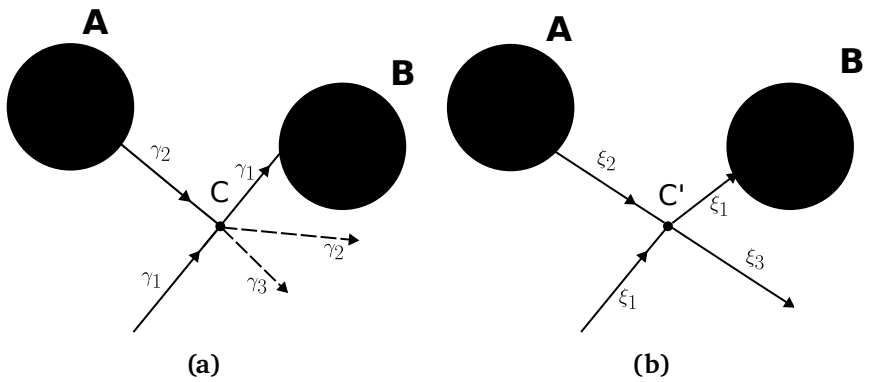


Figure B.1: On the left panel, the paradox of the billiard ball problem is shown: the initial conditions on the ball are such that it moves towards mouth B by following the trajectory γ_1, and exits mouth A on the trajectory γ_2. But as it exits, it hits past-ball at point C, kicking it out on a new trajectory γ_3, which does not enter mouth B. This series of events is inconsistent, and thus impossible. On the right panel a self consistent solution is shown: the trajectory ξ_1 is due to the same initial conditions as γ_1 and is thus the same until point C, where it is hit by future-ball (moving along a trajectory ξ_2 different from γ_2); ξ_1 diverges from γ_1, enters the mouth B, comes out on trajectory ξ_2 and all is well: this event is self-consistent.

3. The collision knocks the past ball onto a new trajectory, γ_3, preventing it from entering mouth B.

This sequence is inconsistent and thus impossible. The root of the paradox is clear: if the ball never enters mouth B, it cannot emerge from mouth A to collide with itself. The resolution lies in accounting for the influence of the future on the past before the ball reaches the wormhole.

It can be shown [121] that for the same initial conditions which give self-inconsistent solutions (like in this first situation), there also exists self-consistent solutions. In Fig. B.1b, such a self consistent solution is shown: the trajectory ξ_1 is due to the same initial conditions as γ_1 in Fig. B.1a and is thus the same until point C, where it is hit by future-ball (moving along a trajectory ξ_2, distinct from γ_2); ξ_1 diverges from γ_1, enters mouth B, comes out on trajectory ξ_2 and all is well: this event is self-consistent.

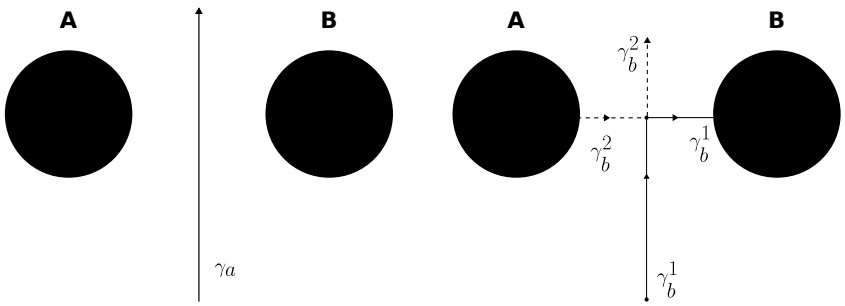


Figure B.2: In the left panel, the trivial solution: the particle follows the trajectory γ_a and passes between the mouths, unaffected. In the right panel, the particle has the same initial and final conditions but passes through the mouths once. Even more solutions can be found that satisfy the initial (and final) condition(s).

Mathematically, constructing such solutions reduces to solving a highly nonlinear system of algebraic equations. For an ideal elastic ball, a solution exists for any initial condition [121]. For an inelastic ball, the number of solutions depends on the initial conditions: there may be infinitely many or only one [122]. Examples are shown in Fig. B.2.

A deeper connection to fundamental physics emerges in [123, 124]. The authors demonstrate that, for the billiard ball(s) problem, the principle of self-consistency directly follows from the principle of least action, provided that the initial and final conditions are fixed. The authors then conjecture that the self-consistency principle follows from the principle of least action in the general case *for all physical phenomena*.

Further support for this conjecture comes from [125], where it is shown that for relativistic point-like billiard balls, the only trajectories for which the action is extremal are those that are self-consistent. More recent work [126] confirms that any set of initial conditions admits one or more self-consistent solutions. However, for one set of initial conditions with multiple self-consistent solutions, the evolution of the system fails to be deterministic, and classical physics do not determine which of the different evolutions would be realized.

Whilst the principle of self-consistency resolves apparent paradoxes in classical physics with CTCs, it raises profound questions about determin-

ism. The breakdown of determinism for certain initial conditions [126] suggests that classical physics alone may be insufficient to fully describe such spacetimes. This limitation echoes broader challenges in reconciling General Relativity with quantum mechanics, where CTCs also pose unresolved issues (e.g., in quantum field theory on curved spacetimes [67]). Future work could explore whether quantum effects restore determinism or introduce new constraints on self-consistent solutions.

B.2 Can particles reach the chronology boundary in the equatorial plane of the gravimagnetic dipole spacetime?

As was said in Chapter 1, closed timelike curves and the subsequent achronal regions are a known pathology of many a spacetime. A possible solution ot this issue is simply to *not enter* the pathological region. In the following, we will look at the possibility for particles to actually reach the achronal region.

Let us first take a look at what has already been done on the subject. In the Kerr black hole spacetime [94, 127] (so $a < M$) for example, the first closed timelike curve, *i.e.* the curve where $g_{\varphi\varphi} = 0$, is in the region hidden behind the inner horizon; thus an observer falling into the black hole could fall into it, but would not be able to come back and speak about it.

In the Kerr naked singularity [94, 128] ($a > M$), the horizon is not there any more to hide causality violation from far observers. However, causality violation is constrained by the existence of (radial) potential barriers: notably, a certain class of orbits, called boreal orbits (*i.e.* non-equatorial geodesics confined to $\theta = \text{cst}$) are entirely prevented from reaching the problematic region—for either massive particles [128] or, as was determined much later, massless particles [94].

More recently, a similar study [129] was performed in the Bonnor spacetime [56]. It shows that particles sent from a fixed space point with a positive value of the angular momentum are repelled and scattered back when they approach the CTC boundary, thus never reaching it. However, particles with a negative value of the angular momentum can reach the pathological region under certain conditions.

Finally, in the Kerr-Newman spacetime, either in the naked singularity or in the black hole, the singularity is concealed by a causality violating region. For neutral particles and particles with an identical charge to the source, only positive angular momentum particles are permitted to go through the closed timelike curves [60]. However, for particles with the opposite charge to the source, all particles, regardless of their angular momentum, can go through the closed timelike curves.

Notice that when comparing the Bonnor cylinder and the Kerr-Newman spacetime, it is particles with opposite values of the angular momentum that are allowed to go through the CTC boundary.

For the gravimagnetic dipole spacetime, we are going to follow the same idea; using the rescaled potential energy defined in Section 2.4.3 of Chapter 2, and particularising it to massless particles on geodesics on the equatorial plane outside the ergoregion, we are going to obtain, for every value of the impact parameter b, the region of space that is allowed for that particle to travel through.

Recall the rescaled potential energy V from eq. (2.48), which looks like this:

$$V = g_{tt}(b - b_+)(b - b_-) \geq 0, \tag{B.1}$$

and should be either positive or zero to satisfy the Hamiltonian constraint. Since we are restricting ourselves to the equatorial plane, the ergoregion is reduced to the singular point $\rho = 0$, which we will ignore, and the impact parameter needs to be in the interval (2.54)

$$b \in [b_-, b_+], \tag{B.2}$$

with $b_\pm$ defined as

$$b_\pm = \omega \pm \frac{\rho}{f}, \tag{B.3}$$

which we have previously called, in this context, the effective impact parameter potentials.

In the following, we chose four different values of the NUT parameter ν, because of their representativeness in terms of photons: $\nu = 0.1$ allows for four photon orbits—two prograde and two retrograde; $\nu = 0.5$ only two retrograde ones; $\nu = 0.79$ only one retrograde and degenerate orbit; and $\nu = 0.9$ none.

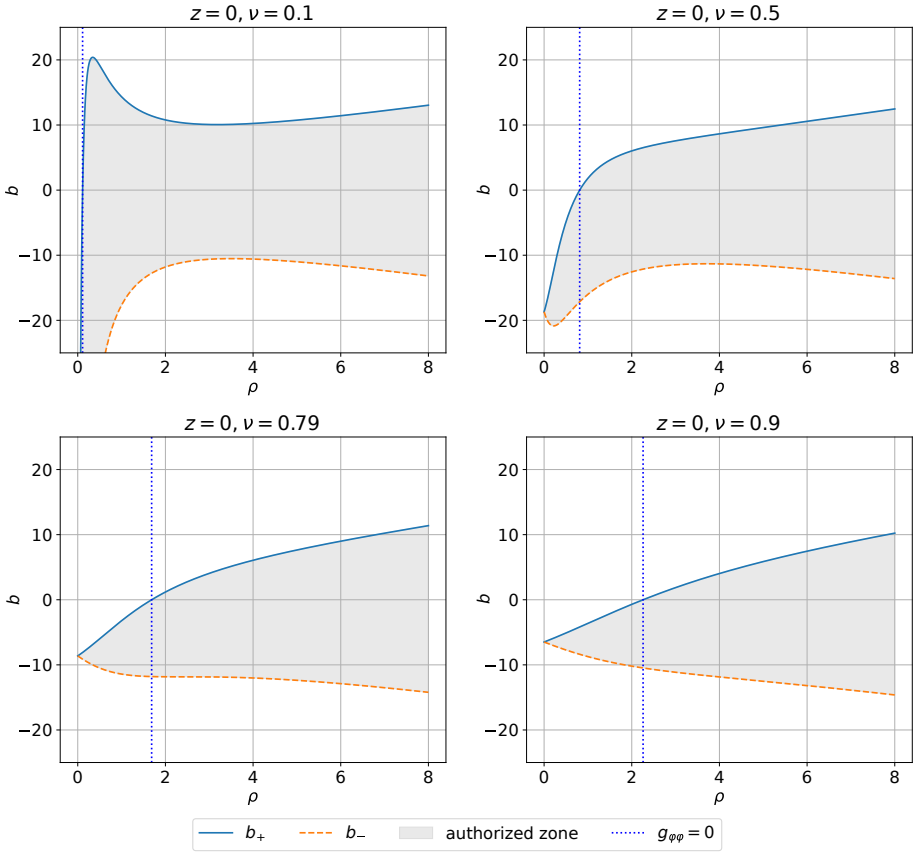


Figure B.3: For four different values of the NUT parameter ν (0.1, 0.5, 0.79 and 0.9), the plain blue (respectively dashed range) line represents the critical impact parameter b_+ (resp. b_-) for a photon in the equatorial plane $z = 0$, as a function of ρ. Since we are located outside the ergoregion, a photon must have an impact parameter within the greyed-out area to be allowed at a given point in space characterised by the ρ coordinate. The dotted bright blue vertical line corresponds to the CTC boundary. The impact parameter of a photon arriving from infinity along a geodesic remains constant. Thus, the corresponding horizontal line indicates the regions of space it can access. When this line intersects either b_+ or b_-, the photon "bounces back" and goes back to radial infinity. Additionally, confinement phenomena occur when two two photon orbits (*i.e.* extrema of $b_\pm$) exist in the same direction—this is the case only in the graphs of the first row.

In Fig. B.3, the four panels show the values of the critical impact parameters b_+ (plain blue) and b_- (dashed orange) for a photon in the equatorial plane, as a function of the radius ρ, with each panel corresponding to different value of ν. The greyed out area represents the "allowed region" for the photon, according to eq. (B.2). The vertical dotted bright blue line represents the chronology boundary.

Let us now examine the behaviour a photon arriving from infinity along its geodesic. Its impact parameter, denoted b_*, is a constant of motion; thus, the photon's trajectory in the graph follows a horizontal line, constrained to the greyed-out region. For example, let us consider, in a spacetime with $\nu = 0.5$ (upper right panel), a photon with impact parameter $b_* = 1$. Approaching from infinity, it can move towards the centre of our spacetime until $\rho \approx 1$, where it meets the b_+ curve and cannot proceed further.

On the graph, the photon is reflected and returns to infinity. In reality, the φ coordinate is not constant, and generally, the photon is simply deflected, $\rho \approx 1$ representing its closest approach radius.

As shown in the graphs, regardless of the value of ν, if $b_* > 0$, the photon "bounces back" before reaching the chronology boundary. If $b_* = 0$, the photon just reaches the chronology boundary but cannot cross it. So, in general, a photon with positive or zero angular momentum cannot access the achronal region.

Conversely, photons with negative b_* (*i.e.* , negative angular momentum) can cross the CTC boundary. However, for $\nu \leq 0.79$, this requires $b_* > \max(b_-)$ (if $b_* = b_-$, the photon will follow the retrograde circular orbit once it arrives at the corresponding value of ρ). For $\nu \geq 0.79$, the condition becomes $b_* > b_-(\rho = -f\omega)$, as it is where the CTC boundary and b_- intersect.

Another notable feature of these graphs is that, as expected, the extrema of $b_\pm$ curves correspond to circular photon orbits. In the top left panel, b_+ exhibits two extrema, as does b_- (though its minimum lies out of frame). The sequence of these extrema create "pockets" of allowed regions where photons with specific values of b are permitted, but confined. For example, for $\nu = 0.1$, a photon with $b_* = 11$ can live in two regions; it may either come in from infinity, bounce back at $\rho \approx 4$, and go back to infinity; or it can live in the confinement region $\rho \in [0.2, 2.8]$—without ever going through the CTC boundary.

Finally, notice that exactly one value of the impact parameter— $b_* = b_+ = b_- = \omega$ —allows the photon to reach the singularity. However, this singularity is always hidden behind the achronal region.

For completeness, it would be interesting to extend this analysis to massive particles. The next step would then be to generalize for non-equatorial particles. This could be achieved in two ways; either by following the same procedure whilst accounting for both directions of movement—which would require a 3D representation of admissible intervals, combining the approach of this section with that of Chapter 4, or to adopt an entirely different method, such as integrating along geodesics or plotting the potential as a function (ρ, z) directly.

To conclude this section, we have demonstrated that for massless particles with positive or zero angular momentum arriving from radial infinity, the conservation of their impact parameter, and the constraint on the rescaled potential energy prevents them from crossing the CTC boundary. For values of ν where two prograde photon orbits exist, a confinement region appears near the CTC boundary, though it dos not permit traversal. For negative angular momentum, the situation is more complex: when two retrograde photon orbits exist, photons with $b_* > \max(b_-)$ can arrive from radial infinity and cross the CTC boundary. Photons with $b_* < b_-$ may either remain in a confinement region (oscillating in and out of the CTC region) or arrive from radial infinity and bounce back. When there are zero or one retrograde photon orbit, the confinement phenomenon disappears.

Whilst particles with positive or zero angular momentum are shielded from chronology violations, issues persist for those with negative angular momentum.

It is worth recalling that the gravimagnetic dipole is a highly theoretical model. A more refined—and thus more complex—model could be developed, for example, by adding matter in the equatorial plane—since we have observed stable circular orbits for massive particles (see Sections 3.6 and 3.7). This could mitigate the issue by either reducing the size of the CTC region or by altering the effective impact parameter potentials in such a way that particles coming from radial infinity would not be able to reach the CTC boundary any more.

Alternatively, another mechanism, yet to be determined, might resolve this. For instance, in the Bonnor cylinder spacetime, particles on geodesic trajectories with certain values of negative angular momentum can cross

the CTC boundary [129]. However, when a friction force—due to the interaction with the back ground fluid (recall that the Bonnor spacetime consists of a rigidly rotating cylinder of dust)—is introduced, the study of non-geodesic motion shows that test particles are slowed down sufficiently to avoid entering the pathological region.

APPENDIX C

ELECTROMAGNETIC KNOTS AND MODMAX

> "We must be willing to get rid of the life we've planned, so as to have the life that is waiting for us."
>
> — attributed to Joseph Campbell (1904 – 1987)

As was noted in the main Introduction, the original subject of my PhD thesis arose from the study of null electromagnetic knot solutions, and the possibility of translating their structure to General Relativity. The main goal was to study particle trajectories—and the velocity rotation curves of circular trajectories—when plunged within such solutions. However, a paper published in 2022 demonstrated that particles in an electromagnetic knot would be rapidly ejected [118], making the study of velocity rotation curves rather impractical. Whilst we abandoned this research avenue, some preliminary work had already been completed and deserves to be included in this thesis. Moreover, several years later, I remain captivated by the elegance of these solutions and the connections they reveal between different domains of physics.

A word of warning first: this thesis being already quite long, we are not going to go into the details of the subject, but rather provide a (very) short heuristic explanation with relevant references for the interested reader.

In Section C.1, we explain what the electromagnetic knots are and their emergence from different mathematical formulations of the theory of electrodynamics. We identified the first step to find analogous solutions in General Relativity as trying to generalise the knots to a non-linear extension of Maxwell's electrodynamics theory; this is described in section C.2.

C.1 Electromagnetic knots: non trivial vacuum solutions and the topological nature of electromagnetism

Despite the inherent linearity of Maxwell's equations, they admit topologically non trivial solutions known as electromagnetic knots [130, 131]. These solutions are such that their electric and magnetic field lines are closed and linked together in torus-like shapes. A particularly interesting subclass consists of null electromagnetic knots, where the electric and magnetic fields maintain equal magnitudes and remain orthogonal to each other throughout space.

Whilst these structures exhibit time-dependent properties (for example, their energy density tends to "spread out" as time passes, after a first contracting moment), their total energy, angular momentum, *etc.*, are constant over time. The same can be said for their topological invariants, especially their winding numbers which quantify their "knottedness".

Among these null knots, we focused on the hopfions—also called Hopf-Rañada knots [130–140], where the winding number is equal to one; each field line (electric or magnetic) is closed and goes through all the other closed field lines exactly once. The first construction—and thus the discovery—of the hopfion was done using the topological formulation of electrodynamics, specifically as a self-dual doublet of Hopf fibrations of the three-sphere (one for the electric field, one for the magnetic field). It was shown afterwards that this configuration can be described by Bateman's construction [141], which uses a pair of self-dual complex scalar potentials. This second formulation has two key advantages: (i)

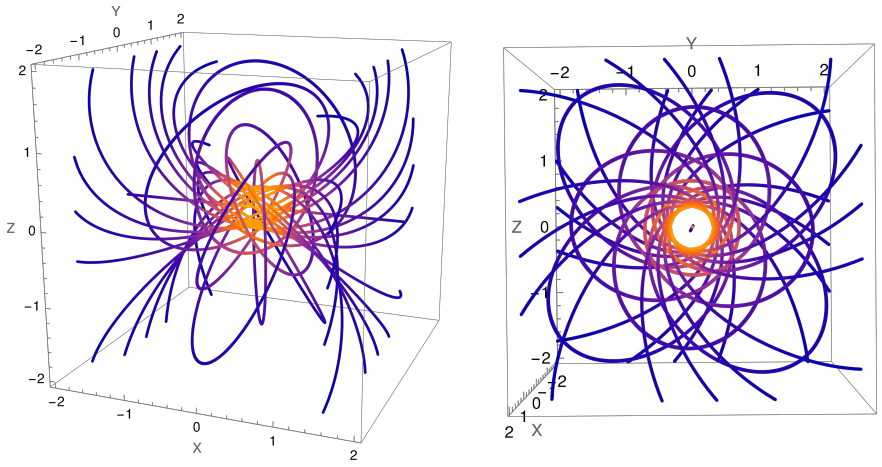


Figure C.1: Electric field lines of a hopfion in Maxwell Linear Electrodynamics, shown from two different perspectives. Each field line is closed (some extending beyond the frame) and links with every other line exactly once.

the scalar potentials are easier to manipulate than vector fields, and (ii) biholomorphic functions of these potentials automatically generate families of knots [142].

Finally, the hopfion can also be constructed by applying a sequence of symmetry-preserving transformations to a static and homogeneous null solution of Maxwell's equations: a conformal inversion followed by a pure imaginary time translation (see Fig. C.1 for an example). The existence of knots is thus closely linked to all the symmetries of Maxwell's equations, namely spacetime conformal covariance and continuous duality invariance between the electric and magnetic fields.

Recent experimental work has demonstrated the physical realization of these knotted structures, at least in water [143, 144], with potential advances in electromagnetic wave manipulation [142].

C.2 ModMax

The first step in generalising Maxwell Linear Electrodynamics (hereafter, MLE) to General Relativity involved extending knot solutions to a non-linear modification of Maxwell's theory. While several nonlinear generalisations of MLE exist, only one—the *Mod*ified *Max*well theory

(ModMax) [145–147]—represents a continuous deformation of MLE that preserves all its symmetries, *i.e.* Poincaré invariance, continuous duality transformations, and conformal symmetry. There actually exists another non-linear extension that preserves all the symmetries of MLE, nicknamed the Bialynicky-Birula electrodynamics, but it is *not* a continuous deformation of MLE [145].

ModMax theory introduces a parameter $\gamma \geq 0$, which recovers MLE when $\gamma = 0$. Within this framework, we were able to demonstrate in our paper [1] that electromagnetic knots persist as solutions, albeit with an interesting subtlety. For $\gamma \neq 0$, an additional discrete parameter $\delta = \pm 1$ emerges, appearing in the solutions as $e^{\gamma\delta}$, thereby producing two distinct knot solutions that coalesce back together when $\gamma = 0$, thus corresponding to the initial MLE solution. The parameter δ arises from the non-analyticity of the Lagrangian for null electromagnetic fields; it actually makes the electromagnetic field non-null (again, this deforms back to a null electromagnetic field when $\gamma = 0$).

Finally, despite this modification and the introduction of the δ parameter, the fundamental properties of knots are preserved, particularly their topological stability and non-trivial structure.

BIBLIOGRAPHY

[1] C. Dassy and J. Govaerts, "Deformed Hopfion-Rañada knots in ModMax electrodynamics", *J. Phys. A*, vol. 54, no. 26, pp. 265201, 2021.

[2] C. Dassy and J. Govaerts, "Velocity rotation curves in the equal mass and net null NUT charge gravimagnetic dipole spacetime", *Class. Quant. Grav.*, vol. 43, no. 3, pp. 035005, 2026.

[3] C. Dassy and J. Govaerts, "Light deflection in the gravimagnetic dipole spacetime", *Journal of Physics: Conference Series*, vol. 3177, no. 1, pp. 012013, February 2026.

[4] C. Dassy and J. Govaerts, "Integrating numerically a conservative hamiltonian dynamics: A two-step iterative process", Unpublished, 2023.

[5] R. Davis, M. Hatch, S. Hoare, S. G. Lewis, C. Lucas, S. A. Parfitt, S. M. Bello, M. Lewis, J. Mansfield, J. Najorka, S. O'Connor, S. Peglar, A. Sorensen, C. Stringer, and N. Ashton, "Earliest evidence of making fire", *Nature*, vol. 649, pp. 631–637, January 2026.

[6] BBC News, "The moment the earliest known human-made fire was uncovered", `https://www.bbc.co.uk/news/resources/idt-b9da7a6d-165b-492a-8785-235cd10e2e8e`, December 2025, Accessed: 2025-12-18.

[7] T. S. Kuhn, *The structure of scientific revolutions*, University of Chicago Press, Chicago, 1962.

[8] A. A. Michelson and E. W. Morley, "On the relative motion of the Earth and the luminiferous ether", *American Journal of Science*, vol. s3-34, no. 203, pp. 333–345, nov 1 1887.

[9] F. Hoyle, "A new model for the expanding universe", *Monthly Notices of the Royal Astronomical Society*, vol. 108, no. 5, pp. 372–382, 10 1948.

[10] U. Le Verrier, "Sur la théorie de mercure et sur le mouvement du périhélie de cette planète", *Comptes rendus hebdomadaires des séances de l'Académie des sciences*, vol. 49, pp. 379–383, 1859.

[11] Hippocrates, *On the Nature of Man*, Loeb Classical Library. Harvard University Press, Cambridge, MA, c. 400 BC.

[12] L. Pasteur, "Mémoire sur les corpuscules organisés qui existent dans l'atmosphère", *Annales de chimie et de physique*, vol. 64, pp. 5–110, 1861.

[13] S. H. Greenblatt, "Phrenology in the science and culture of the 19th century", *Neurosurgery*, vol. 37, no. 4, pp. 00006123–199510000–00025, 1995.

[14] M. W. Rossiter, "The Matthew Matilda effect in science", *Social Studies of Science*, vol. 23, no. 2, pp. 325–341, 1993.

[15] G. Rippon, *The Gendered Brain: The New Neuroscience That Shatters the Myth of the Female Brain*, Bodley Head, London, 2019.

[16] V. C. Rubin, W. K. Ford, and N. Thonnard, "Rotational Properties of 21 Sc Galaxies with a Large Range of Luminosities and Radii, from NGC 4605 (R=4 kpc) to UGC 2885 (R=122 kpc)", *The Astrophysical Journal*, vol. 238, pp. 471–487, June 1980.

[17] J. Bovy, *Dynamics and Astrophysics of Galaxies*, Princeton University Press, Princeton, NJ, 2026.

[18] F. Lelli, S. S. McGaugh, and J. M. Schombert, "SPARC: Mass Models for 175 Disk Galaxies with Spitzer Photometry and Accurate Rotation Curves", *The Astronomical Journal*, vol. 152, no. 6, pp. 157, December 2016.

[19] Particle Data Group, "Review of particle physics: Dark matter", *Progress of Theoretical and Experimental Physics*, vol. 2024, pp. 083C01, 2024.

[20] B. Famaey and St. S. McGaugh, "Modified Newtonian Dynamics (MOND): Observational Phenomenology and Relativistic Extensions", *Living Reviews in Relativity*, vol. 15, pp. 10, 2012.

[21] A. Einstein, "Die feldgleichungen der gravitation", *Sitzungsberichte der Preussischen Akademie der Wissenschaften zu Berlin*, pp. 844–847, 1915, Retrieved 2017-08-21.

[22] K. Schwarzschild, "On the gravitational field of a mass point according to Einstein's theory", *Sitzungsber. Preuss. Akad. Wiss. Berlin (Math. Phys.)*, vol. 1916, pp. 189–196, 1916.

[23] A. Einstein, "On a stationary system with spherical symmetry consisting of many gravitating masses", *Annals of Mathematics*, vol. 40, no. 4, pp. 922–936, 1939.

[24] M. Bartusiak, *Black Hole: How an idea abandoned by Newtonians, hated by Einstein, and gambled on by Hawking became loved*, Yale University Press, New Haven, CT, 2016.

[25] A. Ewing, "Black Holes in space", *Science News Letter*, vol. 85, no. 3, 1964.

[26] T. Siegfried, "50 years later, it's hard to say who named black holes", `https://www.sciencenews.org/blog/context/50-years-later-its-hard-say-who-named-black-holes`, 2013.

[27] H. Reissner, "Über die eigengravitation des elektrischen feldes nach der Einsteinschen theorie", *Annalen der Physik*, vol. 355, no. 9, pp. 106–120, 1916.

[28] G. Nordström, "On the energy of the gravitation field in Einstein's theory", *Koninklijke Nederlandse Akademie van Wetenschappen Proceedings Series B Physical Sciences*, vol. 20, pp. 1238–1245, January 1918.

[29] R. P. Kerr, "Gravitational field of a spinning mass as an example of algebraically special metrics", *Phys. Rev. Lett.*, vol. 11, no. 5, pp. 237–238, September 1963.

[30] E. T. Newman, E. Couch, K. Chinnapared, A. Exton, A. Prakash, and R. Torrence, "Metric of a rotating, charged mass", *Journal of Mathematical Physics*, vol. 6, no. 6, pp. 918–919, June 1965.

[31] E. T. Newman, L. A. Tamburino, and T. W. J. Unti, "Empty-space generalization of the Schwarzschild metric", *Journal of Mathematical Physics*, vol. 4, no. 7, pp. 915–923, July 1963.

[32] R. P. Kerr, "Discovering the Kerr and Kerr–Schild metrics", in *The Kerr Spacetime: Rotating Black Holes in General Relativity*, D. Wiltshire, M. Visser, and S. Scott, Eds. Cambridge University Press, February 2009.

[33] C. W. Misner, "Relativity theory and astrophysics", in *Relativity Theory and Astrophysics*, J. Ehlers, Ed., vol. 1, p. 160. American Mathematical Society, Providence, Rhode Island, 1967.

[34] W. B. Bonnor, "A new interpretation of the NUT metric in general relativity", *Mathematical Proceedings of the Cambridge Philosophical Society*, vol. 66, no. 1, pp. 145–151, 1969.

[35] W. Israel, "Line sources in general relativity", *Phys. Rev. D*, vol. 15, no. 4, pp. 935–941, February 1977.

[36] V. S. Manko and E. Ruiz, "Physical interpretation of the NUT family of solutions", *Classical and Quantum Gravity*, vol. 22, no. 17, pp. 3555, August 2005.

[37] G. Clément, D. Gal'tsov, and M. Guenouche, "Rehabilitating spacetimes with NUTs", *Physics Letters B*, vol. 750, pp. 591–594, 2015.

[38] J. G. Miller, M. D. Kruskal, and B. B. Godfrey, "Taub-NUT (Newman, Unti, Tamburino) metric and incompatible extensions", *Phys. Rev. D*, vol. 4, no. 10, pp. 2945–2948, November 1971.

[39] V. S. Manko, E. D. Rodchenko, and E. Ruiz, "Formation of a Kerr black hole from two stringy NUT objects", *Moscow University Physics Bulletin*, vol. 64, pp. 359–361, 2009.

[40] G. Clément, "Rotating magnetized black diholes", *Phys. Rev. D*, vol. 98, no. 10, pp. 104003, November 2018.

[41] G. Clément, "Balanced magnetized double black holes", *Physics Letters B*, vol. 795, pp. 587–591, August 2019.

[42] G. Clément, "The gravimagnetic dipole", *Classical and Quantum Gravity*, vol. 38, no. 7, pp. 075003, 2021.

[43] Gérard Clément, "The gravimagnetic dipole", revised (2026), arXiv:2010.14473.

[44] T. Lewis, "Some special solutions of the equations of axially symmetric gravitational fields", *Proceedings of the Royal Society of London. Series A, Containing Papers of a Mathematical and Physical Character*, vol. 136, no. 829, pp. 176–192, May 1932.

[45] A. Papapetrou, "Champs gravitationnels stationnaires à symétrie axiale", *Annales de l'institut Henri Poincaré. Section A, Physique Théorique*, vol. 4, no. 2, pp. 83–105, 1966.

[46] H. Stephani, D. Kramer, M. MacCallum, C. Hoenselaers, and E. Herlt, *Exact Solutions of Einstein's Field Equations*, Cambridge Monographs on Mathematical Physics. Cambridge University Press, Cambridge, 2nd edition, 2003.

[47] Jerry B. Griffiths and Jiří Podolský, *Exact Space-Times in Einstein's General Relativity*, Cambridge Monographs on Mathematical Physics. Cambridge University Press, 2009.

[48] F. J. Ernst, "New formulation of the axially symmetric gravitational field problem", *Phys. Rev.*, vol. 167, no. 5, pp. 1175–1178, March 1968.

[49] N. R. Sibgatullin, *Oscillations and Waves: In Strong Gravitational and Electromagnetic Fields*, Theoretical and Mathematical Physics. Springer Berlin Heidelberg, 1991, English translation of the original Russian edition (1984).

[50] V. S. Manko and N. R. Sibgatullin, "Construction of exact solutions of the Einstein-Maxwell equations corresponding to a given behaviour of the Ernst potentials on the symmetry axis", *Classical and Quantum Gravity*, vol. 10, no. 7, pp. 1383, July 1993.

[51] G. Clément and D. Gal'tsov, "Stationary double black hole without naked ring singularity", *Classical and Quantum Gravity*, vol. 35, no. 21, pp. 214002, October 2018.

[52] S. Deser, Jackiw R., and G. 't Hooft, "Three-dimensional einstein gravity: Dynamics of flat space", *Annals of Physics*, vol. 152, no. 1, pp. 220–235, 1984.

[53] P. S. Letelier and S. R. de Oliveira, "Superposition of Weyl solutions: the equilibrium forces", *Classical and Quantum Gravity*, vol. 15, no. 2, pp. 421, February 1998.

[54] P. S. Letelier and S. R. de Oliveira, "Double kerr-nut spacetimes: spinning strings and spinning rods", *Physics Letters A*, vol. 238, no. 2, pp. 101–106, 1998.

[55] W. J. van Stockum, "The gravitational field of a distribution of particles rotating about an axis of symmetry", *Proceedings of the Royal Society of Edinburgh*, vol. 57, pp. 135–154, 1937.

[56] W. B. Bonnor, "The rigidly rotating relativistic dust cylinder", *Journal of Physics A: Mathematical and General*, vol. 13, no. 6, pp. 2121, June 1980.

[57] K. Gödel, "An example of a new type of cosmological solutions of Einstein's field equations of gravitation", *Rev. Mod. Phys.*, vol. 21, no. 3, pp. 447–450, July 1949.

[58] F. J. Tipler, "Rotating cylinders and the possibility of global causality violation", *Phys. Rev. D*, vol. 9, no. 8, pp. 2203–2206, April 1974.

[59] J. R. Gott, "Closed timelike curves produced by pairs of moving cosmic strings: Exact solutions", *Phys. Rev. Lett.*, vol. 66, no. 9, pp. 1126–1129, March 1991.

[60] A. Dutta, D. Roy, and S. Chakraborty, "On the role of closed timelike curves and confinement structure around Kerr-Newman singularity", *International Journal of Modern Physics D*, vol. 33, no. 2450034, pp. 2450034–114, July 2024.

[61] J.-P. Luminet, "Closed timelike curves, singularities and causality: A survey from Gödel to chronological protection", *Universe*, vol. 7, no. 1, pp. 12, 2021.

[62] J. Friedman, M. S. Morris, I. D. Novikov, F. Echeverria, G. Klinkhammer, K. S. Thorne, and U. Yurtsever, "Cauchy problem in spacetimes with closed timelike curves", *Phys. Rev. D*, vol. 42, no. 6, pp. 1915–1930, September 1990.

[63] I. D. Novikov, "Time machine and self-consistent evolution in problems with self-interaction", *Phys. Rev. D*, vol. 45, no. 6, pp. 1989–1994, March 1992.

[64] V. P. Frolov and I. D. Novikov, *Black Hole Physics: Basic Concepts and New Developments*, vol. 96 of *Fundamental Theories of Physics*, Springer, Dordrecht, 1998.

[65] B. Hensen, H. Bernien, A. E. Dréau, A. Reiserer, N. Kalb, M. S. Blok, J. Ruitenberg, R. F. L. Vermeulen, R. N. Schouten, C. Abellán, W. Amaya, V. Pruneri, M. W. Mitchell, M. Markham, D. J. Twitchen, D. Elkouss, S. Wehner, T. H. Taminiau, and R. Hanson, "Loophole-free Bell inequality violation using electron spins separated by 1.3 kilometres", *Nature*, vol. 526, pp. 682–686, 2015.

[66] S. Storz, J. Schär, A. Kulikov, P. Magnard, P. Kurpiers, J. Lütolf, T. Walter, A. Copetudo, K. Reuer, A. Akin, J.-C. Besse, M. Gabureac, G. J. Norris, A. Rosario, F. Martin, J. Martinez, W. Amaya, M. W. Mitchell, C. Abellán, J.-D. Bancal, N. Sangouard, B. Royer, A. Blais, and A. Wallraff, "Loophole-free Bell inequality violation with superconducting circuits", *Nature*, vol. 617, no. 7960, pp. 265–270, May 2023.

[67] D. Deutsch, "Quantum mechanics near closed timelike lines", *Phys. Rev. D*, vol. 44, no. 10, pp. 3197–3217, November 1991.

[68] M. Ringbauer, M. A. Broome, C. R. Myers, A. G. White, and T. C. Ralph, "Experimental simulation of closed timelike curves", *Nature Communications*, vol. 5, pp. 4145, June 2014.

[69] L. G. Bishop, F. Costa, and T. C. Ralph, "Time-traveling billiard-ball clocks: A quantum model", *Phys. Rev. A*, vol. 103, no. 4, pp. 042223, April 2021.

[70] B. S. Kay, M. J. Radzikowski, and R. M. Wald, "Quantum field theory on spacetimes with a compactly generated Cauchy horizon", *Communications in Mathematical Physics*, vol. 183, no. 3, pp. 533–556, February 1997.

[71] S. W. Hawking, "Chronology protection conjecture", *Phys. Rev. D*, vol. 46, no. 2, pp. 603–611, July 1992.

[72] S. W. Kim and K. S. Thorne, "Do vacuum fluctuations prevent the creation of closed timelike curves?", *Phys. Rev. D*, vol. 43, pp. 3929–3947, June 1991.

[73] M. Cvetic, G. W. Gibbons, H. Lu, and C. N. Pope, "Rotating black holes in gauged supergravities; thermodynamics, supersymmetric limits, topological solitons and time machines", 2005.

[74] M. Visser, "The Kerr spacetime: A brief introduction", 2008.

[75] C. W. Misner, K. S. Thorne, and J. A. Wheeler, *Gravitation*, W. H. Freeman, San Francisco, 1973.

[76] R. Gautreau and B. Hoffmann, "The Schwarzschild radial coordinate as a measure of proper distance", *Phys. Rev. D*, vol. 17, no. 10, pp. 2552–2555, May 1978.

[77] R. M. Wald, *General Relativity*, University of Chicago Press, Chicago, 1984.

[78] P. Fromholz, E. Poisson, and C. M. Will, "The Schwarzschild metric: It's the coordinates, stupid!", *American Journal of Physics*, vol. 82, pp. 295, 2014.

[79] E. Poisson and C. M. Will, *Gravity: Newtonian, Post-Newtonian, Relativistic*, Cambridge University Press, 2014.

[80] L. D. Landau and E. M. Lifshitz, *The Classical Theory of Fields: Volume 2 (Course of Theoretical Physics)*, Pergamon Press, 3rd edition, 1971.

[81] J. Govaerts, *Lectures Notes in Mathematical and Theoretical Physics: Hamiltonian Quantisation and Constrained Dynamics*, vol. 4 of *B*, Leuven University Press, 1991.

[82] J. Polchinski, *An Introduction to the Bosonic String*, vol. 1 of *String Theory*, Cambridge University Press, March 1998.

[83] L. D. Landau and E. M. Lifshitz, *Mechanics: Volume 1 (Course of Theoretical Physics)*, Butterworth-Heinemann, 3rd edition, 1976.

[84] N. Beisert and J. Brödel, "Lecture Notes from *Introduction to String Theory*", 2013.

[85] J. M. Bardeen, W. H. Press, and S. A. Teukolsky, "Rotating black holes: Locally nonrotating frames, energy extraction, and scalar synchrotron radiation", *Astrophysical Journal*, vol. 178, pp. 347–370, December 1972.

[86] V. Ferrari, L. Gualtieri, and P. Pani, *General Relativity and its Applications*, CRC Press, December 2020.

[87] T. Igata, "Deflection angle in the strong deflection limit and quasinormal modes in stationary axisymmetric spacetimes", 2025, arXiv:2505.01848.

[88] P. V. P. Cunha, J. Grover, C. Herdeiro, E. Radu, H. Rúnarsson, and A. Wittig, "Chaotic lensing around boson stars and Kerr black holes with scalar hair", *Phys. Rev. D*, vol. 94, no. 10, pp. 104023, November 2016.

[89] J. Govaerts, "The gravito-electromagnetic approximation to the gravimagnetic dipole and its velocity rotation curve", *Classical and Quantum Gravity*, vol. 40, no. 8, pp. 085010, March 2023.

[90] H. Hancock, *Elliptic Integrals*, Dover Publications, 1958, Unabridged republication of the original edition of 1917.

[91] M. Abramowitz and I. A. Stegun, *Handbook of Mathematical Functions with Formulas, Graphs, and Mathematical Tables*, Dover Publications, 1972, Tenth printing.

[92] Inc. Wolfram Research, *Wolfram Mathematica, Version 12.3*, Wolfram Research, Inc., Champaign, IL, 2021, Computer software.

[93] M. Patil, P. Mishra, and D. Narasimha, "Curious case of gravitational lensing by binary black holes: A tale of two photon spheres,

new relativistic images, and caustics", *Phys. Rev. D*, vol. 95, pp. 024026, January 2017.

[94] D. Bini and F. de Felice, "Chronology protection in the Kerr metric", *General Relativity and Gravitation*, vol. 47, no. 131, October 2015.

[95] J. D. Hunter, "Matplotlib: A 2D graphics environment", *Computing in Science & Engineering*, vol. 9, no. 3, pp. 90–95, 2007.

[96] Wikisource, "Translation: On the deflection of a light ray from its rectilinear motion", `https://en.wikisource.org/w/index.php?title=Translation:On_the_Deflection_of_a_Light_Ray_from_its_Rectilinear_Motion&oldid=10821714`, 2021.

[97] A. Einstein, "On the influence of gravitation on the propagation of light", in *The Collected Papers of Albert Einstein. Vol. 3: The Swiss Years: Writings, 1909–1911*, Anna Beck, Ed. Princeton University Press, Princeton, New Jersey, 1994, Translated from "Über den Einfluß der Schwerkraft auf die Ausbreitung des Lichtes", Annalen der Physik 35 (1911).

[98] F. W. Dyson, A. S. Eddington, and C. Davidson, "IX. A determination of the deflection of light by the sun's gravitational field, from observations made at the total eclipse of May 29, 1919", *Philosophical Transactions of the Royal Society of London, Series A: Containing Papers of a Mathematical or Physical Character*, vol. 220, no. 571-581, pp. 291–333, January 1920.

[99] R. Narayan and S. Wallington, "Introduction to basic concepts of gravitational lensing", in *Gravitational Lenses*, R. Kayser, T. Schramm, and L. Nieser, Eds., Berlin, Heidelberg, 1992, pp. 12–26, Springer Berlin Heidelberg.

[100] V. Perlick, "Gravitational lensing from a spacetime perspective", *Living Reviews in Relativity*, vol. 7, no. 1, pp. 9, December 2004.

[101] A. Chowdhuri, S. Ghosh, and A. Bhattacharyya, "A review on analytical studies in gravitational lensing", *Frontiers in Physics*, vol. 11, 2023.

[102] A. Lupsasca, D. R. Mayerson, B. Ripperda, and S. Staelens, "A beginner's guide to black hole imaging and associated tests of general

relativity", in *Recent Progress on Gravity Tests: Challenges and Future Perspectives*, Cosimo Bambi and Alejandro Cárdenas-Avendaño, Eds., pp. 183–237. Springer Nature Singapore, Singapore, 2024.

[103] P. L. Schechter and J. D. Schnittman, "Basic elements of strong gravitational lensing", *Space Science Reviews*, vol. 221, no. 4, pp. 49, May 2025.

[104] V. I. Dokuchaev, "Images of black holes viewed by a distant observer", *Gravitation and Cosmology*, vol. 30, no. 3, pp. 246–253, September 2024.

[105] K. S. Virbhadra and G. F. R. Ellis, "Schwarzschild black hole lensing", *Phys. Rev. D*, vol. 62, pp. 084003, September 2000.

[106] E. F. Eiroa, G. E. Romero, and D. F. Torres, "Reissner-Nordström black hole lensing", *Phys. Rev. D*, vol. 66, pp. 024010, July 2002.

[107] S. U. Islam, J. Kumar, and Sushant G. Ghosh, "Strong gravitational lensing by rotating Simpson-Visser black holes", *Journal of Cosmology and Astroparticle Physics*, vol. 2021, no. 10, pp. 013, October 2021.

[108] M. L. Ruggiero and D. Astesiano, "Gravitational lensing observables in stationary and axisymmetric solutions in general relativity", *Phys. Rev. D*, vol. 112, pp. 104044, November 2025.

[109] X. Ying and J. Jia, "Off-equatorial deflections and gravitational lensing. II. In general stationary and axisymmetric spacetimes", *Chin. Phys. C*, vol. 49, no. 5, pp. 055103, 2025.

[110] V. Bozza, "Quasiequatorial gravitational lensing by spinning black holes in the strong field limit", *Phys. Rev. D*, vol. 67, pp. 103006, May 2003.

[111] V. Bozza, S. Capozziello, G. Iovane, and G. Scarpetta, "Strong field limit of black hole gravitational lensing", *General Relativity and Gravitation*, vol. 33, no. 9, pp. 1535–1548, September 2001.

[112] V. Bozza, "Gravitational lensing in the strong field limit", *Phys. Rev. D*, vol. 66, pp. 103001, November 2002.

[113] V. Bozza, "Gravitational lensing by black holes", *General Relativity and Gravitation*, vol. 42, no. 9, pp. 2269–2300, September 2010.

[114] S. Mendoza and M. Santibañez-Armenta, "A comparison between the deflection angles of massive and massless particles in the Schwarzschild space-time and their consequences on black hole shadows", *International Journal of Geometric Methods in Modern Physics*, vol. 21, no. 12, pp. 2450209, 2024.

[115] S. Weinberg, *Gravitation and Cosmology: Principles and Applications of the General Theory of Relativity*, John Wiley and Sons, New York, 1972.

[116] C. R. Keeton and A. O. Petters, "Formalism for testing theories of gravity using lensing by compact objects: Static, spherically symmetric case", *Phys. Rev. D*, vol. 72, no. 10, November 2005.

[117] T. Igata, "Deflection angle in the strong deflection limit: A perspective from local geometrical invariants and matter distributions", *Phys. Rev. D*, vol. 113, no. 4, February 2026.

[118] K. Kumar, O. Lechtenfeld, and G. P. Costa, "Trajectories of charged particles in knotted electromagnetic fields", *Journal of Physics A: Mathematical and Theoretical*, vol. 55, no. 31, pp. 315401, July 2022.

[119] R. P. Feynman, R. B. Leighton, and M. Sands, *The Feynman Lectures on Physics*, vol. 2, Addison-Wesley, Reading, MA, 1963.

[120] K. S. Thorne, "Closed timelike curves", in *13th Conference on General Relativity and Gravitation (GR-13)*, 1993, pp. 295–315.

[121] F. Echeverria, G. Klinkhammer, and K. S. Thorne, "Billiard balls in wormhole spacetimes with closed timelike curves: Classical theory", *Phys. Rev. D*, vol. 44, no. 4, pp. 1077–1099, August 1991.

[122] E. V. Mikheeva and I. D. Novikov, "Inelastic billiard ball in a spacetime with a time machine", *Phys. Rev. D*, vol. 47, no. 4, pp. 1432–1436, February 1993.

[123] A. Carlini, V. P. Frolov, M. B. Mensky, I. D. Novikov, and H. H. Soleng, "Time machines: the principle of self-consistency as a

consequence of the principle of minimal action", *International Journal of Modern Physics D*, vol. 4, no. 5, pp. 557–580, 1995.

[124] A. Carlini, V. P. Frolov, M. B. Mensky, I. D. Novikov, and H. H. Soleng, "Errata: "time machines: the principle of self-consistency as a consequence of the principle of minimal action"", *International Journal of Modern Physics D*, vol. 5, no. 1, pp. 99–100, 1996.

[125] A. Carlini and I. D. Novikov, "Time machines and the principle of self-consistency as a consequence of the principle of stationary action (ii): the Cauchy problem for a self-interacting relativistic particle", *International Journal of Modern Physics D*, vol. 5, no. 5, pp. 445–479, 1996.

[126] J. Dolanský and P. Krtouš, "Billiard ball in the space with a time machine", *Phys. Rev. D*, vol. 82, no. 12, pp. 124056, December 2010.

[127] G. Battistotti, "Closed timelike curves in the Kerr metric", Master's thesis, Università degli Studi di Trento, 2014.

[128] M. Calvani, F. de Felice, B. Muchotrzeb, and F. Salmistraro, "Time machine and geodesic motion in Kerr metric", *General Relativity and Gravitation*, vol. 9, no. 2, pp. 155–163, 1978.

[129] D. Astesiano, D. Bini, A. Geralico, and M. L. Ruggiero, "Particle motion in a rotating dust spacetime", *Phys. Rev. D*, vol. 109, no. 12, pp. 124011, June 2024.

[130] A. F. Rañada, "A topological theory of the electromagnetic field", *Letters in Mathematical Physics*, vol. 18, pp. 97–106, August 1989.

[131] A. F. Rañada, "Knotted solutions of the maxwell equations in vacuum", *Journal of Physics A: Mathematical and General*, vol. 23, pp. L815–L820, 1990.

[132] H. Hopf, "Über die Abbildungen der dreidimensionalen Sphäre auf die Kugelfläche", *Mathematische Annalen*, vol. 104, no. 1, pp. 637–665, 1931.

[133] A. F. Rañada, "Topological electromagnetism", *Journal of Physics A: Mathematical and General*, vol. 25, pp. 1621–1641, 1992.

[134] A. F. Rañada and J. L. Trueba, "Electromagnetic knots", *Physics Letters A*, vol. 202, pp. 337–342, July 1995.

[135] A. F. Rañada and J. L. Trueba, "The electromagnetic helicity", *European Journal of Physics*, vol. 17, pp. 141–144, 1996.

[136] A. F. Rañada and J. L. Trueba, "Two properties of electromagnetic knots", *Physics Letters A*, vol. 232, pp. 25–33, July 1997.

[137] A. F. Rañada and J. L. Trueba, "A topological mechanism of discretization for the electric charge", *Physics Letters B*, vol. 422, pp. 196–200, March 1998.

[138] A. F. Rañada and J. L. Trueba, "Topological electromagnetism with hidden nonlinearity", in *Modern Non Linear Optics Part III*, M. W. Evans, Ed., vol. 119, pp. 197–253. Wiley, New York, September 2001.

[139] A. F. Rañada, "Interplay of topology and quantization: topological energy quantization in a cavity", *Physics Letters A*, vol. 310, pp. 434–444, April 2003.

[140] A. F. Rañada and J. L. Trueba, "Topological quantization of the magnetic flux", *Foundations of Physics*, vol. 36, no. 3, pp. 427–436, March 2006.

[141] H. Bateman, "The mathematical analysis of electrical and optical wave-motion on the basis of maxwell's equations. homogeneous linear substitutions", *Nature*, vol. 96, no. 2395, pp. 85–86, September 1915.

[142] H. Kedia et al., "Tying knots in light fields", *Physical Review Letters*, vol. 111, pp. 150404, 2013.

[143] J. Leach et al., "Vortex knots in light", *New Journal of Physics*, vol. 7, pp. 55, 2005.

[144] W. T. M. Irvine and D. Bouwmeester, "Linked and knotted beams of light", *Nature Physics*, vol. 4, pp. 716–720, 2008.

[145] I. Bialynicki-Birula, "Helicity amplitudes, polarization of EM waves and Stokes parameters", *Journal of Optics*, vol. 21, pp. 094002, 2019.

[146] I. Bandos, K. Lechner, D. Sorokin, and P. K. Townsend, "Nonlinear duality-invariant conformal extension of Maxwell's equations", *Phys. Rev. D*, vol. 102, pp. 121703, December 2020.

[147] B. P. Kosyakov, "Nonlinear electrodynamics with the maximum allowable symmetries", *Physics Letters B*, vol. 810, pp. 135840, November 2020.